

DISSERTATION

RADAR AND SATELLITE OBSERVATIONS OF PRECIPITATION:
SPACE TIME VARIABILITY, CROSS-VALIDATION, AND FUSION

Submitted by

Haonan Chen

Department of Electrical and Computer Engineering

In partial fulfillment of the requirements

For the Degree of Doctor of Philosophy

Colorado State University

Fort Collins, Colorado

Fall 2017

Doctoral Committee:

Advisor: V. Chandrasekar

Steven C. Reising

Margaret Cheney

Paul W. Mielke

Copyright by Haonan Chen 2017

All Rights Reserved

ABSTRACT

RADAR AND SATELLITE OBSERVATIONS OF PRECIPITATION: SPACE TIME VARIABILITY, CROSS-VALIDATION, AND FUSION

Rainfall estimation based on satellite measurements has proven to be very useful for various applications. A number of precipitation products at multiple time and space scales have been developed based on satellite observations. For example, the National Oceanic and Atmospheric Administration (NOAA) Climate Prediction Center has developed a morphing technique (i.e., CMORPH) to produce global precipitation products by combining existing space-based observations and retrievals. The CMORPH products are derived using infrared (IR) brightness temperature information observed by geostationary satellites and passive microwave (PMW)-based precipitation retrievals from low earth orbit satellites. Although space-based precipitation products provide an excellent tool for regional, local, and global hydrologic and climate studies as well as improved situational awareness for operational forecasts, their accuracy is limited due to restrictions of spatial and temporal sampling and the applied parametric retrieval algorithms, particularly for light precipitation or extreme events such as heavy rain.

In contrast, ground-based radar is an excellent tool for quantitative precipitation estimation (QPE) at finer space-time scales compared to satellites. This is especially true after the implementation of dual-polarization upgrades and further enhancement by urban scale X-band radar networks. As a result, ground radars are often critical for local scale rainfall estimation and for enabling forecasters to issue severe weather watches and warnings. Ground-based radars are also used for validation of various space measurements and products.

In this study, a new S-band dual-polarization radar rainfall algorithm (DROPS2.0) is developed that can be applied to the National Weather Service (NWS) operational Weather Surveillance Radar-1988 Doppler (WSR-88DP) network. In addition, a real-time high-resolution QPE system is developed for the Engineering Research Center for Collaborative Adaptive Sensing of the Atmosphere (CASA) Dallas-Fort Worth (DFW) dense radar network, which is deployed for urban hydrometeorological applications via high-resolution observations of the lower atmosphere. The CASA/DFW QPE system is based on the combination of a standard WSR-88DP (i.e., KFWS radar) and a high-resolution dual-polarization X-band radar network. The specific radar rainfall methodologies at S- and X-band frequencies, as well as the fusion methodology merging radar observations at different temporal resolutions are investigated. Comparisons between rainfall products from the DFW radar network and rainfall measurements from rain gauges are conducted for a large number of precipitation events over several years of operation, demonstrating the excellent performance of this urban QPE system. The real-time DFW QPE products are extensively used for flood warning operations and hydrological modelling. The high-resolution DFW QPE products also serve as a reliable dataset for validation of Global Precipitation Measurement (GPM) satellite precipitation products.

This study also introduces a machine learning-based data fusion system termed deep multi-layer perceptron (DMLP) to improve satellite-based precipitation estimation through incorporating ground radar-derived rainfall products. In particular, the CMORPH technique is applied first to derive combined PMW-based rainfall retrievals and IR data from multiple satellites. The combined PMW and IR data then serve as input to the proposed DMLP model. The high-quality rainfall products from ground radars are used as targets to train the DMLP model. In this dissertation, the prototype architecture of the DMLP model is

detailed. The urban scale application over the DFW metroplex is presented. The DMLP-based rainfall products are evaluated using currently operational CMORPH products and surface rainfall measurements from gauge networks.

ACKNOWLEDGMENTS

First and foremost, I would like to express my deep appreciation to Prof. V. Chandrasekar for accepting me as a graduate research assistant, for introducing me to the radar meteorology and related sciences community, and for all his support during my graduate studies at Colorado State University. It has been a great honor and pleasure to study and conduct research under the supervision of Prof. Chandra. He is my mentor not only in research, but also in life! I would also like to express my sincere thanks to Profs. Steven C. Reising, Margaret Cheney, and Paul W. Mielke for serving as my graduate committee members.

I am grateful to Dr. Robert Cifelli for his guidance and encouragement during my stay at NOAA's Earth System Research Laboratory in Boulder. I also want to thank other NOAA colleagues, in particular Dr. Pingping Xie for his support and many technical discussions.

I wish to thank Patrick Kennedy, Jim George, and Dr. Francesc Junyent of the CSU-CHILL National Radar Facility for their kind help during my graduate studies. Thanks also go to the former and current members of the CSU Radar Group, in particular Drs. Yanting Wang, Sanghun Lim, Renzo Bechini, Nitin Bharadwaj, Cuong M. Nguyen, Joseph C. Hardin, Robert M. Beauchamp, Delbert Willie, and Mr. Haiming Tan for their friendship and assistance in my research work. Some of the key personnel in the CASA team, namely, Brenda Philips, Eric Lyons and Apoorva Bajaj, are also acknowledged for their support during the operation of the CASA Dallas-Fort Worth (DFW) dense urban radar network.

In addition, I would like to thank Dr. Walter A. Petersen and Mr. David B. Wolff for their feedback and discussions on the use of CSU dual-polarization radar rainfall methodologies.

This study was supported by the National Science Foundation (NSF) Engineering Research Center (ERC) program under award number 0313747, the NSF Accelerating Innovation Research (AIR) program, and the NSF Hazards Science, Engineering and Education for Sustainability (SEES) program. The support from NOAA/NWS and the North Central Texas Council of Governments (NCTCOG) is also acknowledged. Additionally, some of the results presented in this dissertation were obtained from research granted by the NASA Global Precipitation Measurement (GPM)/Precipitation Measurement Mission (PMM) program.

DEDICATION

This work is dedicated to my parents (Shuangyue Chen and Yuying Liu), my sisters (Dr. Xudong Chen and Xuhong Chen), and my wife (Dr. Yajing Liu) for their endless love and support.

TABLE OF CONTENTS

Abstract	ii
Acknowledgments	v
List of Tables	x
List of Figures	xii
Chapter 1. Introduction	1
1.1. Problem Statement	4
1.2. Research Objectives.....	6
1.3. Organization of the Dissertation	7
Chapter 2. Challenges of Rainfall Estimation	9
2.1. Rain gauge-based rainfall measurement.....	9
2.2. Satellite-based rainfall estimation	12
2.3. Radar-based rainfall estimation	15
Chapter 3. An Improved Dual-Polarization Radar Rainfall Algorithm (DROPS2.0)...	31
3.1. DROPS2.0 Rainfall Algorithm	35
3.2. Application in NASA IFloodS Field Campaign.....	43
3.3. Summary	57
Chapter 4. Dense Radar Network for Urban Weather Hazards Detection and Mitigation	60
4.1. Background of CASA	61
4.2. CASA Dallas-Fort Worth (DFW) Dense Urban Radar Network.....	67
4.3. Sample CASA/DFW Products in the Presence of Tornado, High Wind, Hail, and Flood.....	73

4.4. Summary	88
Chapter 5. The High-Resolution, Real-Time QPE System for the CASA/DFW	
Network: System Development and Product Performance.....	92
5.1. CASA/DFW QPE System and Sample Products.....	93
5.2. Evaluation of CASA/DFW QPE Products	100
5.3. Summary	115
Chapter 6. Application of High-Resolution Ground Radar Observations to Satellite	
Precipitation Data Fusion	118
6.1. Review of NOAA CMORPH Satellite Precipitation Product.....	123
6.2. A Machine Learning System for Radar and Satellite Precipitation Data Fusion	137
6.3. Urban Scale Application of the Proposed Machine Learning System	149
6.4. Summary	160
Chapter 7. Summary, Conclusions and Future Work	162
7.1. Summary and Conclusions	162
7.2. Future Work.....	165
Bibliography	166

LIST OF TABLES

3.1 NPOL radar and APU disdrometer locations during the NASA IFloodS field experiment. The ranges and bearings relative to NPOL are calculated using the 1980 Geodetic Reference System. 34

3.2 Evaluation results of various rainfall products at different time scales for the 20 May 2013 event. 53

3.3 Evaluation results of various rainfall products at different time scales for the 25 May 2013 event. 54

3.4 Evaluation results of rainfall products at different time scales for the 29 May 2013 event. “-” indicates no rain observed by radar or APU. 55

3.5 Evaluation results of various rainfall products at different time scales for the three events combined. 56

4.1 Longitude/latitude information of the eight dual-polarization X-band radar nodes in the DFW urban network. The altitudes above mean sea level (AMSL), as well as the cities where the radar are deployed are also listed. The one marked with * (i.e., XMKN radar) is yet to be deployed. 68

4.2 System specifications of DFW X-band radar versus WSR-88DP S-band radar. 70

5.1 Real-time rainfall products from DFW urban radar network. 97

5.2 Summary of several precipitation events in 2013. Columns (from left to right) refer to the rainfall date, the time when intense rainfall was passing over the gauge network, and notes regarding the precipitation type and weather impact. 101

5.3	Evaluation results (<i>NMB</i> : normalized mean bias, and <i>NSE</i> : normalized standard error) of various rainfall products at different time scales. ‘-’ indicates that an operational product is not available from the NWS.	109
5.4	Evaluation results (<i>NMB</i> and <i>NSE</i>) of various rainfall products at different time scales for 11 events combined. ‘-’ indicates that an operational product is not available from the NWS. The 11 events are 18 April 2013, 16 May 2013, 09 June 2013, 27 October 2013, 09 May 2014, 18 July 2014, 18 August 2014, 11 May 2015, 29 May 2015, 26 November 2015, and 26 December 2015.	110
6.1	A summary of commonly used satellite precipitation products. The PERSIANN-Cloud Classification System (CCS) is essentially an enhanced PERSIANN products.	122
6.2	PMW sensors whose precipitation retrievals are presently (to date) used in CMORPH.	124
6.3	Characteristics of geostationary IR data used in this study.	126
6.4	Training and testing events for developing the machine learning-based system merging satellite and ground radar rainfall observations.	155
6.5	Evaluation results of the CMORPH, DMLP, and combined PMW-based rainfall estimates for the time frame of 20:00UTC, June 24, 2014.	159

LIST OF FIGURES

1.1	Instrument commonly used to measure precipitation.....	1
2.1	5-min rainfall accumulations from a rain gauge and collocated disdrometer at (42.1224°N, 92.2806°W) during a storm event in Iowa on June 4, 2013.....	11
2.2	Conceptual diagram of rainfall estimation using geostationary satellite Infrared (IR) data.	13
2.3	Conceptual diagram of rainfall estimation using low earth orbit satellite passive microwave (PMW) sensors.	14
2.4	The operational WSR-88DP locations over the United States and its territories. All the radar nodes are operating at S-band frequency.	16
2.5	Weather radar sensing distributed targets within a sample volume. The sample volume size is determined by the radar’s horizontal and vertical beamwidths θ and φ , and range spacing ΔR	16
2.6	Range-time characteristics of a pulse Doppler radar system.....	17
2.7	Scattergram of rainfall rate R versus reflectivity Z . Both R and Z values are computed based on DSD data collected during the NASA IPHEX field experiment. The black curve indicates the best-fitting power-law relation of $R(Z)$. The grey bars stand for the mean and standard deviation of the binned data.	23
2.8	Scattergram of rainfall rate R versus specific differential propagation phase K_{dp} . Both R and K_{dp} values are computed based on DSD data collected during the NASA IFloodS field experiment (Chen and Chandrasekar 2015a). The black curve indicates the best-fitting power-law relation of $R(K_{dp})$	24

2.9	(a) Center beam height as a function of range from radar for the 14 elevation tilts of the WSR-88DP volume coverage pattern 12 (VCP12) scan mode. (b) Height of the lowest (0.5 degree) beam in the VCP12 scan mode. The beam height is calculated based on the 4/3 earth radius model.....	29
2.10	WSR-88DP radar coverage at 1 km AGL over the continental U.S. The coverage map is essentially derived based on the center beam height of 0.5-degree elevation (courtesy of NOAA/NWS/OST).....	30
3.1	Diagram of the blended rainfall algorithm developed at CSU (DROPS1.0). The algorithm is driven by the fuzzy logic-based hydrometeor classification approach..	31
3.2	Generic blocks of a traditional fuzzy logic-based hydrometeor classification approach.....	32
3.3	Deployment of NPOL radar during NASA’s IFloodS field campaign. The red plus signs denote the locations of 14 APU disdrometers. Rain gauges are collocated with 10 disdrometers with underlines.....	35
3.4	Architecture of the DROPS2.0 rainfall algorithm for dual-polarization S-band radar.	36
3.5	Flowchart of differential phase processing, where N_G and N_B are constant numbers of consecutive good and bad gates, respectively.....	37
3.6	S-band NASA NPOL radar observations at 23:43UTC, May 29, 2013. (a) Z , (b) Z_{dr} , (c) K_{dp} , (d) ρ_{hv} , and (e) corresponding hydrometeor classification results.....	40
3.7	(a) Scattergram of estimated rainfall rates with S-band rainfall algorithm in Equation (18) versus rainfall rates directly computed from DSD data. The black	

line indicates the 1:1 line; (b) normalized standard deviation of parameterization errors in various rainfall algorithms as a function of rainfall intensity.....	44
3.8 Sample NPOL radar observations at 03:50 UTC 20 May 2013: (a) Z , (b) Z_{dr} , (c) ϕ_{dp} , (d) ρ_{hv} , and corresponding rainfall-rate estimates using different algorithms: (e) NEXRAD $Z - R$, (f) NEXRAD DP, and (g) DROPS2.0.....	46
3.9 As in Figure 3.8, but for observations at 15:39 UTC 25 May 2013.....	47
3.10 As in Figure 3.8, but for observations at 22:48 UTC 29 May 2013.....	48
3.11 Scatterplots of radar rainfall estimates versus APU observations at different time scales at a sample APU location (APU03): (a) 5-, (b) 15-, (c) 30-, (d) 45-, and (e) 60-min.....	51
3.12 Evaluation results of rainfall products at different time scales with various rainfall algorithms at the location of APU03 for all the events combined: (a) $NMAE$, (b) $RMSE$, and (c) $CORR$	52
3.13 Conceptual diagram showing radar beam broadening effect.....	57
3.14 $CORR$ of rainfall products at different time scales with various rainfall algorithms at different ranges from radar for all the events combined: (a) 5-, (b) 15-, (c) 30-, (d) 45-, and (e) 60-min rainfall.....	58
4.1 Simplified architecture of a distributed collaborative adaptive sensing (DCAS) system. The real-time data and products are disseminated to various end users. Through meteorological command & control (MC&C) the radar network scanning strategy is adapted according to feedback from end users.....	63

4.2	CASA IP1 testbed in Oklahoma. The letter symbols such as KSAO denote the names of the various radars. The circles in blue correspond to the 40 km converge range rings of the X-band radars.	65
4.3	Installation of CASA DFW radars. The letter symbols (e.g., XUTA) correspond to the naming of various radars. More information about DFW radar deployment can be found in Table 4.1.	68
4.4	The layout of S-band KFWS WSR-88DP radar (100 km range ring in red) and DFW dual-polarization X-band radars (40 km range rings in blue). Letter symbols such as XMDL correspond to the names of the various radars.	69
4.5	Closed-loop dataflow architecture of the DFW urban radar network. Through the Internet, the radar data are streamed to DROC, where the majority of the real-time products are generated and archived. The real-time products are available to a variety of end users. Based on the users' feedback, the radar control commands are sent out from the DROC.	71
4.6	Schematic diagram illustrating the space-time integration of DFW observations at different frequencies and time scales.	74
4.7	Diagram of the operational hydrometeor classification and hail detection system for the DFW dense urban radar network.	76
4.8	Sample CASA X-band radar observations and corresponding hydrometeor classification results at 04:15UTC, May 20, 2011: (a) Z , (b) Z_{dr} , (c) ρ_{hv} , (d) classified hydrometeor types. The Z and Z_{dr} fields shown here are after attenuation correction.	77
4.9	DFW hail product at 02:39UTC, March 24, 2016.	78

4.10	Sample dual-polarization observations from a DFW X-band radar (XUTA radar) and corresponding hydrometeor classification results at 20:50UTC, May 12, 2014: (a) Z , (b) Z_{dr} , (c) K_{dp} , (d) ρ_{hv} , and (e) classified hydrometeor types. The Z and Z_{dr} fields shown here are after attenuation correction.	79
4.11	DFW radar network-based hail product (path/duration) over Joe Pool Lake from 20:37 to 20:57UTC, May 12, 2014. The hailfall and hail path were demonstrated by social media reports.	80
4.12	Framework of real-time Doppler wind retrieval system and application for the DFW urban radar network.	83
4.13	NWS tornado report for the EF0 tornado that occurred in Cockrell Hill in the DFW area on May 8, 2014.	85
4.14	Multi-Doppler wind velocity retrieval results based on the DFW dense radar network during the EF0 tornado event on May 8, 2014, at (a) 20:14 and (b) 20:15UTC. The results are at 1 km height level. The arrows denote the magnitude and direction of the retrieved wind velocity. The maximum velocity at 20:14UTC is about 112.7 km hr ⁻¹ , and 119.0 km hr ⁻¹ at 20:15UTC. The color-coded field represents the vertical vorticity. The vortex locations agree fairly well with the NWS tornado report shown in Figure 4.13.	86
4.15	Real-time DFW multiple Doppler radar wind retrieval system product at 1-km height during the high wind event on October 02, 2014, at 20:53UTC: (a) composite reflectivity overlaid with retrieved wind directions, (b) retrieved wind speed and directions.	87

4.16	Sample instantaneous rainfall rate products from the DFW network radar QPE system for a 15-min period (02:01-02:15UTC) during the storm event of May 29, 2015.	89
4.17	Sample instantaneous rainfall rate products from the DFW network radar QPE system for a 10-min period (02:21-02:30UTC) during the storm event of November 27, 2015.....	90
5.1	Key features of the CASA DFW urban radar network for rainfall estimation and hydrological applications.	94
5.2	Schematic diagram of the QPE system for the CASA DFW urban remote sensing network.	95
5.3	Real-time rainfall products from the DFW QPE system on November 27, 2015, at 12:00UTC. (a) instantaneous rainfall rate, (b) 5-min, (c) 15-min, (d) 30-min, (e) 60-min, (f) 3-hr, (g) 6-hr, and (h) 12-hr rainfall.	97
5.4	Sample real-time rainfall products on May 29, 2015, at 03:00UTC. (a) instantaneous rainfall rate, (b) 5-, (c) 15-, (d) 30-, (e) 45-. and (f) 60-min rainfall.	99
5.5	Sample real-time rainfall products for a 10 km by 10 km area during the flash flood event of June 24, 2014, at 21:39UTC.	100
5.6	Sample observations from the S-band KFWS WSR-88DP radar 0.5 degree scan at 08:47UTC, 18 April 2013. (a) Z , (b) Z_{dr} , (c) K_{dp} , and (d) corresponding rainfall rate R	102
5.7	As in Figure 5.6, but for observations at 04:45UTC, 16 May 2013.....	103
5.8	As in Figure 5.6, but for observations at 12:31UTC, 09 June 2013.	104
5.9	As in Figure 5.6, but for observations at 02:39UTC, 27 October 2013.....	105

5.10	Locations of rain gauges (red triangles) used for the DFW rainfall product evaluation. The gauges are managed and operated by the city of Fort Worth and city of Grand Prairie.	106
5.11	15-min rainfall (thin lines) and rainfall accumulations (thick lines) from the DFW radar network and gauges at sample gauge locations during the 2015 Thanksgiving flood event. The upper, middle, and bottom panels illustrate the products at gauges 1100 (32.7952°N, 97.3368°W), 1030 (32.8181°N, 97.4534°W), and 1800 (32.6141°N, 97.3468°W), respectively.	108
5.12	Scatterplots of hourly rainfall accumulations from the CASA DFW QPE system versus rain gauge measurements for the four example events (combined) described in Section 5.2.1. (a) CASA DFW QPE system product, (b) NWS N1P product, (c) NWS OHA product, and (d) NWS DAA product.	112
5.13	The <i>NSEs</i> of hourly rainfall products operationally generated by the NWS and CASA DFW QPE systems for 11 events combined, including 18 April 2013, 16 May 2013, 09 June 2013, 27 October 2013, 09 May 2014, 18 July 2014, 18 August 2014, 11 May 2015, 29 May 2015, 26 November 2015, and 26 December 2015.	113
5.14	Scatterplots of (a) 5-, (b) 10-, (c) 15-, (d) 20-, and (e) 30-min rainfall accumulations from the CASA DFW QPE system versus rain gauge measurements for the four example events described in Section 5.2.1.	114
5.15	The <i>NSEs</i> of the CASA DFW QPE products at different time scales, for the 11 events combined. The error bars in grey represent the variability of performance at different gauge locations.	115

6.1	Typical sampling coverage of current passive microwave sensors for each half-hour window during a 3-hr period on May 29, 2015. The 16 sensors are on board TRMM, Aqua, FY-3B, DMSP, MetOp, and NOAA satellites. The bottom panel shows a 3-h composite of the half-hourly coverage maps in the upper three panels.	120
6.2	Conceptual diagram of CMORPH technique.	123
6.3	Combined PMW-based precipitation retrievals over continental U.S., 00:00-02:30UTC, May 29, 2015. The satellites included here are TRMM, Aqua, FY-3B, DMSP F-13, -14, -15, -16, -17, -18, MetOp-A, -B, and NOAA-15, -16, -17, -18, -19. The spatial resolution is about 8 km × 8 km.	129
6.4	Combined IR brightness temperature data collected at the same time as Figure 6.3. The IR data are based on five geostationary satellites: Himawari-8, GOES-13, GOES-15, Meteosat-7, and Meteosat-10.	130
6.5	Illustration of the propagation and morphing process in CMORPH (adopted from Joyce et al. (2004)). The estimates at time frames 03:30 and 05:00UTC are real PMW-based retrievals with no propagation or morphing applied. The estimates at 04:00 and 04:30UTC are (a) forward propagated in time, (b) backward propagated in time, and (c) morphed from propagation in both directions.	134
6.6	Sample CMORPH products over the continental U.S. on May 29, 2015. The corresponding PMW and IR data are shown in Figures 6.3 and 6.4, respectively.	136
6.7	Simplified diagram of machine learning-based radar and satellite precipitation data fusion.	138
6.8	(a) A 2-layer neural network with three inputs, one hidden layer of 4 neurons, and one output layer with 2 neurons. (b) A 3-layer neural network with three inputs,	

	two hidden layers of 4 neurons each and one output layer. Notice that in both (a) and (b) there are connections between neurons across layers, but not within a layer.	139
6.9	(a) Example of a perceptron. (b) A single layer with two perceptrons. Each output can be related to the three inputs through the perceptrons.	140
6.10	Activation functions and their derivatives commonly used in neural network. (a) The sigmoid function. (b) The rectified linear unit (ReLU).	141
6.11	Generic concept of the application of DMLP model in producing enhanced precipitation products using radar and satellite data.	142
6.12	(a) Overall architecture of the DMLP Model for radar and satellite precipitation estimation.	143
6.13	DMLP model optimization for radar and satellite rainfall estimation.	146
6.14	(a) Example TensorFlow code fragment. (b) Computation graph for (a).	148
6.15	(a) DMLP model update when new training data are available. This is specially for given hyper parameters. (b) Grid approach to the selection of hyper parameters. .	150
6.16	Urban scale application of the deep multi-layer perceptron (DMLP) model for rainfall estimation over DFW Metroplex.	151
6.17	Spatial averaging of satellite IR data (~ 4 km resolution) to match satellite PMW-based rainfall data (i.e., ~ 8 km grids). In this study, a simple linear average is applied. In particular, 2×2 IR grid pixels are averaged. Data shown here were collected on June 23, 2014.	152
6.18	Temporal and spatial averaging of high-resolution DFW radar rainfall products to match satellite PMW-based precipitation retrievals. Temporally, 30 frames of	

DFW radar products from 00-29 mins of each hour are averaged for the first half hour window (a), and 30 frames from 30-59 mins are averaged for the second half hour window (b). Spatially, 250m × 250m high-resolution rainfall products are averaged to 8km × 8km grid. 154

6.19 Cross-comparison of various rainfall products on June 24, 2014, at 20:00UTC. (a) DFW radar network rainfall estimates (after averaging); (b) rainfall estimates from the DMLP model; (c) combined PMW-based rainfall retrieval; (d) CMORPH products. 157

6.20 Cross-comparison of various rainfall products at 23:00UTC, June 24, 2014. (a) DFW radar network rainfall estimates (after averaging); (b) rainfall estimates from the DMLP model; (c) combined PMW-based rainfall retrieval; (d) CMORPH products; (e) high resolution rainfall product from DFW radar network (before averaging); (f) corresponding IR data. 158

6.21 Probability distribution of rainfall rate estimates from the DFW radar network, PMW measurements, CMORPH, and the DMLP model developed in this study. Results show that the DMLP model-based products capture low rainfall rates better than CMORPH or the PMW-only based products. The products presented here are for the time frame of 23:00UTC, June 24, 2014. 160

CHAPTER 1

INTRODUCTION

Water, a primordial element of life, impacts almost every segment of human society. A large amount of infrastructure, including rain gauges, disdrometers, weather radars, and meteorological satellites (see Figure 1.1), has been deployed to directly or indirectly measure rainfall and its space time distribution.

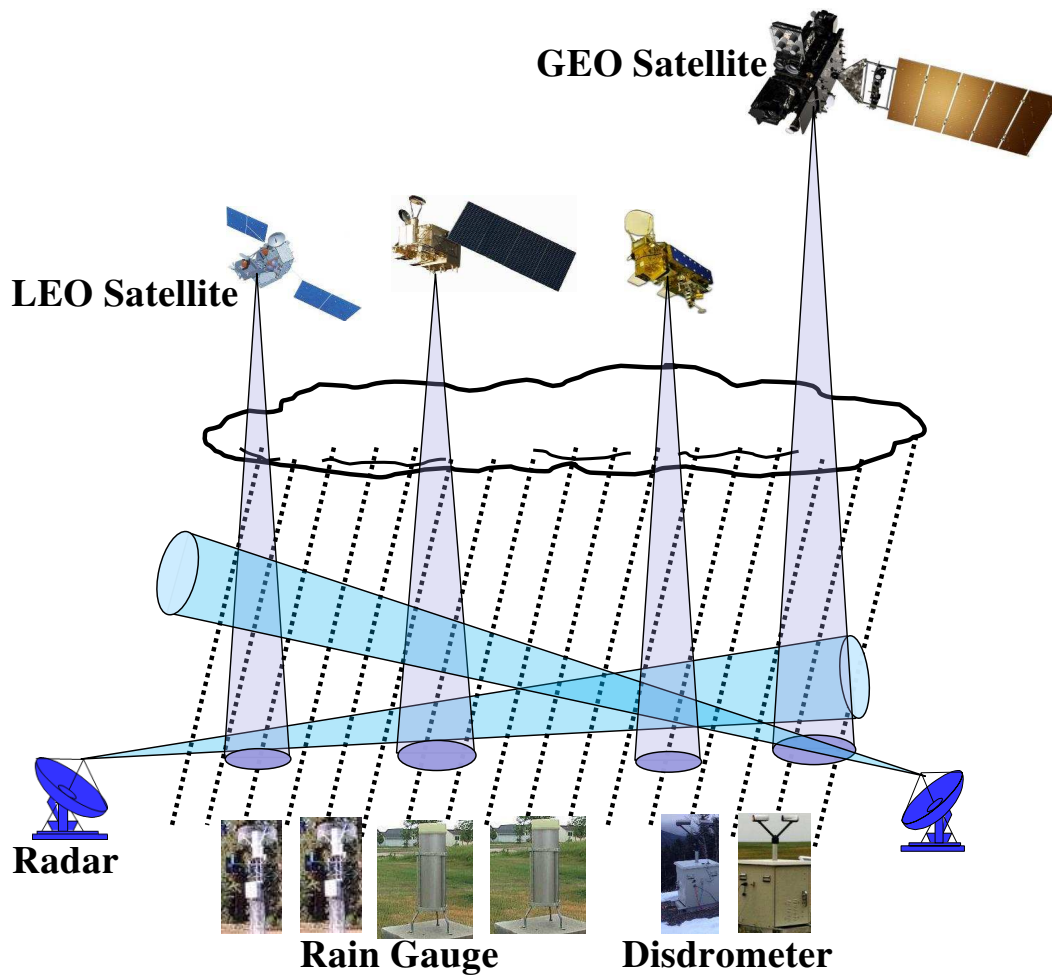


FIGURE 1.1. Instrument commonly used to measure precipitation.

Among these tools, rain gauges are traditionally used and are still widely used today. However, the accuracy of rain gauge data faces a number of error factors. Alongside the

random and systematic errors, the resolution of sampling time and bucket volume of rain gauges may introduce additional uncertainties, especially under light rain circumstances. The most significant limitation of using rain gauges to measure rainfall is that they only provide point-wise observations. A huge number of rain gauges must be deployed in order to capture the complex spatial and temporal variability of precipitation. In the real world, this is neither possible nor necessary due to the arduous nature of the deployment and maintenance of the gauges. Kidd et al. (2017) concluded that the total area measured globally by all currently available rain gauges is surprisingly small, equivalent to less than half a football field or soccer pitch.

Compared to rain gauges, satellites have coverage advantages over most of the globe, especially in the ocean and polar regions. Therefore, rainfall estimation based on satellite measurements has been an important topic since the earliest meteorological application of satellites (Kidd and Levizzani 2011). In recent years, a number of precipitation products at multiple time and space scales have been developed using satellite observations. For example, the National Oceanic and Atmospheric Administration (NOAA) Climate Prediction Center has proposed a morphing technique (CMORPH) to derive global precipitation products by combining existing space-based measurements and retrievals (Joyce et al. 2004). In particular, the geostationary satellite infrared (IR) brightness temperature information and precipitation retrievals from low-earth-orbit passive microwave (PMW) measurements are essentially used to produce CMORPH products (Joyce et al. 2004; Xie et al. 2017). The various satellite-based precipitation products are commonly used for disaster monitoring worldwide and for initializing numerical weather prediction (NWP) models and validation of the model-based precipitation forecasts. However, for many applications such as flash flood

warnings, higher resolution precipitation estimation is needed in both spatial and temporal domains.

According to the U.S. National Academy report, floods are responsible for more deaths nationwide than any other weather phenomenon (NRC National Research Council 2005). In addition, ongoing rapid urbanization has made densely populated areas even more vulnerable to flood risks since the heavy development in urban regions decreases the response time of urban watersheds to rainfall and subsequently increases the chance of localized flooding events over small spatial domains. From a temporal perspective, small-scale urban flash floods can occur within a few minutes after local torrential rainfall due to urban characteristics such as impervious cover and complex drainage system. In such scenarios, accurate and timely estimation of precipitation and streamflow is critical for civil defense, especially in urban areas. High-resolution high-quality precipitation products are also prerequisites for complex hydrological and hydraulic modelling. However, it is challenging to obtain such high-quality rainfall estimates using only rain gauges and/or satellite measurements. In this context, ground-based weather radar has shown great advantages in conducting precipitation observations over wide areas in a relatively short time span. Hence, weather radars have been widely used for rainfall measurement applications and studies of the microphysical characteristics of precipitation. They form the cornerstones of national severe weather warning and forecasting infrastructure in many developed countries.

Traditionally, quantitative precipitation estimation (QPE) with radars starts with reflectivity and rainfall rate relationships, commonly referred to as $Z - R$ relations. These relations have usually been applied to single polarization radar systems and are still in use today. Since 2011, the National Weather Service (NWS) had initiated an effort to upgrade the operational S-band (wavelength ~ 10 cm) Weather Surveillance Radar-1988 Doppler

(WSR-88DP) network to include dual-polarization capabilities. Currently, all the WSR-88DP sites in the contiguous United States (CONUS) operate in dual-polarization mode (<https://www.roc.noaa.gov>). One of the main drivers for dual-polarization upgrade has been better rainfall estimation. The dual-polarization radar observations offer a number of advantages over single-polarization radar by gleaning more information about raindrop size distribution (DSD) and providing more characteristics for discriminating precipitation echoes from non-precipitation echoes. The combination of dual-polarization radar measurements and environmental temperature is also capable of identifying different hydrometeor types over illuminated scanning volumes (Liu and Chandrasekar 2000; Lim et al. 2005; Chandrasekar et al. 2013; Bechini and Chandrasekar 2015). Efficient and effective hydrometeor classification can further enhance the performance of QPE (Cifelli et al. 2011; Chen et al. 2017a).

1.1. PROBLEM STATEMENT

The space-based precipitation product is an excellent tool for regional, local, and global hydrologic and climate studies. It is generally used in operational global weather models for improving situational awareness. However, its accuracy is severely hindered by spatial-temporal sampling limitations as well as uncertainties introduced by the parametric retrieval algorithms, especially for extreme events such as very heavy or very light rain.

On the other hand, although the radar QPE performance has been significantly improved through dual-polarization upgrades, there is still no standard methodology that can be applied to obtain optimal QPE for a given set of dual-polarization measurements. How to fully address the fundamental science in radar QPE remains challenging. In addition, numerous

studies have concluded that the challenges in radar QPE come not only from physical considerations but also from system engineering issues such as radar measurement height, beam broadening, and coverage limitations (Chen and Chandrasekar 2015b). Such engineering challenges are specially obvious in operational or urban environments. Operationally, the S-band radars comprising the WSR-88DP network are spaced about 230 km apart in the eastern U.S. and about 345 km apart in the western U.S. At the maximum coverage range of 230 km, the lowest (0.5 degree) beam is about 5.4 km above ground level (AGL) due to the Earth's curvature. Incomplete low-level coverage and degraded spatial resolution at long distances impede the ability of such systems to detect and monitor fine-scale weather features such as tornadoes and flash floods. In order to overcome the WSR-88DP coverage limitations and improve weather sensing in the lower troposphere (1-3 km AGL), the U.S. National Science Foundation Engineering Center (NSF-ERC) for Collaborative Adaptive Sensing of the Atmosphere (CASA) has introduced an innovative sensing paradigm called Distributed Collaborative Adaptive Sensing (DCAS). The DCAS system utilizes dense network of low-power, low-cost, small X-band (wavelength ~ 3 cm) dual-polarization radars to observe, predict, and respond to hazardous weather events (McLaughlin et al. 2009; Chandrasekar et al. 2017). These short-range radars can also serve as gap fillers for the WSR-88DP network by providing enhanced sampling of precipitation and winds near the ground. The first CASA research test-bed with four radar nodes was deployed in tornado-prone Southwestern Oklahoma at the locations of Cyril, Lawton, Rush Springs, and Chickasha. The high resolution radar observations, post-event analysis, and fundamental multi-disciplinary research during five-years of operation demonstrated the success of the CASA concept (McLaughlin et al. 2009; Chandrasekar et al. 2012).

Since 2012, CASA, in collaboration with the North Central Texas Council of Governments (NCTCOG) and the NWS, has embarked on the development of its first urban test bed in the Dallas-Fort Worth (DFW) metroplex, one of the largest metropolitan areas in the U.S. This urban remote sensing network, centered by the deployment of eight boundary-layer observing dual-polarization X-band radars and a WSR-88DP station (KFWS radar), is expected to provide real-time severe weather products for warning operations in a densely populated urban environment (Chandrasekar et al. 2017). How to produce real-time high-resolution high-quality rainfall products is one of the key research aspects in the deployment of the DFW dense urban radar network.

1.2. RESEARCH OBJECTIVES

The main scientific objective of this research is to explore the potential of ground-based dual-polarization radar network observations for accurate precipitation estimation, and subsequently use the ground radar-derived products to evaluate and improve satellite-based rainfall retrievals. Within this general goal, specific research objectives are devised, including:

- 1) invention of new dual-polarization radar rainfall methodologies that can be applied to operational S-band radar network;
- 2) development of real-time high-resolution high-quality rainfall system for the CASA DFW dense urban (X- and S-band) radar network;
- 3) design of a machine learning-based data fusion system toward improving rainfall estimation using satellite observations (i.e., IR data and PMW-based retrievals). Therein, the ground radar products are used as targets to train the machine learning model.

1.3. ORGANIZATION OF THE DISSERTATION

In Chapter 2, the fundamentals and challenges of rainfall estimation using different platforms are described, including rain gauge, satellite, and weather radar.

Chapter 3 presents a new S-band dual-polarization radar rainfall methodology. This methodology, driven by a region-based hydrometeor classification mechanism, incorporates the spatial coherence and self-aggregation of dual-polarization observables to produce robust rainfall estimates. The proposed algorithm can be easily applied to other radars, including operational WSR-88DP.

Chapter 4 details the development of CASA X-band radar networks. Such networks can overcome the WSR-88DP coverage limitations through enhanced sampling of weather features in the lower troposphere. The dense urban radar network deployed over the DFW metroplex will be described, with an emphasis on its various application products for urban hazard detection and mitigation.

The real-time high-resolution rainfall system designed for the DFW dense urban radar network, as well as the techniques used to integrate radar data at different frequencies and scales, will be detailed in Chapter 5. The DFW QPE system performance will be evaluated using rainfall measurements from a high-quality rain gauge network.

Chapter 6 explores the application of high-resolution ground radar rainfall products to satellite-based precipitation retrievals. The CMORPH technique is implemented first to derive combined IR data from five geostationary satellites and PMW-based precipitation estimates from multiple low earth orbit satellites. Then, a machine learning system is introduced to improve rainfall estimation based on PMW-based retrievals and IR data, using ground radar-derived rainfall products as target labels. An urban-scale application of the proposed Deep Multi-Layer Perceptron (DMLP) model in the DFW area will be presented.

Chapter 7 summarizes the main points of this study and suggests directions for future research.

CHAPTER 2

CHALLENGES OF RAINFALL ESTIMATION

As mentioned in Chapter 1, rainfall estimation is generally conducted using rain gauge, weather radar, and/or satellite. Accurate measurement of rainfall plays a key role in climatological and hydrological modelling. To this end, numerous rainfall estimation systems using one or more of these instruments have been developed for regional, local, or global applications. In this chapter, an overview of the pros and cons of different platforms for rainfall measurement is given, with an emphasis on the fundamentals of radar quantitative precipitation estimation (QPE).

2.1. RAIN GAUGE-BASED RAINFALL MEASUREMENT

Despite recent advances in remote sensing of precipitation, rain gauges are still in use for practical applications in many countries. Point-wise rain gauge data are also used for calibration of remote sensing precipitation products. In general, several types of rain gauges are deployed including weighing gauges, capacitance gauges, tipping bucket gauges, optical gauges, and disdrometers, etc. Among them, tipping bucket rain gauges are the most commonly used for surface rainfall measurement in a number of federal agencies including NWS, the U.S. Forest Service, and the U.S. Geological Survey (USGS). Tipping-bucket gauges are also widely used to provide rainfall depths in hydrological models and flash flood systems that can provide emergency management agencies with warnings.

The operation principle of a tipping bucket gauge is rather simple. Falling rain is collected in a fixed-size bucket that tips and drains when it gets full. Recording the number of tips along with information about their time of occurrence can render estimates of rainfall rates and accumulations. Various recording strategies can be followed to collect the tipping bucket

gauge data. For example, one may record the number of tips that occur during a pre-specified period of time (e.g., number of tips every minute). Alternatively, the time each tip occurs can be recorded with a certain time resolution (e.g., the recording device checks whether the bucket has tipped every 10 seconds). The bucket size and frequency of the recording device samples determine the accuracy of the tipping-bucket gauge. Transforming the recorded number of tips into rainfall intensities can be made on different time scales when providing rainfall data products for subsequent applications.

Tipping bucket gauges have a number of limitations, especially when used in an operational environment. Systematic error is the most significant type of error and includes losses due to wind, wetting, evaporation, and splashing. Wind-induced error, the largest component, has been extensively investigated using different methodologies ranging from field intercomparisons to the use of numerical simulation of the airflow around the gauge site (Nepor and Sevruk 1999). Another significant error source associated with tipping bucket gauges is caused by the nonconformance of the bucket size with the constant calibration volume specified by the manufacturer. Humphrey et al. (1997) recommended a dynamic calibration to account for the nonlinear behaviour of the gauge, especially at the high-intensity rainfall rates. In addition, tipping bucket gauges also suffer from mechanical and electrical problems, as they may occasionally fail to tip during a storm event. The failure may be caused by partial or complete clogging of the funnel that drains into the bucket, data transmission interruption, or even temporary power failure. Such errors are almost always unpredictable.

Beyond the errors that can be either accounted for or removed with a certain degree of accuracy from the rain gauge measurements, the sampling mechanism of the tipping bucket gauge can also introduce significant errors to the rainfall products. In particular, the

uncertainties associated with different recording scenarios and the chosen time scale of the final products need to be carefully investigated. Otherwise, additional sampling errors may be introduced from its working mechanism and the inability to capture the rainfall time series characterized by small temporal features. The gauge’s performance and its associated errors are sensitive to the applied sampling interval and the bucket volume. The ideal setting of the tipping bucket gauge to properly capture rainfall characteristics, such as intensity, especially at small time scales on the order of a few minutes, is a challenging task. For example, under light rain circumstances, for a gauge with bucket volume resolution of 0.254 mm (or 0.01 in), it may take too long to get a tip (Chen and Chandrasekar 2015a).

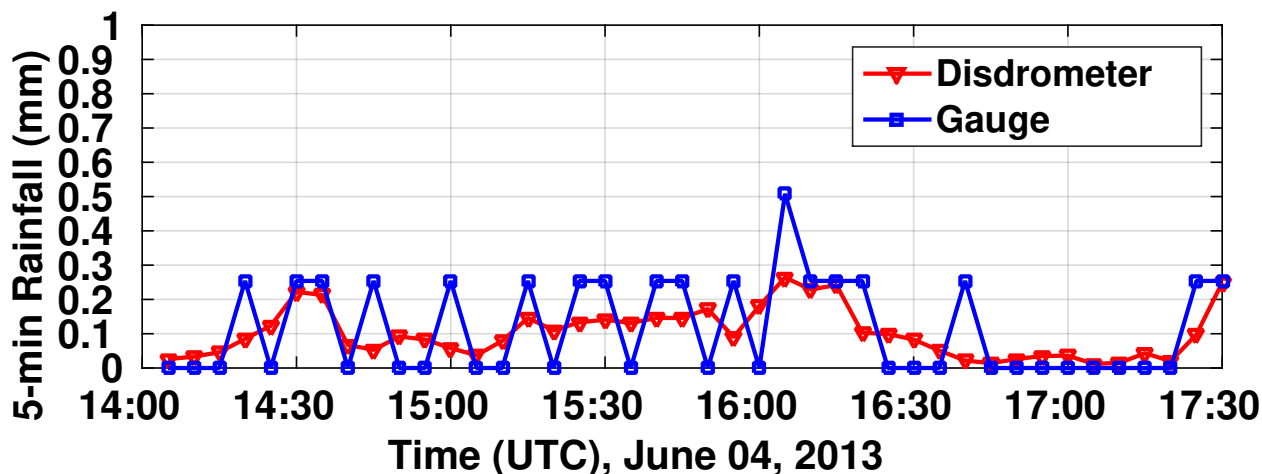


FIGURE 2.1. 5-min rainfall accumulations from a rain gauge and collocated disdrometer at (42.1224°N, 92.2806°W) during a storm event in Iowa on June 4, 2013.

Figure 2.1 illustrates examples of 5-min rainfall accumulations recorded by a tipping bucket gauge and collocated disdrometer during a storm event in Iowa on June 4, 2013. Obviously, compared to the disdrometer, which can measure raindrop size distribution, the gauge can hardly capture the fine temporal structure of rainfall distribution. Chen and Chandrasekar (2015a) also found that as the time scale of rainfall accumulations increases,

the gauge measurement error decreases substantially. In applications, extra attention needs to be paid when configuring the bucket volume and time scale resolution of a gauge system.

Another concern in using a large number of rain gauges to observe the complex distribution of precipitation is the arduous deployment and maintenance of the gauges. The area effectively covered by rain gauges is surprisingly limited over the globe (Kidd et al. 2017). As such, it is almost impossible to use gauge data to study the global or local distribution of precipitation.

2.2. SATELLITE-BASED RAINFALL ESTIMATION

While global rain gauge data are routinely available over land, that information is very sparse in many important regions. In addition, many gauge locations report only six hour or even daily amounts. From a global coverage point of view, meteorological satellites have excellent coverage, especially over the ocean and polar regions. In addition, remote sensing precipitation estimates from a satellite can be acquired with a temporal resolution of three hours or less, which provides the necessary information to enhance the resolution and accuracy of global precipitation products.

Generally, satellite precipitation estimation is conducted either through cloud top temperature in the infrared (IR) images from geostationary satellites or through the passive microwave (PMW) measurements on board low earth orbit satellites. Geostationary IR data are available globally nearly everywhere nearly all the time. This is an ideal tool for global rainfall monitoring due to low latency and frequent refreshing. IR-based algorithms retrieve rain rates based on cloud-top brightness temperatures. Equation (1) illustrates the operational Geostationary Operational Environmental Satellite (GOES) IR rainfall relation

(Vicente et al. 1998):

$$(1) \quad R = 1.1183 \times 10^{11} \exp(-3.6382 \times 10^{-2} \times T^{1.2})$$

where R is the rainfall rate in mm hr^{-1} ; T is the cloud-top brightness temperature in Kelvins.

The algorithm in Equation (1) is derived using a power-law fit between instantaneous radar-based rainfall estimates and satellite measurements of IR brightness temperatures at cloud top. Figure 2.2 shows the conceptual diagram of IR-based rainfall estimation for convective and stratiform precipitation systems. As shown in Figure 2.2 (a), this algorithm works fairly well for convective rainfall. However, the measured cloud-top temperature does not always correlate well with rainfall. In many instances, the cold cloud shield in a precipitation system may be several times larger than the areal coverage of the actual precipitating region. Cirrus cloud or decaying rainfall with cold but nonprecipitating clouds can be easily mistaken for precipitating systems if IR data alone are used. In addition, rainfall is not necessarily just associated with cold clouds. For example, rainfall in the eastern Pacific intertropical convergence zone often occurs as a result of relatively warm clouds (Joyce et al. 2004).

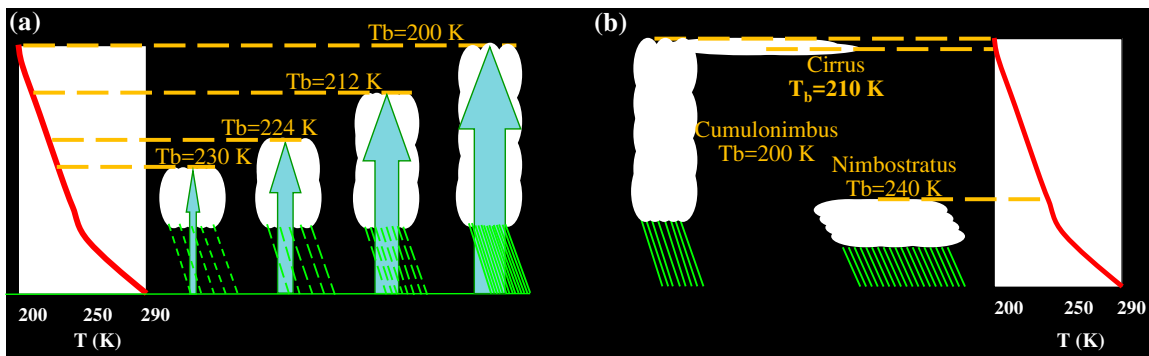


FIGURE 2.2. Conceptual diagram of rainfall estimation using geostationary satellite Infrared (IR) data.

Low earth orbit satellite PMW-based retrieval algorithms have better physics than IR since clouds are semi-transparent at PMW frequencies. The low frequency band PMW signals (10-37 GHz) sense the thermal emission of raindrops, whereas the higher frequencies (85 GHz and higher) sense the scattering of upwelling radiation from the earth to space due to ice particles in the rain layer and tops of convective systems. Figure 2.3 shows a conceptual diagram of rainfall estimation using PMW sensors.

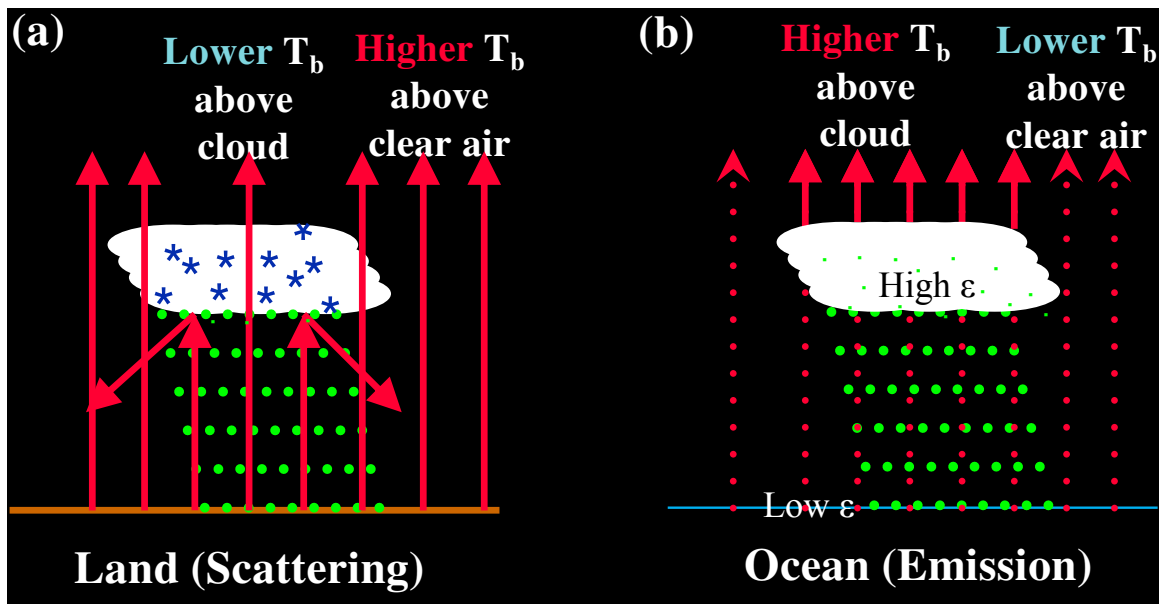


FIGURE 2.3. Conceptual diagram of rainfall estimation using low earth orbit satellite passive microwave (PMW) sensors.

However, due to technical challenges that have precluded the deployment of PMW sensors on geostationary platforms, these instruments are restricted to polar-orbiting satellites. As a result, spatial and temporal sampling limitations from these observations are significant. For a given satellite, the PMW-based retrievals only refresh a few times per day and latency can be up to three hours. In order to produce a complete rainfall product over the globe, a number of such satellites have to be combined and the data need to be averaged substantially over time.

Combining different IR and PMW sensors to take advantage of the strengths of each system provides us a possible solution to accurate estimation of global rainfall. To this end, numerous studies have been devoted to this topic in recent years. More details about merging satellite IR and PMW data will be discussed in Chapter 6.

2.3. RADAR-BASED RAINFALL ESTIMATION

Radar is the acronym for RAdio Detection And Ranging. It is an object-detection system that uses radio waves to determine the range, angle, and/or velocity of targets. Essentially, radar operates by sending electromagnetic waves toward targets to determine their properties based on the return signal. Radar has been used for rainfall estimation since its earliest application in meteorology. Compared to rain gauges and/or satellites, there are a number of advantages of using radar, including the fact that radar can observe precipitation over a wide area in a relatively short span of time. Long-range microwave (S- or C-band) radar networks are used as an integral part of the weather sensing and forecast infrastructure by many nations. Typical examples include the U.S. WSR-88DP network, also known as next-generation radar (NEXRAD) network, which is comprised of about 160 S-band radar sites that are operated according to a set of predefined scan strategies. Figure 2.4 shows the layout of WSR-88DP radars within the U.S. and its territories.

Meteorological targets such as thunderstorms are composed of large numbers of hydrometeors extending over a large space. Modern pulse radars treat these as distributed targets within a sample volume, which is typically defined by the radar's beamwidth and sample range spacing. Figure 2.5 shows the conceptual sample volume illuminated by a pulse Doppler weather radar. The beamwidth is a physical parameter of the radar antenna. The sample range resolution ΔR is determined by the pulse width T_0 , which is often referred to



FIGURE 2.4. The operational WSR-88DP locations over the United States and its territories. All the radar nodes are operating at S-band frequency.

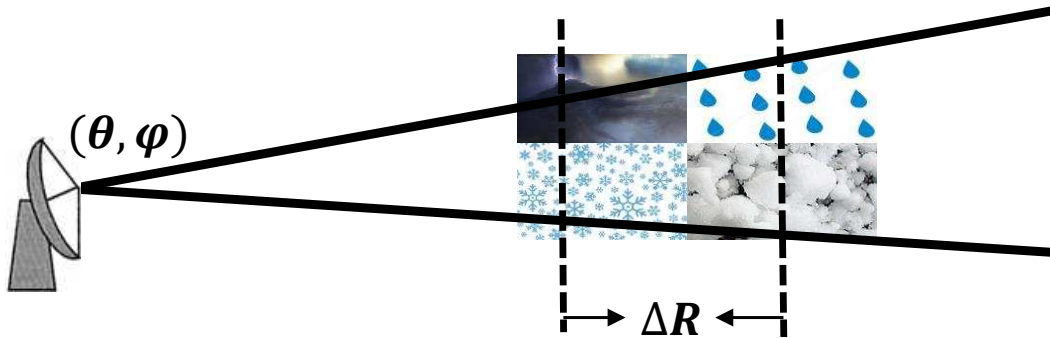


FIGURE 2.5. Weather radar sensing distributed targets within a sample volume. The sample volume size is determined by the radar's horizontal and vertical beamwidths θ and φ , and range spacing ΔR .

as “pulse duration”.

$$(2) \quad \Delta R = \frac{cT_0}{2}$$

where c is the speed of light.

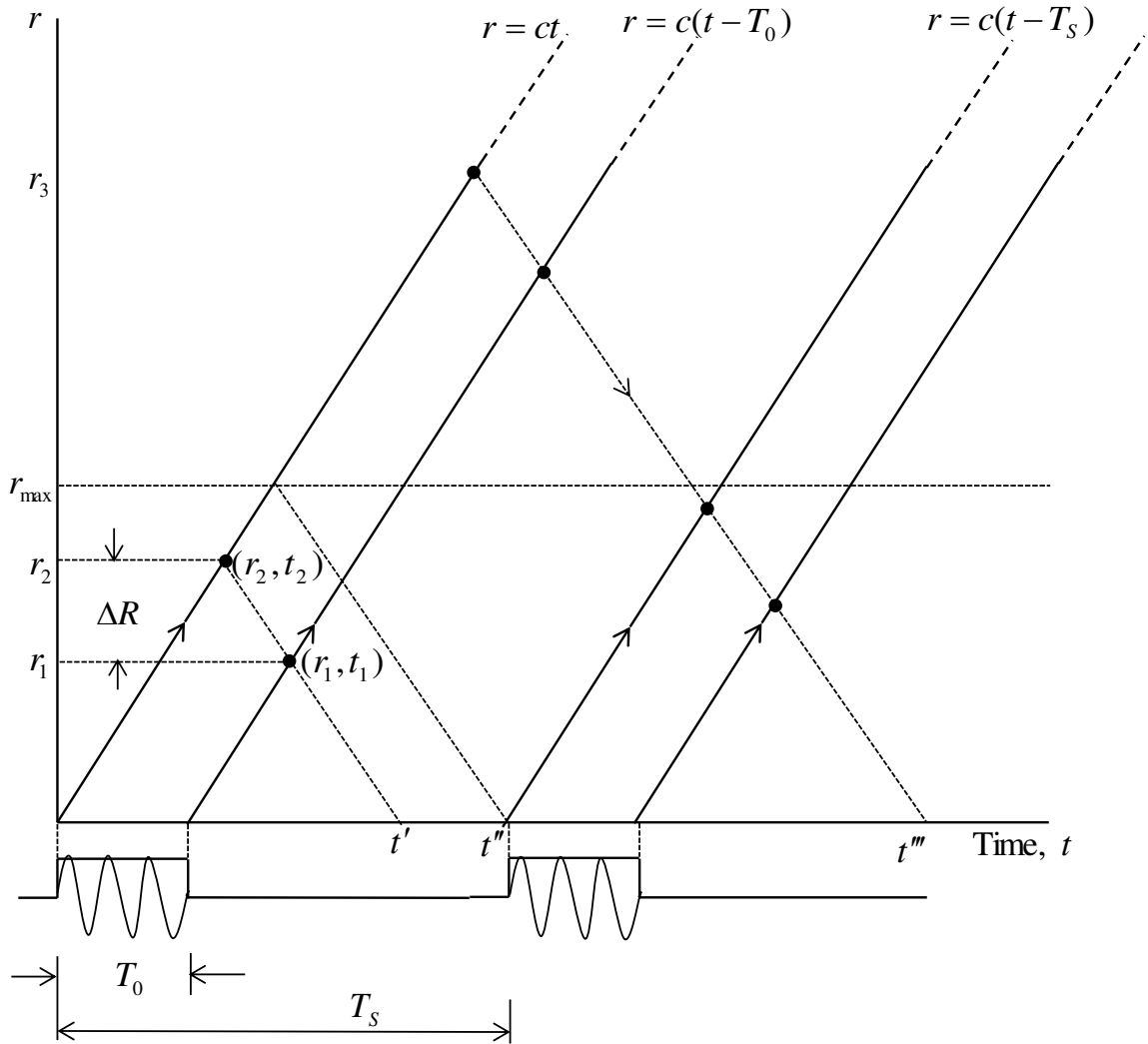


FIGURE 2.6. Range-time characteristics of a pulse Doppler radar system.

The relation in Equation (2) can also be explained by the properties of a finite-duration pulse in the range-time domain, as shown in Figure 2.6 (Brangi and Chandrasekar 2001). The leading and trailing edges of a transmitted pulse are characterized as two lines defined by $r = ct$ and $r = c(t - T_0)$. The return signal at the radar receiver at time t consists of contributions from all the particles in the range between r_1 and r_2 (note $\Delta R = r_2 - r_1$), which are located along the characteristic line whose slope equals $-c$. A well-designed radar should be able to distinguish targets separated by $T_0/2$, which indicates that the pulse width is the

dominant factor of the radar range resolution. The time period between each transmitted pulse T_s in Figure 2.6 is known as the Pulse Repetition Time (PRT).

2.3.1. POLARIMETRIC RADAR RAINFALL RELATIONS.

As the fundamental building block for deriving various radar rainfall algorithms, the raindrop size distribution (DSD) describes the probability density of raindrop sizes. A good knowledge of DSD in the precipitating system is necessary for accurate radar rainfall estimation and forecasting. Since the early work of Marshall and Palmer (1948), various DSD models have been proposed, among which the gamma distribution model can adequately represent many of the natural variations in the shape of the raindrop size distribution (Ulbrich 1983). The corresponding form of gamma DSD can be expressed as:

$$(3) \quad N(D) = N_0 D^\mu e^{-\Lambda D}$$

where N_0 is the intercept parameter in $\text{m}^{-3} \text{mm}^{-1-\mu}$, μ is a distribution shape parameter, Λ is a slope term in mm^{-1} , and D is the volume equivalent diameter in mm. Often, the water content normalized gamma DSD model is used, given by:

$$(4) \quad N(D) = N_w f(\mu) \left(\frac{D}{D_0}\right)^\mu \exp\left[-(3.67 + \mu) \frac{D}{D_0}\right]$$

where N_w is the scaled version of N_0 defined as:

$$(5a) \quad N_w = \frac{N_0}{f(\mu)} D_0^\mu$$

$$(5b) \quad f(\mu) = \frac{6}{3.67^4} \cdot \frac{(3.67 + \mu)^{\mu+4}}{\Gamma(\mu + 4)}$$

Traditionally, rainfall estimation using radar has been accomplished by relating the backscattered power to the rainfall rate through the so-called $Z - R$ relations. These relations have usually been applied to single polarization radar systems and are still in use today. However, it has been found that $Z - R$ relations greatly depend on DSD, which varies across different rainfall regimes, even within a single storm. It is a challenging task to find an ideal $Z - R$ relation for a given region to represent the local rainfall microphysical properties of different types of storms in different seasons. With technologies such as dual-polarization, the sensing capabilities of weather radars have improved considerably over the past 30 years (Bringi and Chandrasekar 2001). Dual-polarization radar offers a number of advantages over conventional single-polarization radar for rainfall estimation because more information about the rainfall microphysics can be obtained from the dual-polarization measurements. In addition, dual-polarization provides us with a better means for radar data quality control, as well as discrimination of meteorological echoes versus non-meteorological echoes such as fires, birds, and insects, etc. (Chandrasekar et al. 2013). The combination of dual-polarization radar measurements, namely, reflectivity (Z_h), differential reflectivity (Z_{dr}), the specific differential propagation phase (K_{dp}), copolar correlation coefficient (ρ_{hv}) and environmental temperature information (T) is also capable of identifying different hydrometeor types to further improve the precipitation estimation (Liu and Chandrasekar 2000; Lim et al. 2005; Cifelli et al. 2011; Chen et al. 2017a). Therefore, all the operational WSR-88DP sites now operate in dual-polarization mode.

The dual-polarization radar measurements are derived from the covariance matrix of the polarized radar return signals. Here, four polarimetric radar variables extensively used in rainfall applications are reviewed, including Z_h , Z_{dr} , K_{dp} , and ρ_{hv} . For details, the interested readers may refer to the text book by Bringi and Chandrasekar (2001). Among the four

variables, Z_h , Z_{dr} , and ρ_{hv} can be directly measured by a dual-polarization radar system, while K_{dp} is estimated as the range derivative of the differential phase shift ϕ_{dp} .

The reflectivity factor at horizontal (Z_h) and vertical polarization (Z_v) can be related to the backscatter properties of raindrops, integrated over the drop size distributions as:

$$(6a) \quad Z_h = \frac{\lambda^4}{\pi^5 |K_w|^2} \int \sigma_h(D) N(D) dD$$

$$(6b) \quad Z_v = \frac{\lambda^4}{\pi^5 |K_w|^2} \int \sigma_v(D) N(D) dD$$

where λ is the radar wavelength; D is the particle equivalent diameter in mm; σ_h and σ_v are the radar cross sections at horizontal and vertical polarization, respectively; $N(D)dD$ is the number of drops per cubic meter in the interval of D to $D + dD$; and $|K_w|^2$ is the dielectric factor of water given by $|K_w|^2 = |(\varepsilon_r - 1)/(\varepsilon_r + 2)|^2$. Here ε_r is the complex dielectric constant of water. In applications, only the horizontal polarization measurement Z_h is used for rainfall estimation. Therefore, for simplicity, Z_h is also referred to Z in this dissertation. The logarithmic transformation $10\log_{10}Z$ is generally used and its units are in decibels of Z relative to $1 \text{ mm}^6\text{m}^{-3}$, which corresponds to 0 dBZ.

The differential reflectivity is the ratio of the reflectivity factor at horizontal polarization to that at vertical polarization state, and can be expressed as follows:

$$(7) \quad Z_{dr} = 10 \log_{10} \frac{Z_h}{Z_v} = 10 \log_{10} \frac{\int \sigma_h(D) N(D) dD}{\int \sigma_v(D) N(D) dD}$$

where Z_h and Z_v are reflectivity factors defined in Equation (6). Z_{dr} is positive for oblate particles, negative for prolate particles, and zero for particles that are ideally spherical. Typically, raindrops are oblate and therefore have positive Z_{dr} values. Conversely, key DSD

parameters can be estimated using Z_{dr} measurements since Z_{dr} is directly related to the particle axis ratio and size. Z_{dr} is also a critical dual-polarization radar variable used to identify rainfall intensities and hydrometeor types. In addition, examining the Z and Z_{dr} space, we can separate hailstones from raindrops because hailstones generally produce larger Z but smaller Z_{dr} relative to raindrops (Aydin et al. 1986).

The specific differential propagation phase is defined as:

$$(8) \quad K_{dp} = \frac{180}{\pi} \lambda Re \int [f_h(D) - f_v(D)] N(D) dD$$

where f_h and f_v are the complex forward scattering amplitudes at horizontal and vertical polarization, respectively. In the dual-polarization radar system, K_{dp} is estimated as the range derivative of the forward propagation phase difference (ϕ_{dp}) between the two polarization channels.

$$(9) \quad \hat{K}_{dp} = \frac{\phi_{dp}(r_2) - \phi_{dp}(r_1)}{2(r_2 - r_1)}$$

However, it should be noted that radar does not measure the forward propagation phase shift ϕ_{dp} directly. Instead, the total differential phase ψ_{dp} is derived from the copolar covariance matrix. ψ_{dp} consists of phase shifts resulting from both forward propagation and backscattering. As such, the estimation of K_{dp} from radar measured ψ_{dp} is a nontrivial task due to measurement noise and backscattering phase (i.e., δ_{co}). In general, range filtering on ψ_{dp} measurement from a radar system is employed to isolate ϕ_{dp} information from δ_{co} and random noise (Hubbert and Bringi 1995). However, by averaging or smoothing over a long path, the peak K_{dp} may get smoothed, which will lead to underestimation of peak rainfall intensity. In this study, the adaptive algorithm proposed by Wang and Chandrasekar (2009)

is implemented for both S- and X-band radars, used in this research in order to mitigate noise fluctuations and suppress the estimation errors. This method is dynamically fine-tuned to local variability and statistical fluctuation and it is performed in the complex domain (Wang and Chandrasekar 2009).

The copolar correlation coefficient is a measurement of the correlation between the reflected horizontal and vertical power returns, which can be expressed in terms of the elements in the backscattering matrix.

$$(10) \quad \rho_{hv}(0) = \frac{\langle S_{vv}S_{hh}^* \rangle}{\langle S_{hh}^2 \rangle^{1/2} \langle S_{vv}^2 \rangle^{1/2}}$$

where S_{hh} and S_{vv} refer to the elements of the backscattering matrix; the asterisk stands for the complex conjugate; and the angle brackets denote the sample average. Although ρ_{hv} is not directly related to rainfall intensity, it is a good indicator of regions where there is a mixture of precipitation types, such as rain and hail (Liu and Chandrasekar 2000; Bechini and Chandrasekar 2015). In this study, ρ_{hv} is used as one of the key parameters for radar data quality control. In addition, ρ_{hv} is sensitive to particle axis ratio and shapes, so it is also utilized in the hydrometeor classification algorithm for the S-band radar data processing prior to the implementation of specific rainfall relations.

With the DSD, the ‘still air’ rainfall rate R is defined as (Bringi and Chandrasekar 2001):

$$(11) \quad R = 0.6\pi \times 10^{-3} \int v(D)D^3N(D)dD$$

where $v(D)$ in m s^{-1} is the raindrop terminal velocity at sea level. In applications, $v(D)$ can be modelled as a function of the particle equivalent diameter through $v(D) = 9.65 - 10.3e^{-0.6D}$ (Atlas et al. 1973).

From Equations (6), (7), (8), and (11), it can be seen that Z , Z_{dr} , K_{dp} , and rainfall rate R are all characterized by the moment of DSD. Subsequently, via the DSD information various empirical rainfall relations can be derived with respect to the dual-polarization radar measurements. For illustration purposes, Figure 2.7 shows the scatter plots of rainfall rate R versus reflectivity Z computed using DSD data collected during the National Aeronautics and Space Administration (NASA) Integrated Precipitation and Hydrology Experiment (IPHEX) field campaign. Similarly, Figure 2.8 shows the scattergram of R versus K_{dp} , both of which are computed based on DSD data collected during the NASA Iowa Flood Studies (IFloodS) field experiment (Chen and Chandrasekar 2015a). The black curves in Figures 2.7 and 2.8 indicate the best-fitting power-law rainfall relations.

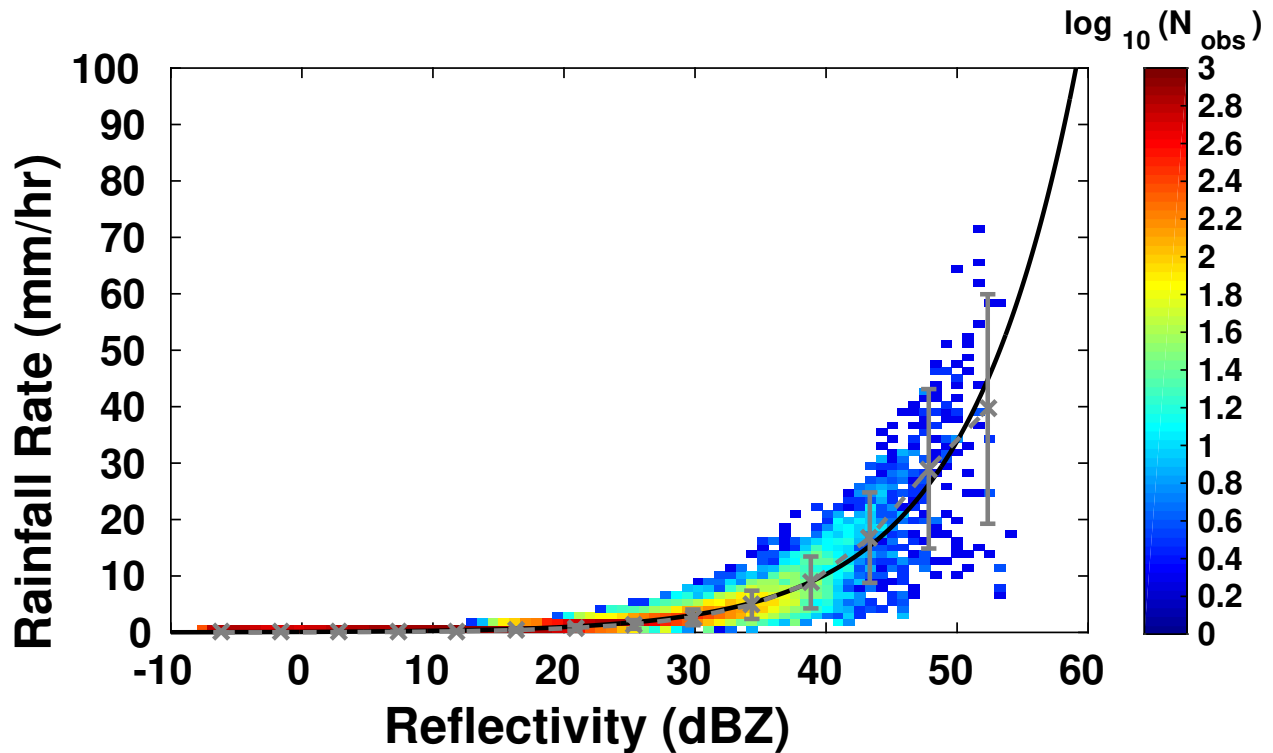


FIGURE 2.7. Scattergram of rainfall rate R versus reflectivity Z . Both R and Z values are computed based on DSD data collected during the NASA IPHEX field experiment. The black curve indicates the best-fitting power-law relation of $R(Z)$. The grey bars stand for the mean and standard deviation of the binned data.

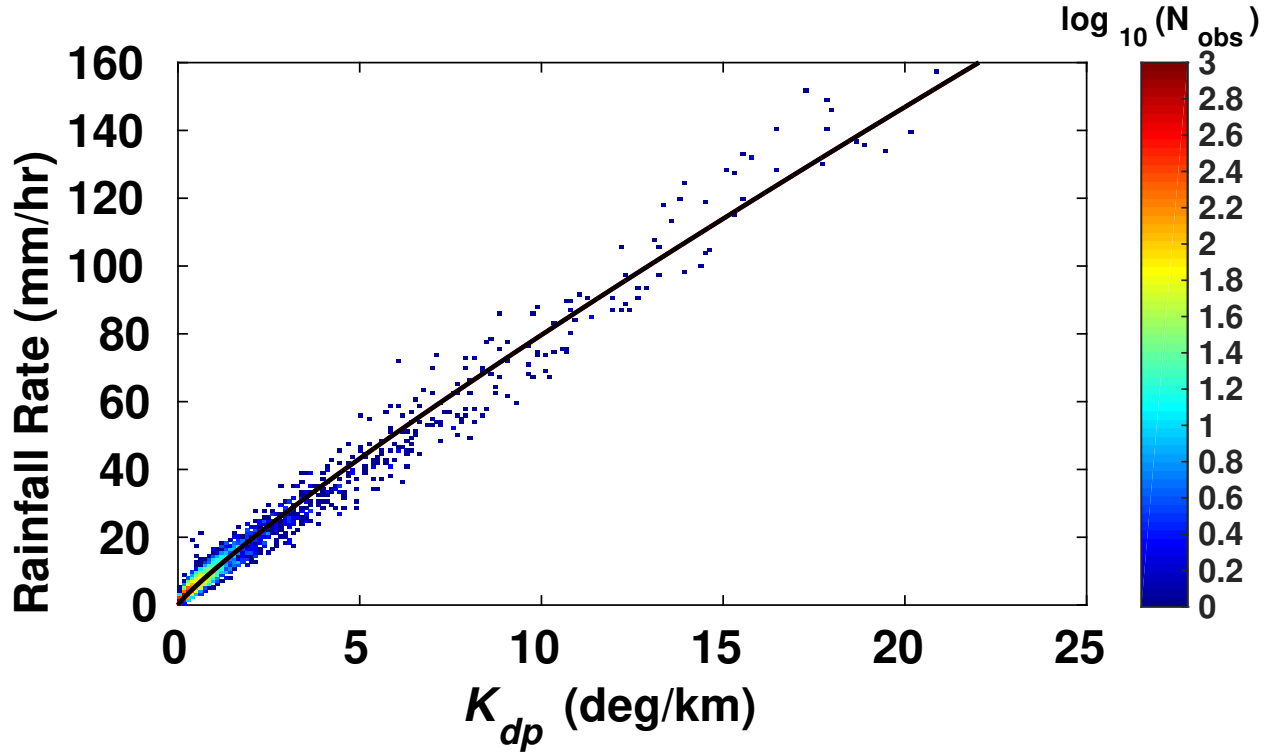


FIGURE 2.8. Scattergram of rainfall rate R versus specific differential propagation phase K_{dp} . Both R and K_{dp} values are computed based on DSD data collected during the NASA IFloodS field experiment (Chen and Chandrasekar 2015a). The black curve indicates the best-fitting power-law relation of $R(K_{dp})$.

In general, radar rainfall algorithms can be broadly classified into four categories: $R(Z)$, $R(Z, Z_{dr})$, $R(K_{dp})$, and $R(Z_{dr}, K_{dp})$ in the following forms:

$$(12) \quad R(Z) = aZ^b$$

$$(13) \quad R(Z, Z_{dr}) = aZ^b Z_{dr}^c$$

$$(14) \quad R(K_{dp}) = aK_{dp}^b$$

$$(15) \quad R(Z_{dr}, K_{dp}) = aZ_{dr}^b K_{dp}^c$$

It should be noted that in the above equations a , b , and c are generic constants determined by the natural distribution of rainfall regimes and radar operating frequencies. In addition, the specific attenuation A has also been used for rainfall estimation in a number of previous studies such as Ryzhkov et al. (2014) and Junyent and Chandrasekar (2016). Here, $R(A)$ is not classified as a separate category since the attenuation is essentially estimated from the polarimetric radar variables.

It is well known that each dual-polarization parameter-based rainfall estimator has its advantages and disadvantages. As a result, Z , Z_{dr} , and K_{dp} are often combined to derive rainfall products. Although there is still no standard criterion to adopt regarding which estimator to apply for a given set of dual-polarization measurements, a few approaches have been suggested in previous studies and are commonly used by the weather radar community. For example, Chandrasekar et al. (1993) attempted to minimize the standard error of rainfall rate estimates by selecting rainfall relations according to rainfall intensities. The rainfall intensity-based method was also applied during the Joint Polarization Experiment (Ryzhkov et al. 2005). Petersen et al. (1999) selected different rainfall relations based on thresholds on the values of Z , Z_{dr} , and K_{dp} . In recent years, the hydrometeor classification-based rainfall methodologies have been extensively used for operational applications (Cifelli et al. 2011; Giangrande and Ryzhkov 2008; Chen et al. 2017a). Such rainfall systems typically consist of three modules-data quality control, classification of different hydrometeor types, and precipitation quantification with appropriate rainfall relations. At Colorado State University (CSU), an optimization algorithm has been developed by Cifelli et al. (2011)

using hydrometeor identification results to guide the choice of particular radar rainfall relations, namely, $R(Z)$, $R(K_{dp})$, $R(Z, Z_{dr})$, and $R(K_{dp}, Z_{dr})$. This optimization algorithm is commonly referred to as CSU-HIDRO (Cifelli et al. 2011) or the CSU Dual-polarization (CSU-DP) algorithm (Seo et al. 2015). It is a key component of the Dual-Polarization Radar Operational Processing System (DROPS) developed at CSU. Therefore, it will be referred to as DROPS1.0 in this dissertation. DROPS1.0 has been used in a number of previous studies. For instance, Cifelli et al. (2011) demonstrated the encouraging performance of DROPS1.0 in the high plains environment with data collected from the S-band CSU-University of Chicago-Illinois State Water Survey (CSU-CHILL) radar and a network of rain gauges in Denver, Colorado. Pei et al. (2014) used DROPS1.0 rainfall algorithms to study the impacts of raindrop fall speed and axis ratio errors. Seo et al. (2015) showed that DROPS1.0 was superior to a single-polarization-based rainfall algorithm during the NASA Global Precipitation Measurement (GPM) satellite mission’s Iowa Flood Studies (IFloodS) field experiment in central and northeastern Iowa, especially for intense rainfall estimation.

Besides the research-based rainfall methodologies described above, a couple of operational rainfall systems have been developed for the WSR-88DP network. For example, a nationwide multisensor precipitation estimator (MPE) system was developed by the NWS Office of Hydrologic Development (OHD: reorganized into the National Water Center as of April 1, 2015) as part of the Advanced Weather Interactive Processing System (AWIPS) (Kitzmilller et al. 2011). The MPE system, which produces rainfall estimates on 4 km by 4 km grids and updated every hour, is widely used by the Weather Forecast Offices (WFOs) and River Forecast Centers (RFCs). Recently, a comparative package termed the multi-radar multi-sensor (MRMS) system was developed by the National Severe Storms Laboratory (NSSL) to produce severe weather and precipitation products (Zhang et al. 2011).

However, most of the hydrometeor classification-based rainfall systems, including the one implemented by WSR-88DP dual-polarization systems (Giangrande and Ryzhkov 2008), are designed using traditional bin-by-bin based fuzzy logic classification methods. They are not sufficient for operational applications, especially when the input radar data are noisy. That is because the hydrometeor identification results will be noisy and unrealistic if the radar data quality is low since the classification quality and correlation with adjacent range gates are not taken into account. In addition, traditional fuzzy logic approaches suffer severely from brightband contamination due to the challenges of mixed-phase precipitation classification in the melting layer. In this study, an improved S-band radar rainfall algorithm termed DROPS2.0 will be introduced. The advanced classification technique implemented in DROPS2.0 exploits the spatial information content of dual-polarization radar observables. Compared to traditional fuzzy logic-based classifications, it also considers spatial coherence, the quality of the classification itself, and the self-aggregation propensity of polarimetric radar measurements (Bechini and Chandrasekar 2015). Details about the improved rainfall methodology will be presented in Chapter 3.

In addition, it should be noted that the choice of rainfall estimator gets more complicated at higher frequencies (e.g., X-band) when Z and Z_{dr} must be corrected for attenuation before being used for any quantitative applications such as QPE. Therefore, this study takes advantage of the differential phase measurements which are not affected by radar calibration and attenuation. In particular, only the $R(K_{dp})$ -based rainfall algorithm is considered at X-band. The specific X-band $R(K_{dp})$ relation for the X-band radar network developed in this study will be detailed in Chapter 5.

2.3.2. LIMITATIONS OF CONVENTIONAL OPERATIONAL RADAR NETWORK.

Although dual-polarization technologies are now moving into operational applications, fundamental challenges in radar rainfall estimation remain. To this end, numerous experiments have been conducted to quantify the error structure of various radar rainfall algorithms. The net result of these experiments has shown two fundamental aspects of rainfall estimation: the physical science aspect and the system engineering consideration. The physical science process essentially represents the tracking of rainfall microphysical properties from radar observations. It is fundamentally related to the physical model of DSD and relation of the model to radar parameters. Chapter 3 develops an improved rainfall methodology by taking into account the microphysical constraints and spatial coherence of the dual-polarization measurements.

In spite of the improvements in rainfall estimation realized from dual polarization, various experiments done to compare rainfall from radar with ground observations have exposed extensive challenges that were not purely rainfall physics but were related to system engineering issues, such as beam averaging, radar measurement bias, bright band contamination, and sampling and geometry considerations. Again, taking the WSR-88DP network as an example, the S-band radars comprising this operational network are spaced about 230 km apart in the eastern U.S. and about 345 km apart in the western U.S. From a temporal resolution perspective, individual radars in the WSR-88DP network are operated with a predefined volume coverage pattern (VCP) mode that is repeated. The update rate, the same for all areas under the radar umbrella, will increase as the number of elevation angles of VCP increases. Figure 2.9 shows the 14 tilts from 0.5° to 19.5° elevation angles for the commonly used VCP12 scanning strategy. It takes five to six minutes to finish a volume scan task, which is too long to capture weather evolution details, especially for high-impact localized

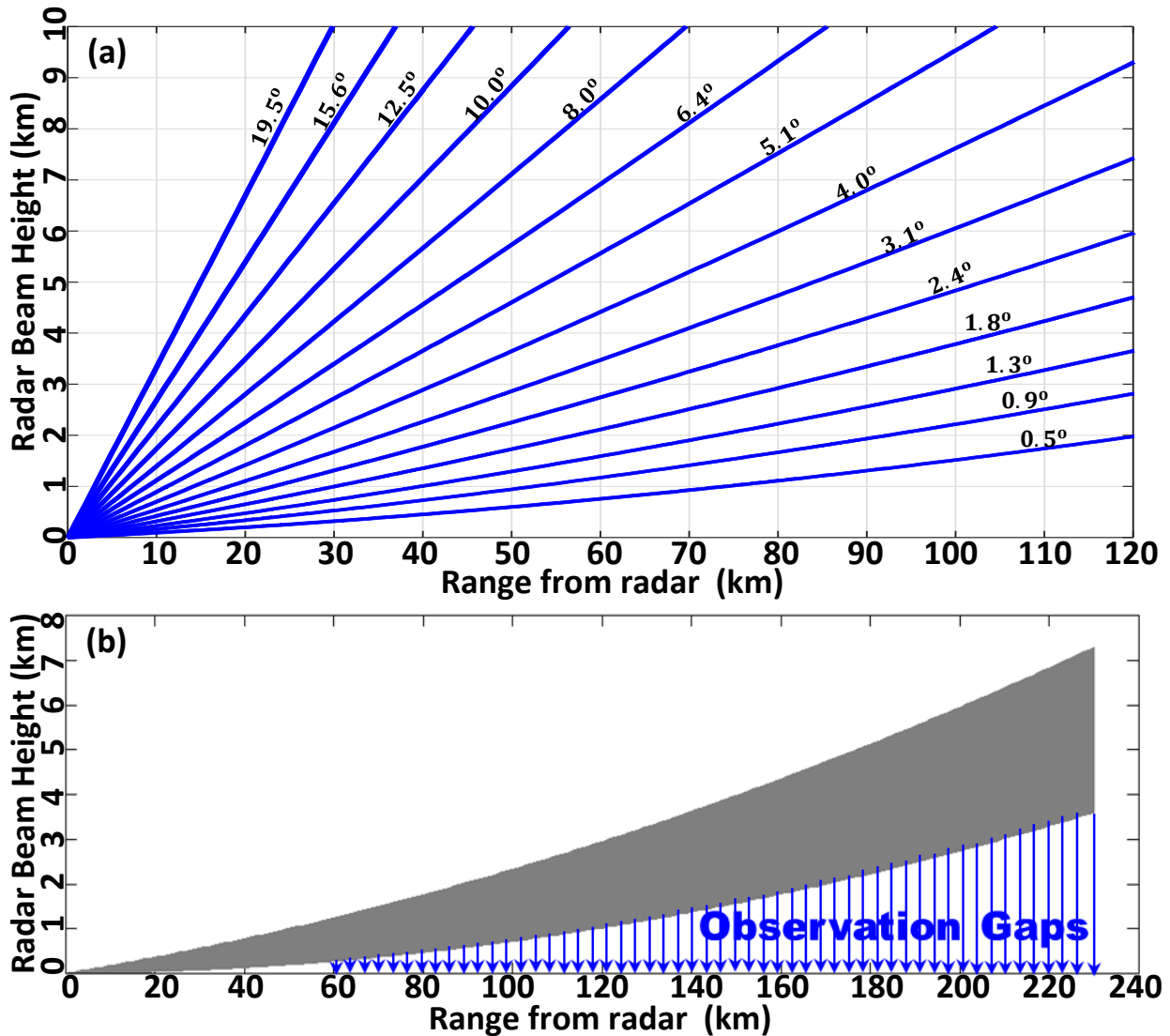


FIGURE 2.9. (a) Center beam height as a function of range from radar for the 14 elevation tilts of the WSR-88DP volume coverage pattern 12 (VCP12) scan mode. (b) Height of the lowest (0.5 degree) beam in the VCP12 scan mode. The beam height is calculated based on the 4/3 earth radius model.

meteorological phenomena such as tornadoes and flash floods. Figure 2.9 also illustrates the lowest (0.5 degree) beam height of VCP12 as a function of distance from radar. The beam height is calculated based on the 4/3 earth radius model. At the maximum coverage range of 230 km, the lowest beam center is about 5.4 km above ground level (AGL). Compounding the terrain blockage, more than 70% of the atmosphere below 1 km altitude AGL cannot be observed over the continental U.S. (see Figure 2.10).

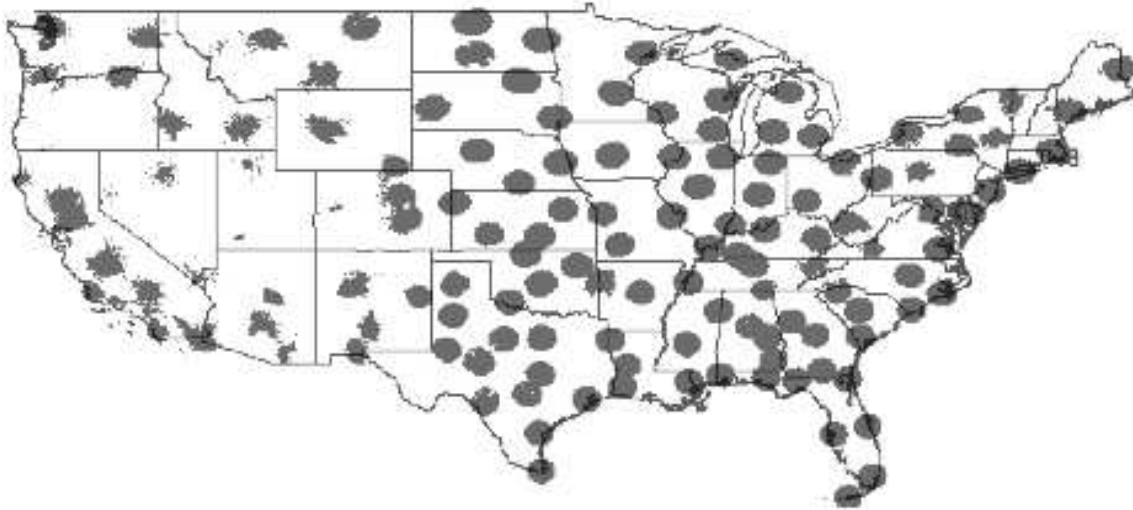


FIGURE 2.10. WSR-88DP radar coverage at 1 km AGL over the continental U.S. The coverage map is essentially derived based on the center beam height of 0.5-degree elevation (courtesy of NOAA/NWS/OST).

From the spatial resolution perspective, WSR-88DP radar sample volumes extend to many cubic kilometers as the range increases. The incomplete low-level coverage and limited spatial resolution at long distances impedes the ability of such systems to identify and detect fine-scale weather features. As a result, the performance of operational rainfall products derived based on the WSR-88DP network gets significantly degraded, especially in the western U.S. (Willie et al. 2017).

In order to overcome the sampling and coverage limitations of WSR-88DP, the National Science Foundation Engineering Research Center for Collaborative Adaptive Sensing of the Atmosphere (CASA) has proposed a new weather sensing paradigm through the use of a large number of small X-band radars. The X-band systems are appropriately spaced to overcome the terrain blockage and effect of the earth's curvature. The adaptive sensing concept developed by CASA and its urban implementation will be detailed in Chapter 4.

AN IMPROVED DUAL-POLARIZATION RADAR RAINFALL ALGORITHM (DROPS2.0)

As presented in Section 2.3 in Chapter 2, $R(Z)$, $R(Z, Z_{dr})$, $R(K_{dp})$, and $R(Z_{dr}, K_{dp})$ are often combined to derive rainfall products. Among various radar rainfall methodologies, the hydrometeor identification- (HID) based rainfall algorithms have been fairly successful in recent years. Such an algorithm is also applied to the operational S-band WSR-88DP network. Figure 3.1 illustrates a flowchart describing the CSU DROPS1.0 algorithm, which is one of the earliest studies of HID-based rainfall estimation. The specific rainfall estimators

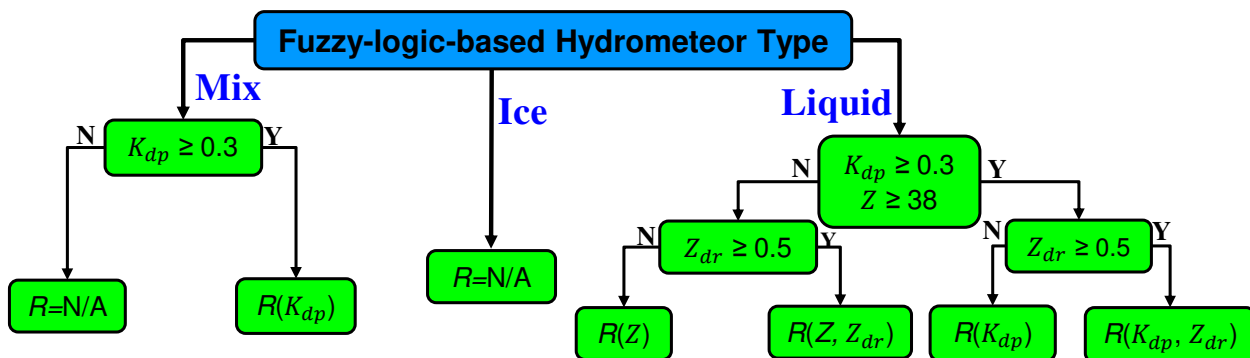


FIGURE 3.1. Diagram of the blended rainfall algorithm developed at CSU (DROPS1.0). The algorithm is driven by the fuzzy logic-based hydrometeor classification approach.

are given by Cifelli et al. (2011):

$$(16a) \quad R(Z) = 0.017Z^{0.714}$$

$$(16b) \quad R(K_{dp}) = 40.5K_{dp}^{0.85}$$

$$(16c) \quad R(Z, Z_{dr}) = 6.7 \times 10^{-3} Z^{0.927} Z_{dr}^{-3.43}$$

$$(16d) \quad R(Z_{dr}, K_{dp}) = 90.8 Z_{dr}^{-1.69} K_{dp}^{0.93}$$

where Z (mm^6m^{-3}) and $Z_{dr} = 10^{Z_{dr}/10}$ are reflectivity and differential reflectivity in linear scale.

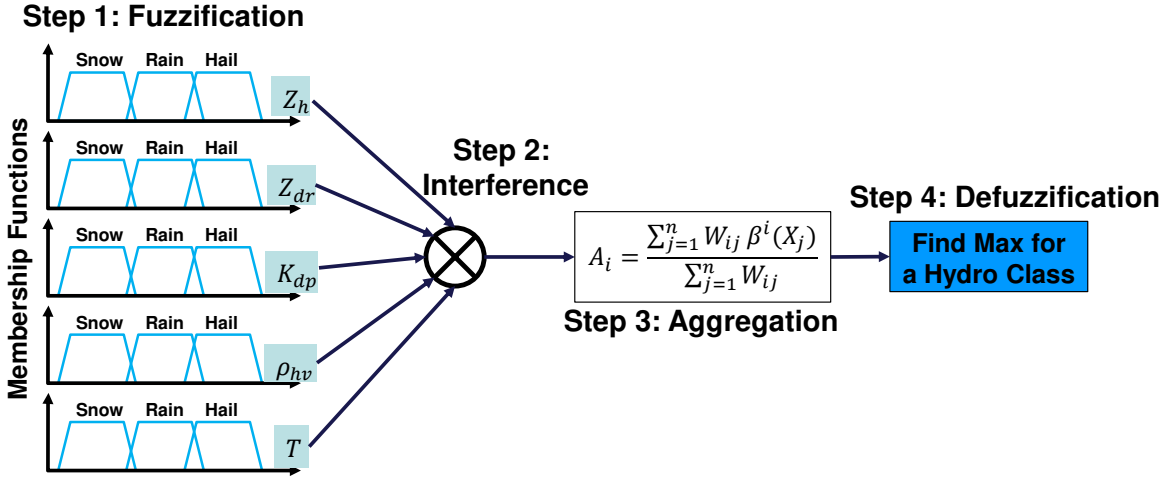


FIGURE 3.2. Generic blocks of a traditional fuzzy logic-based hydrometeor classification approach.

The hydrometeor classification module in most of the HID-based rainfall systems, including DROPS1.0, is based on a fuzzy logic approach, which typically includes four steps: fuzzification, inference, aggregation, and defuzzification (see Figure 3.2). However, the bin-by-bin-based fuzzy logic algorithm may not be sufficient for operational applications, especially when the radar data quality is low. That is, for a given range gate, the hydrometeor classification result can be noisy if the input radar measurements are noisy since the information from adjacent gates is not considered. In addition, the bin-by-bin-based approach is severely affected by partial beam blockage and/or bright band contamination. Even if the radar data are not polluted by clutter or partial beam blockage, the radar beam can

overshoot precipitation at long distances from the radar, especially during stratiform rain events. In the regions close to or within the melting layer, the bin-by-bin-based classification approach is not able to clearly identify the mixed-phase precipitation. All these factors will greatly affect the subsequent rainfall estimation. A smoother and clearer output is desirable in an operational environment to ease the interpretation by the end users. Furthermore, the rainfall relations in DROPS1.0 are derived based on simulated drop size distribution (DSD) data (Cifelli et al. 2011), which may not be sufficient to represent real rainfall microphysical properties.

In this chapter, an improved dual-polarization algorithm called DROPS2.0 is developed for more accurate and robust rainfall estimation, especially in an operational environment. Compared with the method in Cifelli et al. (2011), the improved method incorporates a region-based hydrometeor classification methodology (Bechini and Chandrasekar 2015). In addition, the specific rainfall relations have been upgraded based on real DSD observations collected during the NASA IFloodS field experiment. This study also attempts to quantify rainfall estimation errors introduced by radar beam broadening. Although the dual-polarization techniques provide us with a better means of radar system calibration, data quality control, and rainfall estimation, the geometry of radar measurements combined with the variability of spatial distribution of precipitation still pose challenges. A number of studies have been devoted to the correction of range-dependent errors in rainfall estimates obtained from gridded radar reflectivity data (Chumchean et al. 2004). Nevertheless, the quantification of dual-polarization radar rainfall errors introduced by beam broadening and beam tilting in native radar polar coordinates is relatively rare. One of the challenges that limit such research is the ad hoc deployment of ground validation instruments (e.g., rain

TABLE 3.1. NPOL radar and APU disdrometer locations during the NASA IFloodS field experiment. The ranges and bearings relative to NPOL are calculated using the 1980 Geodetic Reference System.

	Latitude ($^{\circ}$ N)	Longitude ($^{\circ}$ W)	Range (km)	Azimuth($^{\circ}$)
NPOL	42.2681	92.5096	-	-
APU01	42.2388	92.4637	4.99	130.60
APU02	42.1823	92.3654	15.24	128.60
APU03	42.1260	92.2817	24.56	129.89
APU04	42.1224	92.2807	24.88	130.45
APU05	41.9927	92.0602	48.12	129.31
APU06	41.9782	92.0758	48.20	131.76
APU07	41.9926	92.0914	46.17	131.36
APU08	41.9927	92.0709	47.45	129.98
APU09	41.8614	91.8854	68.62	130.95
APU10	41.8605	91.8737	69.42	130.48
APU11	41.8471	91.8603	71.24	130.80
APU12	41.8474	91.8458	72.13	130.15
APU13	41.6406	91.5418	106.28	130.65
APU14	41.6406	91.5416	106.28	130.64

gauges or disdrometers) relative to radar. During the NASA IFloodS field campaign, a variety of ground-based instruments were deployed to collect high-quality *in situ* precipitation data. Among them, 14 autonomous particle size and velocity (Parsivel) unit (APU) disdrometers were deployed along the NASA Polarimetric (NPOL) S-band radar azimuthal radials at different ranges, and tipping-bucket gauges were collocated with 10 APU disdrometers (see Figure 3.3). The disdrometer locations, relative to the NPOL radar, are listed in Table 3.1. This unique instrument layout provides us with an ideal environment in which to investigate the impact of beam broadening on radar rainfall estimation. Therefore, this study takes the opportunity to quantify rainfall errors of a few rainfall algorithms, namely, DROPS2.0, the WSR-88D default $R(Z)$ (hereafter referred to as NEXRAD $Z - R$), and the dual-polarization rainfall relation proposed by Giangrande and Ryzhkov (2008) that is adopted by NEXRAD.

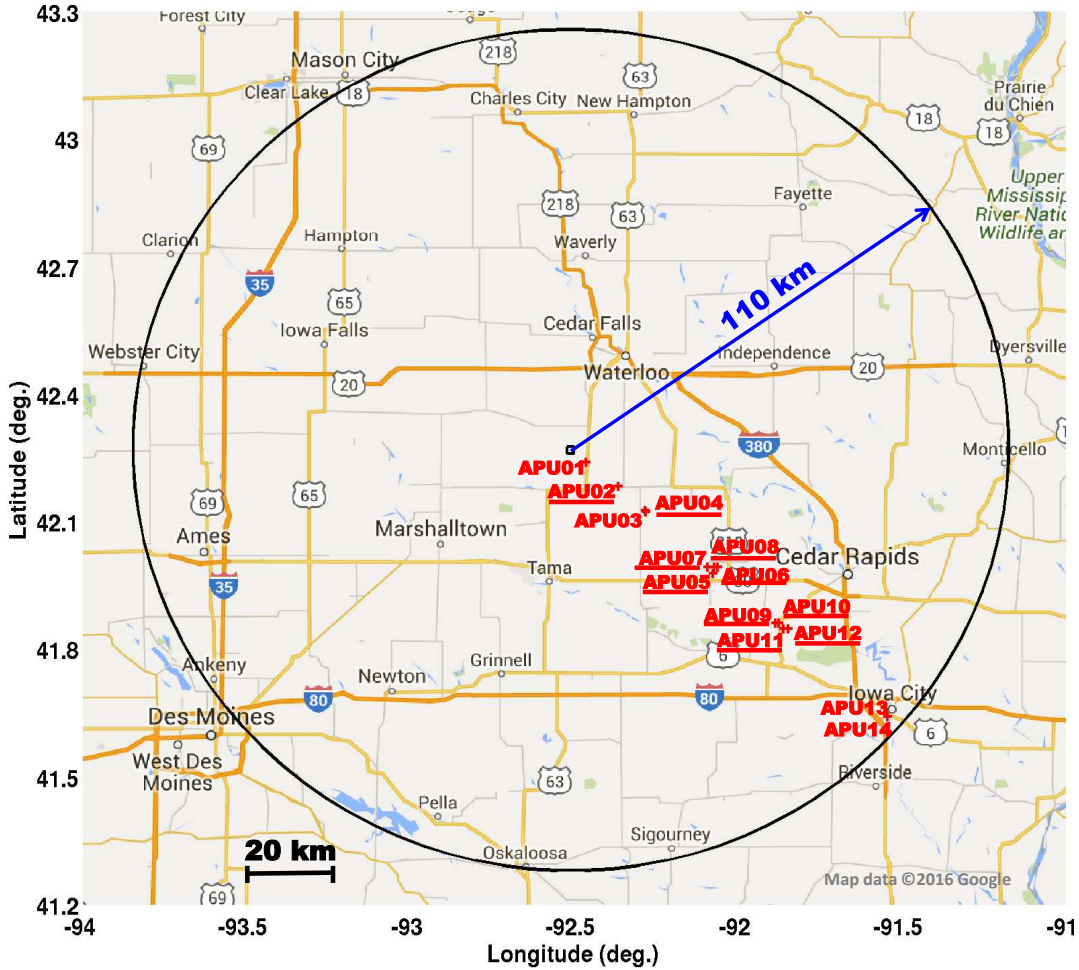


FIGURE 3.3. Deployment of NPOL radar during NASA’s IFloodS field campaign. The red plus signs denote the locations of 14 APU disdrometers. Rain gauges are collocated with 10 disdrometers with underlines.

3.1. DROPS2.0 RAINFALL ALGORITHM

The architecture of the DROPS2.0 rainfall algorithm is similar to DROPS1.0 (see Figure 3.1). In the following, the important features of DROPS2.0, as well as the specific rainfall relations used by DROPS2.0, are presented. The logic of DROPS2.0 is shown in Figure 3.4, which includes three main steps:

- Step 1: data quality control and K_{dp} estimation;
- Step 2: region-based hydrometeor classification;
- Step 3: rainfall estimation.

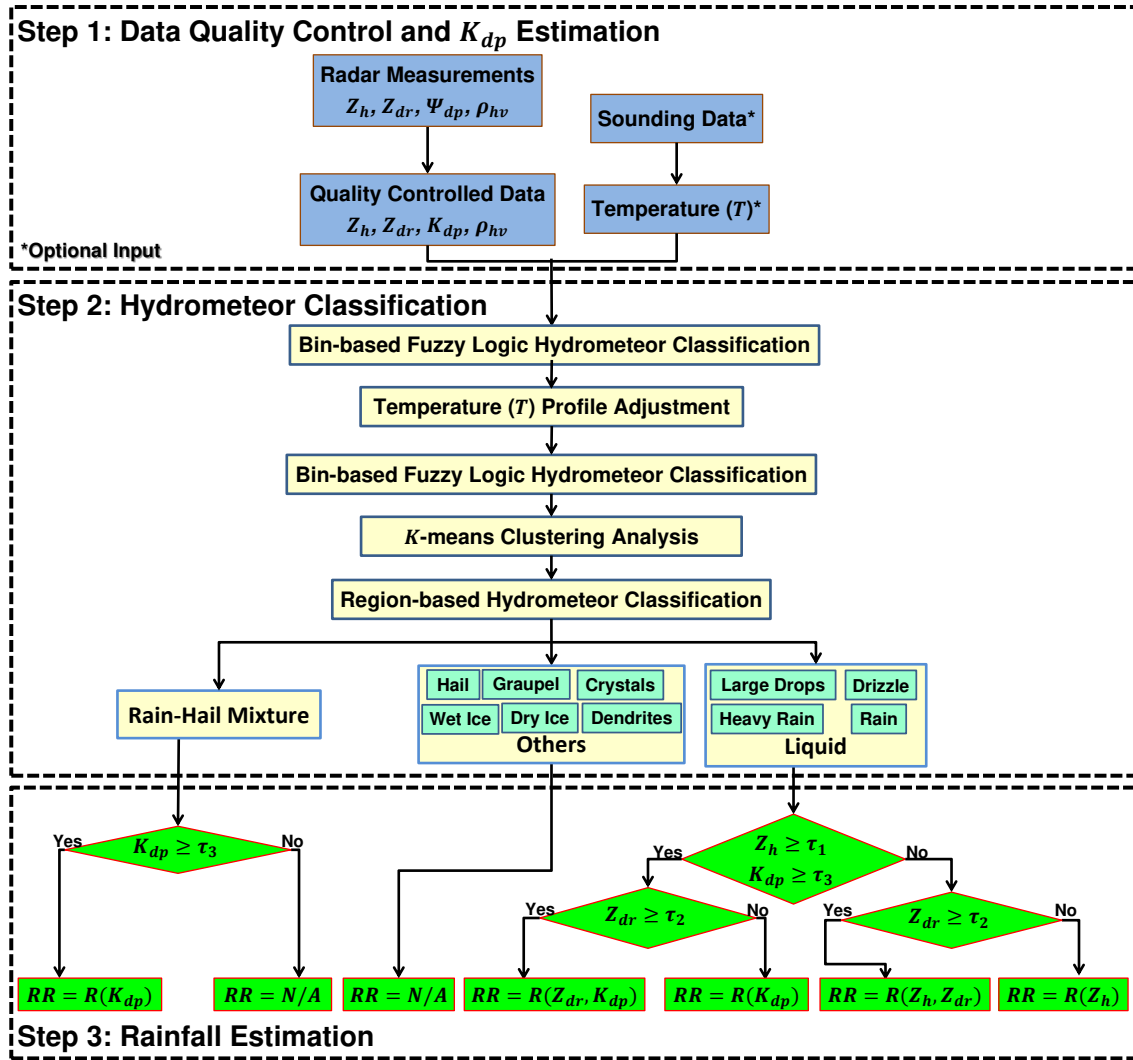


FIGURE 3.4. Architecture of the DROPS2.0 rainfall algorithm for dual-polarization S-band radar.

In the data quality control step, the adaptive algorithm developed by Wang and Chandrasekar (2009) is implemented to estimate K_{dp} and remove ground clutter and non-meteorological echoes. Figure 3.5 illustrates the flowchart of the differential phase-based data quality control process. Essentially, the non-meteorological echoes are identified based on the characteristics of differential phase (ψ_{dp}) and co-polar correlation coefficient (i.e., ρ_{hv}) measurements. As aforementioned, the estimation of K_{dp} is a nontrivial task because fundamentally it is a slope measurement. Compared to traditional K_{dp} estimation methods such as Hubbert and Bringi

(1995), the adaptive technique in Wang and Chandrasekar (2009) does not smooth the peak K_{dp} by averaging over a long path. In this study, the K_{dp} estimation method in Wang and Chandrasekar (2009) is implemented for both S-band WSR-88DP radar and X-band CASA DFW radars.

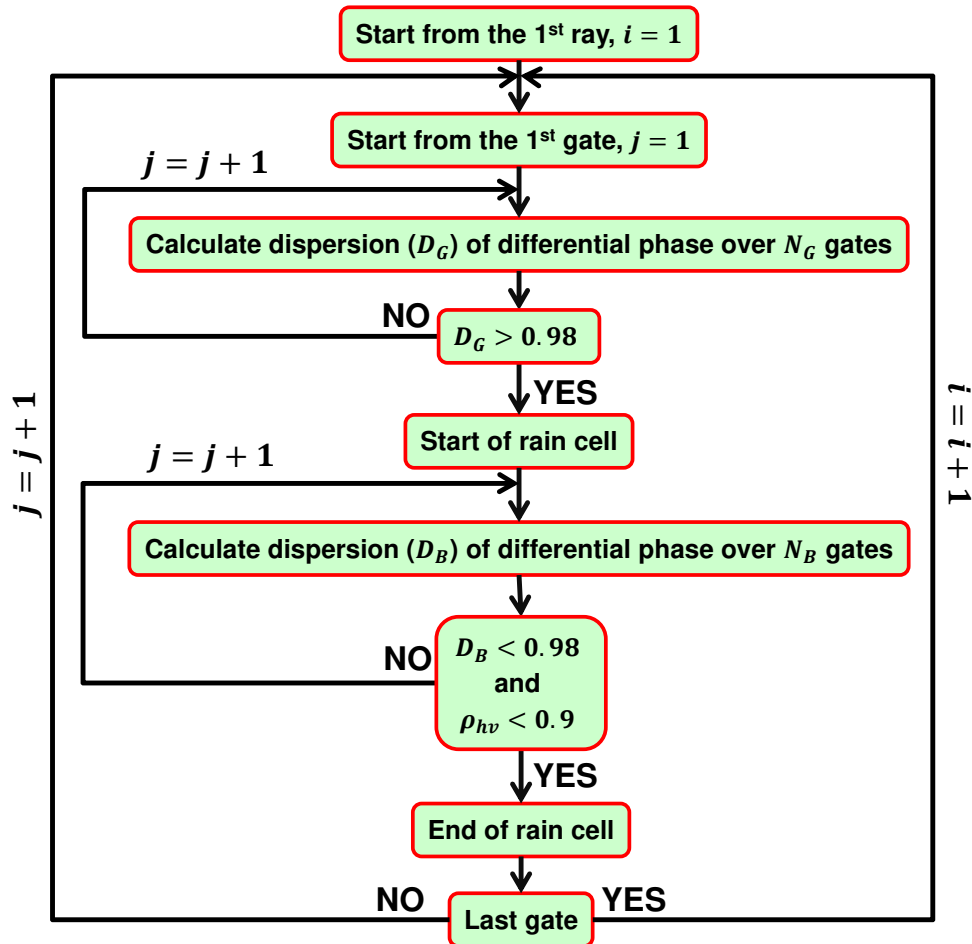


FIGURE 3.5. Flowchart of differential phase processing, where N_G and N_B are constant numbers of consecutive good and bad gates, respectively.

The quality-controlled S-band dual-polarization radar measurements then serve as input to the hydrometeor classification module. In this research, the region-based hydrometeor classification proposed by Bechini and Chandrasekar (2015) is applied. A brief description of this methodology is provided here. For details, the reader is referred to Bechini and Chandrasekar (2015). The input radar data for hydrometeor classification include Z , Z_{dr} , K_{dp} ,

and ρ_{hv} . The vertical profile of temperature (T) observed from a nearby sounding station is also used as an optional input. The overall structure of this region-based classification methodology is depicted in Step 2 in Figure 3.4. First, a traditional bin-based fuzzy logic approach (Liu and Chandrasekar 2000; Lim et al. 2005) with four general blocks (see Figure 3.2) is implemented to get initial classification results. The temperature profile is then adjusted based on the quality of wet ice classification, which is essentially the average confidence of all the bins identified as wet ice based on the inference rule (Bechini and Chandrasekar 2015). Second, a modified K -means clustering technique is applied to incorporate the spatial contiguity and microphysical constrains. Then, the connected component labelling algorithm is employed to derive connected regions (Gonzalez and Woods 2002), and the final classification is performed over connected regions where unique labelling of regions populated with adjacent bins are assigned to the same hydrometeor type. In total, 11 hydrometeor types are classified, namely, large drops (LD), drizzle (DR), rain (RA), heavy rain (HR), rain hail mixture (RH), hail (HA), graupel (GR), wet ice (WI), dry ice (DI), crystals (CR), and dendrites (DN). Ground clutter and non-meteorological echoes are also classified, and marked as clutter (CL). Compared to the conventional fuzzy logic method, this region-based approach is appealing in terms of operational application and easy interpretation. Figure 3.6 illustrates sample NASA S-band NPOL radar observations and corresponding hydrometeor classification results for a range height indicator (RHI) scan at 23:43UTC, May 29, 2013. For the sake of precipitation estimation, a similar concept to DROPS1.0 (Cifelli et al. 2011) is adopted and the hydrometeor classes are narrowed down to three categories: liquid, rain-hail mixture, and others, where “liquid” includes LD, DR, RA, and HR; “rain-hail mixture” is RH; and “others” includes HA, GR, WI, DI, CR, DN, and CL. Rainfall estimation is then conducted based on the hydrometeor categories and thresholds on Z_h , Z_{dr} , and K_{dp} . At

S-band frequency, the thresholds on Z_h , Z_{dr} , and K_{dp} are 38 dBZ, 0.5 dB and 0.3 degree km^{-1} , respectively. However, the thresholds may need to be adjusted based on measurement quality, which can vary from system to system due to a number of factors such as radar signal processing algorithms.

In order to attain the specific rainfall relations, the DSD measurements from 14 Parsivel disdrometers deployed during NASA’s IFloodS field campaign were used for simulation purposes. The Parsivel’s DSD data is essentially the number of raindrops in a 32-by-32 size versus fall velocity matrix (Tokay et al. 2014). In total, 13772 one-minute-averaged DSDs were used for deriving polarimetric rainfall relations. This DSD dataset (training data) consists of nine precipitation days, including a couple of severe multicellular convective thunderstorms and a few widespread stratiform rain cases. The dual-polarization radar moments (i.e., Z , Z_{dr} , K_{dp}) were simulated at S-band frequency using the T -matrix method (Waterman 1965). The drop shape model used in the simulation is the one proposed by Brandes et al. (2002). The temperature information is obtained from a local sounding station. Rainfall rates are also computed directly from the DSD data using the following equation:

$$(17) \quad R = 0.6\pi \times 10^{-3} \sum_{n=1}^{32} V(D_n) D_n^3 N(D_n) S_n$$

where R is rainfall rate in mm hr^{-1} ; D_n is raindrop mean diameter in mm; S_n is diameter spread in mm; $N(D_n)$ is the number of drops, and $V(D_n)$ is the raindrop terminal velocity in m s^{-1} , at diameter size level n . The diameter level D_n and spread S_n are specified for a given type of disdrometer (Tokay et al. 2014). Equation (17) is essentially the discrete form of the definition of rainfall rate given by Equation (11). In this study, the fall velocity measured by disdrometers was not used due to its inaccuracy, particularly at larger size and higher fall speeds. For details, the interested reader is referred to Tokay et al. (2014). Instead, the

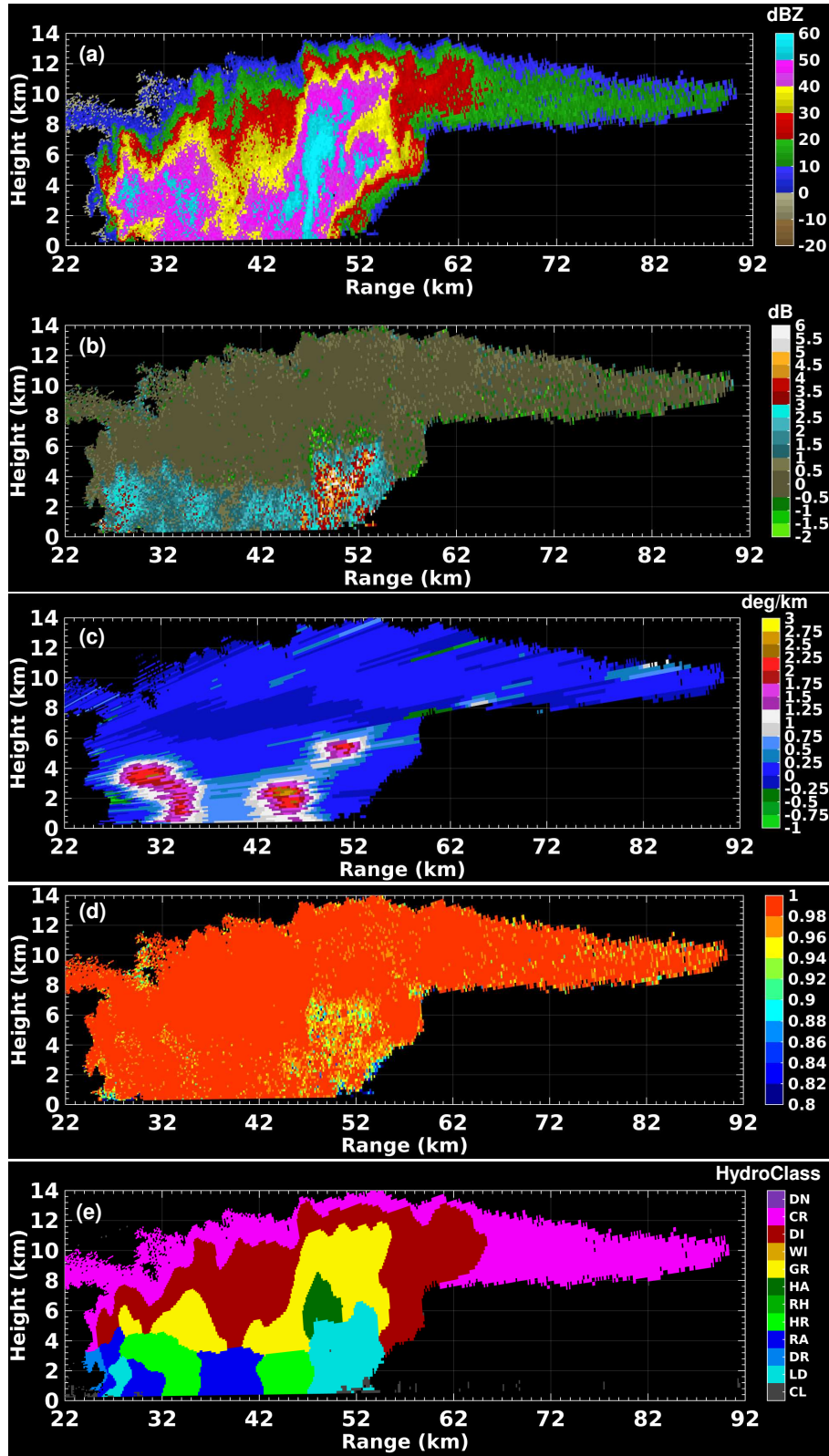


FIGURE 3.6. S-band NASA NPOL radar observations at 23:43UTC, May 29, 2013. (a) Z , (b) Z_{dr} , (c) K_{dp} , (d) ρ_{hv} , and (e) corresponding hydrometeor classification results.

model-based relation $V(D) = 9.65 - 10.3e^{-0.6D}$ from Atlas et al. (1973) is adopted when calculating rainfall rate from DSD data.

Then, nonlinear regression is conducted between rainfall rates and dual-polarization measurements in order to get the specific rainfall relations given below:

$$(18a) \quad R(Z) = 0.02Z^{0.657}$$

$$(18b) \quad R(K_{dp}) = 39.84K_{dp}^{0.851}$$

$$(18c) \quad R(Z, Z_{dr}) = 5.4 \times 10^{-3} Z^{0.94} Z_{dr}^{-3.593}$$

$$(18d) \quad R(Z_{dr}, K_{dp}) = 93.154Z_{dr}^{-1.752} K_{dp}^{0.953}$$

again, Z is in the units of mm^6m^{-3} , and $Z_{dr} = 10^{Z_{dr}/10}$ is differential reflectivity in linear scale.

In addition, this chapter compares the proposed rainfall method with the standard NEXRAD $Z - R$ relation in Equation (16a), and the $R(Z, Z_{dr})$ relation used by WSR-88DP (Giangrande and Ryzhkov 2008). However, it should be noted that this study will not fully implement the blended WSR-88DP rainfall methodology found in Giangrande and Ryzhkov (2008). Instead, only the rainfall relation used in liquid regions is referred since the current operational version of the WSR-88DP rainfall algorithm only estimates the amount of liquid precipitation, in which case Equation (19) is adopted. Hereafter, Equation (19) will

be referred to as the NEXRAD DP relation.

$$(19) \quad R(Z, Z_{dr}) = 1.42 \times 10^{-2} Z^{0.77} Z_{dr}^{-1.67}$$

Before the implementation of DROPS2.0, NEXRAD $Z - R$, and NEXRAD DP relations, the data quality control in step 1 of DROPS2.0 is applied. In addition, NEXRAD $Z - R$ and DP relations are only applied when the precipitation type is classified as liquid (based on step 2 in DROPS2.0), and zeros are assigned for the regions where nonliquid precipitation types are identified. To investigate the parameterization error structure of various rainfall algorithms, another DSD dataset (testing data) is used to quantify the parameterization errors, particularly for liquid precipitation estimation. Although collected in the same field experiment, the testing dataset is independent from the training data used to derive Equation (18). The normalized standard deviation (σ_p) of rainfall rate estimates (for liquid regions), defined as follows, is computed at different rainfall intensity ranges:

$$(20) \quad \sigma_p = \frac{SD(R_{DSD} - R_{EST})}{\langle R_{DSD} \rangle}$$

where R_{EST} represents the estimated rainfall rates using radar rainfall relations in Equations (16a), (18), and (19); R_{DSD} stands for rainfall rates directly computed from testing DSD data using Equation (17). $SD(\cdot)$ stands for standard deviation. The angle bracket stands for sampling average.

Figure 3.7(a) shows the scattergram of rainfall rates estimated using the improved rainfall relations in DROPS2.0 versus rainfall rates directly computed from testing DSD data using Equation (17), whereas Figure 3.7(b) illustrates σ_p due to parameterization of various rainfall algorithms. From a theoretical perspective, for liquid precipitation estimation, we can strive

to achieve the error rates in Figure 3.7(b) provided the measurement errors can be eliminated by spatial or temporal averaging. Figure 3.7(b) also shows that the improved rainfall relations developed in this study have a better performance than the NEXRAD $Z - R$ or NEXRAD DP relations.

In Section 3.2, the performance of various algorithms are demonstrated and evaluated with S-band NPOL radar data collected for three precipitation events during the NASA IFloodS field experiment.

3.2. APPLICATION IN NASA IFLOODS FIELD CAMPAIGN

During the IFloodS experiment, the NPOL radar was deployed at an ideal location to fill the gap of WSR-88DP low-elevation coverage, and for proximity to local river basins. NPOL was operated in several modes, including the two-sweep (i.e., 0.7° and 1.4°) full plan position indicator (PPI), RHIs over the APU disdrometers, PPI sector (PPS) scans of precipitation systems over principal river basins, and “bird bath” scans that can be used for monitoring Z_{dr} biases. The RHI sector scans covered an azimuth range of 8° above locations of ground-based instrumentation (i.e., APU disdrometers). The PPI and RHI scan tasks were repeated every 3 min when precipitation was detected anywhere within NPOL’s coverage domain, and they were performed throughout the campaign. Other scans, such as PPS and bird-bath scans, were scheduled between rain scans on an event-by-event basis, among which three options for PPS scans were considered depending on echo-top height and range to NPOL radar in order to obtain high-resolution rainfall mapping over the local river basins. In this section, three precipitation events characterized by different meteorological features were selected for rainfall validation analysis. In the following, these three events are briefly described. Sample

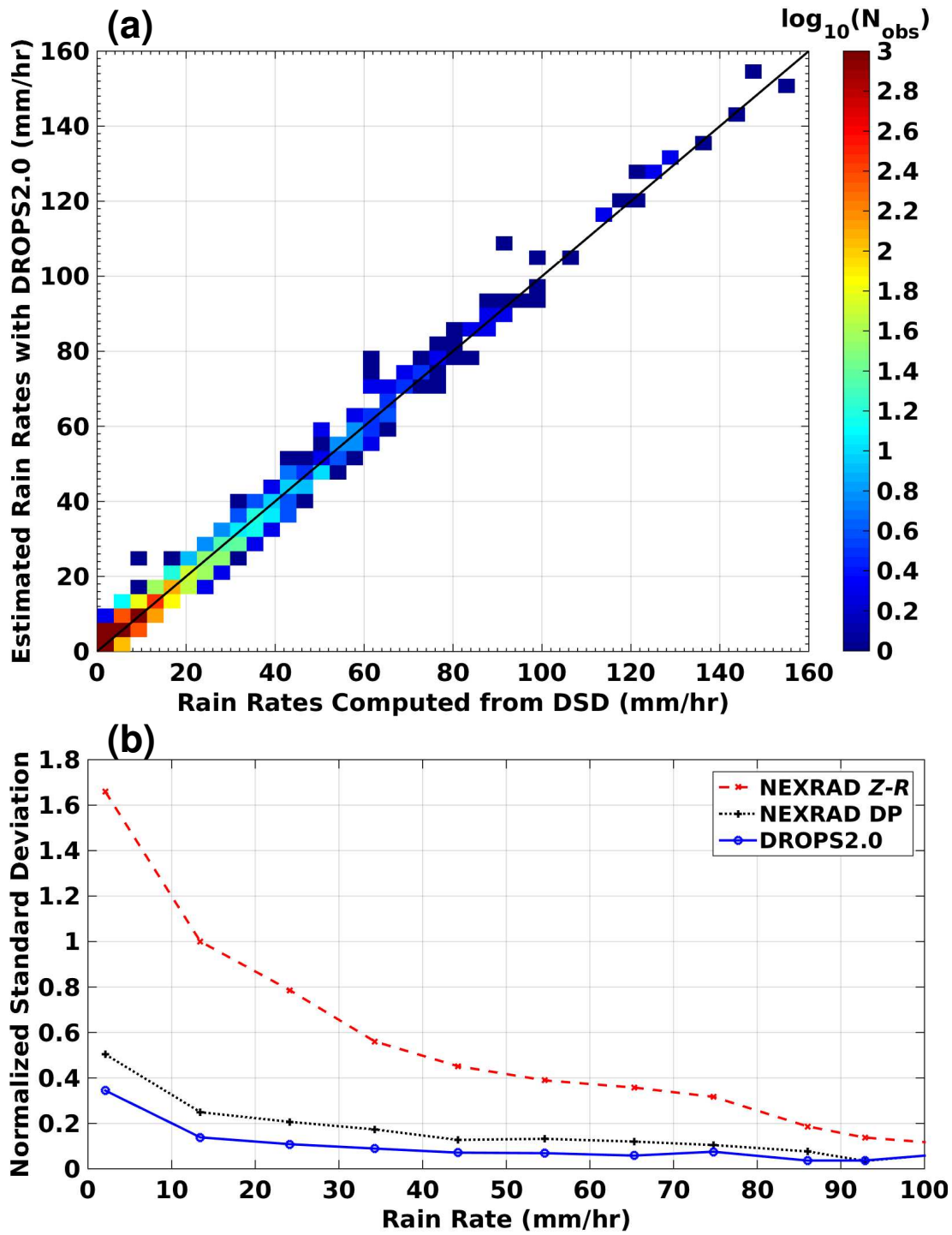


FIGURE 3.7. (a) Scattergram of estimated rainfall rates with S-band rainfall algorithm in Equation (18) versus rainfall rates directly computed from DSD data. The black line indicates the 1:1 line; (b) normalized standard deviation of parameterization errors in various rainfall algorithms as a function of rainfall intensity.

products during the events are also provided, with an emphasis on quantitative evaluation of various rainfall algorithms.

3.2.1. RAINFALL EVENTS AND DATASET DESCRIPTION.

20 May 2013 Case: This event, characterized by a mesoscale convective system (MCS), began as strong, tornadic storms near the KDMX radar (NEXRAD deployed in Des Moines, Iowa). From the evening hours of May 19 to the very early morning hours of May 20 local time (central daylight time, i.e., UTC-5hr), a few isolated cells developed in the IFloodS domain. In particular, a strong line of convection was observed to the west of the NPOL radar moving to the east shortly after 00:00UTC, May 20. Followed by an asymmetric MCS from the southwest, this convective line passed over the NPOL site around 01:45UTC. For validation purposes, we only make use of the NPOL data collected during 02:00-05:00UTC, May 20, when the rainfall was significantly impacting the disdrometer network. During this period, NPOL was conducting regular RHI and full surveillance PPI scans. In addition, a few PPS scans were conducted over the Turkey River basin (northeast of the NPOL radar) and the disdrometer network near the 130 radial (southeast of the NPOL radar) when strong convection moved to the regions of interest. In this research, the lowest (0.7° elevation) PPI as well as PPS scans over the disdrometer network were used to generate various rainfall products. In Figure 3.8, sample NPOL radar observations and corresponding rainfall rate estimates using different algorithms are shown for the event of 20 May 2013. It is worth mentioning that, because of the high winds (about 31 m s^{-1}) at the radar site, it was decided to stow the NPOL radar antenna in the vertical position at 01:26UTC, and it was restored at 01:45UTC. This may slightly affect radar data processing and subsequent rainfall product performance.

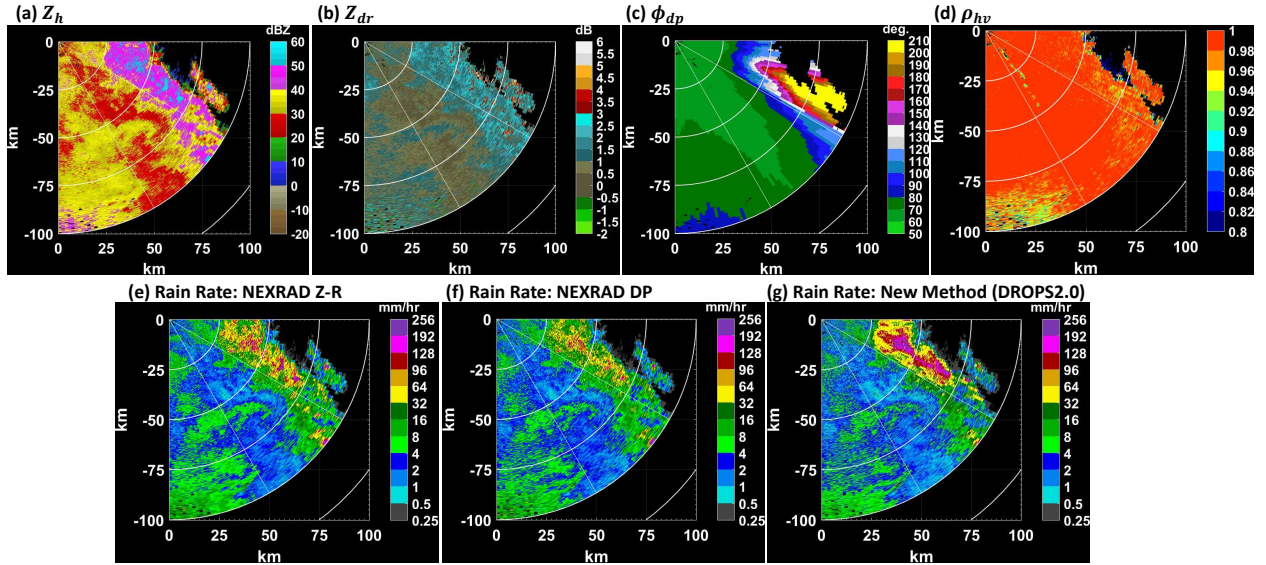


FIGURE 3.8. Sample NPOL radar observations at 03:50 UTC 20 May 2013: (a) Z , (b) Z_{dr} , (c) ϕ_{dp} , (d) ρ_{hv} , and corresponding rainfall-rate estimates using different algorithms: (e) NEXRAD $Z - R$, (f) NEXRAD DP, and (g) DROPS2.0.

25 May 2013 Case: This is a typical stratiform event. Rain showers were observed in the IFloodS domain all through the night of May 24. The stratiform precipitation became more widespread in the morning of May 25, especially to the south and east of the NPOL site, and it lasted until late afternoon. Several flood and flash flood watches and warnings were issued in the IFloodS and nearby regions. NPOL radar was fully staffed again after maintenance on the previous day. It had been continuously conducting PPI and RHI scans during this event. PPS scans near the 130° azimuthal angle were also scheduled around 12:00-18:00UTC in coordination with the instrumented disdrometer array as precipitation was focused there. It is a good case for horizontal variability studies of precipitation properties. Similar to the previous event, the lowest PPI and PPS sweeps (0.7° elevation) collected during 12:00-21:00UTC May 25 were used to derive rainfall products when fairly uniform precipitation coverage was observed over the disdrometer network in the NPOL domain.

Figure 3.9 shows sample NPOL radar observations and corresponding rainfall rate estimates using different algorithms during this stratiform case.

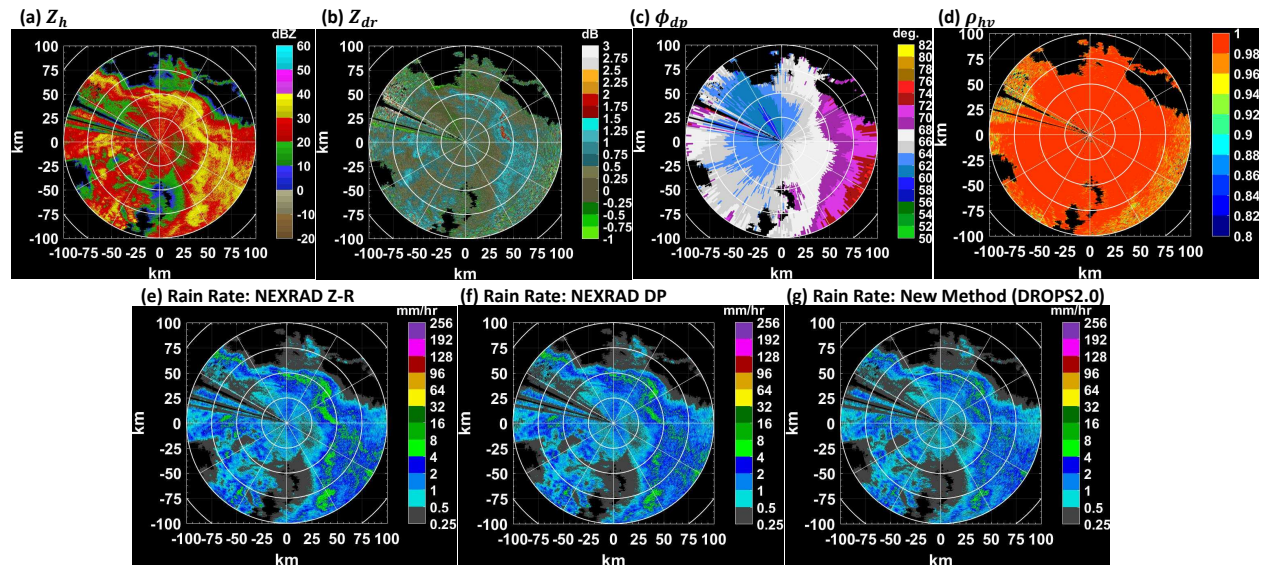


FIGURE 3.9. As in Figure 3.8, but for observations at 15:39 UTC 25 May 2013.

29 May 2013 Case: With a major MCS passing through the entire IFloodS domain, this is another well-documented case with severe weather and heavy rain. Besides the regular PPI and RHI scans, NPOL performed many hours (around 17:15-21:00UTC) of dedicated PPS scans for high temporal-resolution rain mapping. Around 21:00-24:00UTC, the strong convective cells moved to the southeast of the NPOL coverage domain, where the disdrometer arrays were deployed. Therefore, the lowest PPI scan data collected during this period were utilized for rainfall analysis. In addition, single RHI scans over the disdrometer radial were also conducted regularly in order to investigate the vertical structure of precipitation. Nevertheless, characterization of the vertical structure/distribution of rainfall is beyond the scope of this paper. Similar to Figures 3.8 and 3.9, Figure 3.10 illustrates sample NPOL radar observations and corresponding rainfall estimates for this event.

Radar and APU Data Processing: During IFloodS, a number of disdrometers and tipping-bucket rain gauges were deployed within the NPOL radar coverage to provide *in*

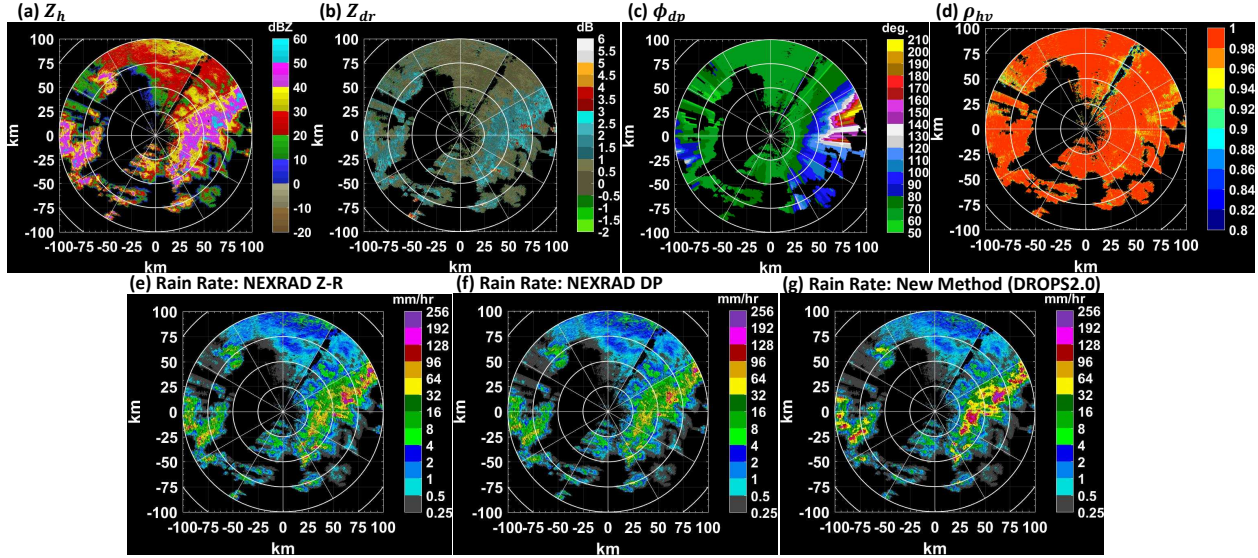


FIGURE 3.10. As in Figure 3.8, but for observations at 22:48 UTC 29 May 2013.

situ validation data (see Figure 3.3). A number of previous studies have shown that the use of rain gauges can introduce significant biases to high temporal-resolution radar QPE validation due to the limitations on sampling time and bucket volume resolution, particularly in light rainfall cases (Chen and Chandrasekar 2015a). Therefore, this study will use only APU data for radar rainfall product evaluation. During the three precipitation events, some of the APUs had malfunctions. Only the APUs that were working fine all through the three precipitation events are used in this paper, namely, APU02, APU03, APU05, APU06, APU08, APU09, APU11, APU13, and APU14. Each APU, equipped with a Parsivel unit (version 2) developed by OTT Hydromet in Germany, is an optical disdrometer that can measure raindrop size and falling speed (Tokay et al. 2014). During the field experiment, the APU sampling resolution was configured to 1 min. With the drop size distribution, rainfall rate can be computed using Equation (17). For the sake of evaluation, the consecutive 1-min APU rainfall rate data were aggregated to get 5-, 15-, 30-, 45-, and 60-min rainfall accumulations.

The data quality control and K_{dp} estimation procedure in Section 3.1 was applied to NPOL radar data before implementing various rainfall relations. The estimated NPOL radar rainfall rates corresponding to APU rainfall observation times were used to produce matched radar rainfall amounts. For the time frames when APU or radar did not report rain, zeros were assigned. The radar-APU rainfall pairs were then used for quantitative evaluation. For the time frames when there was no NPOL radar data/scan (not often), a piecewise cubic Hermite interpolating polynomial (PCHIP)-based interpolation methodology (Fritsch and Carlson 1980) was applied in order to get radar rain rates that exactly match APU rainfall measurements.

3.2.2. EVALUATION RESULTS AND DISCUSSION.

It is well known that radar observations represent a unit of illuminated volume in polar coordinate with a resolution of $0.98^\circ \times 150$ m, whereas APUs provide point-wise measurements. In this study, the radar range gate closest to the APU location was selected for the purpose of quantitative evaluation. The discrepancies caused by wind drift on radar-APU comparison were neglected. Assuming the APU measurements are the “ground truth,” a set of metrics are computed for rainfall estimates at different time scales at each APU location. The evaluation metrics, including the normalized mean absolute error ($NMAE$), root-mean-square error ($RMSE$), and Pearson correlation coefficient ($CORR$), are respectively defined as follows:

$$(21) \quad NMAE = \frac{\langle |R_R - R_A| \rangle}{\langle R_A \rangle}$$

$$(22) \quad RMSE = \sqrt{\langle (R_R - R_A)^2 \rangle}$$

$$(23) \quad CORR = \frac{\sum[(R_{R-} \langle R_{R-} \rangle)(R_{A-} \langle R_{A-} \rangle)]}{\sqrt{\sum(R_{R-} \langle R_{R-} \rangle)^2} \sqrt{\sum(R_{A-} \langle R_{A-} \rangle)^2}}$$

where the angle brackets stand for sample average, and R_R and R_A denote the estimated rainfall amount at different time scales (i.e., 5-, 15-, 30-, 45-, or 60-min) from NPOL radar and APU, respectively.

$NMAE$, $RMSE$, and $CORR$ results for each of the events, as well as for all three events combined, are shown in Tables 3.2-3.5. It should be noted that the $NMAE$ s in Tables 3.2-3.5 are in percentage (%), $RMSE$ s are in mm, and Z-R and DP represent NEXRAD $Z - R$ and NEXRAD DP algorithms, respectively.

Scrutinizing Tables 3.2-3.5, it can be concluded that DROPS2.0 generally has the best performance in terms of $NMAE$ and $RMSE$. Surprisingly, NEXRAD $Z - R$ has lower $NMAE$ compared to the NEXRAD DP relation for most of the cases, although NEXRAD DP generally has a slightly higher $CORR$. Nevertheless, there is no big statistical difference among the three rainfall algorithms in terms of $CORR$. That is, all of the algorithms can provide QPE with high $CORR$ with respect to APU rainfall observations. However, it should be noted that the $CORR$ has an increasing trend as the rainfall accumulation time increases from 5 to 60 min. On the other hand, the $NMAE$ has a decreasing trend. This can be attributed to the reduction of random error in radar measurements due to temporal and spatial averaging. The $RMSE$ increases as the rainfall accumulation time increases (i.e., rainfall amount gets larger). In order to further demonstrate the rainfall performance, Figure 3.11 shows scatterplots of the radar-APU rainfall comparisons at a sample APU location (APU03) for the three cases combined. Corresponding evaluation results are shown in Figure 3.12. Scatterplots of the individual events are not shown because they show essentially similar results to those in Figures 3.11 and 3.12.

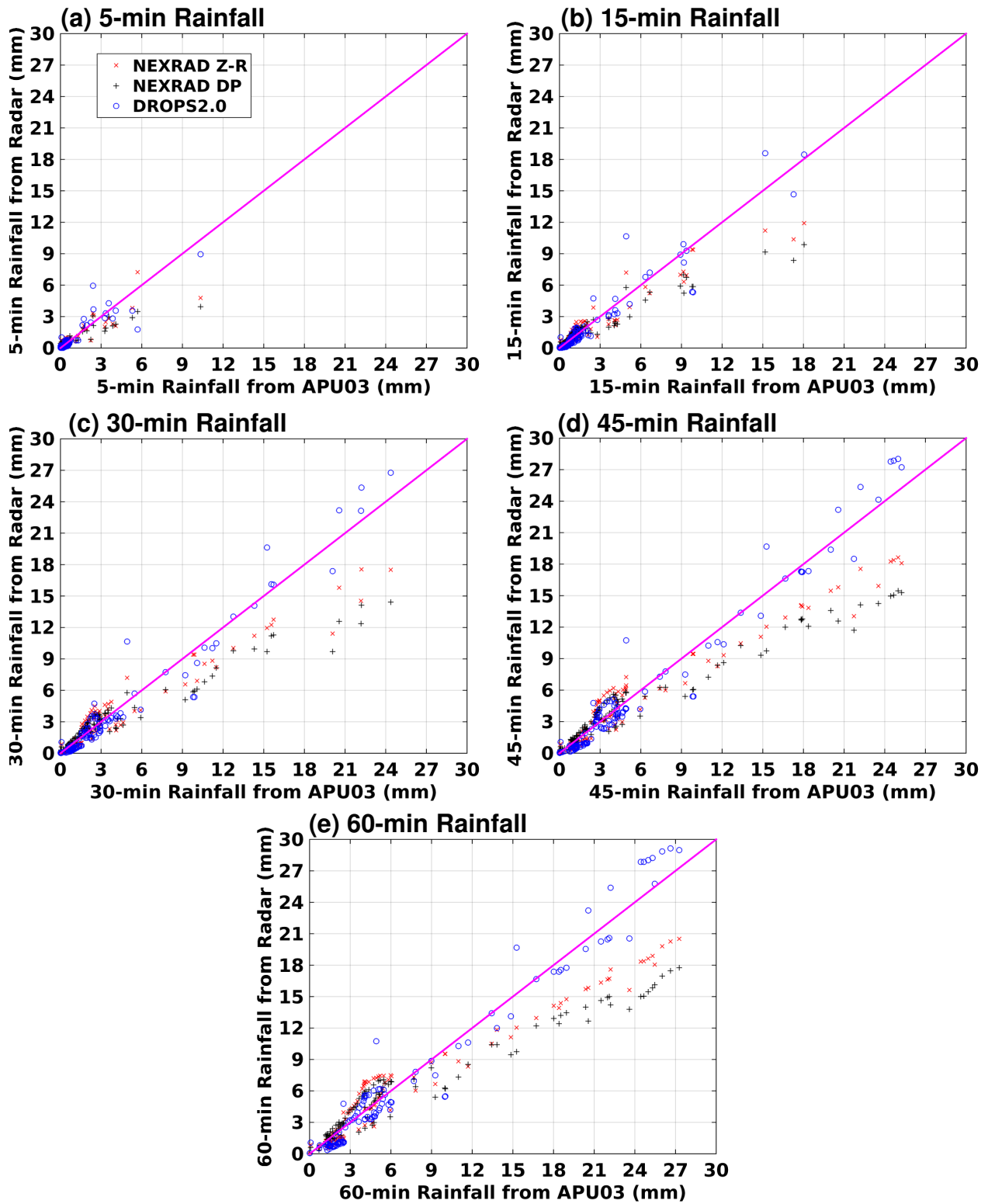


FIGURE 3.11. Scatterplots of radar rainfall estimates versus APU observations at different time scales at a sample APU location (APU03): (a) 5-, (b) 15-, (c) 30-, (d) 45-, and (e) 60-min.

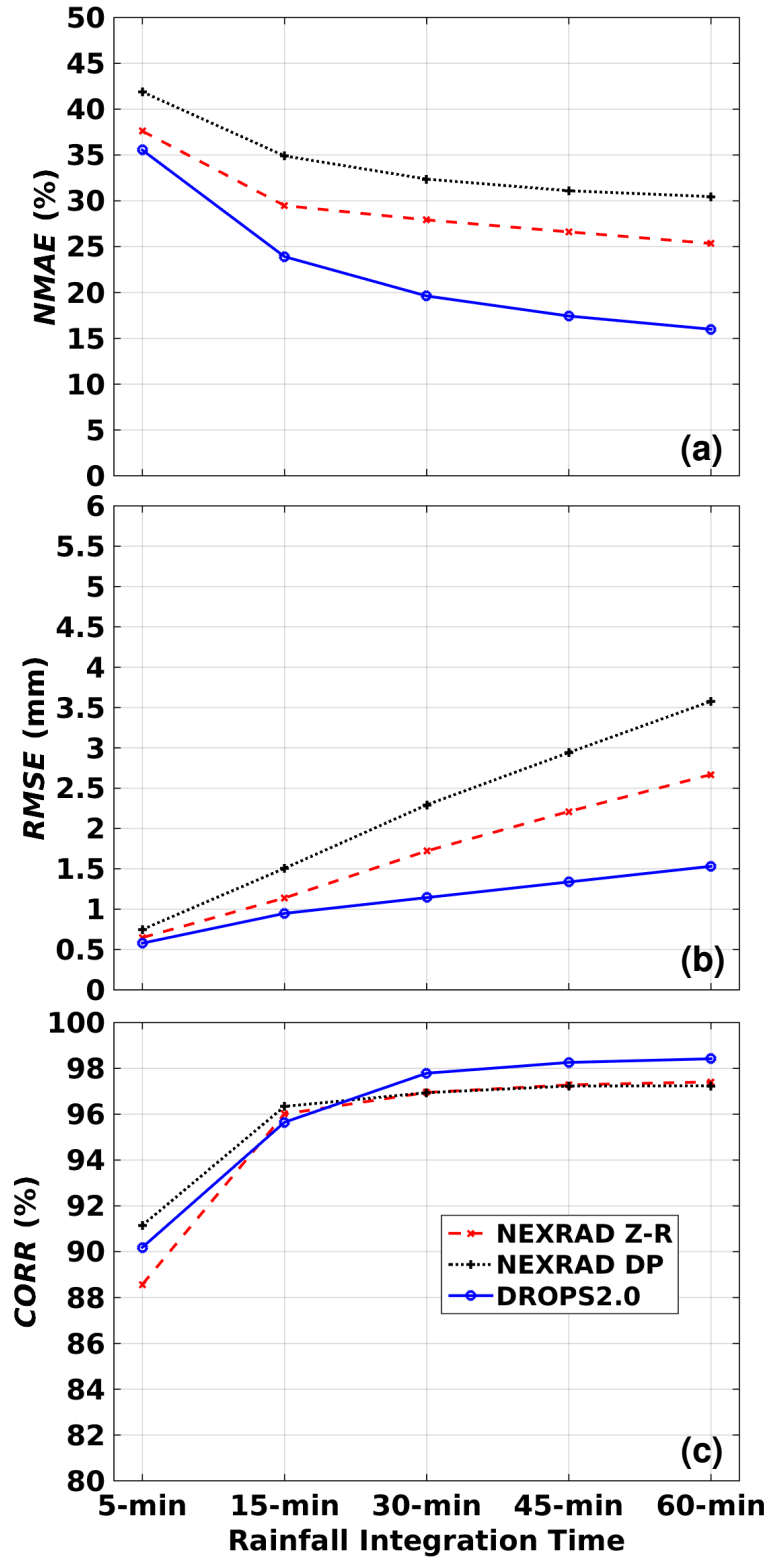


FIGURE 3.12. Evaluation results of rainfall products at different time scales with various rainfall algorithms at the location of APU03 for all the events combined: (a) *NMAE*, (b) *RMSE*, and (c) *CORR*.

TABLE 3.2. Evaluation results of various rainfall products at different time scales for the 20 May 2013 event.

	<i>NMAE</i> (%)			<i>RMSE</i> (mm)			<i>CORR</i>		
	Z-R	DP	DROPS2	Z-R	DP	DROPS2	Z-R	DP	DROPS2
				5-min	Rainfall	Product			
APU02	36.47	44.92	39.16	0.61	0.79	0.62	0.95	0.97	0.94
APU03	43.23	45.62	38.13	1.24	1.42	0.91	0.88	0.88	0.91
APU05	54.06	43.80	39.36	0.78	0.72	0.48	0.81	0.89	0.93
APU06	48.84	57.20	48.44	0.94	1.00	0.76	0.73	0.80	0.90
APU08	33.04	33.25	42.91	0.48	0.53	0.56	0.92	0.96	0.94
APU09	39.28	47.00	29.19	0.67	0.84	0.43	0.99	0.99	0.97
APU11	62.60	69.17	53.07	2.00	2.26	1.93	0.80	0.72	0.73
APU13	57.55	52.93	34.78	0.34	0.32	0.17	0.72	0.81	0.93
APU14	53.76	57.95	59.64	0.38	0.41	0.41	0.73	0.85	0.67
				15-min	Rainfall	Product			
APU02	31.83	40.92	31.72	1.36	1.82	1.11	0.97	0.98	0.97
APU03	34.74	37.33	22.40	2.16	2.76	1.50	0.96	0.96	0.96
APU05	32.33	33.10	22.62	1.27	1.29	0.69	0.90	0.93	0.97
APU06	41.75	52.86	43.77	1.80	2.29	1.72	0.91	0.93	0.97
APU08	23.41	31.82	26.93	0.90	1.23	0.75	0.96	0.98	0.98
APU09	38.56	46.81	21.72	1.40	1.76	0.70	0.99	0.99	0.98
APU11	59.47	67.42	52.21	4.10	4.73	3.56	0.92	0.90	0.90
APU13	34.96	51.03	28.16	0.50	0.78	0.37	0.89	0.86	0.96
APU14	39.83	53.81	48.49	0.74	1.05	0.89	0.86	0.93	0.81
				30-min	Rainfall	Product			
APU02	29.38	40.55	25.97	2.26	3.14	1.71	0.98	0.99	0.99
APU03	30.06	35.06	17.51	3.04	4.09	1.79	0.97	0.98	0.98
APU05	20.72	29.54	18.95	1.24	1.66	0.87	0.95	0.97	0.99
APU06	38.02	51.73	42.20	2.60	3.49	2.67	0.96	0.96	0.99
APU08	18.37	32.02	17.99	1.10	1.91	0.92	0.98	0.99	0.98
APU09	38.51	46.92	17.63	2.23	2.75	1.06	0.99	0.99	0.98
APU11	58.60	67.44	52.15	5.97	6.89	5.19	0.95	0.94	0.93
APU13	23.47	47.50	25.06	0.53	1.19	0.54	0.96	0.92	0.98
APU14	33.19	53.22	42.25	1.07	1.70	1.28	0.92	0.97	0.89
				45-min	Rainfall	Product			
APU02	29.80	41.20	25.34	3.39	4.65	2.46	0.99	0.99	0.99
APU03	27.24	34.17	15.48	3.71	5.13	2.13	0.98	0.98	0.98
APU05	15.87	28.58	17.21	1.26	2.06	1.10	0.97	0.99	0.99
APU06	38.30	52.32	42.40	3.35	4.54	3.52	0.97	0.96	0.99
APU08	16.11	32.62	14.18	1.32	2.55	1.09	0.99	0.99	0.98
APU09	38.72	47.26	15.85	3.06	3.74	1.31	0.99	0.99	0.98
APU11	58.84	68.22	52.32	7.15	8.25	6.24	0.97	0.96	0.96
APU13	17.21	46.06	24.10	0.56	1.57	0.72	0.98	0.94	0.99
APU14	32.38	54.53	40.65	1.32	2.23	1.62	0.95	0.98	0.93
				60-min	Rainfall	Product			
APU02	29.96	41.79	24.86	4.46	6.13	3.27	0.99	0.99	0.99
APU03	24.42	33.61	14.03	4.36	6.25	2.44	0.99	0.98	0.98
APU05	13.47	28.43	16.31	1.37	2.56	1.40	0.97	0.99	0.99
APU06	38.55	52.96	42.31	4.18	5.75	4.51	0.98	0.96	0.99
APU08	15.52	32.98	11.92	1.54	3.25	1.24	0.99	0.99	0.98
APU09	38.93	47.43	13.92	3.79	4.64	1.49	0.99	0.99	0.98
APU11	59.40	68.87	52.45	8.68	10.03	7.62	0.98	0.98	0.97
APU13	17.56	47.13	23.64	0.70	1.91	0.90	0.98	0.94	0.99
APU14	31.31	55.12	38.88	1.50	2.67	1.88	0.97	0.99	0.95

3.2.3. RANGE IMPACT ON QPE PERFORMANCE.

As mentioned above, from a theoretical point of view, the advanced dual-polarization techniques have made it generally possible to obtain rainfall algorithms less sensitive to DSD.

TABLE 3.3. Evaluation results of various rainfall products at different time scales for the 25 May 2013 event.

	<i>NMAE</i> (%)			<i>RMSE</i> (mm)			<i>CORR</i>		
	Z-R	DP	DROPS2	Z-R	DP	DROPS2	Z-R	DP	DROPS2
				5-min	Rainfall	Product			
APU02	34.89	35.94	42.97	0.13	0.13	0.15	0.78	0.82	0.81
APU03	39.41	42.71	37.44	0.14	1.14	0.12	0.81	0.78	0.79
APU05	32.66	35.73	42.83	0.12	0.13	0.15	0.86	0.85	0.80
APU06	35.33	33.44	37.44	0.14	0.12	0.13	0.84	0.87	0.85
APU08	33.43	34.59	40.38	0.13	0.13	0.16	0.85	0.85	0.80
APU09	38.49	42.83	48.86	0.16	0.17	0.19	0.82	0.82	0.81
APU11	41.82	44.32	49.58	0.18	0.19	0.21	0.74	0.76	0.77
APU13	40.50	40.74	47.16	0.15	0.15	0.17	0.79	0.80	0.75
APU14	41.22	40.61	47.25	0.15	0.15	0.17	0.78	0.79	0.74
				15-min	Rainfall	Product			
APU02	34.42	35.13	43.00	0.39	0.39	0.45	0.68	0.71	0.68
APU03	34.03	30.27	33.00	0.36	0.27	0.29	0.87	0.92	0.86
APU05	25.93	29.21	35.91	0.26	0.30	0.36	0.91	0.92	0.91
APU06	24.73	23.91	26.61	0.24	0.21	0.23	0.94	0.95	0.95
APU08	25.63	27.69	33.18	0.28	0.30	0.35	0.92	0.92	0.91
APU09	35.67	41.11	48.15	0.43	0.47	0.53	0.86	0.87	0.87
APU11	38.82	42.65	49.09	0.50	0.54	0.58	0.78	0.80	0.81
APU13	33.95	32.52	39.90	0.36	0.35	0.40	0.85	0.88	0.87
APU14	34.74	32.59	40.39	0.37	0.36	0.41	0.85	0.87	0.86
				30-min	Rainfall	Product			
APU02	30.08	30.53	37.83	0.65	0.66	0.77	0.78	0.81	0.81
APU03	32.22	26.12	31.61	0.66	0.49	0.54	0.89	0.95	0.89
APU05	22.81	26.54	34.13	0.44	0.52	0.65	0.94	0.94	0.94
APU06	22.05	21.27	22.86	0.39	0.35	0.38	0.96	0.96	0.97
APU08	21.29	25.31	31.10	0.44	0.51	0.60	0.95	0.95	0.95
APU09	33.69	40.63	48.45	0.80	0.89	1.01	0.88	0.90	0.90
APU11	37.79	42.62	49.30	0.95	1.02	1.11	0.81	0.82	0.83
APU13	28.71	28.63	37.03	0.59	0.60	0.71	0.91	0.92	0.92
APU14	29.44	28.76	37.10	0.61	0.61	0.71	0.90	0.91	0.92
				45-min	Rainfall	Product			
APU02	27.71	28.46	36.47	0.88	0.91	1.09	0.84	0.86	0.87
APU03	30.69	24.15	30.26	0.94	0.69	0.74	0.90	0.95	0.90
APU05	20.83	25.32	33.99	0.57	0.73	0.92	0.95	0.95	0.96
APU06	18.95	18.89	21.01	0.51	0.46	0.51	0.96	0.97	0.98
APU08	19.12	24.25	30.04	0.60	0.71	0.86	0.96	0.96	0.97
APU09	33.22	40.78	48.66	1.15	1.29	1.48	0.89	0.90	0.91
APU11	37.36	42.74	49.52	1.38	1.50	1.64	0.82	0.83	0.85
APU13	24.95	27.52	36.98	0.74	0.80	0.98	0.94	0.95	0.95
APU14	25.81	27.76	37.10	0.77	0.82	0.99	0.93	0.94	0.95
				60-min	Rainfall	Product			
APU02	26.47	28.13	36.29	1.10	1.16	1.40	0.87	0.89	0.89
APU03	29.94	23.44	28.05	1.21	0.90	0.91	0.91	0.96	0.92
APU05	19.46	25.14	34.18	0.68	0.93	1.19	0.96	0.96	0.97
APU06	17.55	17.55	20.34	0.61	0.57	0.63	0.97	0.97	0.98
APU08	18.10	23.56	30.31	0.74	0.90	1.10	0.97	0.97	0.97
APU09	32.52	40.61	48.47	1.49	1.69	1.94	0.89	0.91	0.92
APU11	36.46	42.38	49.15	1.78	1.95	2.14	0.83	0.84	0.86
APU13	23.62	27.39	37.21	0.89	0.99	1.25	0.95	0.96	0.97
APU14	24.67	27.58	37.37	0.92	1.01	1.25	0.95	0.96	0.97

However, from an operational point of view, the geometry of radar measurements combined with the variability of the spatial structure of precipitation still limits the radar rainfall accuracy, especially for the regions far from radar (Ryzhkov 2007; Gorgucci and Baldini 2015).

TABLE 3.4. Evaluation results of rainfall products at different time scales for the 29 May 2013 event. “-” indicates no rain observed by radar or APU.

	<i>NMAE</i> (%)			<i>RMSE</i> (mm)			<i>CORR</i>		
	Z-R	DP	DROPS2	Z-R	DP	DROPS2	Z-R	DP	DROPS2
				5-min	Rainfall	Product			
APU02	38.16	43.95	21.42	2.59	2.83	1.37	0.84	0.90	0.94
APU03	31.15	37.81	31.98	0.71	0.85	0.90	0.91	0.96	0.85
APU05	45.68	42.25	42.76	1.07	0.84	0.85	0.86	0.90	0.89
APU06	47.85	31.41	37.42	1.07	0.67	0.74	0.90	0.90	0.87
APU08	41.66	33.51	38.72	1.11	0.98	1.06	0.91	0.91	0.87
APU09	89.03	50.51	58.20	0.29	0.15	0.18	0.93	0.95	0.88
APU11	41.36	22.53	42.45	0.05	0.02	0.05	0.92	0.99	0.99
APU13	-	-	-	-	-	-	-	-	-
APU14	-	-	-	-	-	-	-	-	-
				15-min	Rainfall	Product			
APU02	36.80	43.69	18.23	6.07	6.87	2.97	0.93	0.95	0.97
APU03	21.42	35.12	20.14	1.06	1.73	1.35	0.98	0.98	0.94
APU05	30.88	30.54	28.11	1.80	1.33	1.13	0.91	0.95	0.96
APU06	41.98	19.94	17.37	2.04	0.86	0.72	0.96	0.97	0.97
APU08	32.32	25.16	28.17	2.19	1.58	1.60	0.93	0.95	0.92
APU09	86.65	44.91	39.97	0.51	0.25	0.22	0.98	0.98	0.97
APU11	25.03	18.58	40.33	0.05	0.03	0.09	0.98	0.99	0.99
APU13	-	-	-	-	-	-	-	-	-
APU14	-	-	-	-	-	-	-	-	-
				30-min	Rainfall	Product			
APU02	35.52	43.70	13.73	8.64	10.31	3.38	0.98	0.98	0.99
APU03	22.68	33.35	14.22	1.74	2.52	1.39	0.99	0.99	0.97
APU05	31.55	29.34	25.39	2.60	1.89	1.59	0.94	0.97	0.97
APU06	42.67	15.92	9.06	3.45	1.23	0.63	0.98	0.99	0.99
APU08	33.53	21.37	18.70	3.52	2.00	1.59	0.96	0.97	0.97
APU09	84.14	42.27	32.52	0.66	0.32	0.25	0.99	0.99	0.98
APU11	21.32	16.81	39.42	0.05	0.04	0.12	0.99	0.99	0.99
APU13	-	-	-	-	-	-	-	-	-
APU14	-	-	-	-	-	-	-	-	-
				45-min	Rainfall	Product			
APU02	35.09	43.70	12.52	10.64	13.05	3.70	0.99	0.99	0.99
APU03	23.17	32.09	11.24	2.43	3.34	1.44	0.99	0.99	0.99
APU05	31.52	28.60	24.49	3.32	2.33	1.99	0.98	0.99	0.99
APU06	43.31	15.88	7.35	4.73	1.57	0.66	0.99	0.99	0.99
APU08	35.52	19.70	11.89	4.60	2.23	1.20	0.99	0.99	0.99
APU09	84.41	41.98	30.53	0.82	0.40	0.30	0.99	0.99	0.99
APU11	17.73	13.39	38.15	0.06	0.05	0.15	0.99	0.99	0.99
APU13	-	-	-	-	-	-	-	-	-
APU14	-	-	-	-	-	-	-	-	-
				60-min	Rainfall	Product			
APU02	35.26	44.33	11.70	13.39	16.63	4.47	0.99	0.99	0.99
APU03	23.44	31.36	10.39	3.20	4.27	1.64	0.99	0.99	0.99
APU05	28.64	29.96	25.67	3.68	3.19	2.65	0.98	0.99	0.99
APU06	42.15	15.43	5.90	5.83	1.91	0.72	0.99	0.99	0.99
APU08	32.74	19.69	11.99	5.24	2.78	1.54	0.99	0.99	0.99
APU09	85.31	42.20	30.50	0.96	0.47	0.34	0.99	0.99	0.99
APU11	15.18	11.50	37.89	0.07	0.05	0.17	0.99	0.99	0.99
APU13	-	-	-	-	-	-	-	-	-
APU14	-	-	-	-	-	-	-	-	-

Here, the unique instrument layout during the NASA IFloodS field campaign is investigated to quantify the rainfall errors introduced by range impact.

TABLE 3.5. Evaluation results of various rainfall products at different time scales for the three events combined.

	<i>NMAE</i> (%)			<i>RMSE</i> (mm)			<i>CORR</i>		
	Z-R	DP	DROPS2	Z-R	DP	DROPS2	Z-R	DP	DROPS2
				5-min	Rainfall	Product			
APU02	37.14	42.79	30.65	0.90	1.01	0.56	0.92	0.95	0.96
APU03	37.61	41.89	35.54	0.65	0.75	0.58	0.88	0.91	0.90
APU05	43.51	40.52	41.88	0.52	0.44	0.40	0.86	0.91	0.91
APU06	44.44	39.69	40.82	0.56	0.48	0.42	0.83	0.86	0.89
APU08	37.17	34.05	40.52	0.47	0.43	0.47	0.92	0.93	0.89
APU09	41.31	45.24	42.94	0.30	0.35	0.23	0.92	0.94	0.96
APU11	51.21	55.16	51.52	0.71	0.80	0.68	0.80	0.73	0.76
APU13	46.89	42.66	51.82	0.21	0.18	0.22	0.70	0.76	0.67
APU14	44.59	45.19	50.58	0.20	0.21	0.22	0.76	0.74	0.73
				15-min	Rainfall	Product			
APU02	35.19	41.50	26.77	2.31	2.66	1.25	0.95	0.97	0.98
APU03	29.48	34.90	23.91	1.14	1.51	0.95	0.96	0.96	0.96
APU05	29.67	30.81	29.40	0.93	0.79	0.61	0.92	0.95	0.97
APU06	36.61	30.72	27.95	1.14	1.02	0.79	0.88	0.90	0.94
APU08	28.29	27.83	29.76	1.01	0.86	0.78	0.94	0.96	0.95
APU09	39.03	43.69	39.08	0.69	0.81	0.52	0.92	0.94	0.96
APU11	47.80	53.23	50.66	1.51	1.74	1.35	0.87	0.84	0.91
APU13	36.34	35.19	42.75	0.43	0.44	0.48	0.83	0.85	0.82
APU14	36.20	38.22	42.63	0.45	0.54	0.51	0.85	0.81	0.85
				30-min	Rainfall	Product			
APU02	33.03	40.51	21.64	3.82	4.61	1.73	0.98	0.98	0.99
APU03	27.92	32.37	19.62	1.72	2.29	1.14	0.96	0.96	0.98
APU05	25.82	28.47	26.85	1.24	1.12	0.90	0.95	0.97	0.98
APU06	34.60	27.98	23.13	1.83	1.58	1.19	0.90	0.92	0.95
APU08	25.87	25.56	23.02	1.57	1.22	0.89	0.95	0.97	0.98
APU09	37.52	43.13	37.41	1.15	1.35	0.93	0.92	0.94	0.95
APU11	46.55	52.93	50.52	2.38	2.74	2.16	0.86	0.83	0.93
APU13	28.89	32.10	37.38	0.62	0.73	0.75	0.90	0.89	0.90
APU14	30.52	35.18	38.53	0.71	0.92	0.85	0.89	0.84	0.91
				45-min	Rainfall	Product			
APU02	32.45	40.26	20.40	5.05	6.25	2.14	0.99	0.99	0.99
APU03	26.61	31.10	17.43	2.21	2.94	1.33	0.97	0.97	0.98
APU05	23.67	27.45	26.11	1.55	1.42	1.18	0.97	0.98	0.99
APU06	33.46	27.59	22.33	2.46	2.06	0.57	0.90	0.93	0.95
APU08	24.99	24.77	19.24	2.05	1.52	0.94	0.97	0.98	0.99
APU09	37.11	43.15	36.72	1.61	1.88	1.62	0.91	0.93	0.95
APU11	46.19	53.13	50.55	3.15	3.61	2.89	0.85	0.82	0.94
APU13	24.93	31.29	36.17	0.76	0.98	0.99	0.93	0.91	0.93
APU14	27.52	34.56	38.04	0.90	1.24	1.13	0.91	0.87	0.93
				60-min	Rainfall	Product			
APU02	32.32	40.64	19.81	6.17	7.73	2.61	0.99	0.99	0.99
APU03	25.35	30.46	15.99	2.67	3.58	1.53	0.97	0.97	0.98
APU05	21.31	27.78	26.50	1.70	1.83	1.54	0.97	0.98	0.99
APU06	32.22	27.27	21.86	3.00	2.54	1.95	0.91	0.93	0.96
APU08	23.01	24.68	19.11	2.33	1.90	1.18	0.97	0.98	0.99
APU09	36.67	43.00	35.99	2.02	2.36	1.70	0.90	0.93	0.95
APU11	45.83	53.11	50.39	3.86	4.43	3.59	0.84	0.81	0.94
APU13	23.16	31.10	35.56	0.89	1.21	1.24	0.94	0.93	0.95
APU14	26.30	34.35	37.74	1.07	1.52	1.41	0.93	0.89	0.95

As shown in Figure 3.3, APU05, APU06, and APU08 are almost collocated; APU09 and APU11 are very closely deployed; and APU13 and APU14 are collocated. Therefore, for the sake of comparison, this study takes the mean of ranges and rainfall evaluation results for

those APUs that are closely deployed. Figure 3.13 shows a conceptual diagram illustrating the radar beam broadening effect. The mean ranges, radar center beam heights, and radar range gate volumes at these ranges are also indicated in Figure 3.13.

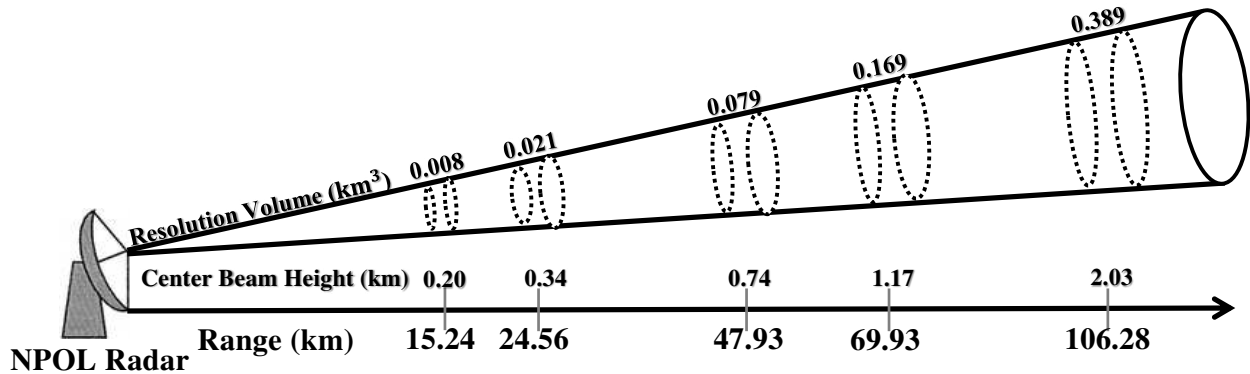


FIGURE 3.13. Conceptual diagram showing radar beam broadening effect.

Figure 3.14 shows the *CORR* results of different rainfall products as a function of range for all three events combined. Clearly, there is a decreasing trend in *CORR*, which indicates that the radar-estimated rainfall and APU-observed rainfall are less correlated as the range from the radar moves farther away. This again poses the challenge of using weather radar to capture complex spatial and temporal variabilities of precipitation at long distances.

3.3. SUMMARY

Although a number of radar rainfall algorithms are available in the literature, there is no standard approach to radar rainfall estimation. In particular, when solid or mixed phase precipitation is involved, it is difficult to determine which rainfall relation to apply to a given set of radar measurements.

In this chapter, an improved S-band dual-polarization algorithm (DROPS2.0) has been developed. DROPS2.0 is essentially an HID-guided approach. The advanced classification technique implemented in DROPS2.0 exploits the spatial correlation of dual-polarization

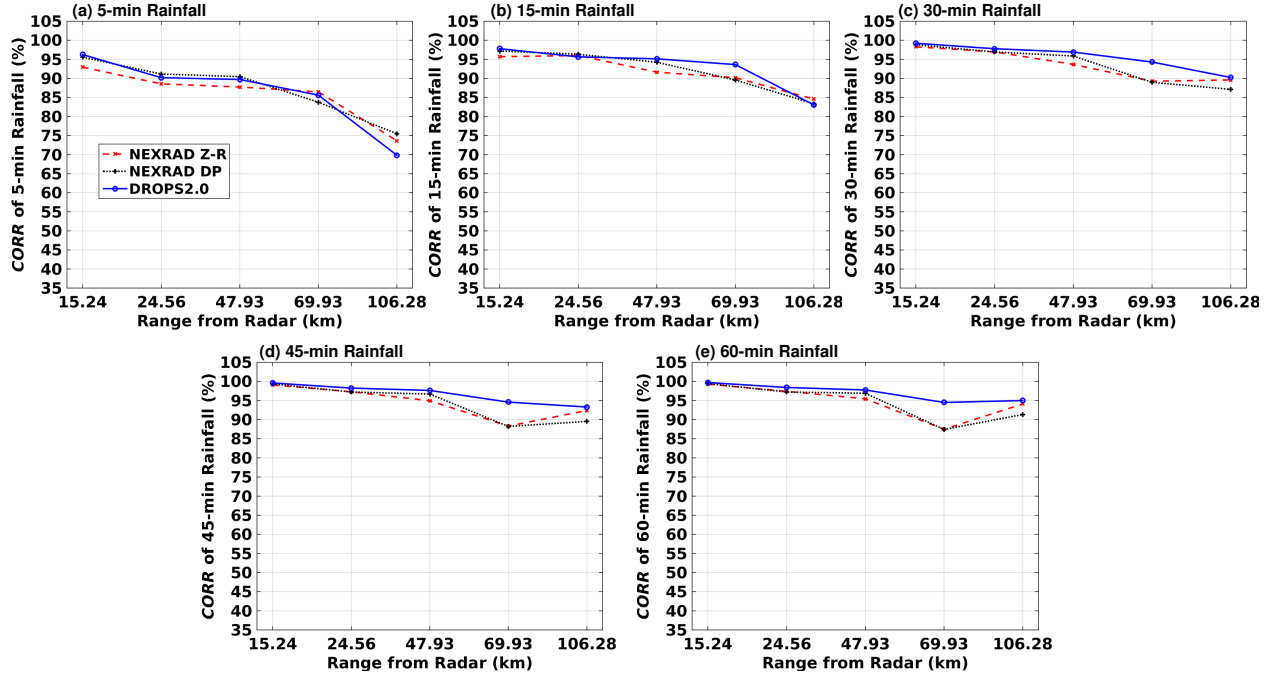


FIGURE 3.14. *CORR* of rainfall products at different time scales with various rainfall algorithms at different ranges from radar for all the events combined: (a) 5-, (b) 15-, (c) 30-, (d) 45-, and (e) 60-min rainfall.

radar observations from adjacent range bins. Compared to traditional fuzzy logic-based methods, this hydrometeor identification methodology also takes into account the hydrometeor microphysical constraints and the classification quality. Even in the case of limited melting layer contamination, it can provide a clean classification that allows the application of appropriate rainfall relations.

The proposed rainfall methodology has been demonstrated and evaluated with S-band NPOL radar data collected during the IFloodS field campaign. It is shown that DROPS2.0 performs better compared to the NEXRAD $Z - R$ relation or the dual-polarization algorithm adopted by NEXRAD. In addition, the impact of radar beam broadening on various rainfall algorithms has been investigated within the framework of the IFloodS field experiment. It was found that the radar-estimated rainfall is less correlated with ground truth (i.e., disdrometer measurements) when the beam goes farther from the radar. Hence, it can be

a challenging task to use weather radar to characterize the complex spatial and temporal variabilities of precipitation at long distances (e.g., beyond 100 km).

DROPS2.0 is very robust, and it worked continuously without any incident during the NASA IFloodS field experiment. Since S-band is one of the standard radar operating frequencies in many countries, the rainfall system designed in this chapter can potentially be applied in a broader domain with operational dual-polarization radars.

CHAPTER 4

DENSE RADAR NETWORK FOR URBAN WEATHER HAZARDS

DETECTION AND MITIGATION

Most parts of the world are becoming increasingly urbanized. This rapid urbanization has made densely populated areas more vulnerable to natural disasters such as urban flash floods. Therefore, monitoring weather conditions in a timely manner at good spatial resolution is critical in terms of protecting personal and property safety. To this end, a variety of product systems have been developed based on the long-range microwave operational radar networks (e.g., WSR-88DP in the U.S.). However, as described in Section 2.3.2 in Chapter 2, one limitation of today's large weather radar installations is their inability to cover the lower part of the atmosphere due to the earth's curvature and terrain blockage. The incomplete low-level coverage, limited spatial resolution at long distances, and slow scan rate impede the ability of such systems to identify and detect fine-scale weather phenomena such as tornadoes and downbursts.

In this chapter, the principles of short-wavelength (i.e., X-band) radar technology and networking are presented. The dense radar network developed by the Center for Collaborative Adaptive Sensing of the Atmosphere (CASA) will be detailed, with an emphasis on the development of application products for urban hazard detection and mitigation.

4.1. BACKGROUND OF CASA

Radar sampling resolution is primarily determined by the transmitted pulse width, antenna beamwidth, and range from radar. For an ideal uniformly illuminated parabolic reflector, the sampling resolution is given by:

$$(24a) \quad \textit{Resolution cell length} \approx cT/2$$

$$(24b) \quad \textit{Resolution cell width} \approx \lambda R/d$$

where c is the speed of light; T is the transmitted pulse width typically in the order of μs ; λ is radar wavelength; d is the antenna aperture size; and R is the range from radar.

A study by McLaughlin et al. (2009) concluded that a reasonable antenna size for unobtrusive equipment deployment is of the order of 1 to 1.5 meters. Assuming the frequency of the NWS WSR-88DP system (S-band), operating a radar with a 1-m antenna will result in a resolution cell width of 3 km at 30 km range. The fine-scale weather features such as tornadoes and localized flash floods cannot be resolved at this coarse resolution. In reality, each WSR-88DP system is equipped with a 9 m diameter antenna. In addition, as aforementioned, the WSR-88DP radar coverage is non-overlapping (at very high altitudes, if any), and the spacing between radars is about 230 km in the eastern U.S. and 345 km in the western U.S. The illuminated volume will be tremendously expanded as the distance from the radar increases. Further, because of the earth's curvature and terrain blockage, more than 70% of the atmosphere below 1 km altitude AGL cannot be observed. From a temporal resolution perspective, individual radars in the WSR-88DP network conduct volume scans updated every five to six minutes, which is too long for applications such as urban flash flood

monitoring. Moreover, deployment and maintenance of such high-powered large radars (12-m radomes) are expensive in terms of cost efficiency and operational complexity. By going to a shorter wavelength (X-band), higher spatial resolution can be attained with a smaller antenna. Compared to the WSR-88DP radar, the easier manipulation of X-band radar can also provide us with higher temporal resolution. In addition, the compact X-band system can be readily deployed on small towers with small land footprints or existing infrastructure elements such as rooftops and communication towers. Therefore, because of its low power low cost, the small X-band radar has gained increasing interest in recent years.

As a prestigious National Science Foundation (NSF) Engineering Research Center (ERC), CASA was established in 2003, dedicated to revolutionizing the ability to observe, understand, predict, and respond to hazardous weather events (McLaughlin et al. 2009). It is a multi-sector partnership among academia, industry, and government with over 50 million USD in federal, university, industry, and state funding. In particular, the multidisciplinary CASA research team, including radar engineers, computer scientists, meteorologists, sociologists, and hydrologists, have aimed to overcome the resolution and coverage limitations of traditional weather radar networks through deploying dense networks of shorter-range, high-resolution X-band dual-polarization Doppler radars (Junyent et al. 2010; Chandrasekar et al. 2012). The innovative collaborative and dynamic sensing paradigm proposed by CASA, called Distributed Collaborative Adaptive Sensing, or DCAS, can significantly enhance weather observations, especially in the lower troposphere (1-3 km AGL). Figure 4.1 illustrates the simplified architecture of a typical DCAS system, which includes distributed high-resolution X-band Doppler radars, algorithms that dynamically process the collected data, detect ongoing weather features, and manage system resource allocations as well as interfaces that enable end-users to interact with the system.

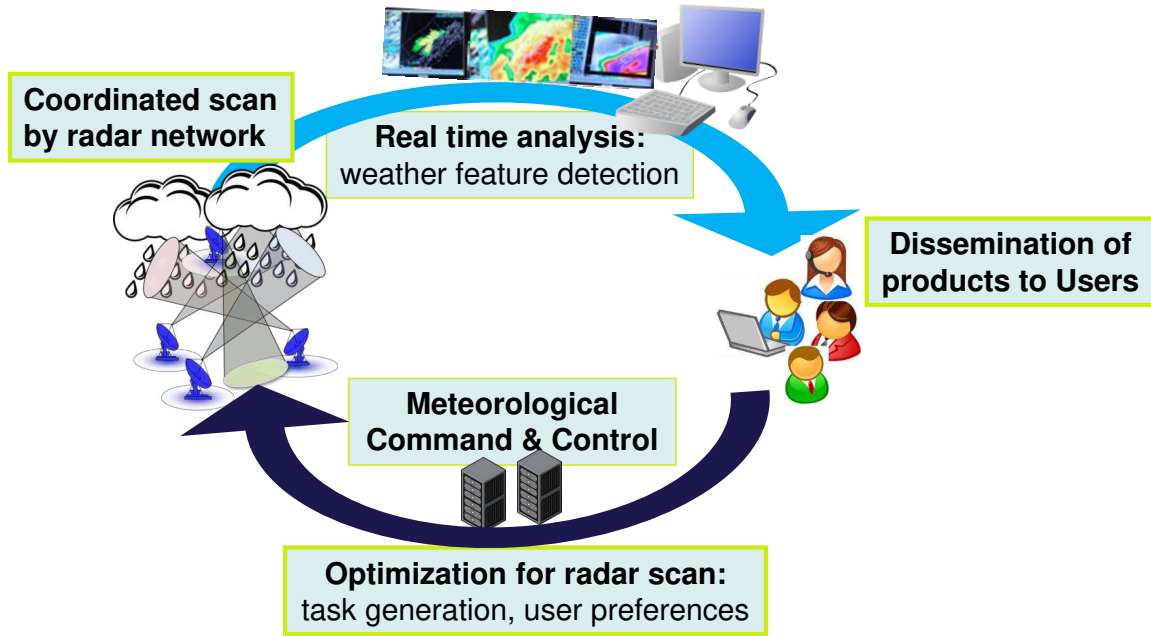


FIGURE 4.1. Simplified architecture of a distributed collaborative adaptive sensing (DCAS) system. The real-time data and products are disseminated to various end users. Through meteorological command & control (MC&C) the radar network scanning strategy is adapted according to feedback from end users.

Compared to the static scanning strategy adopted by WSR-88DP radars, the DCAS approach employed by CASA adaptively operates the radars within a dynamic information technology infrastructure, directing the radars to scan areas of interest according to changing weather conditions and end-user needs (McLaughlin et al. 2009; Chen and Chandrasekar 2018). In this way, CASA’s multidisciplinary team conducts end-to-end research from sensor observation to product development and validation linked to end user decision-making and response. The DCAS system uses a Meteorological Command and Control (MC&C) component to collaboratively coordinate the scanning strategy of distributed radars in a network environment. Through a space-time adaptive targeted sector-scan approach, or a collaborative processing approach, the network-level performance is superior to the capabilities of individual radars in terms of update rate on key weather features, minimum beam height, and spatial resolution (Junyent and Chandrasekar 2009). In addition, the requirement for

radar transmitter power is lower in DCAS mode than it would be if the radars were operated independently in order to achieve a certain level of sensitivity. As well as the high-resolution observations of the lower troposphere provided by CASA radars, the network topology of CASA allows for large areas of overlapping coverage. At the overlapping regions, multiple Doppler analyses can be conducted to retrieve the vector wind velocity and wind patterns. The dense network topology also provides a fault-tolerant system that can operate and re-configure itself if one of the radars is down. Overall, through mapping storms, winds, and rain, the CASA radar network serves as a critical emergency weather warning tool that can save lives and property.

The first research network developed by CASA, termed Integrated Project 1 (IP1), which consisted of four radar nodes, was deployed in the “tornado alley” over southwestern Oklahoma for the study of tornadoes, severe thunderstorms, and other severe weather hazards (McLaughlin et al. 2009). The test bed, covering an area of about 7,000 km², was located approximately 45 km southwest of Oklahoma City, Oklahoma. Figure 4.2 illustrates the coverage map of the CASA IP1 radars. These radars-KCYR, KLWE, KRSP, and KSAO-were installed in the towns of Cyril, Lawton, Rush Springs, and Chickasha, Oklahoma, respectively. Each radar node was approximately 30 km away from the next unit. The blue circles in Figure 4.2 correspond to a 40 km range from the radars. The range resolution of IP1 radars is 75 m. The location of the test bed was chosen based on its climatological and meteorological properties. Being in tornado alley, this test bed has about a 77% chance of experiencing at least one tornado each year, and severe storms are almost 100% guaranteed every year. This area receives an average of four tornado warnings and 53 thunderstorm warnings per year (www.spc.noaa.gov). This four-node DCAS system was operated in a tight loop with an end user group comprised of the NWS Weather Forecast Office (WFO)

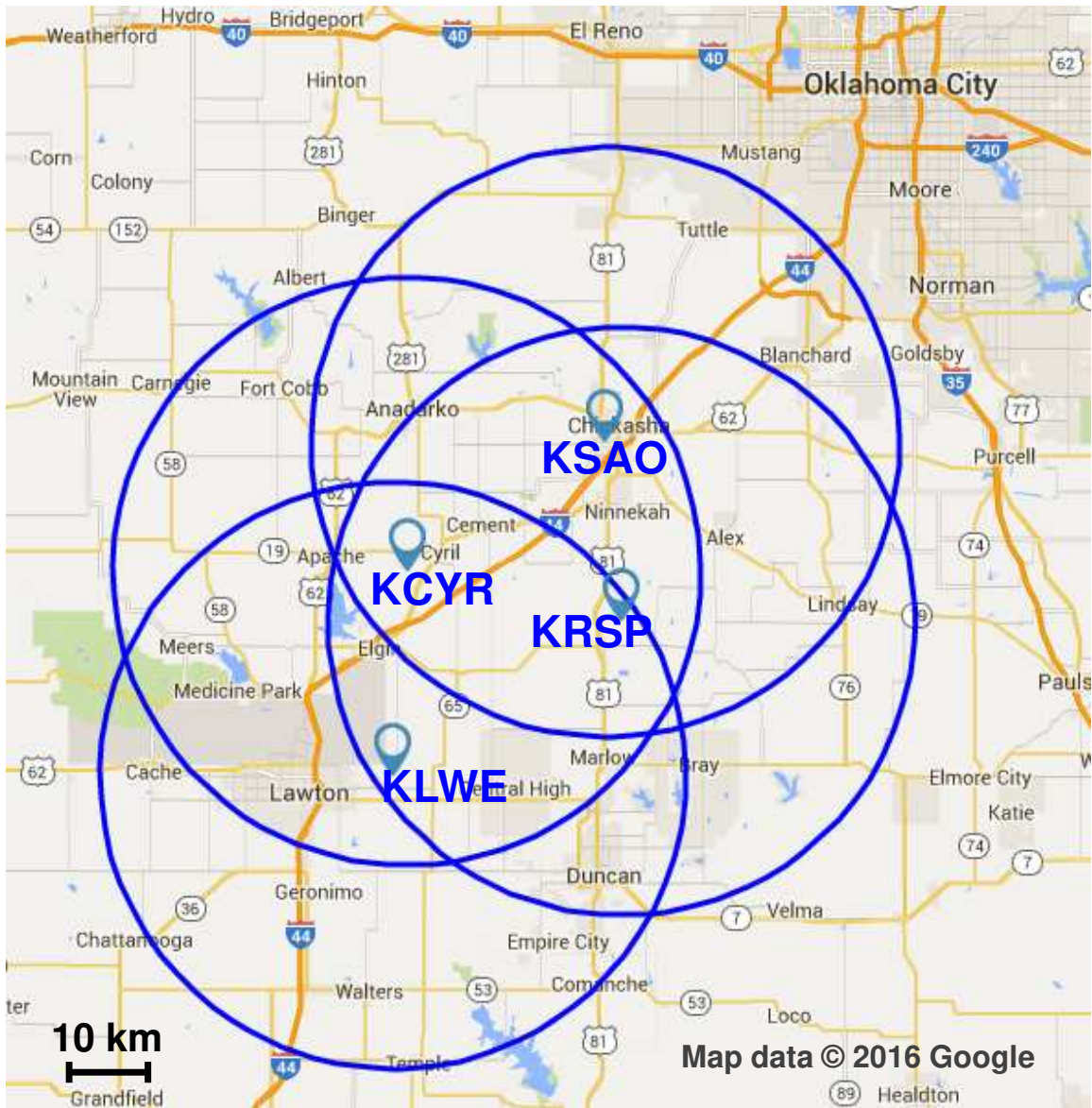


FIGURE 4.2. CASA IP1 testbed in Oklahoma. The letter symbols such as KSAO denote the names of the various radars. The circles in blue correspond to the 40 km converge range rings of the X-band radars.

in Norman, Oklahoma, emergency managers who have jurisdictional authority within and upstream of the test bed area, and CASA researchers. The high-resolution observations, post-event case studies, and fundamental multi-disciplinary research during the five years' operation (2007-2011) demonstrated the excellent performance of the CASA DCAS concept (McLaughlin et al. 2009; Junyent et al. 2010; Chandrasekar et al. 2012).

However, it should be noted that moving to X-band from conventional S-band research did not come easily, as technical solutions needed to be found for several basic limitations, such as attenuation, range velocity ambiguity, etc. In particular, the attenuation induced by propagation in rain media was an important challenge in X-band applications. Extensive research in CASA and elsewhere demonstrated that this can be overcome by using some modern attenuation correction techniques that include dual-polarization (Lim and Chandrasekar 2016). Similarly, using a standard uniform pulsing scheme at X-band will result in a reduced maximum observable velocity due to the range velocity ambiguity (Bringi and Chandrasekar 2001). As documented in Bharadwaj et al. (2010), modern pulsing schemes with advanced signal processing were developed in CASA to overcome this limitation. Another critical problem with short range operations in an urban environment is the high clutter environment. One needs to pay extra attention to clutter suppression. While clutter suppression by itself is not complicated, all the advanced clutter suppression techniques must work in conjunction with the operational mode for clutter suppression as well as range velocity mitigation. CASA researchers such as Nguyen et al. (2008) and Bharadwaj et al. (2010) invested heavily in this, and advanced clutter suppression techniques were developed to handle the high clutter environment.

Since spring 2012, CASA, in collaboration with the NWS and the North Central Texas Council of Governments (NCTCOG), has been operating its first dense urban radar network in the Dallas-Fort Worth (DFW) area, one of the largest inland metropolitan areas in the U.S. All the major technological advances developed through CASA have been put into operation in most of the radars in the network at DFW, with a demonstration of research in operations for urban weather hazard detection and mitigation. In the following sections,

the CASA DFW dense urban radar network and examples of its operational products will be detailed.

4.2. CASA DALLAS-FORT WORTH (DFW) DENSE URBAN RADAR NETWORK

The DFW metroplex is among the fastest-growing major urban areas in the country. It is home to two major airports, including DFW International Airport, the third busiest airport in the world; numerous regional airports; and many large sports complexes. The DFW area experiences a wide range of natural hazardous events such as severe winds, tornadoes, and flash floods. It is an ideal place to demonstrate the application of a dense radar network for urban weather disaster monitoring.

Centered in the DFW urban remote sensing network are eight dual-polarization X-band radars that can provide coverage to most of the 6.5 million people in this region. Figure 4.3 shows photos taken during the installation of various DFW radars, while 4.4 illustrates the geographical deployment of the eight X-band radars as well as the S-band WSR-88DP deployed in Fort Worth (the KFWS radar). The letter symbols in Figure 4.4 correspond to the names of the various radars. The specific locations of each radar node, including longitude, latitude, and altitude information, as well as the cities where the radars are installed, are listed in Table 4.1.

The radar system deployed in the DFW urban testbed is based on new technologies developed within the CASA project. The system specifications and data products produced by the DFW radars are listed in Table 4.2. More details about the CASA X-band radar system can be found in Junyent et al. (2010). Table 4.2 also shows the key parameters of a typical WSR-88DP radar system for comparison purposes. The DFW X-band radars sit atop



FIGURE 4.3. Installation of CASA DFW radars. The letter symbols (e.g., XUTA) correspond to the naming of various radars. More information about DFW radar deployment can be found in Table 4.1.

TABLE 4.1. Longitude/latitude information of the eight dual-polarization X-band radar nodes in the DFW urban network. The altitudes above mean sea level (AMSL), as well as the cities where the radar are deployed are also listed. The one marked with * (i.e., XMKN radar) is yet to be deployed.

Radar Name	Latitude (°N)	Longitude (°W)	Altitude (m)	City
XUTA	32.7306	97.1125	300	Arlington
XMDL	32.4921	96.9973	250	Midlothian
XFTW	32.8385	97.4257	300	Fort Worth
XUNT	33.2536	97.1520	224	Denton
XJCO	32.3717	97.3890	263	Cleburne
XADD	32.9814	96.8391	210	Addison
XMSQ	32.7556	96.5332	148	Mesquite
XMKN*	33.2118	96.6572	225	McKinney

a high-performance pedestal assembly capable of high accelerations and rapid back-and-forth PPI and RHI scans.

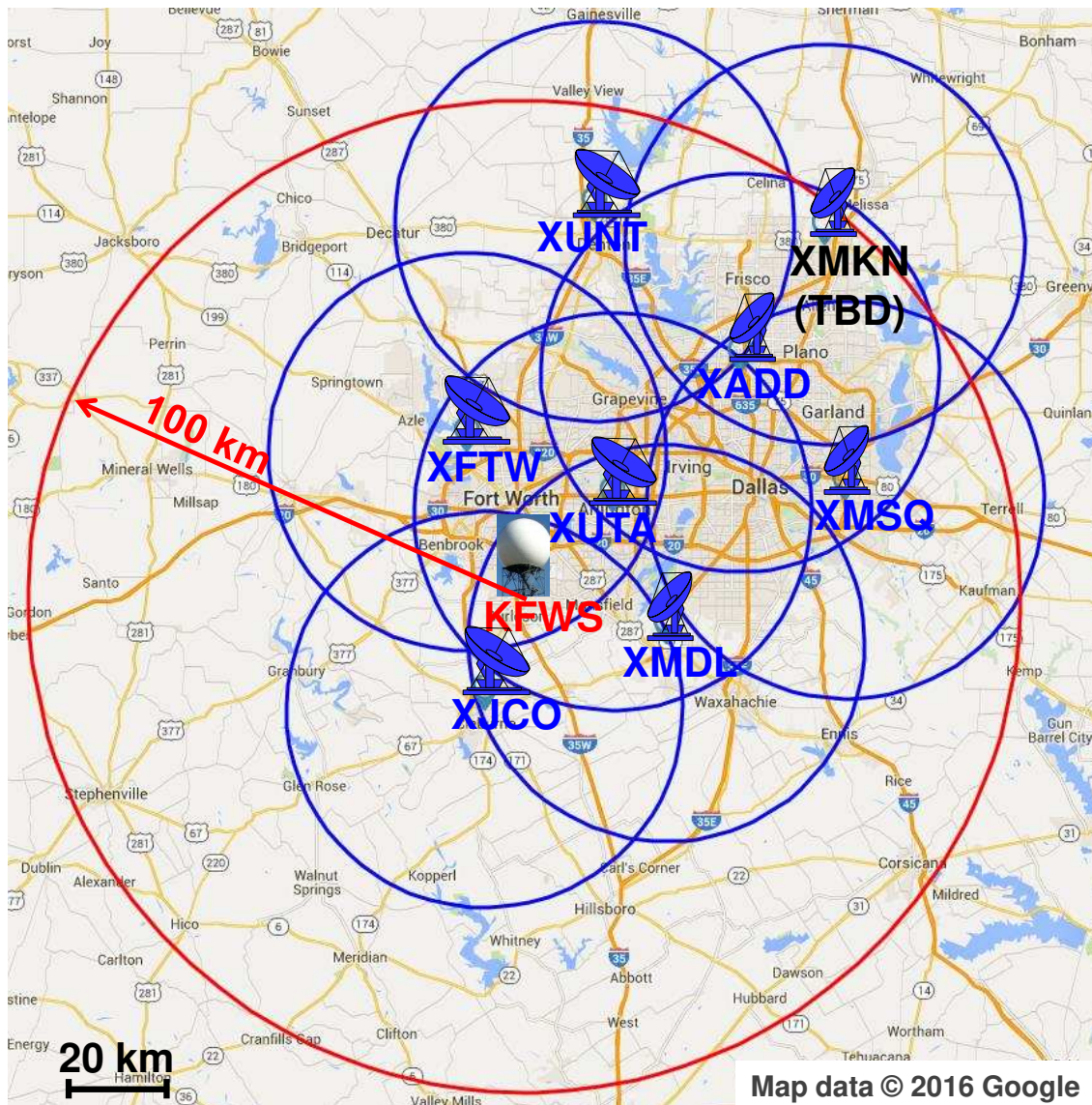


FIGURE 4.4. The layout of S-band KFWS WSR-88DP radar (100 km range ring in red) and DFW dual-polarization X-band radars (40 km range rings in blue). Letter symbols such as XMDL correspond to the names of the various radars.

The major objectives of the development of this dense urban remote sensing network are:

- 1) To develop high-resolution, three-dimensional mapping of atmospheric conditions, focusing on the boundary layer, to detect and forecast severe hazards including high wind, tornado, hail, and flash flood;

TABLE 4.2. System specifications of DFW X-band radar versus WSR-88DP S-band radar.

	WSR-88DP S-band Radar	DFW X-band Radar
Transmitter		
Transmitter Type	Klystron	Magnetron
Center Frequency	2.7-3GHz	9.41GHz
Wavelength	10 cm	3.2cm
Peak Power	750kw	8kw
Average Power	1000w	12w
Max. Duty Cycle	0.2%	0.16%
Pulse repetition	Long: 318 to 452 Hz; Short: 318 to 1304 Hz	2.0KHz (maximum)
Polarization	Dual linear, H and V channel	Dual linear, H and V channel
Receiver		
Type	Dual channel, linear output I/Q, log output	Parallel, dual channel, linear output I/Q
Dynamic range	95 dB(0.795MHz)	90 dB (1MHz)
Noise figure	4.6 dB (540 Kelvin)	≤5dB
Antenna and Pedestal		
Antenna type (diameter)	Center-feed, parabolic (9m)	Front-fed parabolic (1.8 m)
Antenna feed	Orthogonal dual polarization	Orthogonal dual polarization
3-dB beam width	0.95 degree	1.4 degree
Gain	45.5 dB	41dB
Azimuth motion range	Unlimited	Unlimited
Elevation motion range	N/A	0°-180°
Scan speed	Up to 36 degree/sec	Up to 60 degree/sec
Scan acceleration	Up to 17 degree/s ²	Up to 60 degree/s ²
Data Products		
Range resolution	1km (250m super resolution)	60 m
Update rate	five-six minutes	Less than 1 minute
Variables	Level II base data and level III products	$Z, Z_{dr}, V, W, NCP, \psi_{dp}, K_{dp}, \rho_{hv}$

2) To create neighbourhood-scale warnings and forecasts that are based on impact for a range of public and private sector decision-makers that result in benefit for public safety and the economy;

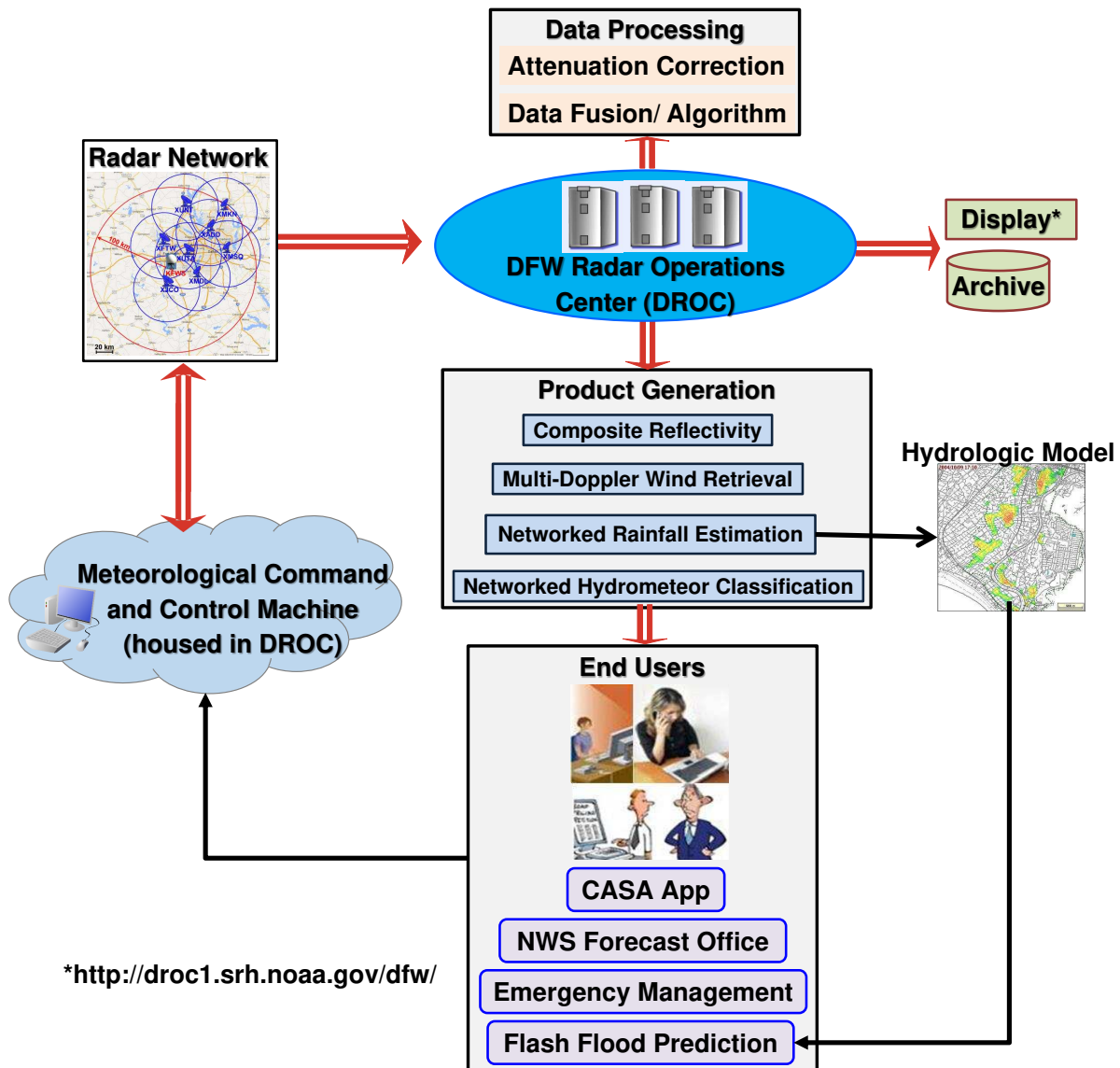


FIGURE 4.5. Closed-loop dataflow architecture of the DFW urban radar network. Through the Internet, the radar data are streamed to DROC, where the majority of the real-time products are generated and archived. The real-time products are available to a variety of end users. Based on the users' feedback, the radar control commands are sent out from the DROC.

3) To demonstrate the added value of collaborative, adaptive X-band radar networks to the existing and future NWS sensors, products, performance metrics, and decision-making and to assess optimal combinations of observing systems;

4) To develop models for federal/municipal/private partnerships to introduce new observation technologies for ongoing operational and interdisciplinary weather system research.

The research and research-to-operation topics include, but are not limited to:

- 1) Quantitative precipitation estimation (QPE) and forecasting (QPF)
- 2) Urban hydrologic modelling for flood and streamflow prediction
- 3) Hydrometeor identification and hail detection
- 4) 3-D multi-Doppler wind retrieval
- 5) High-resolution radar-driven numerical weather prediction (NWP)

New product research and transition of research to operations in the DFW remote sensing network occur in a quasi-operational environment (Chen and Chandrasekar 2015b; Chandrasekar et al. 2017). The real-time products are used and evaluated by a variety of users, including NWS forecasters and emergency managers and users from transportation, utilities, regional airports, arenas, and the media. Figure 4.5 shows the overall dataflow architecture for the DFW urban radar network. The entire DFW testbed is fundamentally considered an integrated networked radar operation platform. Transferred through the Internet, the data and products include single and multi-radar data, model-based assimilated data, vector wind, hydrometeor classification, rainfall, and numerical weather prediction (NWP) products, etc. In particular, the radar data are streamed to the DFW Radar Operations Center (DROC), which is located at the Southern Regional Headquarters (SRH) of the National Oceanic and Atmospheric Administration (NOAA). The bandwidth of the network between DROC and individual radar nodes depends on the local environment and the “last mile” setup. A bandwidth of 10 mbps is requested from each radar node to DROC, but it is different for different radar nodes. Generally, it is much higher than 10 mbps (e.g., XUNT and XUTA are 60-70 mbps, XMDL is 25-50 mbps, XADD is 10-12 mbps). In theory, the bandwidth from DROC to WFO is 45 mbps. The majority of the processes for range velocity ambiguity mitigation, clutter suppression, and single node-based attenuation correction are

implemented in the radar node computers. However, other product generation such as QPE, hydrometeor classification, hail product, and multiple Doppler processing are done at DROC servers. Subsequently, the forecast results and alerts are sent to a variety of end users, including the NWS forecast office, emergency managers, and flood control districts. The end users, depending on their level of interest, have access to both the individual radar and the networked products. With the end users' feedback, the radar control commands are sent out from the DROC. The DROC also serves as the data archive center. The computation and processing are distributed throughout the DFW metroplex.

In addition to providing real-time high-resolution radar and other data to users for warning operations, the DFW testbed is expected to be an ideal research platform, with major research thrusts including convective initiation, nowcasting, and fusion of data from *in situ* and remote sensors such as S-band KFWS radar, rain gauges, local profilers, and even satellite observations.

4.3. SAMPLE CASA/DFW PRODUCTS IN THE PRESENCE OF TORNADO, HIGH WIND, HAIL, AND FLOOD

4.3.1. SPACE-TIME INTEGRATION OF DFW OBSERVATIONS AND PRODUCTS.

It can be seen from the CASA radar network topology that observations are available from multiple radars with multiple looks (views from different vantage points) in most parts of the network. As such, data fusion between a high-resolution X-band radar network and other instrumentation became one of the critical research efforts in the development of the DFW urban remote sensing network. Integration of different data sources is also an indispensable step for creating high-quality networked products. In the following, this study takes

the S-band KFWS WSR-88DP radar as an example to illustrate CASA’s solution to the spatiotemporal sampling differences among various radar sensors.

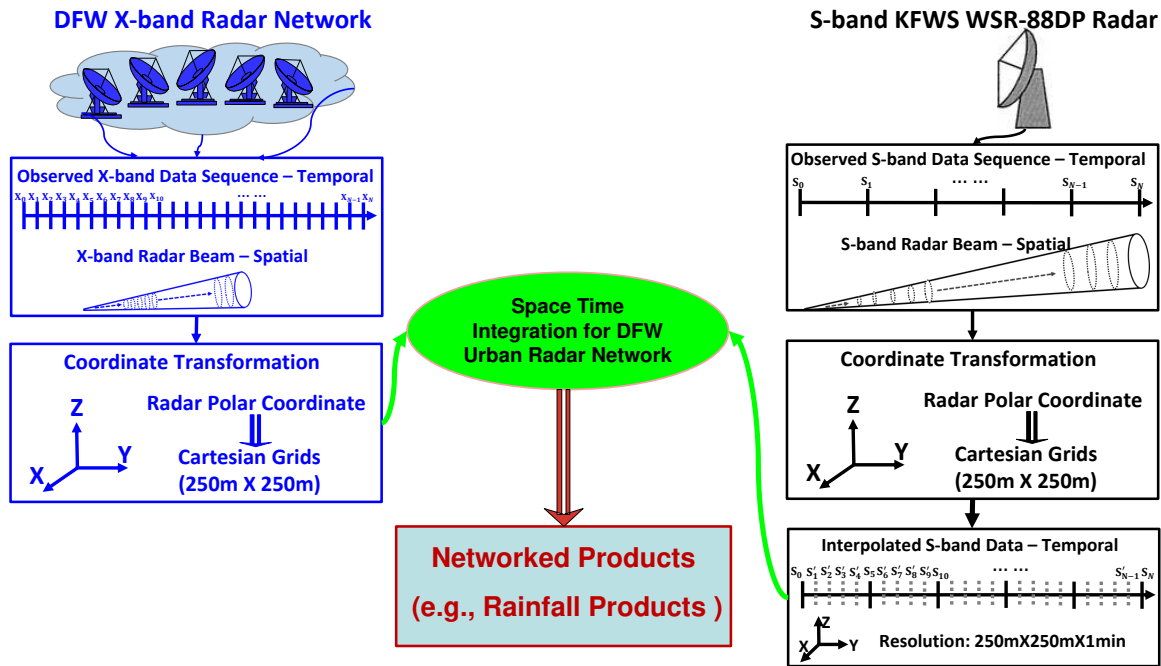


FIGURE 4.6. Schematic diagram illustrating the space-time integration of DFW observations at different frequencies and time scales.

As aforementioned (see also Table 4.2), the S- and X-band radar systems operate very differently. From the observation resolution point of view, the KFWS radar generates an update every five to six minutes, whereas the X-band radar network produces observations updated within one minute. Spatially, the KFWS radar sampling resolution is severely degraded due to beam broadening as distance from the radar increases, whereas the X-band radar network has much higher resolution since the individual radar coverage range is limited to within 40 km. Figure 4.6 shows a conceptual diagram illustrating the space-time integration of DFW observations at different scales. Multiple X-band radars are combined first as a unitary network to produce high-resolution products (e.g., 250 m×250 m×1 min). In order to match the resolution of X-band network products, the S-band KFWS radar based products (e.g., rainfall rate field) are temporally interpolated to one-minute resolution using

a piecewise cubic polynomial Hermite interpolation approach (Fritsch and Carlson 1980). Spatially, the KFWS radar products in polar coordinates within 100 km from the radar are mapped onto 250 m by 250 m grids using Cressman weighting (Cressman 1959). The 100 km range is selected mainly because of the radar beam size and beam broadening effect (details can be found in Section 4.1). It should be noted that instead of interpolating radar data, it was decided to interpolate products to avoid nonlinear error propagation. Subsequently, products at the same spatiotemporal scale from both the KFWS radar and the X-band radar network are merged together to create network-level products. The scheme in Figure 4.6 is particularly suitable for deriving networked rainfall rates and amounts, which will be detailed in Chapter 5.

4.3.2. SAMPLE CASA/DFW PRODUCTS.

Hail Detection: As detailed in Chapter 3, fuzzy logic-based approaches are conventionally used for radar hydrometeor classification. Those approaches are designed to work on each radar resolution cell represented by azimuthal angle and range gate. However, such bin-by-bin-based methodologies have limitations when applied to “noisy” radar data that could be caused by ground clutter, partial beam blockage, and/or bright band contamination. To overcome these issues, a region-based hydrometeor classification approach has been implemented for S-band radar rainfall estimation (see Chapter 3). Here, the same approach is applied for the DFW X-band radar network. The overall structure of this region-based classification methodology in the context of operational applications is depicted in Figure 4.7. For illustration purposes, Figure 4.8 shows sample dual-polarization observations from a CASA X-band radar and corresponding hydrometeor classification results at 04:15UTC, May 20, 2011. Overall, the classification product shown in Figure 4.8 looks reasonable, with a few well-defined regions. It is interesting to note that at approximately 2-3 km height

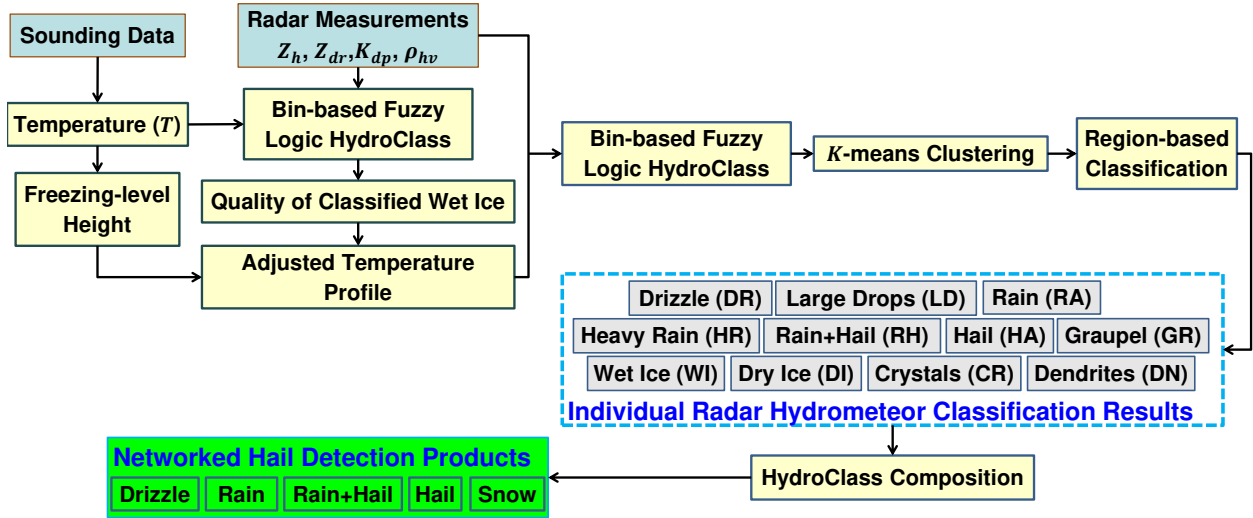


FIGURE 4.7. Diagram of the operational hydrometeor classification and hail detection system for the DFW dense urban radar network.

and 30 km range, where high reflectivity values are present, rain-hail mixtures are identified. Some negative Z_{dr} values are observed beyond the rain plus hail region, which is possibly due to the underestimation of the difference of path-integrated-attenuation between two polarization channels. However, the negative Z_{dr} values at approximately 10 km height and 30 km range are considered to be real, which implies the existence of vertically oriented ice crystals associated with electrical activity inside the storm (Carey and Rutledge 1996; Caylor and Chandrasekar 1996).

For the sake of operational interpretation and clean hail product generation, the hydrometeor classes from individual DFW radar nodes are merged together using clustering analysis to produce a network-level product. In addition, the number of hydrometeor types is narrowed down to five categories: drizzle, rain, rain+hail, hail, and snow. LD, RA, HR, and WI are grouped as rain; DI, CR, and DN are grouped as snow and HA and GR are grouped as hail. These five categories were essentially determined based on the requests of a variety of end users. Figure 4.9 shows an example hail product during the storm event of March 24, 2016. In the following figure, a hailstorm that occurred on May 12, 2014, is

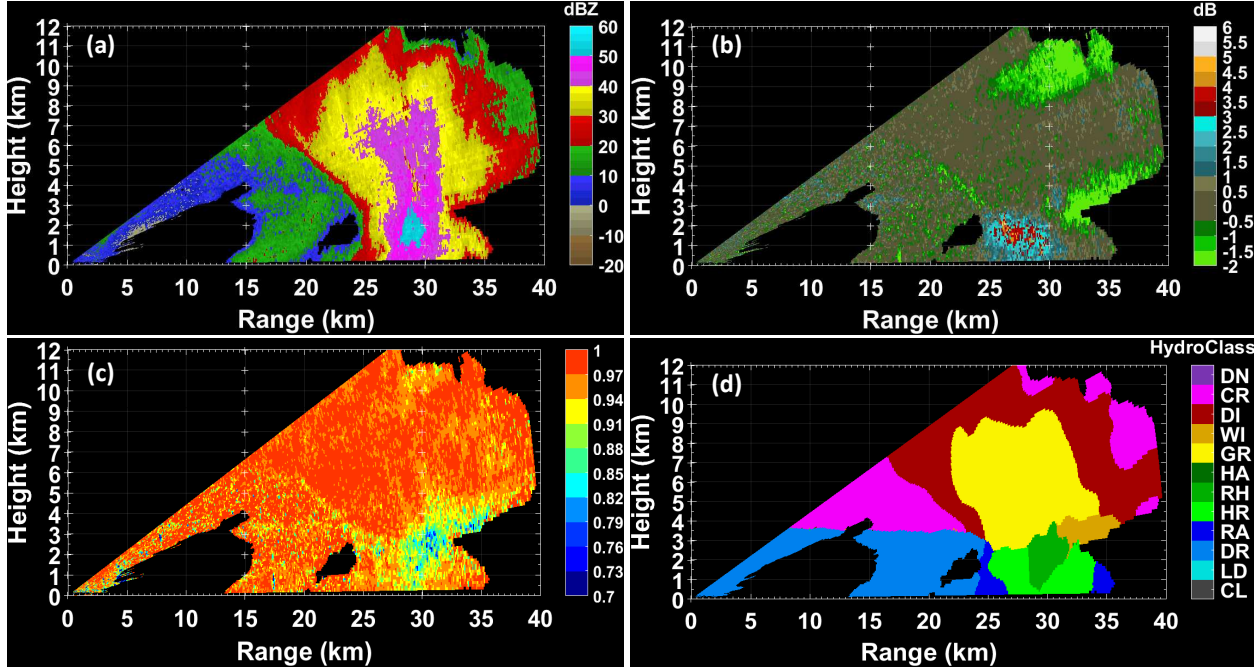


FIGURE 4.8. Sample CASA X-band radar observations and corresponding hydrometeor classification results at 04:15UTC, May 20, 2011: (a) Z , (b) Z_{dr} , (c) ρ_{hv} , (d) classified hydrometeor types. The Z and Z_{dr} fields shown here are after attenuation correction.

presented as an example to further illustrate the DFW hail product and demonstrate the product performance through comparison with ground weather reports.

A strong line of thunderstorms stretching from Brownwood, Texas, northeast to Tulsa, Oklahoma, began pushing east-northeast through the DFW area shortly before 15:00UTC, May 12, 2014. In a very short time span, the storm produced more than 30 mm of rain along with hail as large as golf balls at many locations in North Texas. Power outages to more than 60,000 people were reported, with hundreds of flights at North Texas's two major airports delayed or cancelled. Figure 4.10 shows the dual-polarization measurements of Z , Z_{dr} , ρ_{hv} , and K_{dp} , from a DFW X-band radar (XUTA radar) at 20:50UTC, May 12, 2014. It is worth noting that differential phase-based attenuation correction (Chen et al. 2017b) was applied on measured Z and Z_{dr} . The fields shown in Figure 4.10(a)(b) are after attenuation correction. The high Z but low ρ_{hv} values near (10 km, -10 km) indicate that

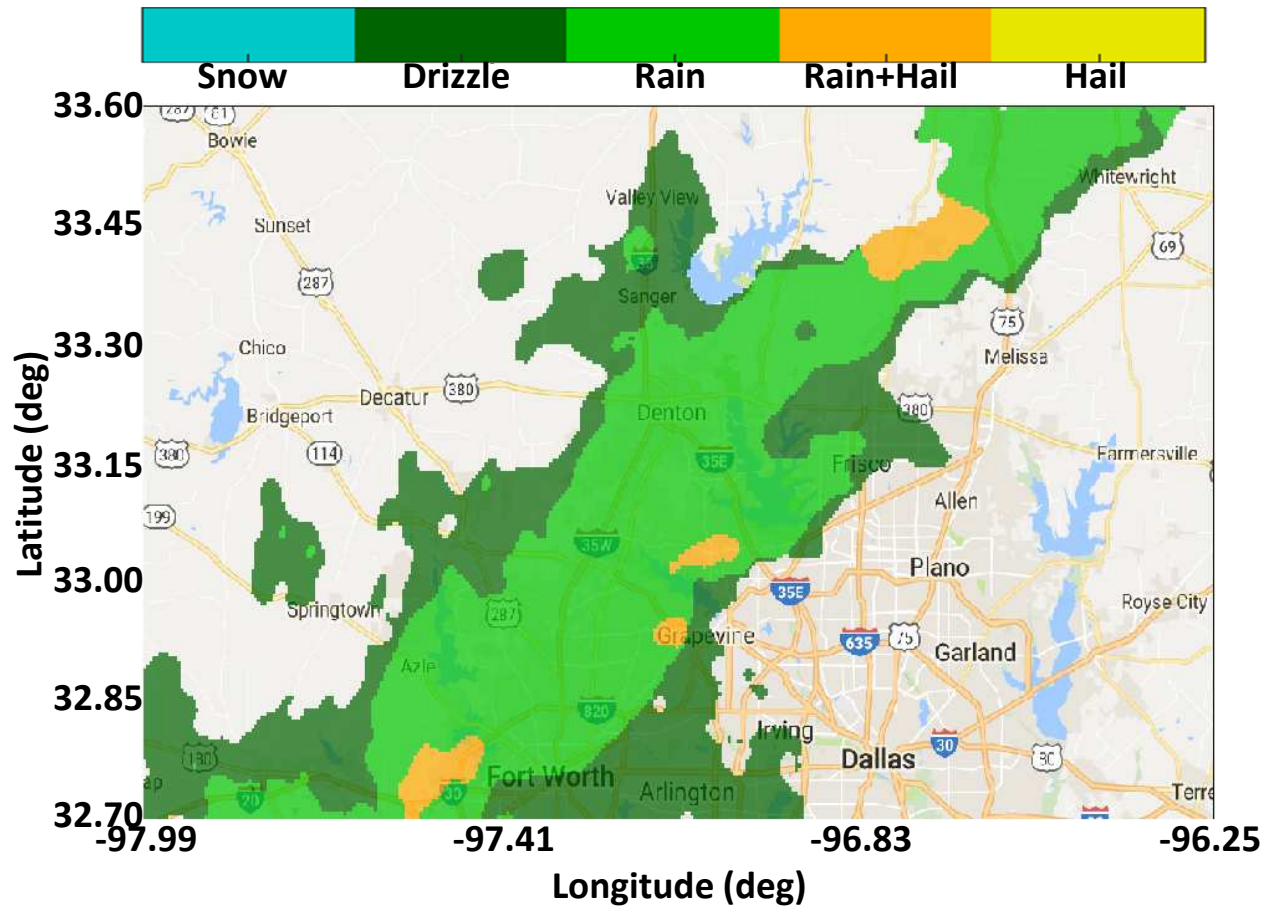


FIGURE 4.9. DFW hail product at 02:39UTC, March 24, 2016.

the precipitation was not purely liquid, which is identified as a rain hail mixture in the DFW hail system product shown in Figure 4.10(e).

With the real-time hail products, a hail path is generated for operational warning applications. The hail path is created based on the duration of hailfall at a given location. Figure 4.11 illustrates the estimated hail path for a 20-minute period, from 20:37 to 20:57UTC, May 12, 2014. It can be seen from Figure 4.11 that dense hail occurred near the Joe Pool Lake. Figure 4.11 also shows hail pictures and screenshots of ground hail reports from social media. The reported locations and times agree very well with the hail observations from the DFW radar network, which demonstrates the excellent performance of the DFW hail system.

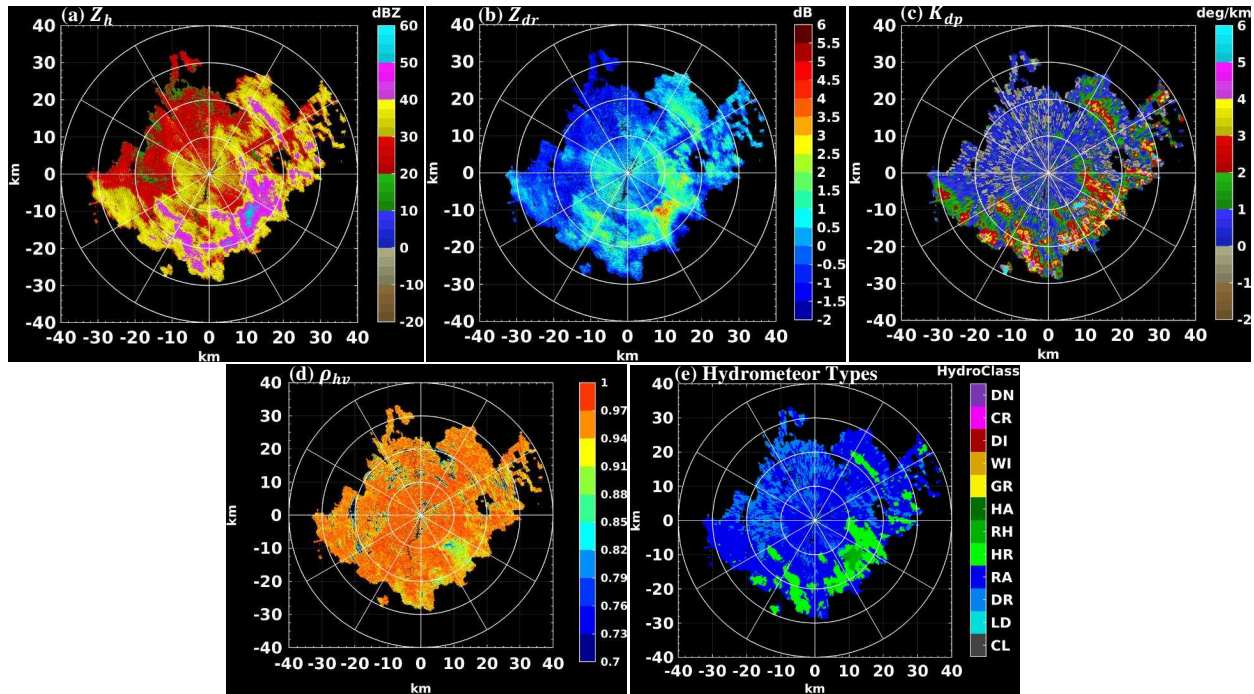


FIGURE 4.10. Sample dual-polarization observations from a DFW X-band radar (XUTA radar) and corresponding hydrometeor classification results at 20:50UTC, May 12, 2014: (a) Z , (b) Z_{dr} , (c) K_{dp} , (d) ρ_{hv} , and (e) classified hydrometeor types. The Z and Z_{dr} fields shown here are after attenuation correction.

Nevertheless, it should be noted that although CASA has devoted extensive efforts to ground hail report collection and *in situ* instrument deployment for hail observations over the DFW metroplex, verification of hydrometeor classification (hail) products has never become a straightforward task, especially when mixed-phase precipitation is observed.

Multiple Doppler Wind Retrieval: Close to the tornado alley, the topology of the DFW radar network allows for high-resolution observation of the lower troposphere while providing large areas of overlapping coverage (see also Figure 4.4). In addition, either under the DCAS scan strategy or the regular PPI scan mode, each radar node is able to finish a volume scan within one minute, which makes the high-resolution X-band radar network more appealing for retrieving Doppler velocity information and subsequently issuing tornado or high-wind warnings. In the following, the fundamental concept of vector wind velocity

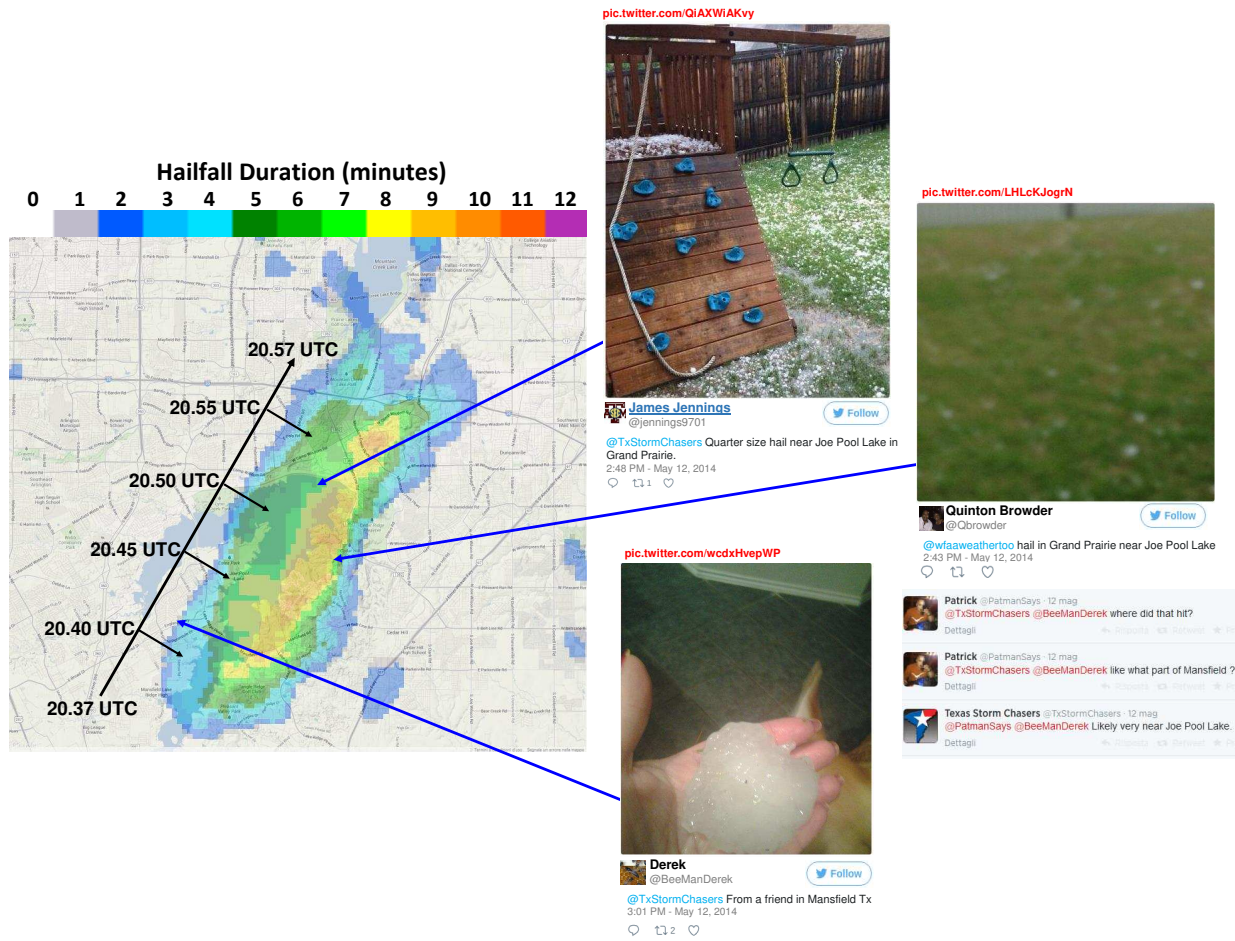


FIGURE 4.11. DFW radar network-based hail product (path/duration) over Joe Pool Lake from 20:37 to 20:57UTC, May 12, 2014. The hailfall and hail path were demonstrated by social media reports.

retrieval using a Doppler radar network is reviewed. The real-time multi-Doppler system designed for the DFW dense urban radar network is described, including the multi-Doppler scan strategy, system integration of high-resolution observations, as well as sample real-time products generated during tornado and high wind events.

The essence of multi-Doppler wind retrieval from a radar network is to get the three-dimensional velocity components in a Cartesian coordinate from the non-orthogonal radial velocities measured by individual radars (Miller and Strauch 1974; Ray et al. 1980; Chen and Chandrasekar 2018). In the Cartesian coordinate system, the velocity of a particle at (x, y, z) within a thunderstorm can be expressed by a triplet $(u, v, w + w_f)$, where u , v , and

w are the velocity components in eastward, northward, and vertical directions, respectively. w_f is the particle fall speed. The projections of the particle's motion onto the radars' line of sight are:

$$(25) \quad \begin{aligned} V_R^1 &= u \sin \phi_1 \cos \theta_1 + v \cos \phi_1 \cos \theta_1 + (w + w_f) \sin \theta_1 \\ &\vdots \end{aligned}$$

$$V_R^m = u \sin \phi_m \cos \theta_m + v \cos \phi_m \cos \theta_m + (w + w_f) \sin \theta_m$$

where V_R^m is the radial velocity measured by radar node m and ϕ_m and θ_m are respectively the azimuth and elevation angles of the radial beam. Taking into account the geometric relation in Cartesian coordinates, Equation (25) can also be expressed as:

$$(26) \quad V_R^m = \frac{1}{r_m} [u(x - x_m) + v(y - y_m) + (w + w_f)(z - z_m)]$$

for a radar at (x_m, y_m, z_m) with slant range $r_m = \sqrt{(x - x_m)^2 + (y - y_m)^2 + (z - z_m)^2}$.

Putting the radial velocities into a vector form $\mathbf{V}_R = [V_R^1 \ \cdots \ V_R^m]^T$, and using the following matrix form:

$$(27) \quad \mathbf{H} = \begin{bmatrix} \sin \phi_1 \cos \theta_1 & \cos \phi_1 \cos \theta_1 & \sin \theta_1 \\ \vdots & \vdots & \vdots \\ \sin \phi_m \cos \theta_m & \cos \phi_m \cos \theta_m & \sin \theta_m \end{bmatrix}$$

a linear system can be obtained as follows:

$$(28) \quad \mathbf{V}_R = \mathbf{H}[u \quad v \quad w + w_f]^T$$

The 3D wind velocity components can be retrieved using the generalized least square method, in the following form:

$$(29) \quad [u \quad v \quad w + w_f]^T = (\mathbf{H}^T \mathbf{H})^{-1} \mathbf{H}^T \mathbf{V}_R$$

The horizontal wind components u and v can be retrieved directly from the solution in Equation (29), provided that at least two radars are available. However, the vertical velocity from the least square solution may not be reliable due to the small vertical component of radar-measured radial velocities. More accurate retrieval of the vertical wind component can be obtained using the mass continuity equation (Miller and Strauch 1974):

$$(30) \quad \frac{\partial \rho u}{\partial x} + \frac{\partial \rho v}{\partial y} + \frac{\partial \rho w}{\partial z} = 0$$

where ρ is the air density that is modelled as a function of the altitude in this study. In addition, its local variation is assumed to be negligible. This study focuses more on horizontal wind retrieval, with an emphasis on engineering issues and application products.

It should be noted that simultaneous measurements from individual radar nodes are required for applying the multi-Doppler techniques. Therefore, effective and efficient scans should be conducted for multi-Doppler retrieval by taking into account resource limitations such as time constraints and computational complexity. As aforementioned, the DFW network is designed with a small “heartbeat” for a volume scan to ensure data synchronization and meet the computational requirements at the same time. In addition, multiple candidate pairs may exist for dual-Doppler synthesis in the overlapping regions and a choice has to be made in order to select the best pair. In the DFW network system, the selection is made according to the optimal radar beam-crossing angles for the target areas (Chen and

Chandrasekar 2018). Figure 4.12 illustrates the real-time data flow and system operation for multi-Doppler retrieval. There are three major steps: real-time data acquisition, ingestor, and main processing for Doppler wind synthesis.

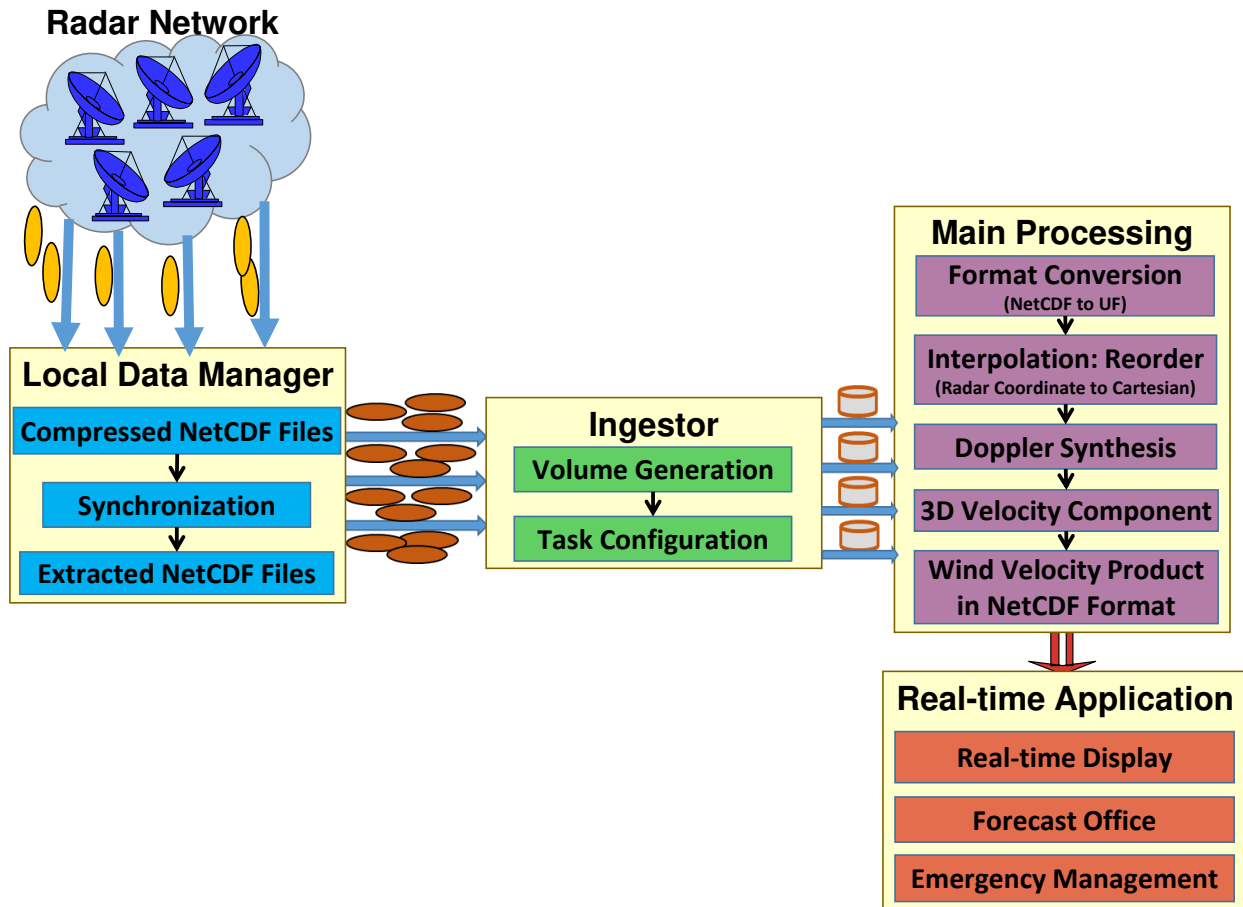


FIGURE 4.12. Framework of real-time Doppler wind retrieval system and application for the DFW urban radar network.

Through data transmission protocols, the moment data from each radar node in compressed NetCDF format are streamed to the radar operation center (see also Figure 4.5), which houses the rest of the processing sub-systems. In this step, radar data are also broken down into elevation-denominated PPI sweeps. Then, the ingestor program will decompress the incoming data, extract their scanning information, and synchronize them to respective radar and volumes for the subsequent Doppler synthesis. In the main processing, the data

in the radar polar coordinates are first mapped onto a common Cartesian space so a multi-Doppler wind synthesis can be conducted (Chen and Chandrasekar 2018). In the Doppler synthesis step, if the data are available from only one radar node, no wind velocity information will be produced. If two or more radars are available, the horizontal components (u and v) of wind velocity will be retrieved. The whole system is automated and the processing continuously updates every minute, which makes it suitable for real-time detection of sudden wind-related hazards such as tornadoes and microbursts. The real-time wind products are immediately sent to the forecast and emergency management offices for issuing tornado and high wind warnings. In the following, the EF0 tornado on May 8, 2014, and high wind on October 2, 2014, are investigated to demonstrate the performance of DFW multiple Doppler wind products.

On May 8, 2014, large-scale lift ahead of an upper level shortwave, combined with ample instability and adequate moisture, evolved in North Texas. Severe thunderstorms were observed moving through this area. Scattered convection developed in the afternoon, and a linear mesoscale convective system had formed by the late afternoon hours. Although there were no fatalities or injuries, the damaging downburst winds produced a great deal of tree damage and brought down power lines across areas in and around the city of Dallas. An EF-0 tornado was reported in Cockrell Hill (32.757°N, 96.889°W) in Dallas County around 20:14UTC, May 8, 2014. Figure 4.13 shows a screenshot of the NWS tornado report for this event. The tornado path length was about 800 meters and path width was about 137 meters, according to the NWS report. Although the tornado only lasted two minutes (20:14-20:15UTC), it caused damage to a warehouse building in Cockrell Hill. Several windows were blown out of the warehouse, and the building also suffered roof damage as the tornado moved from the southwest to northeast. During the entire event, the DFW multi-Doppler

wind retrieval system was continuously operating, monitoring the weather conditions. Figure 4.14 shows the multi-Doppler velocity retrieval results at 1 km height during this EF0 tornado event. At 20:14UTC, the retrieved maximum velocity was about 112.7 km hr⁻¹, and it became 119.0 km hr⁻¹ at 20:15UTC. The estimated vorticities are also shown in Figure 4.14, from which we can clearly see the vortex evolution and tornado movement in a two-minute span. The vortex locations in Figure 4.14 agree fairly well with where the tornado was reported.

PUBLIC INFORMATION STATEMENT

**NATIONAL WEATHER SERVICE FORT WORTH TX
411 PM CDT SAT MAY 10 2014**

**...NWS DAMAGE SURVEY FOR 05/08/14 TORNADO AND THUNDERSTORM WIND EVENT
UPDATE...**

**.OVERVIEW...SEVERE THUNDERSTORMS MOVED THROUGH THE NORTH TEXAS REGION ON
THURSDAY MAY 8TH. SURVEY CREWS FOUND EVIDENCE OF STRAIGHT LINE WIND DAMAGE IN
PARTS OF DALLAS AND JOHNSON COUNTIES IN THE DAMAGE SURVEYS CONDUCTED ON
FRIDAY. AN ADDITIONAL CREW WENT BACK OUT THIS MORNING AND FOUND DEFINITIVE
EVIDENCE OF A TORNADO IN COCKRELL HILL...IN THE AREA SOUTH OF I-30 AND NORTH
OF U.S. 180...AND EAST OF NORTH COCKRELL HILL ROAD...AND WEST OF NORTH
WESTMORLAND ROAD.**

.TORNADO #1 COCKRELL HILL...

RATING:	EF-0
ESTIMATED PEAK WIND:	80 MPH
PATH LENGTH /STATUTE/:	0.5 MILES
PATH WIDTH /MAXIMUM/:	150 YARDS
FATALITIES:	0
INJURIES:	0
START DATE:	MAY 08 2014
START TIME:	314 PM CDT
START LOCATION:	COCKRELL HILL
START LAT/LON:	32.757 / -96.889
END DATE:	MAY 08 2014
END TIME:	315 PM CDT
END LOCATION:	COCKRELL HILL
END LAT/LON:	32.760 / -96.882

FIGURE 4.13. NWS tornado report for the EF0 tornado that occurred in Cockrell Hill in the DFW area on May 8, 2014.

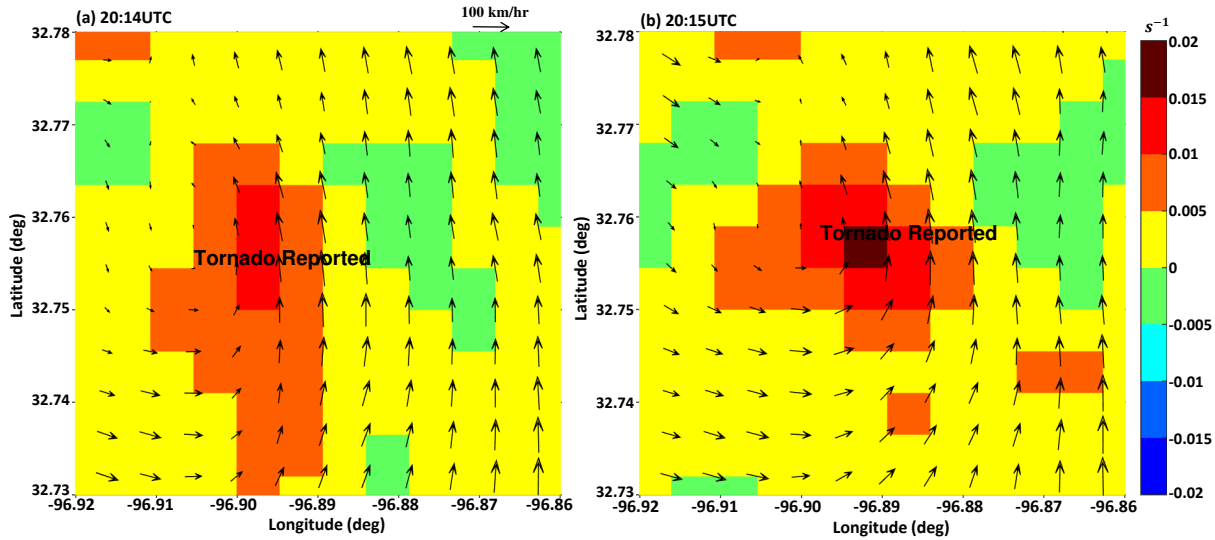


FIGURE 4.14. Multi-Doppler wind velocity retrieval results based on the DFW dense radar network during the EF0 tornado event on May 8, 2014, at (a) 20:14 and (b) 20:15UTC. The results are at 1 km height level. The arrows denote the magnitude and direction of the retrieved wind velocity. The maximum velocity at 20:14UTC is about 112.7 km hr^{-1} , and 119.0 km hr^{-1} at 20:15UTC. The color-coded field represents the vertical vorticity. The vortex locations agree fairly well with the NWS tornado report shown in Figure 4.13

On October 2, 2014, severe thunderstorms packing winds of up to 200 km hr^{-1} tore through the DFW area. The severe storm began to develop shortly before 18:00UTC, when a severe thunderstorm watch was issued for most of North Texas. The storms developed near Jack, Wise, and Parker counties, about 70 km to the northwest of the city of Fort Worth, before moving east. A severe thunderstorm warning was effective until 22:00UTC for Dallas County. This fast-moving storm left widespread damage and power outages as winds downed utility poles and tree limbs. Many flights were canceled at DFW International Airport. It was concluded that the significant damage was not caused by rain (less than 10mm of rain was observed in DFW airport), but the straight-line winds. The real-time DFW multiple Doppler wind retrieval system was operating during this high-wind event. Figure 4.15 shows the DFW network reflectivity observation and retrieved wind speed and directions at 1-km height at 20:53UTC, when the peak wind was reported. The peak wind

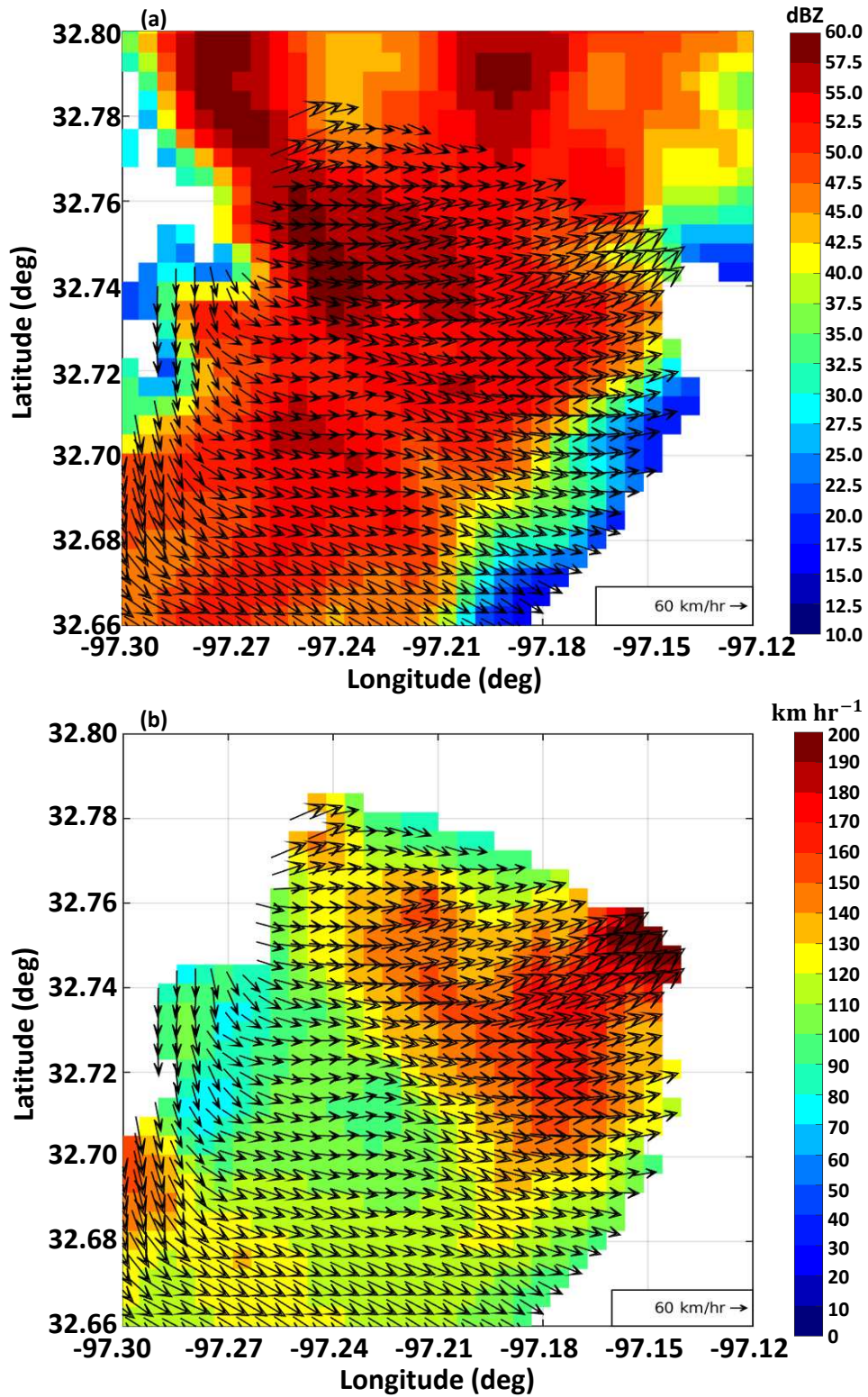


FIGURE 4.15. Real-time DFW multiple Doppler radar wind retrieval system product at 1-km height during the high wind event on October 02, 2014, at 20:53UTC: (a) composite reflectivity overlaid with retrieved wind directions, (b) retrieved wind speed and directions.

speed reached about 200 km hr^{-1} at the location near (97.15°W , 32.75°N). The retrieved peak wind and corresponding location agree fairly well with the ground weather report (<http://www.spc.noaa.gov/exper/archive/event.php?date=20141002>).

Rainfall Estimation: High-resolution QPE for the DFW dense radar network is derived based on the combination of dual-polarization X-band radars and the KFWS WSR-88DP radar. Figure 4.16 illustrates sample instantaneous rainfall rate products from the DFW network radar QPE system for a 15-min period (02:01-02:15UTC) during the storm event of May 29, 2015. Similarly, Figure 4.17 shows sample rain rate products for the event of November 27, 2015. Spatially, the rainfall products are produced on 250 m by 250 m grids. Temporally, the instantaneous rainfall rates are updated every minute. Based on the instantaneous rainfall rates, various rainfall accumulation products can be computed. Beyond the real-time warning applications, the high-resolution QPE products are used for urban flash flood forecasting through coupling with hydrological models.

The details of the DFW QPE system, including specific dual-polarization rainfall algorithms applied at different frequencies (i.e., S- and X-band) and the fusion methodology combining observations at different resolutions, will be presented in Chapter 5. In addition, extensive evaluation of the real-time rainfall products from this urban radar QPE system will be given in that chapter.

4.4. SUMMARY

Due to the earth's curvature, complex terrain, and/or urban deployment challenges, the physically large, high-power, long-range radars in the current operational network have severe limitations for observing the lower part of troposphere where many hazardous weather events occur. Furthermore, the space-time resolutions of measurements and products based

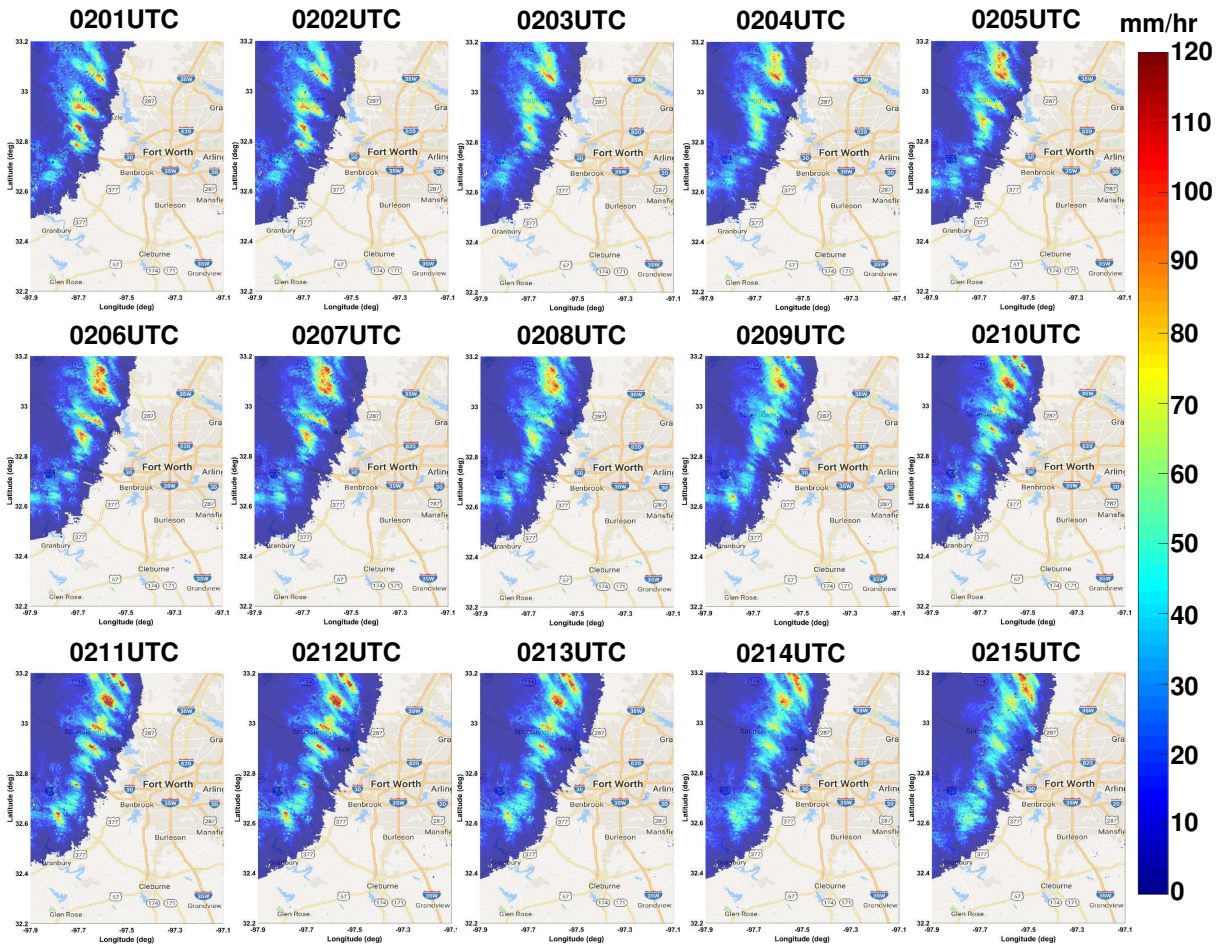


FIGURE 4.16. Sample instantaneous rainfall rate products from the DFW network radar QPE system for a 15-min period (02:01-02:15UTC) during the storm event of May 29, 2015.

on the current operational radars are not sufficient for monitoring high-impact localized weather phenomena such as tornadoes and urban flash floods. To this end, the center for CASA has developed an alternative weather sensing approach by deploying dense networks of low-power small X-band dual-polarization radars. The CASA radar network can provide enhanced sampling of weather features near the ground, which is beyond the capability of state-of-the-art operational radars.

This chapter discusses the rationales and principles of short-wavelength (X-band) operations. In addition, the CASA DFW urban radar network is presented as an example of using such high-resolution radar networks for urban hazard mitigation and disaster management.

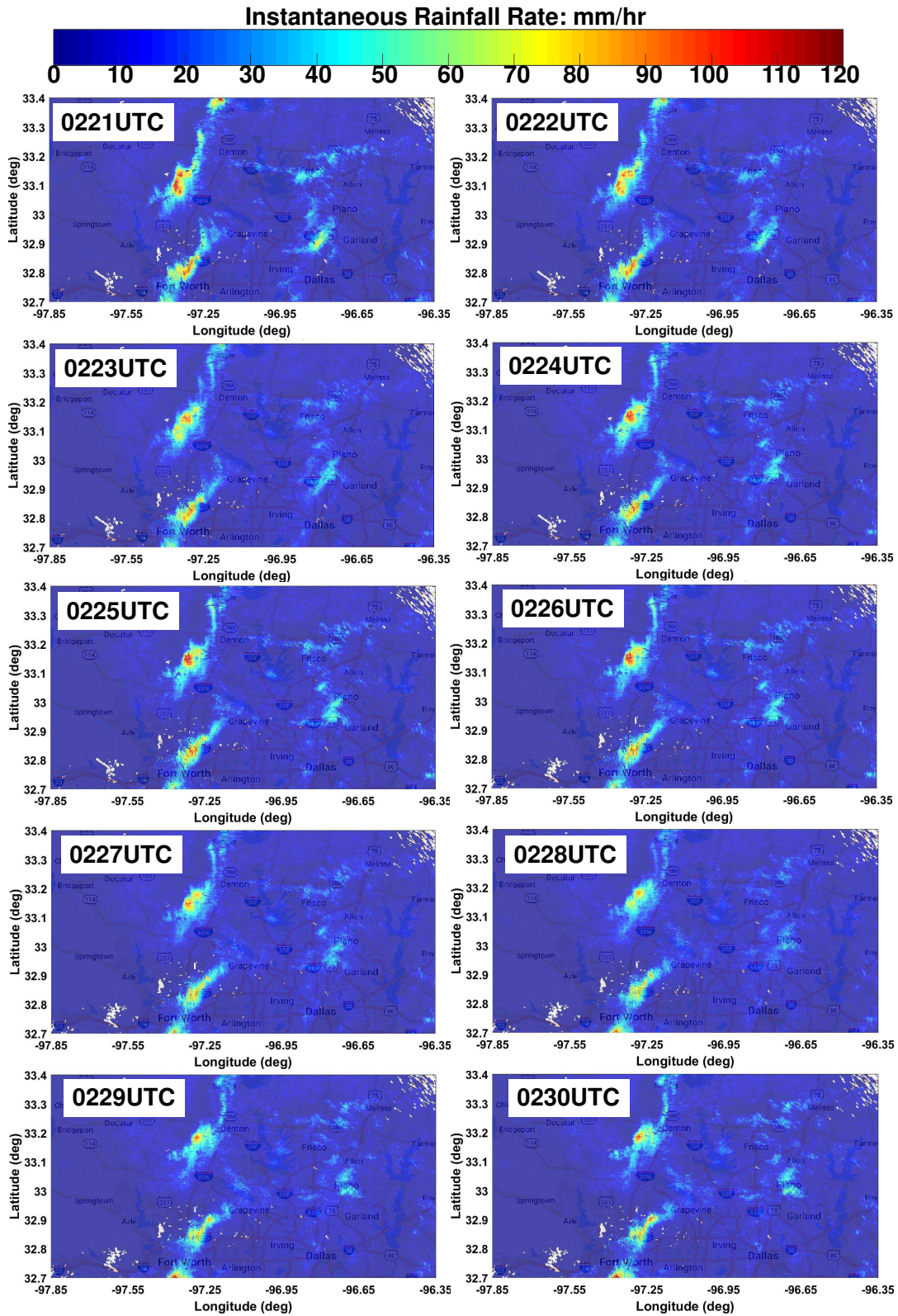


FIGURE 4.17. Sample instantaneous rainfall rate products from the DFW network radar QPE system for a 10-min period (02:21-02:30UTC) during the storm event of November 27, 2015.

Various real-time weather products produced by the DFW urban radar network are also presented. In particular, sample products of precipitation classification and quantification are illustrated for improving hail and flash flood monitoring. The multiple Doppler wind retrieval system is also detailed; it should improve high-wind and tornado detection and tracking and reduce the rate of false alarms. All these real-time products are integrated to operational platforms for evaluation by a variety of users, including NWS forecasters, emergency managers, and social media.

CHAPTER 5

THE HIGH-RESOLUTION, REAL-TIME QPE SYSTEM FOR THE CASA/DFW NETWORK: SYSTEM DEVELOPMENT AND PRODUCT PERFORMANCE

Flooding is a common natural hazard that produces substantial loss of life and property. According to the U.S. National Academy report, floods are responsible for more deaths nationwide than any other weather phenomenon (NRC National Research Council 2005). Furthermore, heavy development in urban regions decreases urban watersheds' response time to rainfall and increases the chance of localized flooding events over a small spatial domain. The scales of urban floods are fairly small and intense and have a large temporal variability with fast response time. They can occur immediately after heavy rainfall because of the complex hydrologic and hydraulic characteristics of the urban environment. Therefore, real-time monitoring of urban floods requires high spatio-temporal resolution and accurate estimations of precipitation and streamflow.

As discussed in Chapter 2, numerous types of infrastructure have been deployed to directly or indirectly measure rainfall rates and amounts, including rain gauges, weather radars, and satellites. Among these tools, the radar network is the primary system used for QPE in many nations. Through raindrop size distribution information, various radar rainfall algorithms have been developed with respect to dual-polarization measurements (for details, see Section 2.3 in Chapter 2). Presently, the NWS operational WSR-88DP radar-based rainfall products are commonly used to understand rainfall distribution nationwide and feed the subsequent hydrological models. However, due to sampling limitations, the operational QPE products based on the WSR-88DP network are typically produced on 1 km by 1 km

spatial grids (Zhang et al. 2011), and focus on rainfall accumulations at temporal scales of 1-, 3-, 6-, 12-, and/or 24-hrs. Such coarse resolution hinders the WSR-88DP-based rainfall products for local flash flood applications, especially high-impact urban flash floods which can occur a few minutes after torrential rainfall. Chapter 4 presented the applications of the CASA dense radar network for urban disaster detection and mitigation. High-resolution, high-quality QPE is one of the main drivers of the deployment of such dense radar networks. This chapter will detail the real-time QPE system developed for the CASA DFW urban radar network.

5.1. CASA/DFW QPE SYSTEM AND SAMPLE PRODUCTS

The rainfall system for the DFW urban network was designed via a combination of observations from both the X-band radar network and the S-band KFWS radar. The advantages of rapid X-band radar scan strategy are taken into account, which can produce high-resolution observations in both space and time domains. In real time, the high-resolution rainfall products from the CASA DFW QPE system are used as input to flash flood forecast models. Figure 5.1 summarizes the key features of this dense urban radar network in the context of QPE and urban hydrologic applications. Figure 5.2 shows a schematic diagram of the real-time DFW QPE system, which consists of the dual-polarization S-band KFWS WSR-88DP radar and a high-resolution X-band polarimetric radar network. As shown in Figure 5.2, different rainfall methodologies are used for S-band KFWS radar and X-band DFW radars.

For S-band, the blended rainfall algorithm (DROPS2.0) detailed in Chapter 3 is implemented where the specific rainfall relations are guided by hydrometeor classification results. The estimated rainfall rates in the radar's native (polar) coordinates are then mapped onto

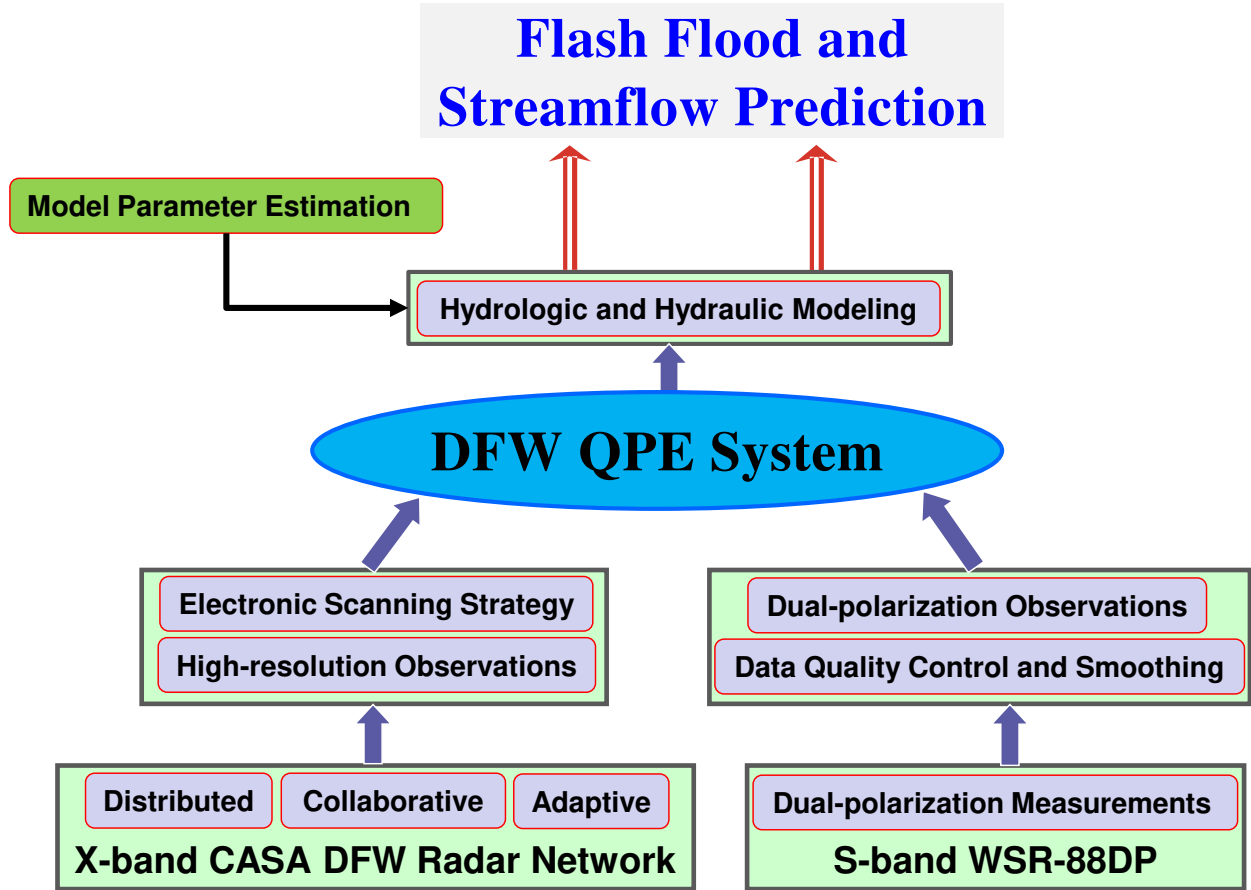


FIGURE 5.1. Key features of the CASA DFW urban radar network for rainfall estimation and hydrological applications.

Cartesian grids using a Cressman weighting scheme to match the X-band network product resolution.

For X-band, only $R(K_{dp})$ is considered. As discussed in Section 2.3.1 of Chapter 2, the selection of an X-band algorithm is influenced by attenuation induced by propagation in rain. The power-based measurements, including Z and Z_{dr} , should be corrected before they can be used for quantitative applications such as rainfall estimation. At X-band, rainfall estimation from K_{dp} is particularly appealing because (1) it avoids the uncertainty in attenuation correction; (2) due to the frequency scaling, K_{dp} responds well to low rainfall rates at X-band (compared to S-band) such that $R - K_{dp}$ conversion can be directly applied in light rain circumstances; on the other hand, K_{dp} can also exhibit a steeper slope within an

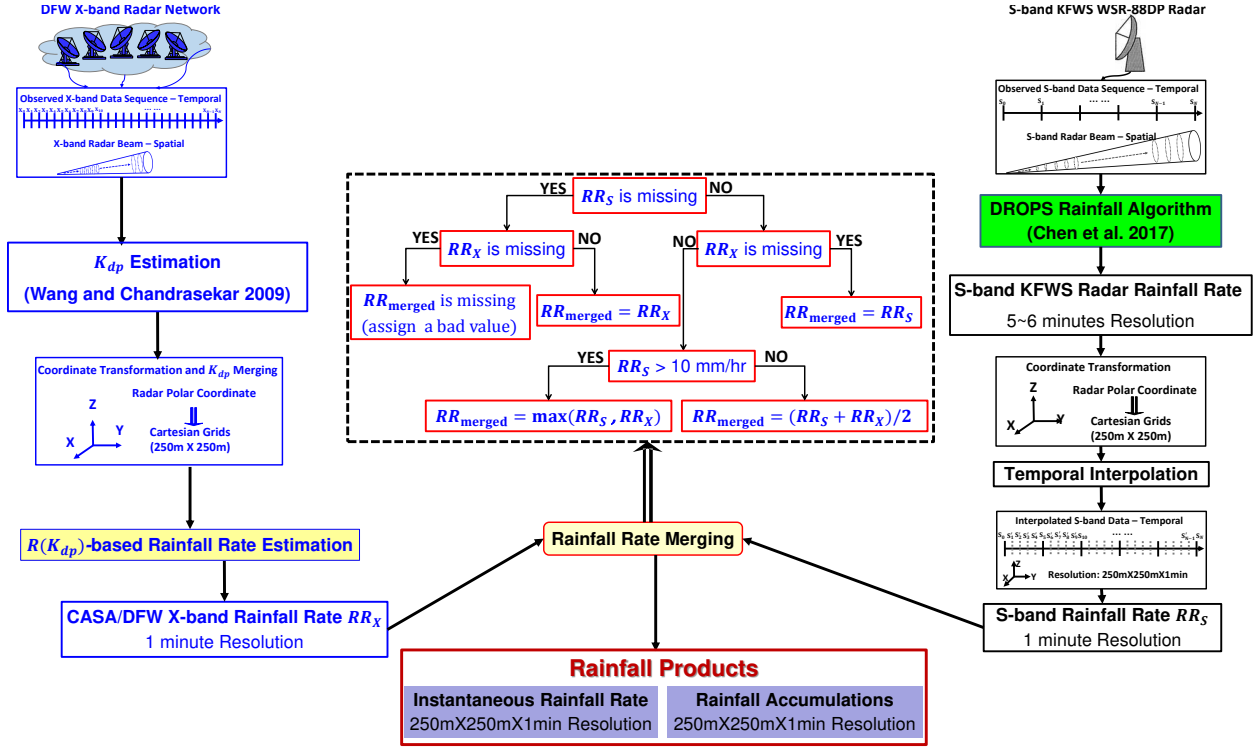


FIGURE 5.2. Schematic diagram of the QPE system for the CASA DFW urban remote sensing network.

intense rain cell; (3) as a phase based term, it does not need network calibration for multiple radar nodes (Chandrasekar et al. 1990; Aydin et al. 1995).

In practice, K_{dp} is estimated as the range derivative of the differential phase. However, it should be noted again that K_{dp} estimation is a non-trivial task since the differential phase measurements are subject to substantial fluctuations, especially at low rain rates. Often, a radar-measured differential phase is firstly suppressed with a strong filter. However, the filter may smooth out the peaks and introduce biases at high rain rates. In this study, the adaptive K_{dp} estimation algorithm developed by Wang and Chandrasekar (2009) was implemented, which is automatically tuned to the spatial gradient of K_{dp} . In this way, the fluctuation in light rain and the bias in heavy rain observations are substantially reduced (Wang and Chandrasekar 2009). With the K_{dp} estimates, the following power law $R - K_{dp}$

relation is applied for X-band DFW radar rainfall estimation:

$$(31) \quad R = 18.15K_{dp}^{0.79}$$

This relation is obtained based on the frequency adjustment of one of the S-band KOUN's $R(K_{dp})$ relations described in Ryzhkov et al. (2005), which is repeated here as:

$$(32) \quad R = 47.3K_{dp}^{0.791}$$

The DFW network is designed with extensive overlapping coverage among its radar nodes (see Figure 4.4). As such, data availability can be enhanced, especially in cases of heavy rainfall, beam blockage, or in the need for redundancy to demonstrate the operational strength of the network centric system. In the real-time CASA DFW QPE system, the X-band radar nodes are considered as an integrated unit when generating QPE products. The observation fields (e.g., K_{dp}) from synchronized X-band radar scans are projected onto the same Cartesian grids at first. Then they are merged together to produce K_{dp} -based rainfall rates. The K_{dp} field, rather than the rainfall rate field, is merged in order to reduce the variation introduced by the nonlinear $R - K_{dp}$ conversion. The independence of K_{dp} on the radar calibration enables flexibility in combining the collocated K_{dp} estimates from all the radar nodes. In this study, for an overlapping grid pixel, the closest radar has the highest priority in the merging process to ensure high resolution and low level samples (Chandrasekar et al. 2012; Chen and Chandrasekar 2015b; Chandrasekar et al. 2017). The quality of K_{dp} fields is also taken into account in the merging process, especially during an extreme rainfall event when signal extinction may occur. The composite K_{dp} field is much better than individual radar observations for surface rainfall estimation. In addition,

TABLE 5.1. Real-time rainfall products from DFW urban radar network.

Rainfall Product	Update Rate	Spatial Resolution
Instantaneous Rainfall Rate	60 secs	250 m \times 250 m
5-min Rainfall	60 secs	250 m \times 250 m
15-min Rainfall	60 secs	250 m \times 250 m
30-min Rainfall	60 secs	250 m \times 250 m
60-min Rainfall	60 secs	250 m \times 250 m
3-hr Rainfall	60 mins	250 m \times 250 m
6-hr Rainfall	60 mins	250 m \times 250 m
12-hr Rainfall	60 mins	250 m \times 250 m

it should be noted that additional considerations must be given in practical and urban operational environments. Critical evaluation of a large number of data sets reveals that the ground clutters, clutters from sidelobes, and their impacts would be minimal for the 2° elevation scans after filtering. Therefore, the 2° sweep datasets from X-band radars are used to derive rainfall products.

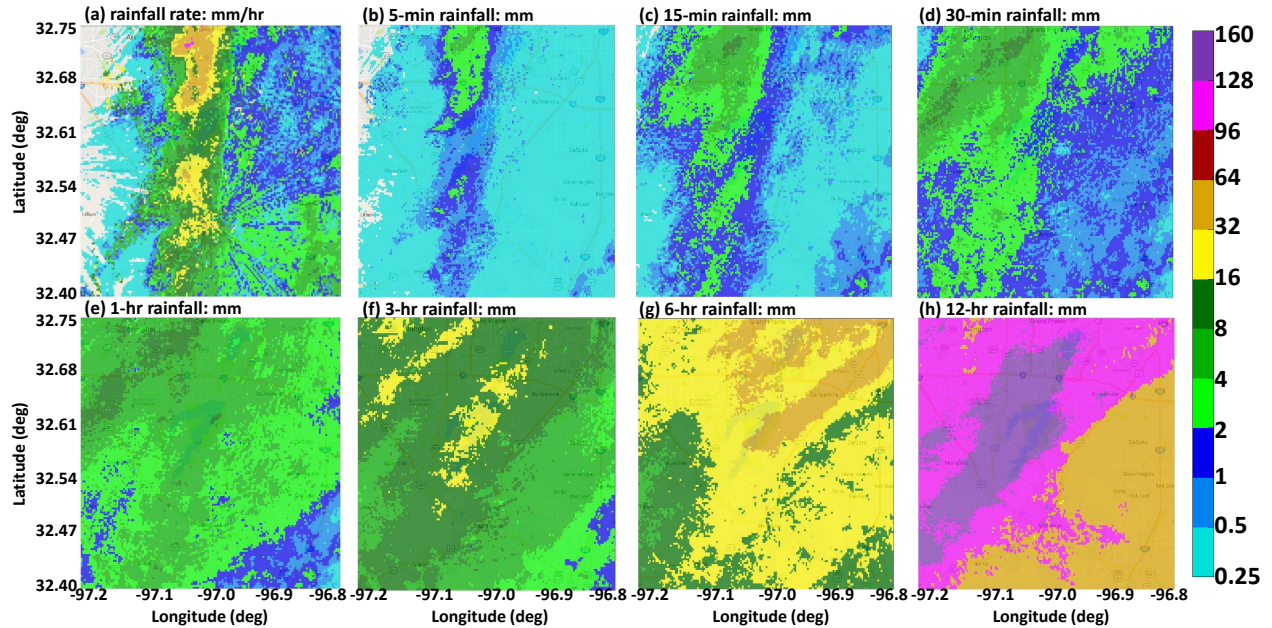


FIGURE 5.3. Real-time rainfall products from the DFW QPE system on November 27, 2015, at 12:00UTC. (a) instantaneous rainfall rate, (b) 5-min, (c) 15-min, (d) 30-min, (e) 60-min, (f) 3-hr, (g) 6-hr, and (h) 12-hr rainfall.

Details about the integration of measurements at different frequencies and time scales is described in Section 4.3.1. Over all, the DFW QPE system produces real-time rainfall rate estimates at 250 m by 250 m scale in spatial terms, and temporally the instantaneous rainfall rates are updated every minute. With the one-minute resolution rainfall rate field, running accumulations of rainfall at different time scales are produced in real time, including 5-, 15-, 30-, 60-min, and 3-, 6-, 12-hr rainfall amounts. The various real-time rainfall products for the DFW network and their update rates are listed in Table 5.1. For illustration purpose, Figure 5.3 shows real-time rainfall products from the DFW QPE system on November 27, 2015, at 12:00UTC. Similarly, Figure 5.4 illustrates sample real-time rainfall products during the flood event of May 29, 2015, at 03:00UTC. All the products have the capacity of being updated every minute. However, in a real-time environment, the instantaneous rainfall rates and 5-, 15-, 30-, and 60-min rainfall accumulations are updated every 60 seconds, whereas the 3-, 6-, and 12-hr rainfall products are generated at the top of the hour (every 60 minutes). The high-resolution products are particularly useful during localized flash flood events. For example, Figure 5.5 shows sample rainfall products for a 10 km by 10 km area during the flash flood event of June 24, 2014, at 21:39UTC. The peak rainfall rate reached about 200 mm hr⁻¹. Some regions in the city of Fort Worth were completely flooded within less than two hours of rain. Such localized extreme events can hardly be captured using the current operational radars.

The DFW QPE system has been operating for a number of years. Over all, it is very robust and continuously works well without any incidents. In the following section, quantitative evaluation of various CASA DFW rainfall products will be conducted through comparison with rain gauge measurements.

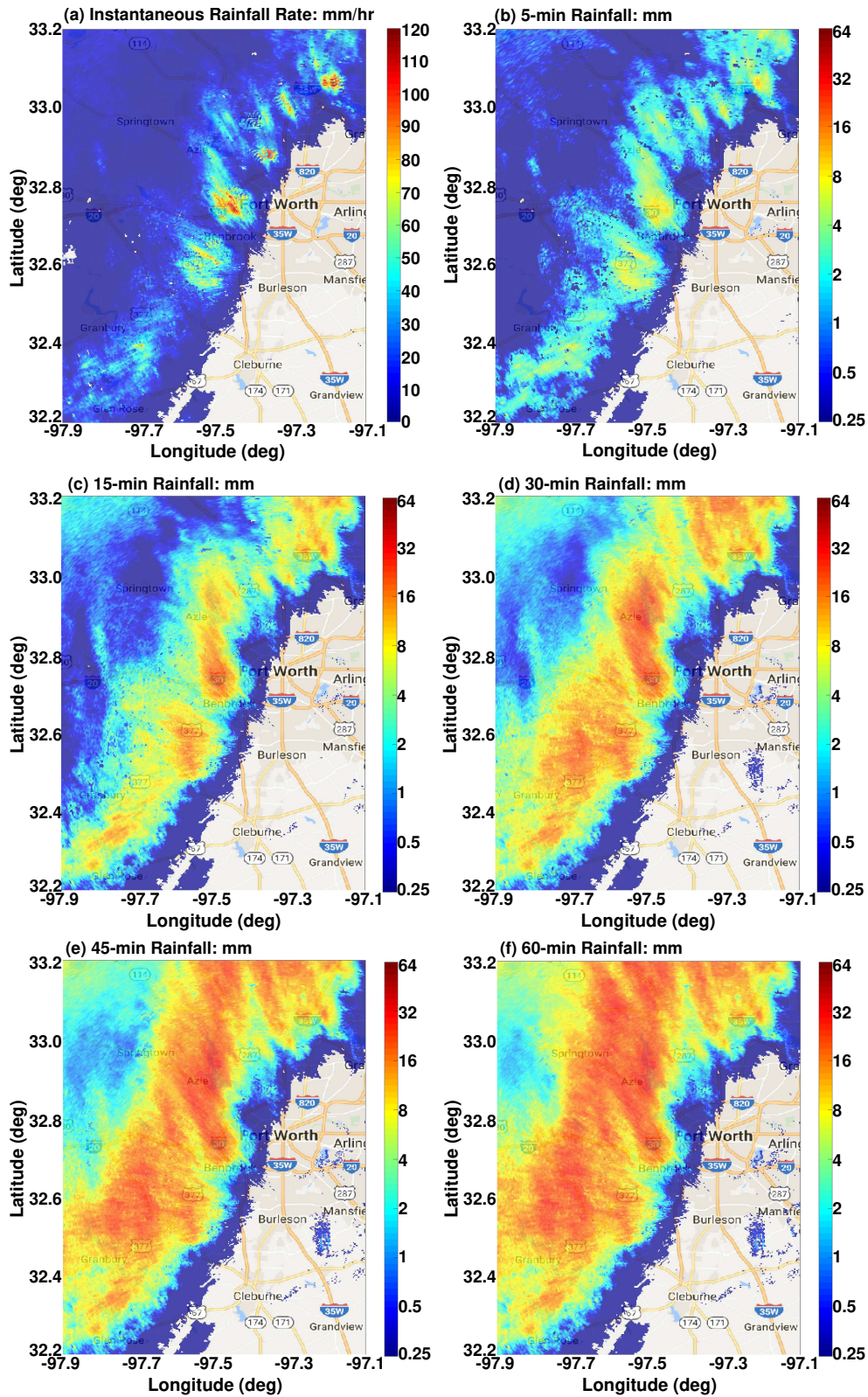


FIGURE 5.4. Sample real-time rainfall products on May 29, 2015, at 03:00UTC. (a) instantaneous rainfall rate, (b) 5-, (c) 15-, (d) 30-, (e) 45- and (f) 60-min rainfall.

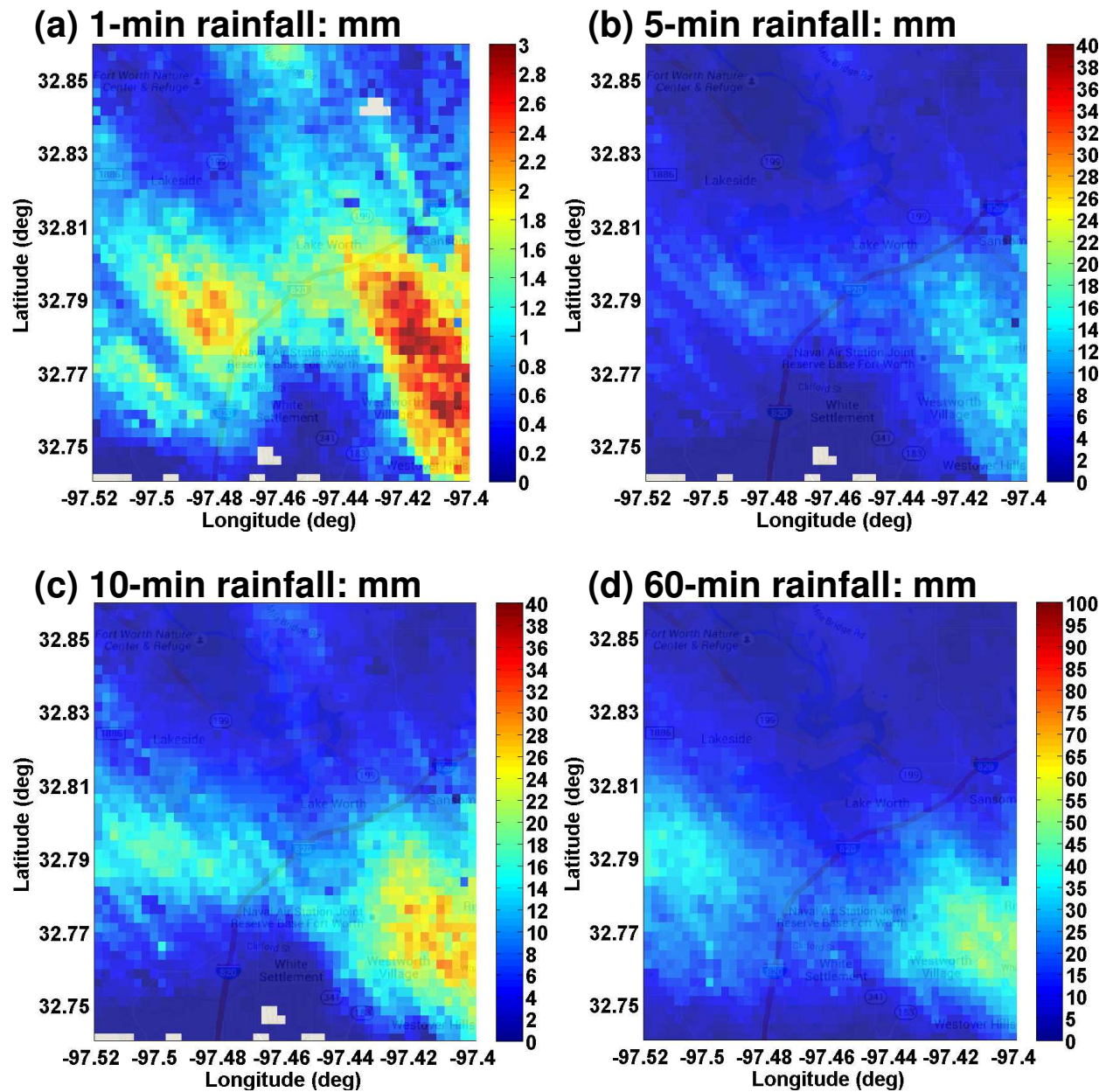


FIGURE 5.5. Sample real-time rainfall products for a 10 km by 10 km area during the flash flood event of June 24, 2014, at 21:39UTC.

5.2. EVALUATION OF CASA/DFW QPE PRODUCTS

5.2.1. EXAMPLE EVENTS.

A large number of precipitation events were investigated in order to quantitatively evaluate the performance of the CASA DFW QPE system. Here, several example rainfall cases from 2013 are described that are characterized by different meteorological phenomena. Table 5.2

TABLE 5.2. Summary of several precipitation events in 2013. Columns (from left to right) refer to the rainfall date, the time when intense rainfall was passing over the gauge network, and notes regarding the precipitation type and weather impact.

Date	Intense rain hours over gauges	Remarks
18 April 2013	09:40-10:40UTC	Squall line
16 May 2013	01:15-02:15UTC, 04:00-05:00UTC	Supercells, tornadoes, lightning, flash flooding in north Texas
09 June 2013	11:35-12:35UTC	Classical summer convective storm
27 October 2013	01:55-02:55UTC	Winter storm, lightning

presents an overview of the meteorological features of these events, including the time when intense rainfall occurred over the gauge network (see Figure 5.10 for gauge network location). The data collected during these time periods are used in the comparison between rainfall estimates by DFW dense radar network and rain gauge measurements.

18 April 2013: In the early morning of 18 April 2013, a squall line evolved ahead of a strong cold front and moved west to east in the DFW area. Wind gusts with the frontal passage were observed around 55 to 65 km hr⁻¹. Heavy rainfall was observed in the DFW metroplex around 09:00-13:00UTC. Figure 5.6 shows sample observations of reflectivity Z , differential reflectivity Z_{dr} , specific differential phase K_{dp} , and corresponding rainfall rate estimates from the S-band KFWS WSR-88DP radar. Figure 5.6 is based on the observations from a 0.5 degree elevation sweep at 08:47UTC. A severe thunderstorm watch was issued in north Texas for this event, but no significant severe weather was reported to the Storm Prediction Center (SPC). The real-time DFW QPE system was operating during the entire event, providing references to a variety of users.

16 May 2013: This event was characterized by supercells, flash flooding, lightning, and several tornadoes. In mid-May 2013, an upper-level shortwave trough causing a tornado outbreak moved northeastward from Mexico into the Southern Plains states. The low-pressure

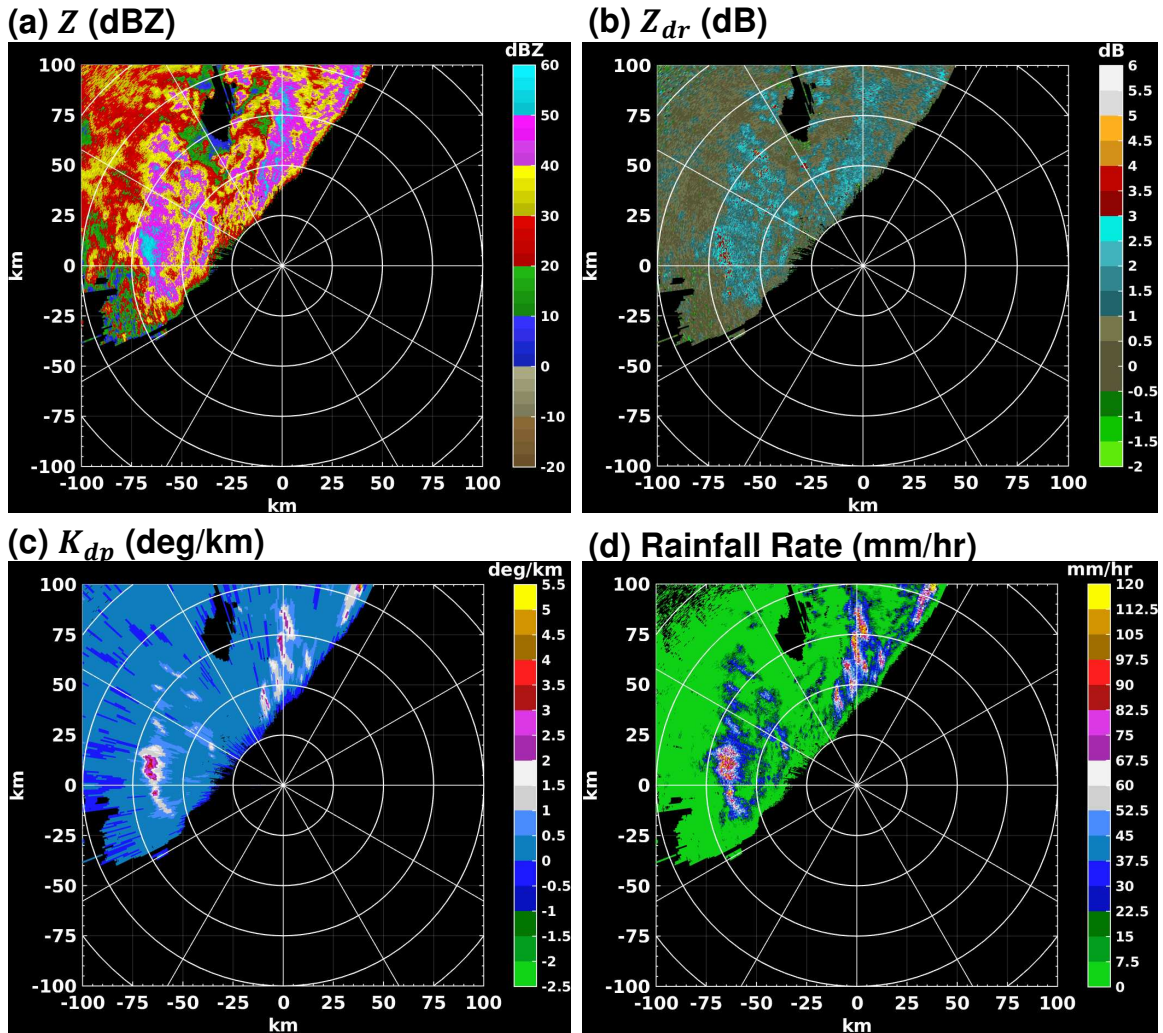


FIGURE 5.6. Sample observations from the S-band KFWS WSR-88DP radar 0.5 degree scan at 08:47UTC, 18 April 2013. (a) Z , (b) Z_{dr} , (c) K_{dp} , and (d) corresponding rainfall rate R .

area and atmospheric instability resulted in the formation of tornadoes across northern Texas and Oklahoma on May 15. This small but intense and deadly tornado outbreak produced several damaging tornadoes in north and central Texas, Louisiana, and Alabama in the two days following May 15. In addition to tornadoes, large hail was reported, peaking at approximately 10 cm in diameter near Mineral Wells, Texas, on May 15. Severe thunderstorms were observed in the DFW metroplex and southern Oklahoma. For the sake of QPE validation, the S-band KFWS radar data and DFW X-band network data collected during

01:00-05:00UTC, 16 May 2013, were used for generating rainfall products when the strong thunderstorm passed over the rain gauge network. Figure 5.7 illustrates sample observations of Z , Z_{dr} , K_{dp} , and corresponding rainfall rate estimates based on the S-band KFWS WSR-88DP radar 0.5 degree elevation scan at 04:45UTC.

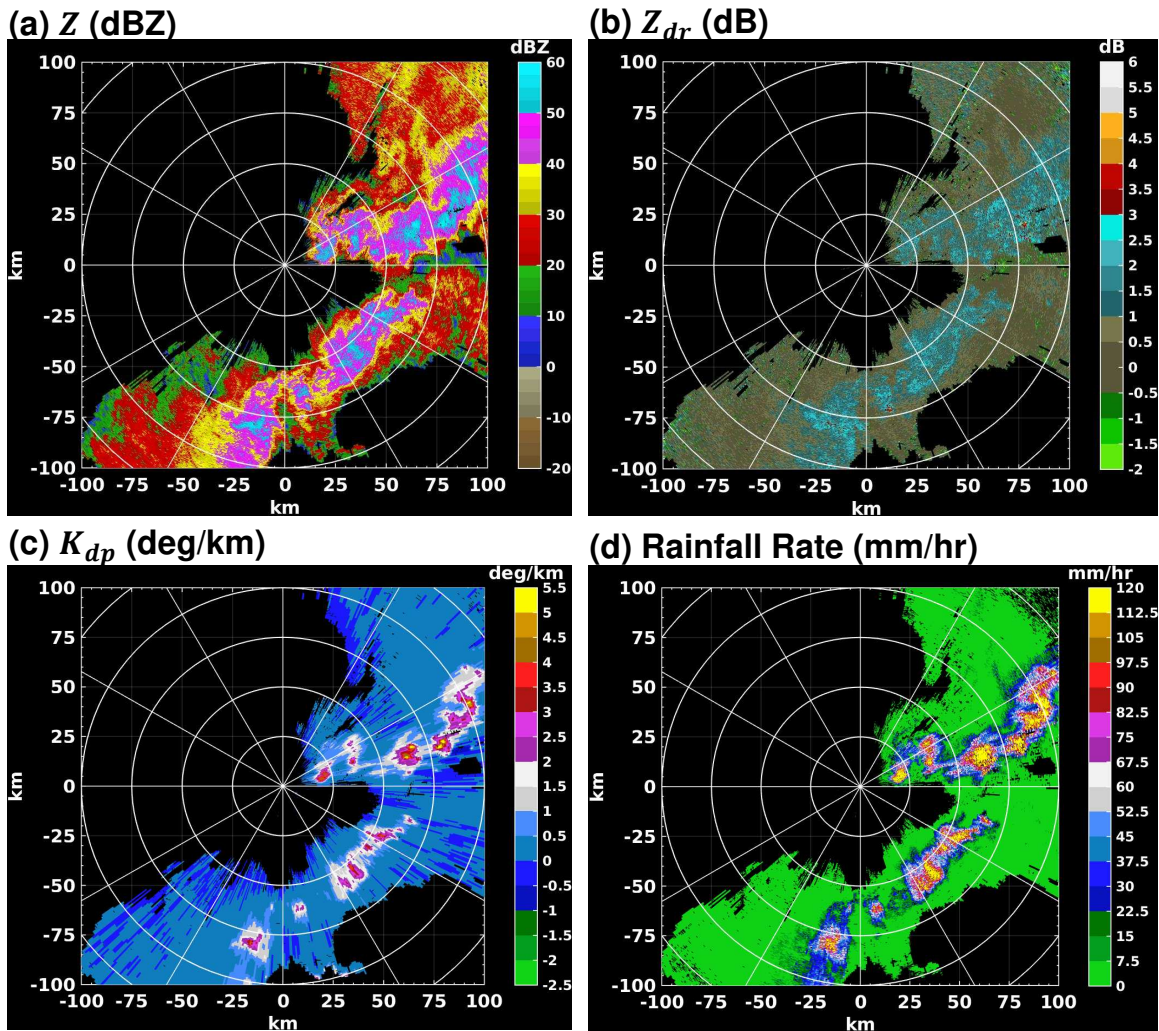


FIGURE 5.7. As in Figure 5.6, but for observations at 04:45UTC, 16 May 2013.

09 June 2013: A widespread severe thunderstorm moving from northwest to southeast entered the DFW area around 09:00UTC, 09 June 2013. A severe thunderstorm warning was issued by the NWS for several counties in northern Texas. The thunderstorm lasted a few hours and weakened around 13:00UTC. This event was a common summer convective

rainfall case. The dense radar network data, including S-band and X-band, collected around 11:35-12:35UTC, were used in the QPE validation analysis. Similarly, Figure 5.8 shows the sample observations of Z , Z_{dr} , K_{dp} , and corresponding rainfall rate estimates based on the S-band KFWS radar 0.5 degree elevation scan at 12:31UTC during this event.

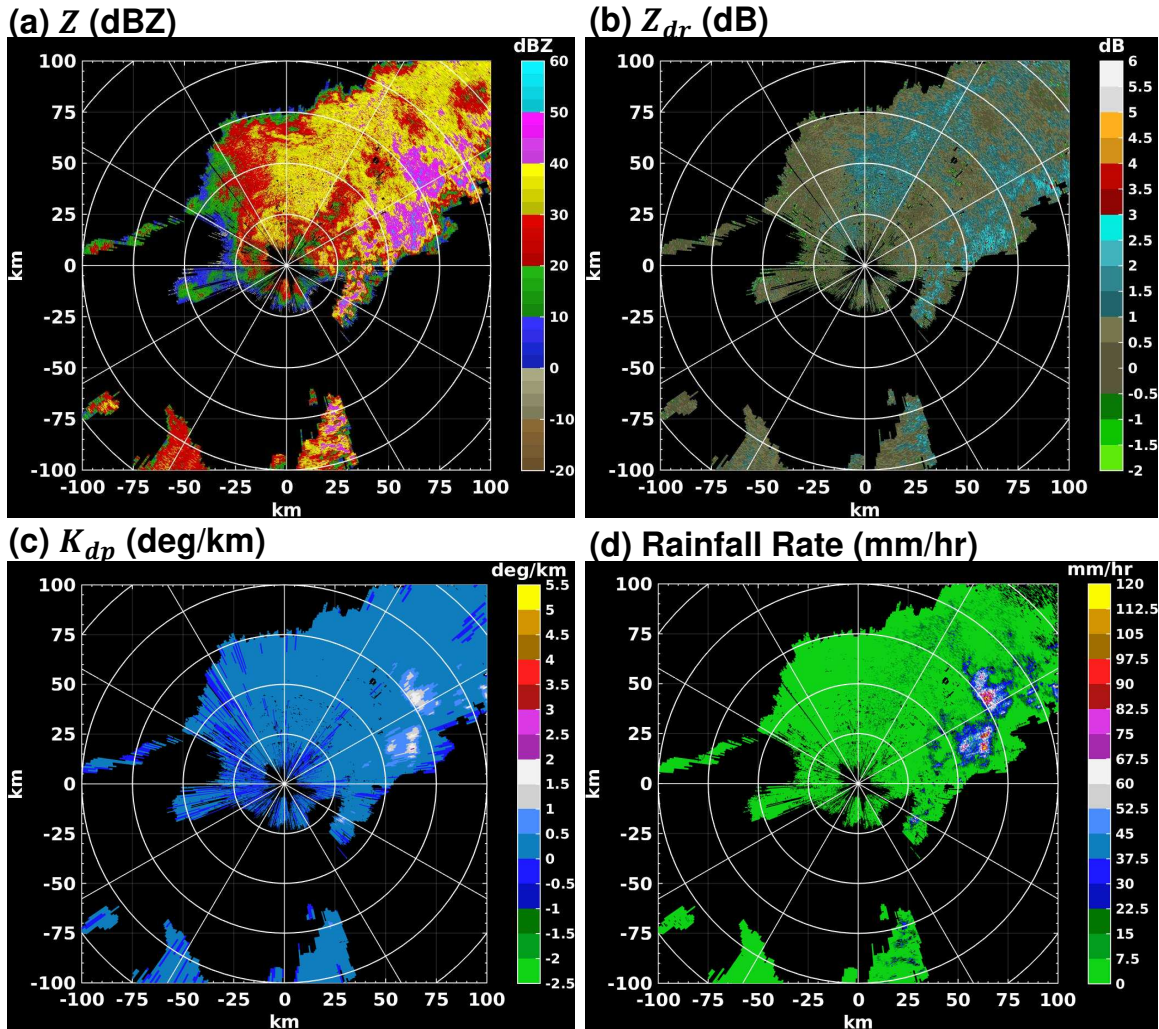


FIGURE 5.8. As in Figure 5.6, but for observations at 12:31UTC, 09 June 2013.

27 October 2013: This event was characterized by large hail and lightning. On October 26, a cluster of severe storms extended from Eagle Mountain eastward to the DFW metroplex. Golfball size hail was reported in Eagle Mountain and Southlake around 01:20UTC on October 27. High winds were also observed around 95-115 km hr⁻¹. A severe thunderstorm

warning was in effect in the DFW area until 02:30UTC, October 27. Figure 5.9 shows sample radar observations and rainfall rate estimates during this event at 02:39UTC.

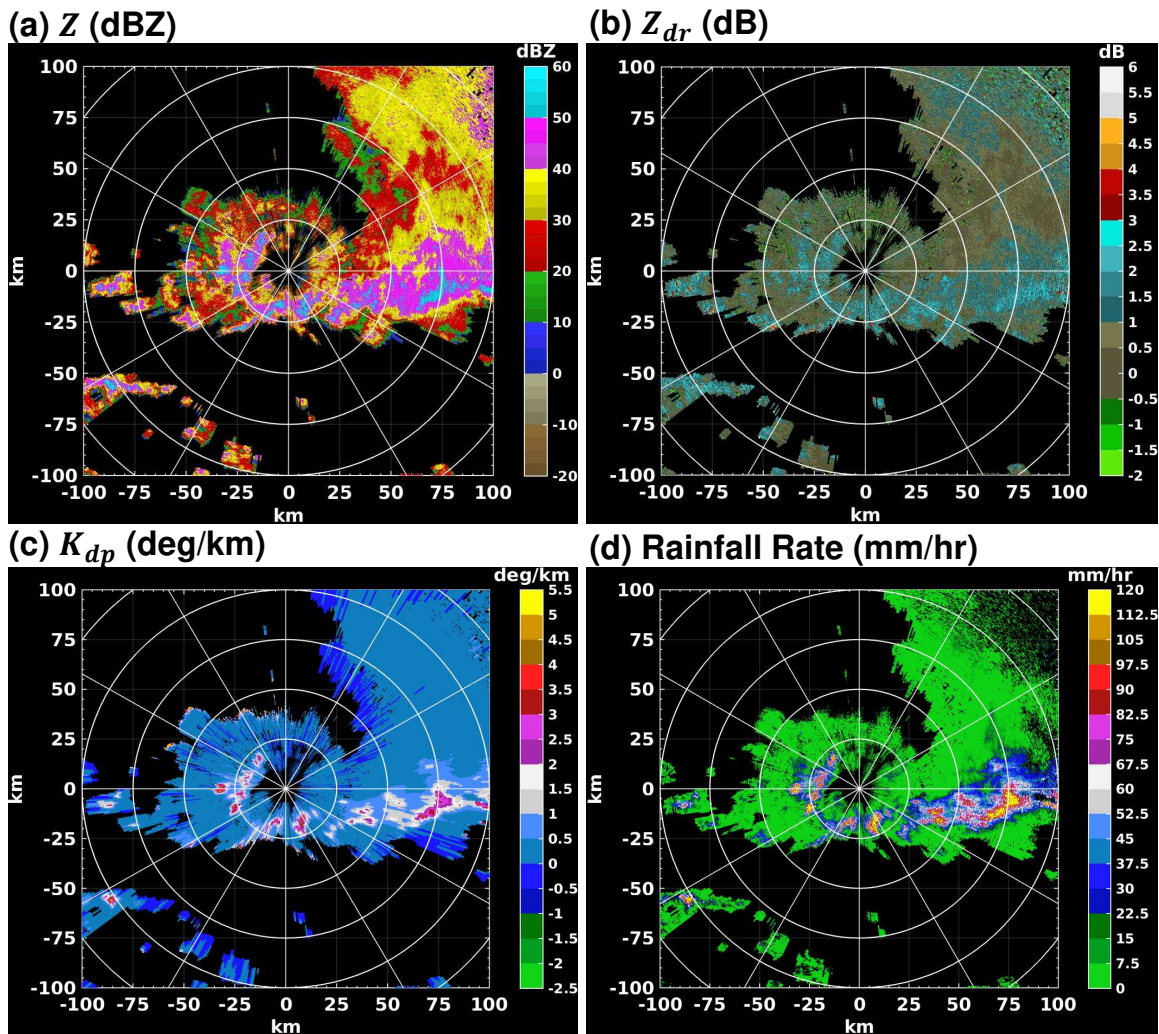


FIGURE 5.9. As in Figure 5.6, but for observations at 02:39UTC, 27 October 2013.

5.2.2. QUANTITATIVE EVALUATION OF CASA/DFW RAINFALL PRODUCTS.

In order to quantitatively evaluate the performance of the CASA DFW QPE system, rainfall records from a rain gauge network were used for comparison. The gauge network, consisting of about 60 gauge stations, is deployed and managed by the city of Fort Worth and city of Grand Prairie. Figure 5.10 shows the locations of gauge stations with respect to the S-band KFWS radar and several X-band radars in the DFW network.

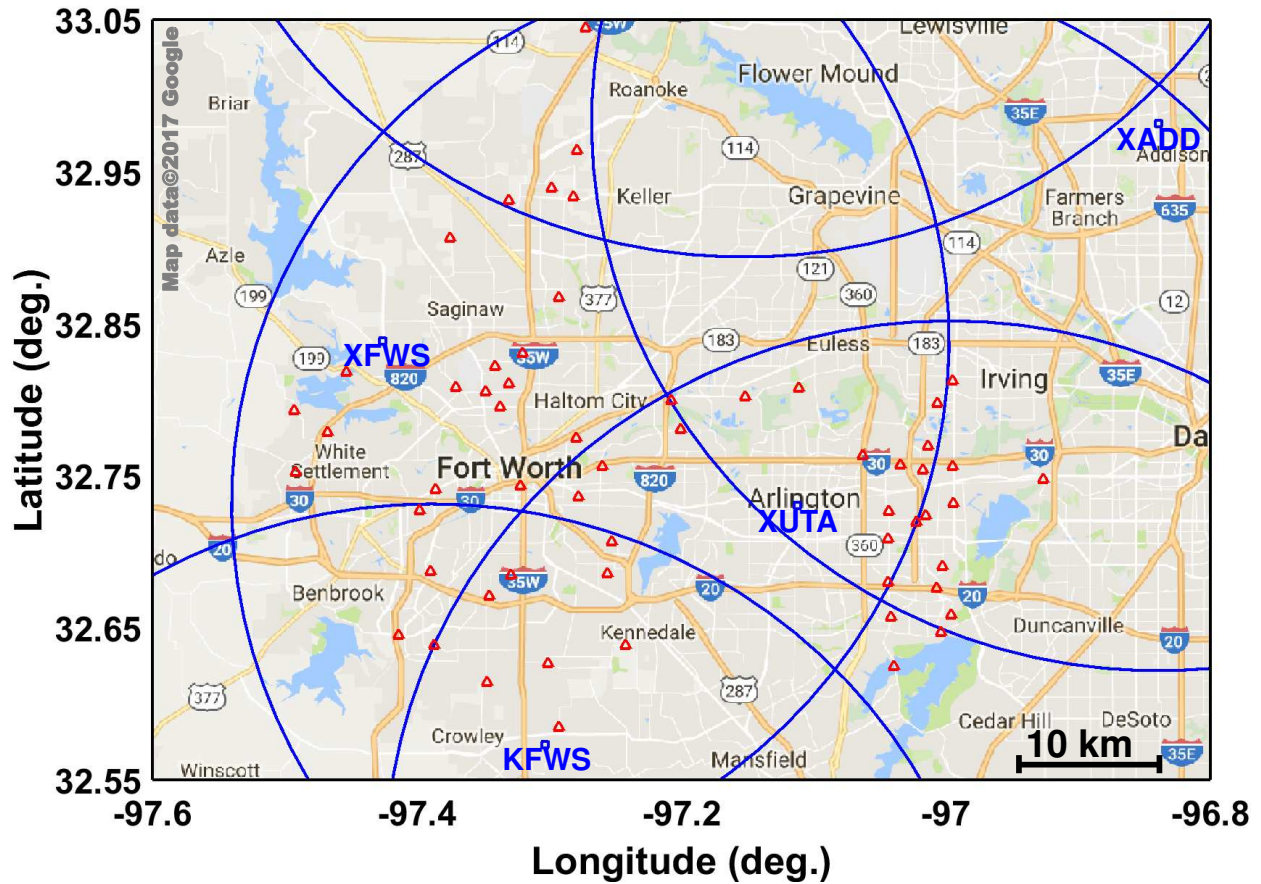


FIGURE 5.10. Locations of rain gauges (red triangles) used for the DFW rainfall product evaluation. The gauges are managed and operated by the city of Fort Worth and city of Grand Prairie.

At each rain gauge, rainfall data is archived based on the Automated Local Evaluation in Real Time (ALERT) transmission system. Each time one millimeter (0.04 inch) of rainfall occurs, that information is transmitted to the base station and the data are stored to the nearest second. For the sake of comparison, the rainfall data are accumulated to rainfall amounts in 5-min intervals over every 24-hr period. The 5-min rainfall accumulations from gauges are then used as the baseline for evaluating various CASA DFW radar rainfall products.

However, it should be noted that radar observations represent a unit of illuminated resolution volume, whereas the gauges provide point-wise measurements. Considerable literature

exists documenting the scale mismatch between radar and gauge rainfall observations. In this study, the radar measurements are spatially chosen at the location of the rain gauges for validation. Temporally, the one-minute resolution radar rainfall rates are used for calculating the running accumulations of rainfall to match the gauge observation frequencies (a five-minute interval). Rainfall amounts at longer time scales are then obtained by aggregating the 5-min rainfall data.

In addition, point-wise traces at each gauge station are generated for diagnostic purposes. As an example, a detailed comparison of the DFW radar network rainfall product against gauges at several stations during the 2015 Thanksgiving event is illustrated in Figure 5.11. The upper, middle, and bottom panels of Figure 5.11 show the rainfall measurements at gauges 1100 (32.7952°N, 97.3368°W), 1030 (32.8181°N, 97.4534°W), and 1800 (32.6141°N, 97.3468°W), respectively. The thin lines represent 15-min rainfall estimates, while the thick lines denote rainfall accumulations. Clearly, Figure 5.11 shows that the rainfall estimates from the DFW radar QPE system agree very well with the rain gauge measurements.

In order to quantify the accuracy of the CASA DFW QPE system, the normalized mean bias (NMB) and normalized standard error (NSE) of rainfall amounts at different time scales are computed. Assuming the rain gauge measurements are the “ground truth”, the NMB and NSE are respectively defined as:

$$(33a) \quad NMB = \frac{\langle R_R - R_G \rangle}{\langle R_G \rangle}$$

$$(33b) \quad NSE = \frac{\langle |R_R - R_G| \rangle}{\langle R_G \rangle}$$

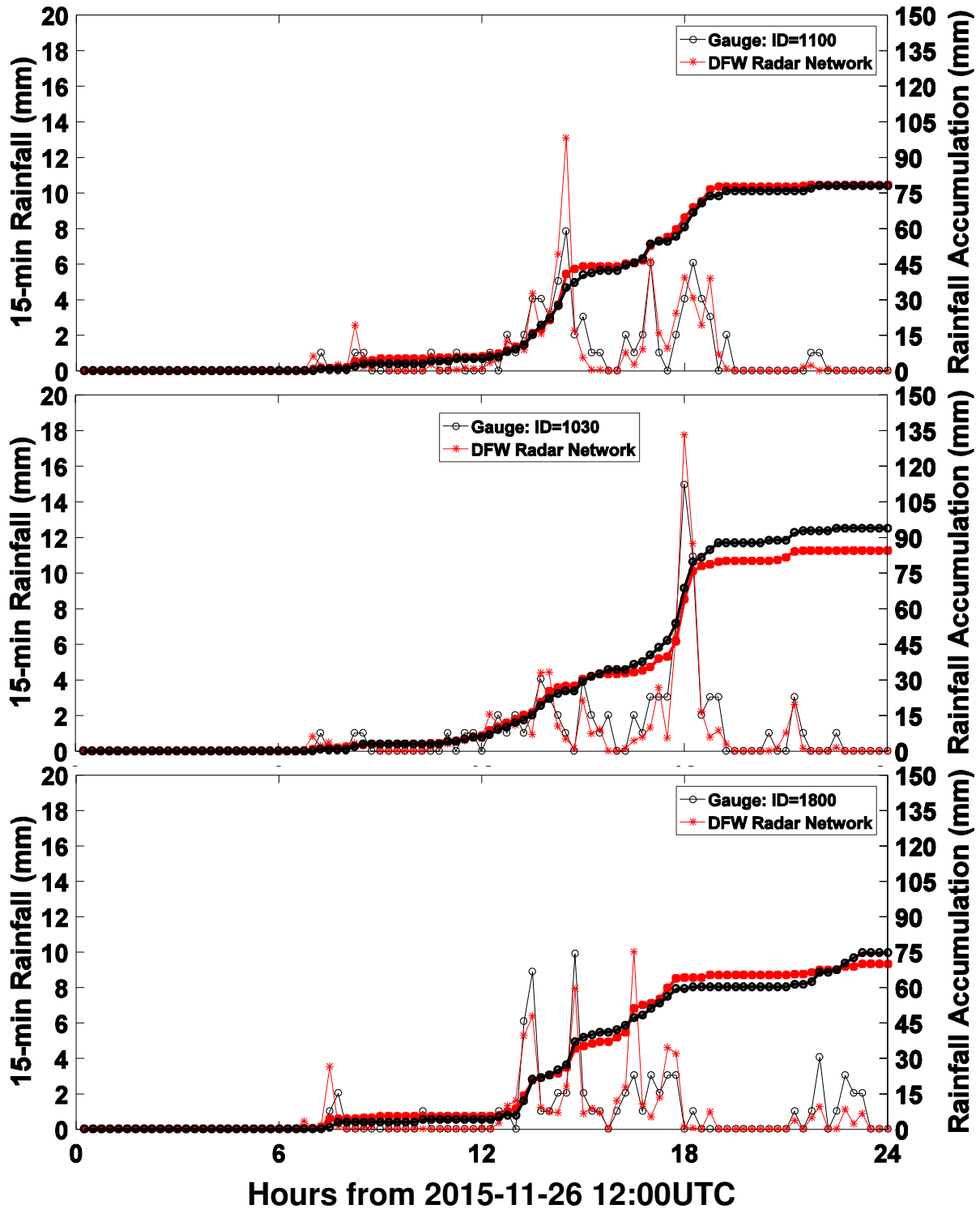


FIGURE 5.11. 15-min rainfall (thin lines) and rainfall accumulations (thick lines) from the DFW radar network and gauges at sample gauge locations during the 2015 Thanksgiving flood event. The upper, middle, and bottom panels illustrate the products at gauges 1100 (32.7952°N, 97.3368°W), 1030 (32.8181°N, 97.4534°W), and 1800 (32.6141°N, 97.3468°W), respectively.

TABLE 5.3. Evaluation results (*NMB*: normalized mean bias, and *NSE*: normalized standard error) of various rainfall products at different time scales. ‘-’ indicates that an operational product is not available from the NWS.

Time scale	<i>NSE</i> (%)				<i>NMB</i> (%)			
	DFW Network	N1P	OHA	DAA	DFW Network	N1P	OHA	DAA
18 Apr 2013								
5-min	30.8	-	-	-	-2.8	-	-	-
10-min	20.1	-	-	-	-1.2	-	-	-
15-min	17.7	-	-	-	-0.5	-	-	-
20-min	14.7	-	-	-	-0.3	-	-	-
30-min	13.9	-	-	-	-0.6	-	-	-
60-min	10.6	42.7	22.5	16.2	-3.4	-42.7	-18.2	-1.6
16 May 2013								
5-min	37.0	-	-	-	-4.2	-	-	-
10-min	31.5	-	-	-	2.7	-	-	-
15-min	27.6	-	-	-	3.8	-	-	-
20-min	24.0	-	-	-	4.6	-	-	-
30-min	19.6	-	-	-	4.4	-	-	-
60-min	14.6	25.4	24.6	27.4	2.0	-19.3	-1.8	11.3
09 Jun 2013								
5-min	39.1	-	-	-	-2.7	-	-	-
10-min	34.2	-	-	-	8.9	-	-	-
15-min	30.4	-	-	-	10.6	-	-	-
20-min	27.2	-	-	-	10.2	-	-	-
30-min	20.7	-	-	-	9.0	-	-	-
60-min	15.5	28.2	29.7	22.9	11.1	-25.2	-1.4	7.8
27 Oct 2013								
5-min	33.9	-	-	-	-8.0	-	-	-
10-min	26.5	-	-	-	-5.1	-	-	-
15-min	21.8	-	-	-	-5.2	-	-	-
20-min	19.2	-	-	-	-5.6	-	-	-
30-min	16.5	-	-	-	-7.8	-	-	-
60-min	14.6	52.0	46.9	29.8	-2.4	-51.7	-46.9	-26.6

where R_R and R_G denote the DFW radar network and gauge rainfall measurements (mm), respectively. The angle brackets stand for sample averages. It should be noted that the errors associated with rain gauge measurements were neglected in the evaluation. Interested readers are referred to Habib et al. (2001) and Chen and Chandrasekar (2015a) for sampling errors of tipping-bucket gauges.

NMB and *NSE* results for rainfall estimates at different time scales (5-min, 10-min, 15-min, 20-min, 30-min, and 60-min) for each of the example events described in Section 5.2.1 are shown in Tables 5.3.

In addition, the overall *NMB* and *NSE* are calculated for each time scale based on the entire observations, combining the four example events and a number of other interesting

TABLE 5.4. Evaluation results (*NMB* and *NSE*) of various rainfall products at different time scales for 11 events combined. ‘-’ indicates that an operational product is not available from the NWS. The 11 events are 18 April 2013, 16 May 2013, 09 June 2013, 27 October 2013, 09 May 2014, 18 July 2014, 18 August 2014, 11 May 2015, 29 May 2015, 26 November 2015, and 26 December 2015.

Time scale	<i>NSE</i> (%)				<i>NMB</i> (%)			
	DFW Network	N1P	OHA	DAA	DFW Network	N1P	OHA	DAA
5-min	35.4	-	-	-	-5.7	-	-	-
10-min	29.0	-	-	-	0.3	-	-	-
15-min	25.6	-	-	-	1.4	-	-	-
20-min	22.6	-	-	-	2.0	-	-	-
30-min	18.8	-	-	-	1.5	-	-	-
60-min	14.8	34.1	29.3	25.0	0.4	-30.7	-13.3	1.2

events, including 09 May 2014, 18 July 2014, 18 August 2014, 11 May 2015, 29 May 2015, 26 November 2015, and 26 December 2015. The results are shown in Table 5.4.

For a side-by-side peer comparison, the operational products generated by the NWS for the S-band KFWS WSR-88DP radar (both single- and dual-polarization products) are also included in the validation analysis. The NWS single-polarization rainfall algorithm is presented in Fulton et al. (1998) and the dual-polarization rainfall algorithms are described in Giangrande and Ryzhkov (2008). Both are generated on polar grids centered at the radar, and are available from the National Centers for Environmental Information (NCEI). The single-pol product included in the evaluation study is one-hour precipitation (N1P), which has a spatial resolution of 2 km in range by 1.0 degree in azimuth. The dual-polarization-based hourly rainfall accumulations are produced in two different formats: one hour accumulation (OHA) and digital accumulation array (DAA). The NWS/OHA product has 16 data levels (4-bit) with the same spatial resolution of NWS/N1P, while the NWS/DAA product has 256 data levels (8-bit) and a spatial resolution of 0.25 km by 1.0 degree (<https://www.ncdc.noaa.gov/data-access/radar-data/nexrad-products>). The DAA never has a rain gauge bias correction applied, but the OHA product can potentially

have bias applied. Both N1P, OHA, and DAA are estimates of precipitation accumulation over the past hour, and are updated every five to six minutes. The *NMB* and *NSE* of NWS/N1P, NWS/OHA, and NWS/DAA for each of the example events, as well as for all 11 events combined, are shown in Tables 5.3 and 5.4. The evaluation statistics for rainfall products at other time scales are not included because higher temporal-resolution products are not operationally available from the NWS.

The main findings from the evaluation results of different rainfall products, including the CASA DFW radar network and the NWS single- and dual-polarization QPE, are summarized as follows:

(1) As expected, the three dual-polarization hourly rainfall products (CASA DFW network QPE, NWS/OHA, and NWS/DAA) have a better performance than the single-polarization products (i.e., NWS/N1P) in terms of *NMB* and *NSE* for each of the four example events or the 11 events combined. Among the four types of hourly rainfall products, the CASA DFW QPE system products have the best performance, which is further illustrated by the scatter plots shown in Figure 5.12 and the *NSE* histograms in Figure 5.13.

(2) For the 11 events combined, the *NMBs* of 5-, 10-, 15-, 20-, 30- and 60-min rainfall from the CASA DFW QPE system are -5.7%, 0.3%, 1.4%, 2.0%, 1.5%, and 0.4%, respectively; and the *NSEs* are 35.4%, 29.0%, 25.6%, 22.6%, 18.8%, and 14.8%, respectively. In particular, the 5-, 10-, 15-, 20-, and 30-min products are not available from the operational NWS radars. The excellent performance of the DFW QPE system is further demonstrated by the scatter plots shown in Figures 5.14 and 5.12(a).

(3) The *NSEs* of the CASA DFW radar network QPE products have a decreasing trend as the rainfall accumulation time increases from five minutes to one hour (see also Figure

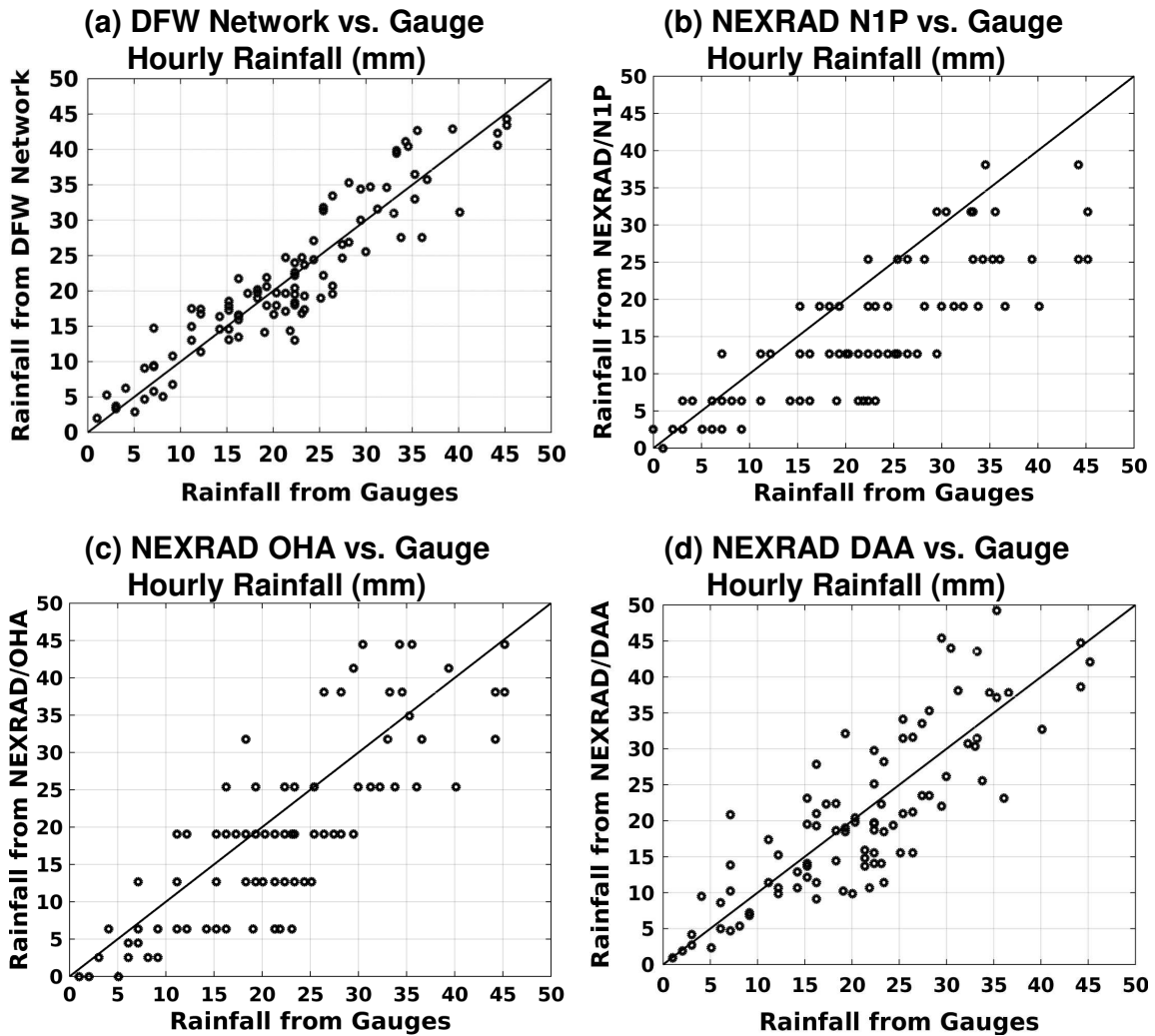


FIGURE 5.12. Scatterplots of hourly rainfall accumulations from the CASA DFW QPE system versus rain gauge measurements for the four example events (combined) described in Section 5.2.1. (a) CASA DFW QPE system product, (b) NWS N1P product, (c) NWS OHA product, and (d) NWS DAA product.

5.15). This is because the random radar measurement errors are reduced by temporal and spatial averaging.

(4) For all four example events or the 11 events combined, the NWS N1P and OHA products underestimate rainfall compared with the gauge network observations (see also Figure 5.12(b)(c)). The overall *NMB* and *NSE* for the NWS/N1P are -30.7% and 34.1%, respectively, for the 11 events combined, and -13.3% and 29.3% for the NWS/OHA. Other than the spatial resolution difference, the impact of data quantization on NWS N1P and

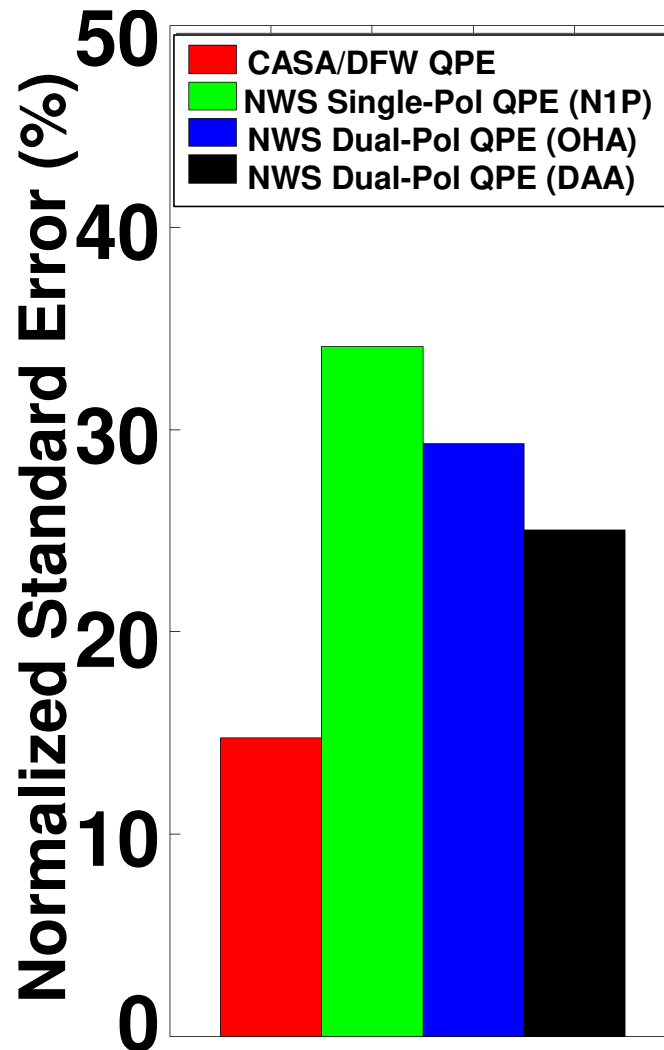


FIGURE 5.13. The *NSEs* of hourly rainfall products operationally generated by the NWS and CASA DFW QPE systems for 11 events combined, including 18 April 2013, 16 May 2013, 09 June 2013, 27 October 2013, 09 May 2014, 18 July 2014, 18 August 2014, 11 May 2015, 29 May 2015, 26 November 2015, and 26 December 2015.

OHA may have introduced significant errors to the products. Detailed investigation of the quantization error in the NWS operational products is beyond the scope of this study. The interested reader is referred to documents about the WSR-88DP Open Radar Product Generator (ORPG) from <http://www.roc.noaa.gov/>.

(5) Overall, the NWS/DAA products have better performance than OHA in terms of *NMB* and *NSE*. The overall *NMB* is about 1.2% and the *NSE* is about 25.0%. Besides

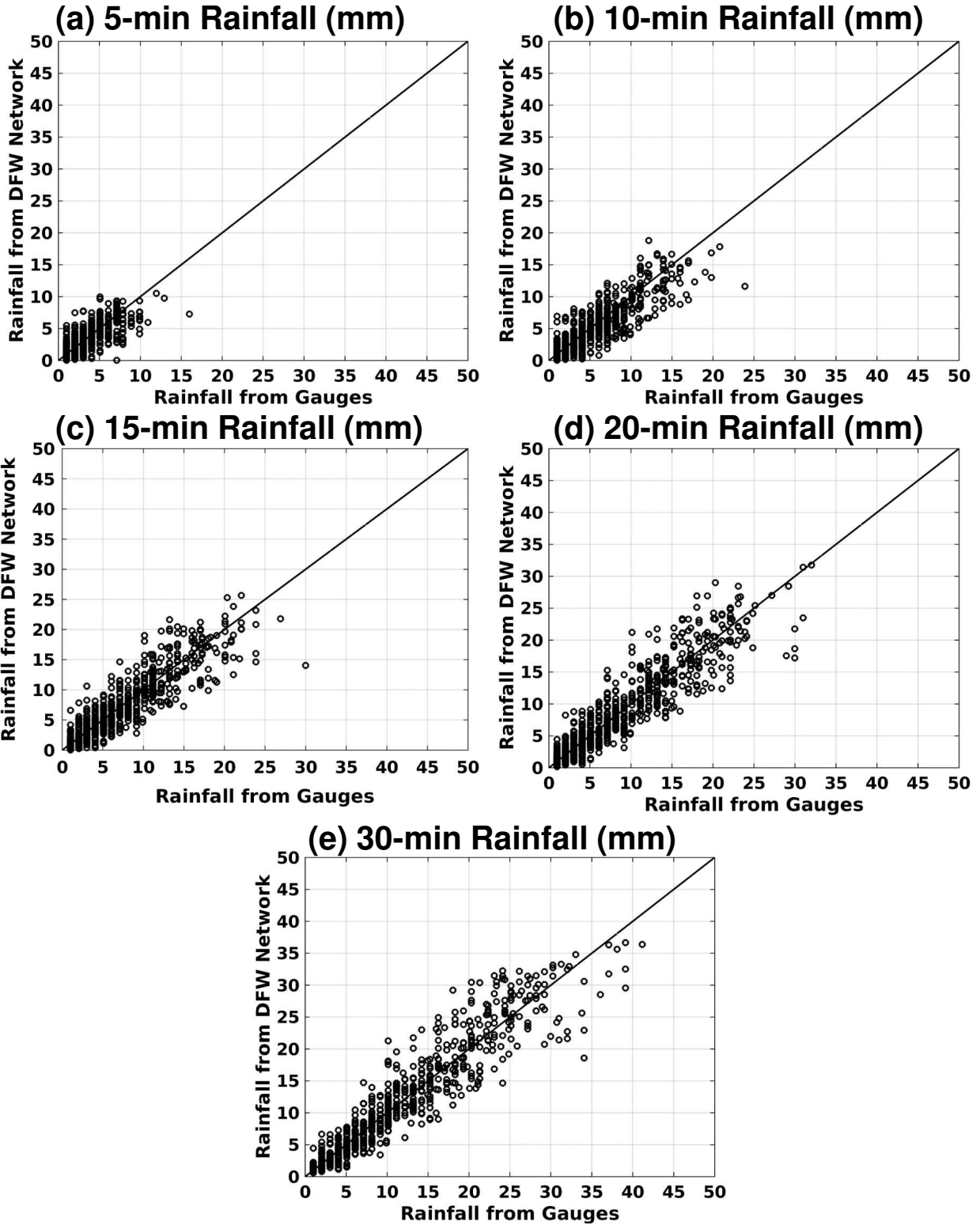


FIGURE 5.14. Scatterplots of (a) 5-, (b) 10-, (c) 15-, (d) 20-, and (e) 30-min rainfall accumulations from the CASA DFW QPE system versus rain gauge measurements for the four example events described in Section 5.2.1

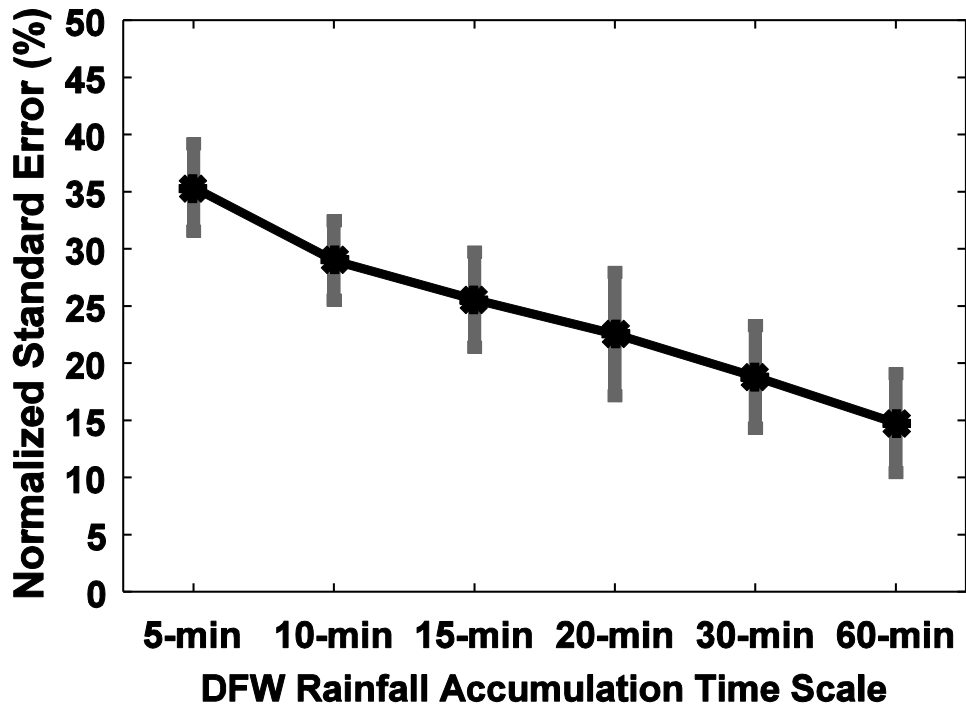


FIGURE 5.15. The *NSEs* of the CASA DFW QPE products at different time scales, for the 11 events combined. The error bars in grey represent the variability of performance at different gauge locations

the aforementioned spatial averaging and degraded quantization, the worse performance of OHA may be attributable to the bias applied to it (for details, see documents from <http://www.roc.noaa.gov/>).

5.3. SUMMARY

High spatiotemporal resolution QPE is one of the essential requirements for the prediction of urban flash floods, which are usually associated with heavy rainfall over a short time span. It has been shown in Chapter 3 that the dual-polarization radar techniques can improve the QPE accuracy over the traditional single-polarization radars by rendering more measurements to enhance the data quality, providing more information about rain DSD, and implying more characteristics of different hydrometeor types. However, doing QPE in complex terrain is still a large challenge due to the sampling limitations of the NWS operational

radar. Spatially, the NWS radars are normally separated by distances of over 200 km, and the radar resolution volume is continuously enlarged with increasing range. Subsequently, the QPE accuracy will suffer from beam broadening, beam overshooting, and the earth's curvature. In addition, it is an overwhelming task to find proper infrastructure to support a large radar system in an urban environment and to avoid local terrain blockage. Temporally, the NWS radar observations are updated every five to six minutes in precipitation mode, which is too long for urban flash flood modeling and forecasting.

CASA has proposed a solution to the sampling dilemma of WSR-88DP by deploying a network of higher-frequency (X-band) dual-polarization radars to fill the gaps in the operational S-band weather radar coverage (detailed in Chapter 4). This small X-band radar system has gained increasing interest in recent years due to its cost efficiency and compact configurations, especially for urban deployment and applications (Chen et al. 2017b; Chandrasekar et al. 2017; Cifelli et al. 2017). In addition, at X-band, the differential phase-based rainfall approaches can better address the physical sciences in precipitation estimation. At the same time, the deployment of a dense radar network can address engineering challenges such as beam height and resolution (Cifelli and Chandrasekar 2010; Chandrasekar et al. 2012).

In this chapter, the real-time high-resolution ($250 \text{ m} \times 250 \text{ m} \times 1 \text{ min}$) QPE system designed for the CASA DFW dense urban radar network has been presented. This real-time rainfall system is built based upon a local polarimetric S-band WSR-88DP radar (i.e., KFWS radar) and the CASA/DFW X-band radar network. The performance of the CASA DFW QPE system was evaluated in an operational environment during a number of precipitation events that occurred in 2013, 2014 and 2015. In addition, the NWS hourly rainfall products (note that the NWS does not generate rainfall products in shorter time scales than one hour)

were also evaluated. Comparisons between radar rainfall estimates and rainfall measurements from ground rain gauges have demonstrated the excellent performance of the CASA DFW urban QPE system. In particular, the hourly rainfall performance of the CASA DFW QPE system is about 20% better in *NSE* than the operational NWS single-polarization product, and 10% better than the NWS dual-polarization products.

Coupled with hydrologic models, the high-resolution real-time rainfall products from the DFW radar network are being used in downstream applications such as urban flash flood forecasting. The high-quality DFW radar network rainfall products can also serve as reliable datasets for validation of satellite precipitation retrievals (Chen and Chandrasekar 2016).

APPLICATION OF HIGH-RESOLUTION GROUND RADAR OBSERVATIONS TO SATELLITE PRECIPITATION DATA FUSION

The high-performance precipitation products derived from ground radars have been used in a number of applications for disaster mitigation and numerical weather prediction. Ground-based dual-polarization radar is also a powerful tool for validation of satellite measurements and associated precipitation retrieval algorithms (Schwaller and Morris 2011; Kirstetter et al. 2012; Chen and Chandrasekar 2016). Taking the Global Precipitation Measurement (GPM) satellite mission (Hou et al. 2014) initiated by the National Aeronautics and Space Administration (NASA) and the Japan Aerospace Exploration Agency (JAXA) as an example, ground radar is always a key component in GPM ground validation field campaigns. However, most previous research only focused on using ground radar products to evaluate various satellite precipitation products. The ground radar observations or products themselves are not essentially incorporated in the satellite product development phase. In this chapter, the application of high-resolution ground radar observations to satellite precipitation estimation and fusion will be investigated.

As discussed in Section 2.2 in Chapter 2, precipitation retrieval using satellites is generally conducted through cloud top brightness temperatures in the infrared (IR) images from geostationary satellites and/or passive microwave (PMW) measurements from low earth orbit satellites (Kummerow et al. 2000; Kidd et al. 2003). IR data are available globally nearly everywhere nearly all the time. Global rainfall mapping can be obtained by correlating rainfall rates with cloud top brightness temperatures measured by the IR channels. In contrast

to IR, relatively low frequency (10-37 GHz) PMW signals sense the thermal emission of raindrops while higher frequency (85 GHz and higher) signals sense the scattering of upwelling radiation from the earth to space due to ice particles. PMW-based retrieval has better physics than that based on IR data. However, the space time coverage of PMW sensors is very limited compared to IR sensors. Figure 6.1 shows a typical sampling of 16 PMW satellites over the continental U.S. (CONUS) at each half-hour window during a 3-hr period (00:00-02:30UTC) on May 29, 2015. Obviously, at each half hour, only a small portion of CONUS is covered. The PMW data have to be substantially averaged over time in order to provide full coverage. Figure 6.1 (bottom panel) also shows a 3-hr composite of six half-hourly converge maps, which demonstrates that most of the regions are currently scanned by PMW sensors during a 3-hr period.

A number of techniques have been developed to produce precipitation products over the globe, using either IR or PMW data or IR and PMW in combination. The IR data are generally manipulated in a statistical fashion to mimic the behavior of ground radar or PMW-derived precipitation estimates. For example, Miller et al. (2001) developed a technique in which PMW-derived precipitation estimates are regressed with collocated observations of IR brightness temperatures to generate precipitation estimates when and where PMW data are unavailable. Huffman et al. (2007) proposed a scheme in which PMW observations are used to calibrate the more frequently available IR data. Turk et al. (2008) developed a scheme to determine the IR brightness temperature threshold for precipitation estimation by comparing the distribution of IR data with collocated rainfall estimates from PMW sensors, and the resulting relationship is used to estimate rainfall using IR data in locations and instances where PMW data are not available.

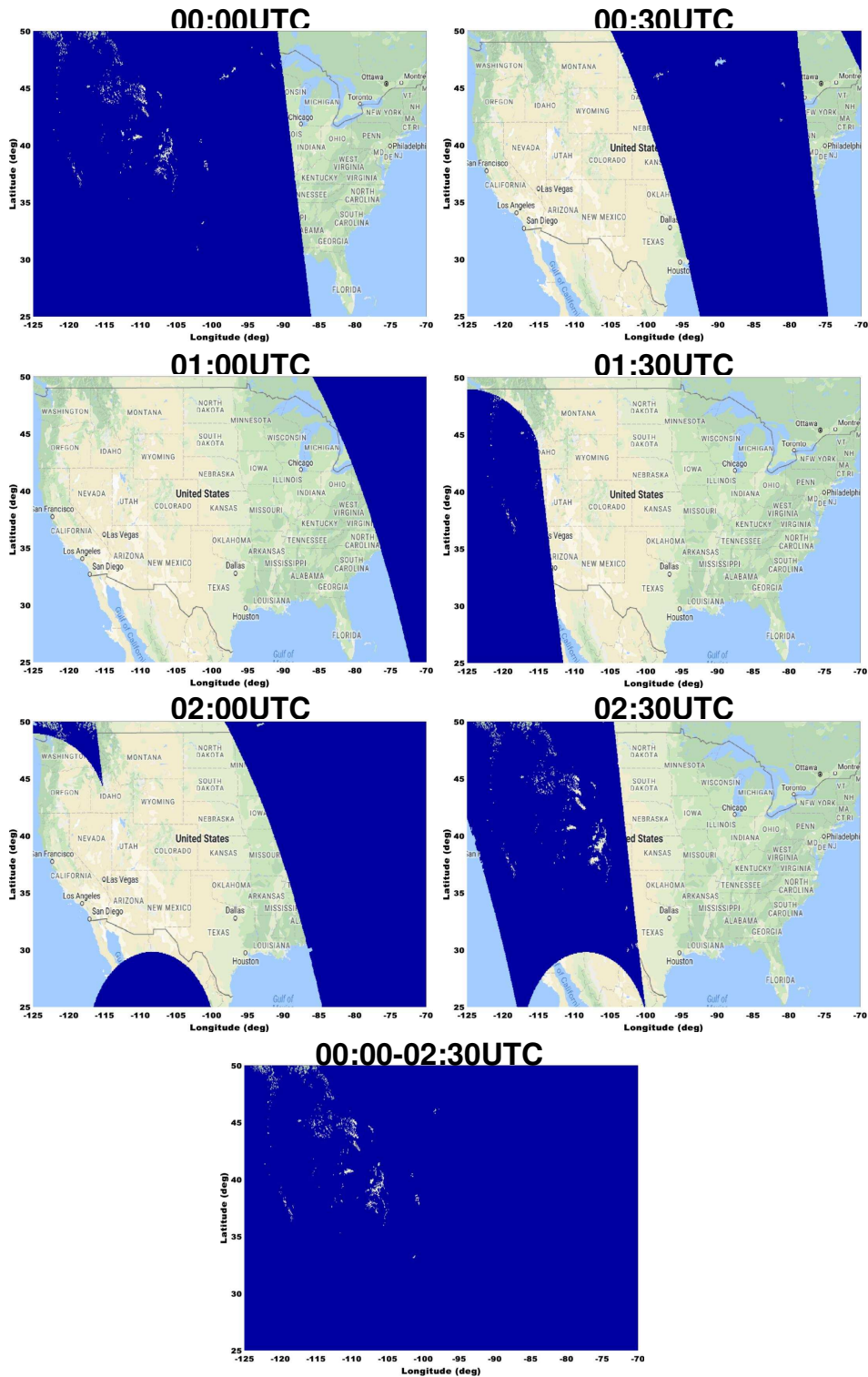


FIGURE 6.1. Typical sampling coverage of current passive microwave sensors for each half-hour window during a 3-hr period on May 29, 2015. The 16 sensors are on board TRMM, Aqua, FY-3B, DMSP, MetOp, and NOAA satellites. The bottom panel shows a 3-h composite of the half-hourly coverage maps in the upper three panels.

With these techniques, several global precipitation products have been derived. Traditional examples include the Tropical Rainfall Measuring Mission (TRMM) Multisatellite Precipitation Analysis (TMPA) described in Huffman et al. (2007), the Precipitation Estimation from Remotely Sensed Information Using Artificial Neural Networks (PERSIANN) in Sorooshian et al. (2000), the Passive Microwave-Calibrated Infrared algorithm (PMIR) (Kidd et al. 2003), the Naval Research Laboratory Global Blended-Statistical Precipitation Analysis (NRLGeo) (Turk and Miller 2005), and the Goddard profiling algorithm (GPROF), which is also applied in TMPA (Kummerow et al. 2001). On 27 February 2014, the GPM Core Observatory was successfully launched in Japan (Hou et al. 2014). The application goals of this science mission are to advance our understanding of global precipitation microphysics and distribution, and improve the accuracy and frequency of precipitation measurements. In the GPM era, new products have been developed based on recent developments in satellite-sensing technologies. Typical examples include the Integrated Multisatellite Retrievals for GPM (IMERG) (Liu 2016) and the Global Satellite Mapping of Precipitation (GSMaP) estimates (Kubota et al. 2007; Aonashi et al. 2009; Ushio et al. 2009). Both IMERG and GSMaP seek to produce high-precision, high-resolution global precipitation maps using both IR and PMW data. These two products are often referred to as GPM flagship level 3 products. NOAA’s Climate Prediction Center (CPC) has developed a morphing method for combining IR data and PMW-based precipitation retrievals (Joyce et al. 2004). This morphing technique, termed CMORPH, uses precipitation estimates derived from PMW observations exclusively whose features are transported via spatial propagation information obtained from IR data during periods when instantaneous PMW retrievals are not available. The motion (or propagation) vectors are produced by computing spatial lag correlations on successive IR images and then used to propagate the PMW-derived precipitation estimates in time and

TABLE 6.1. A summary of commonly used satellite precipitation products. The PERSIANN-Cloud Classification System (CCS) is essentially an enhanced PERSIANN products.

Product	Spatial Resolution	Temporal Resolution	Data Source
TMPA 3B42RT	$0.25^\circ \times 0.25^\circ$	3-hr	https://mirador.gsfc.nasa.gov
PERSIANN	$0.25^\circ \times 0.25^\circ$	1-hr	ftp://persiann.eng.uci.edu/CHRSdata/PERSIANN
PERSIANN CCS	$0.04^\circ \times 0.04^\circ$	0.5-hr	ftp://persiann.eng.uci.edu/CHRSdata/PERSIANN-CCS
CMORPH	$0.25^\circ \times 0.25^\circ$	1-hr	https://rda.ucar.edu/datasets
GSMaP	$0.1^\circ \times 0.1^\circ$	1-hr	ftp://rainmap@hokusai.eorc.jaxa.jp
IMERG	$0.1^\circ \times 0.1^\circ$	0.5-hr	ftp://jsimpson.pps.eosdis.nasa.gov

space when updated PMW data are not available. This morphing process is very flexible in that any precipitation estimates from any PMW satellite source can be incorporated.

The spatial and temporal resolution of a few popular satellite precipitation products are summarized in Table 6.1. As mentioned above, although ground radar rainfall estimates are used when developing some of the IR- or PMW-based algorithms, the radar measurements are not directly incorporated in producing any of the operational satellite precipitation products. This chapter describes a machine learning system that has been developed to improve satellite precipitation data fusion through combining ground radar observations. The CMORPH mechanism is referred to extensively in the development of this machine learning-based radar and satellite data fusion framework. Therefore, a brief overview of the CMORPH technique is provided in Section 6.1. For more details, interested readers are referred to Joyce et al. (2004) and Xie et al. (2017). In Section 6.2, the machine learning system for merging IR, PMW observations from satellites, and high-resolution rainfall products from ground radar networks is detailed. An urban-scale application of the proposed machine learning approach is presented in section 6.3.

6.1. REVIEW OF NOAA CMORPH SATELLITE PRECIPITATION PRODUCT

As shown in Figure 6.2, the input to CMORPH includes both IR data and PMW-based retrievals. However, the CMORPH products only use precipitation estimates derived from PMW sensors. For a given location, the features of PMW-based precipitation retrievals are transported via spatial propagation information obtained from IR data during periods when instantaneous PMW retrievals are not available. In particular, the spatial correlations between successive IR images are applied to derive PMW-based precipitation retrievals in time and space when updated PMW data are unavailable. Overall, CMORPH produces high-resolution global (60°S-60°N) precipitation estimates at a spatial resolution of about 8 km \times 8 km, and a temporal resolution of 30 min.

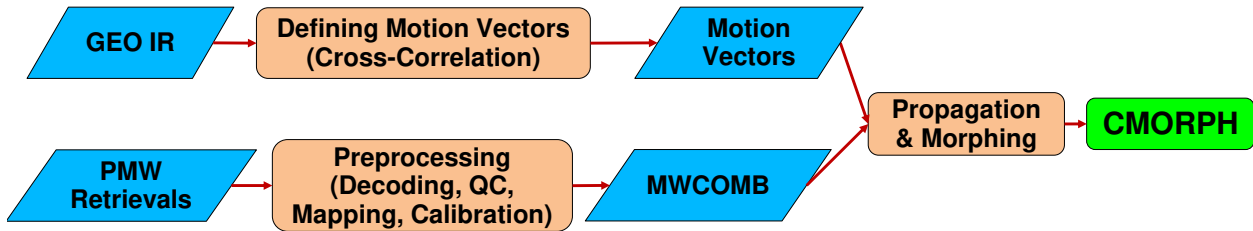


FIGURE 6.2. Conceptual diagram of CMORPH technique.

6.1.1. INPUT DATA.

PMW Retrievals: The PMW-based precipitation retrievals that are currently used in CMORPH are generated from observations from NOAA polar-orbiting operational meteorological satellites (NOAA-15, -16, -17, -18, -19), polar-orbiting meteorological satellites (MetOp-A, -B) developed by the European Space Agency (ESA) and operated by the European Organization for the Exploitation of Meteorological Satellites (EUMETSAT), the U.S. Defense Meteorological Satellite Program (DMSP) satellites (DMSP-13, -14, -15, -16, -17, -18), the second generation of Chinese polar-orbiting meteorological satellites (FY-3B), and NASA’s TRMM and Aqua satellites. The PMW sensors aboard these satellites are Advanced

TABLE 6.2. PMW sensors whose precipitation retrievals are presently (to date) used in CMORPH.

PMW sensor (decreasing quality from top to bottom)	LEO platforms (decreasing quality from left to right)	Quality ranking
TMI	TRMM	1
AMSR	Aqua	2
MWRI	FY-3B	3
SSMIS	DMSP F-18, F-17, and F-16	4
SSM/I	DMSP F-15, F-14, and F-13	5
MHS	MetOp-B, MetOp-A, NOAA-19, and NOAA-18	6
AMSU	NOAA-17, NOAA-16, and NOAA-15	7

Microwave Sounding Unit-B (AMSU-B; NOAA-15, -16, -17), Microwave Humidity Sounder (MHS; NOAA-18, -19, MetOp-A, -B), the Special Sensor Microwave Imager (SSM/I; DMSP F-13, -14, -15), the Special Sensor Microwave Imager Sounder (SSMIS; DMSP F-16, -17, -18), the Microwave Radiation Imager (MWRI; FY-3B), the TRMM Microwave Imager (TMI), and the Advanced Microwave Scanning Radiometer - Earth Observing System (AMSR-E; AQUA). Table 6.2 lists the satellite PMW sensors whose measurements are used to derive the precipitation retrievals served as inputs to CMORPH. The quality of retrievals from various PMW sensors is also ranked in Table 6.2.

Different PMW sensors have different characteristics in terms of retrieval algorithm, resolution, and coverage (Joyce et al. 2004; Xie et al. 2017). For example, the TMI is a nine-channel radiometer that operates at five frequencies similar to the SSM/I instrument. Its geographic coverage is restricted to 38°N to 38°S latitude due to the limits of the TRMM spacecraft orbit. But the TMI offers higher spatial resolution than SSM/I because of the relatively lower orbit of the TRMM spacecraft. Surface rainfall derived from TMI is based on the TRMM 2A25 algorithm, which essentially relates the vertical profiles of liquid and ice to surface rain rates in a radiative model context, and rainfall estimates are derived over land and ocean (Kummerow et al. 2001). In addition, matching between the convective/stratiform

fraction of a satellite view of precipitation and that of a cloud model is applied in the retrieval (Hong et al. 1999). Precipitation estimates from SSM/I sensors aboard the DMSP platforms utilize the 85-GHz vertically polarized channel to relate the scattering of upwelling radiation by precipitation-sized ice particles within the rain layer and in the tops of convective clouds to surface precipitation (Ferraro 1997). The scattering technique is applicable to both land and ocean. A precipitation rate derived empirically from the relationship between ice amount in the rain layer and in the tops of convective clouds to actual surface rainfall is used to estimate precipitation amounts. The absorption of the upwelling radiation by rainwater and cloud water at 19 and 37 GHz is used to derive rainfall rates over oceans (Joyce et al. 2004). In contrast to TMI or SSM/I, the AMSU-B instrument has five window channels, and its cross-track swath width (approximately 2200 km) contains 90 fields of view per scan. The AMSU-B rainfall algorithm first performs a physical retrieval of ice water path and particle size from the 89 and 150 GHz channels (Ferraro 1997). Then a conversion from the ice water path to the rain rate is made based on cloud data from the Pennsylvania State University-National Center for Atmospheric Research (PSU/NCAR) mesoscale model (also known as MM5) and on comparisons with *in situ* measurements.

IR Data: In CMORPH, the geostationary satellite IR brightness temperature information is extracted through the Man-computer Interactive Data Access System (McIDAS). Currently, the IR data from five satellites are used. Starting from the Pacific, the five satellites are Japan Meteorological Agency (JMA) satellite Himawari-8, GOES-West (currently GOES-15), GOES-East (currently GOES-13), Meteosat-10, and Meteosat-7. Sometimes, GOES-14 (normally in standby mode) is put into action as GOES-West or East when GOES-15 or 13 is in some anomaly. The characteristics of these five satellite IR sensors are listed in Table 6.3.

TABLE 6.3. Characteristics of geostationary IR data used in this study.

Satellite	Nadir location (at equator)	IR central wavelength (microns)
Himawari-8	140.7°E	11.0
GOES-15/WEST	135°W	10.7
GOES-13/EAST	75°W	10.7
Meteosat-10	0°	11.5
Meteosat-7	0°	11.5

Global IR images are available from both the Meteosat-10 and Meteosat-7 satellites every 30 min, but only every 3 hours from the GOES although northern and southern hemispheric images are available from the GOES spacecraft during the intervening 30-min intervals. CPC maps each satellite IR image to a rectilinear grid at 0.03635° of latitude and longitude resolution (about 4 km at the equator) using the method described in Janowiak et al. (2001). The global IR data (60°S - 60°N) are then constructed by compositing IR window channel measurements from the five geostationary satellites listed in Table 6.3, the equator at the Atlantic Ocean, Africa, the Indian Ocean, the western Pacific Ocean, and the eastern Pacific Ocean. The full-resolution global cloud-top temperature data ($4\text{ km} \times 4\text{ km} \times 30\text{ min}$) are then used to derive cloud motion vectors as part of the CMORPH processing (Joyce et al. 2004; Xie et al. 2017).

6.1.2. DATA PROCESSING AND MORPHING.

As aforementioned, the input IR data are available at half-hour intervals (Janowiak et al. 2001). This temporal resolution is selected to produce spatially complete PMW precipitation analyses (Joyce et al. 2004). Spatially, CMORPH uses 0.0727° latitude and longitude (8 km at the equator) grid resolution, which is determined by compromising the spatial resolution of various input data sources: 5-km (Meteosat IR), 4-km (GOES IR), and the greater-than-13-km resolution of the AMSU-B and SSM/I-derived precipitation estimates. The PMW-based rainfall estimates are first mapped to the nearest grid point on global (60°N - 60°S) rectilinear

grids at 0.0727° of latitude and longitude resolution. Such mapping is done for each half hour and each satellite. If two or more estimates from the same satellite sensor are available for a given grid pixel, the average rainfall rates will be calculated and used for this grid pixel. In reality, this only happens for high resolution TMI-based precipitation retrievals. At grid pixels within the satellite swath but with no rainfall estimates available, an inverse distance squared weighting interpolation of the nearest rainfall estimates is performed to create a spatially complete field. But it should be noted that CMORPH does not perform extrapolation beyond the last gridded estimate at the edge of a scan. For each half hour, after this process is completed for all the individual satellites, precipitation retrievals from multiple satellites are combined by sensor type (TMI, MWRI, SSM/I, AMSU, SSMIS, AMSR, and MHS) and the combined fields are saved to separate files. Basically, the precipitation fields composed of estimates with scan-swath time tags from 0 to 29 min after the hour are in a separate file from those with time tags ranging from 30 to 59 min after the hour. In applications, the TRMM spacecraft underflies all other satellites used in CMORPH so that TMI may have more frequent observations. In addition, some slight coverage overlap exists between the NOAA-17 and DMSP F-15 satellites in the half-hourly mapped precipitation files. Therefore, an optimization procedure is adopted to determine which estimate to use when PMW-based retrievals from more than one sensor are available at the same location for a given half-hour period (Joyce et al. 2004). In CMORPH, the order of precedence is established based on spatial resolution and the availability of both emission and scattering-based estimates over the oceans. The resulting order of precedence in regions of overlap is to use estimates from TMI first, then from AMSR if no estimate from TMI is available, and then MWRI, SSMIS, SSM/I, MHS, and finally AMSU (Xie et al. 2017). This procedure is

also adopted in developing the machine learning-based fusion system for radar and satellite precipitation estimation that is detailed in Sections 6.2 and 6.3.

Figure 6.3 illustrates sample combined PMW-based rainfall rate estimates over the continental U.S. during a 3-hr period on May 29, 2015. Figure 6.4 shows the combined IR data for the same region during the same time as Figure 6.3. However, the IR data shown here have a higher resolution ($4 \text{ km} \times 4 \text{ km}$) than combined PMW-based retrievals. The half-hourly global IR data are averaged to 8 km resolution in order to match exactly the grids that contain the PMW-based rainfall estimates. The averaged IR data are then used to propagate the PMW-based retrievals. In the following, more details about the generation of IR-based cloud motion vectors in CMORPH and how to use these motion vectors to propagate the PMW-based precipitation products will be provided.

There are two main advantages of using IR data to propagate PMW-based retrievals. On the one hand, the IR data are available globally every half hour. In addition, the IR sensors provide good measurements of cloud-top properties so that the cloud systems and their movements can be detected from the IR data. Essentially, the cloud system advection vectors are derived based on the correlation between collocated IR imagery at two different time intervals. However, it is well known that the direction and speed of cloud tops as detected by satellite IR sensors may not always correlate well with the propagation of the precipitating system in the lower layers. In addition, the direction of the wind may change and wind speed generally increases in magnitude with height from the earth's surface. In applications, the spatial scale of lag correlation should be large enough to include the sharp contrast of the cloud shield edges with the earth's surface. At the same time, the spatial resolution should not be too large in case the variability of the steering currents that provide propagation of the cloud system may be missed. In CMORPH, 5° latitude/longitude IR

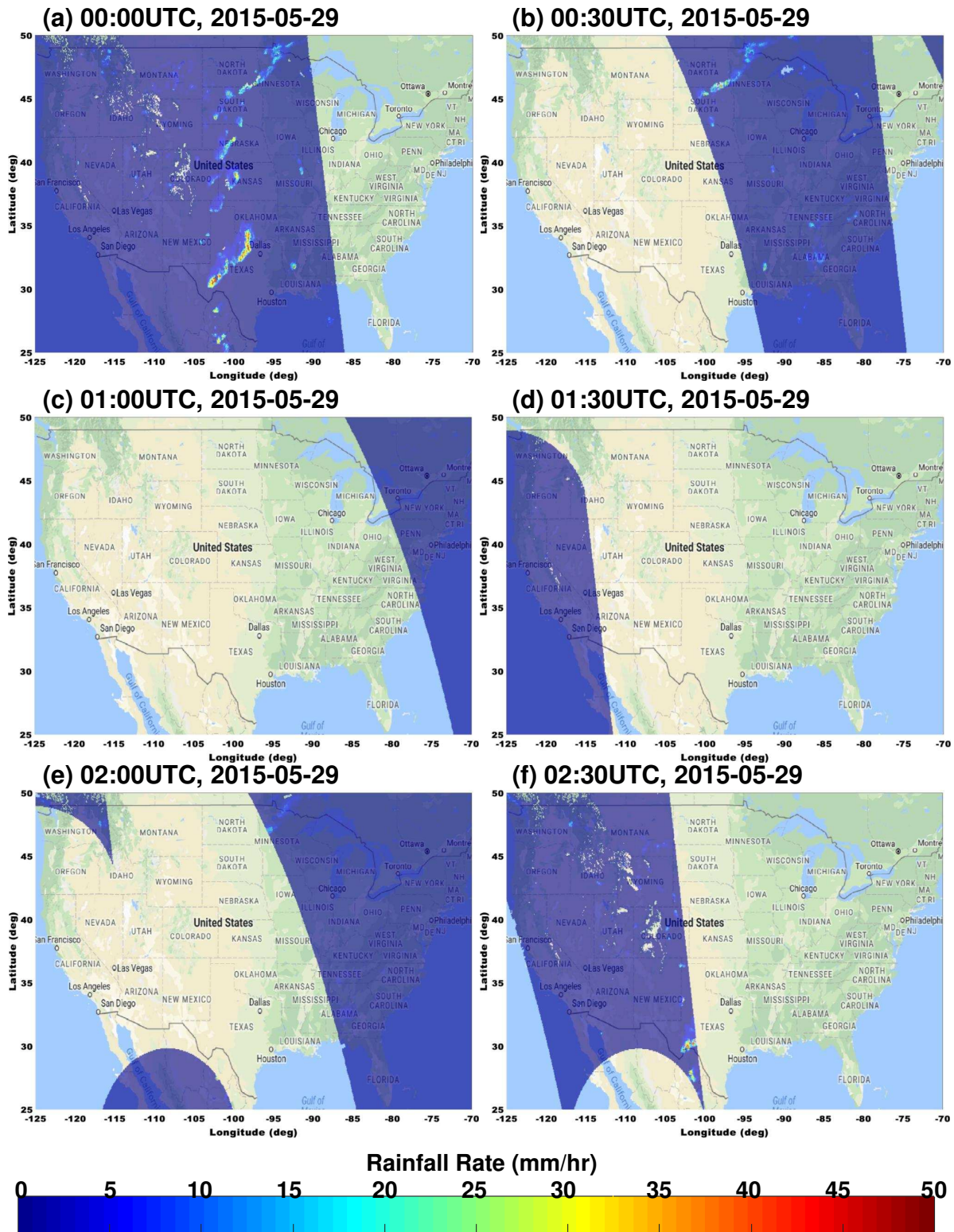


FIGURE 6.3. Combined PMW-based precipitation retrievals over continental U.S., 00:00-02:30UTC, May 29, 2015. The satellites included here are TRMM, Aqua, FY-3B, DMSF F-13, -14, -15, -16, -17, -18, MetOp-A, -B, and NOAA-15, -16, -17, -18, -19. The spatial resolution is about 8 km \times 8 km.

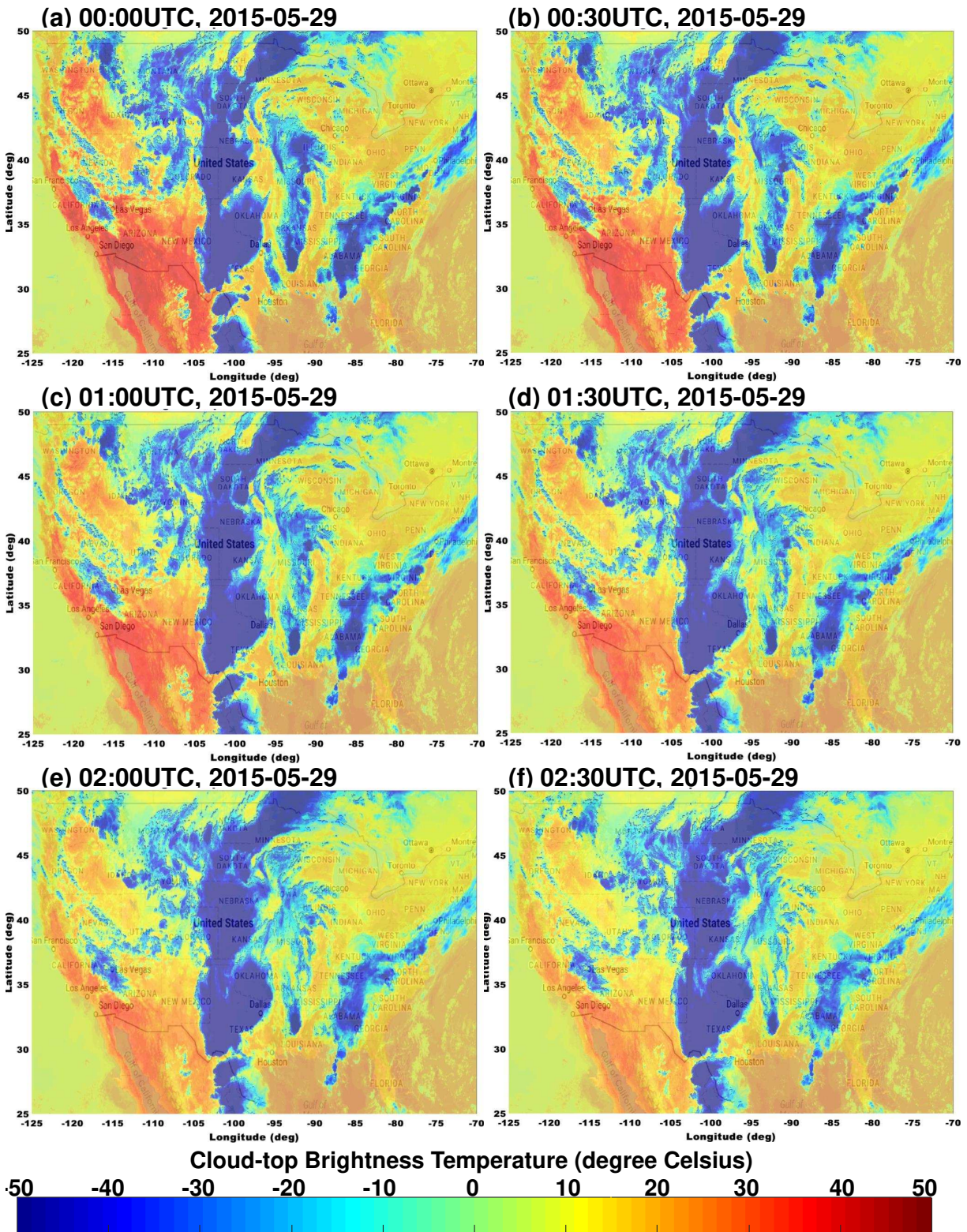


FIGURE 6.4. Combined IR brightness temperature data collected at the same time as Figure 6.3. The IR data are based on five geostationary satellites: Himawari-8, GOES-13, GOES-15, Meteosat-7, and Meteosat-10.

regions centered at 2.5° intervals are used for spatial lagging. Such resolution can provide a good measure of the movement of entire cloud systems while capturing the bulk of variations in the steering currents. Specifically, at a given 5° latitude/longitude grid box that contains ~ 8 km pixel resolution IR data at time $t = 0$, a spatial correlation is performed among the IR pixel brightness temperatures in that grid box with those in the same domain but from the $t + 0.5hr$ image. This process is repeated, but with each iteration the spatial domain of the $t + 0.5hr$ grid box is shifted pixel by pixel in the zonal or meridional directions. The combination of lags that yields the highest correlation determines the cloud motion vectors. If only hourly data are available for some satellites, the same procedure as described above is used except that the motion vector magnitudes are divided into two and are assumed to be the same for both half-hour periods within the hour. A primary domain is defined for each satellite, demarked by the midpoints between the nadir positions of primary and neighbouring satellites. Within each primary domain, the cloud motion vectors are derived solely from the primary satellite IR images unless the daily image count is less than half of the overlapping neighbouring satellite daily image count, in which case the information from the neighbouring satellite is used instead. If the IR data are missing for a particular half hour, vectors are determined by a linear temporal interpolation between the nearest past and future half-hourly vectors, weighted by the time distance from the missing time. If the missing vectors remain in very small regions, a spatial interpolation of the motion vector fields is performed. However, it should be noted that no spatial or temporal interpolation is performed over the GOES and Himawari-8 domains south of 50°S latitude, where IR data are very sparse. The motion vectors in those regions are assigned to zero.

In addition, a speed adjustment mechanism is applied in CMORPH in order to compensate for the fast advection rates in the northern hemisphere mid-latitudes. The adjustment

first computes rainfall advection vectors by spatially lagging operational hourly WSR-88DP rainfall products (regridded to the same 8-km resolution) in the exact same dimensions and manner cloud motion vectors are computed from IR data. The half-hourly cloud motion vectors are then combined to hourly to match the radar rainfall advection vectors. Comparisons between hourly cloud motion vectors and radar rainfall advection rates indicate that north-to-south rates are quite similar but the west-to-east cloud motion vector speeds are about twice as fast compared to the radar-derived vectors, and south-to-north rates are about 3-4 times faster. The incorporation of such adjustment procedures has resulted in improved propagation of precipitation features (Joyce et al. 2004). For consistency with the northern hemisphere, the meridional adjustment is applied to the derived cloud motion vectors of the opposite sign in the southern hemisphere in order to reduce the same long-wave trough effect (Xie et al. 2017).

With the derived cloud motion vectors, the propagation of PMW-based precipitation retrievals starts from spatially propagating the current ($t + 0hr$) fields of 8-km half-hourly PMW rainfall estimates forward in time. During the forward propagation, two auxiliary fields are maintained along with each precipitation estimate, including time stamps ($t = 0hr$ for current) in half-hourly increments, in which the units represent the time since the scan of the PMW satellite overpass used to define that grid pixel and the satellite identification associated with the retrievals. All the PMW satellite grid pixels within each $2.5^\circ \times 2.5^\circ$ region, including those with zero precipitation, are propagated in the same direction and distance to produce the analysis for the next half hour ($t + 0.5hr$). If a PMW precipitation feature is on the border between two of the $2.5^\circ \times 2.5^\circ$ regions, the rainfall field is propagated evenly if the vector pairs from both regions match exactly. If two grid pixels from different regions are propagated to the same pixel location by convergence, the average of the two

values is used. If a data gap in the estimated rainfall field is created due to divergence, a bilinear interpolation of the rainfall features across the gap is computed. Finally, if a PMW-derived precipitation estimate from a new scan at $t + 0.5hr$ is available at a particular grid location, that estimate will overwrite the propagated estimate and the associated time stamp for that pixel set to a value of zero. Otherwise, the time stamp is incremented by a value of 1.

This entire morphing process is repeated every half hour. For illustration purpose, Figure 6.5 shows the fundamental concept of the propagation process. An initial 03:30UTC time analysis of current PMW-based retrievals ($t = 0hr$) consisting of two precipitation clusters is propagated forward to produce analyses at $t + 0.5hr$ and $t + 1hr$ using the IR-derived cloud motion vectors. The continuity of the propagated rainfall clusters in the $t + 0.5hr$ and $t + 1.0hr$ fields can be appreciated by comparing them with the updated PMW analysis. It should be noted that the shape and intensity of the features have not changed in the propagated plots (Joyce et al. 2004). Also, this analysis can possibly be propagated one more time step to $t + 1.5h$, in which case all values will be overwritten by precipitation estimates from an updated PMW scan that became available at the $t + 1.5hr$ time step (i.e., 05:00UTC).

In addition to the forward propagation, a similar process is invoked in which current rainfall estimates are spatially propagated backward in time using the same cloud motion vectors as those used in the forward propagation, except for reversing the sign of those vectors. Corresponding results are stored separately from those computed in the forward propagation process. Thus, for the above example in Figure 6.5, if the $t = 1.5hr$ updated PMW precipitation estimates are available, they will be propagated backward to the $t = 0hr$ time frame. After all propagated fields have been computed, the precipitation analysis at

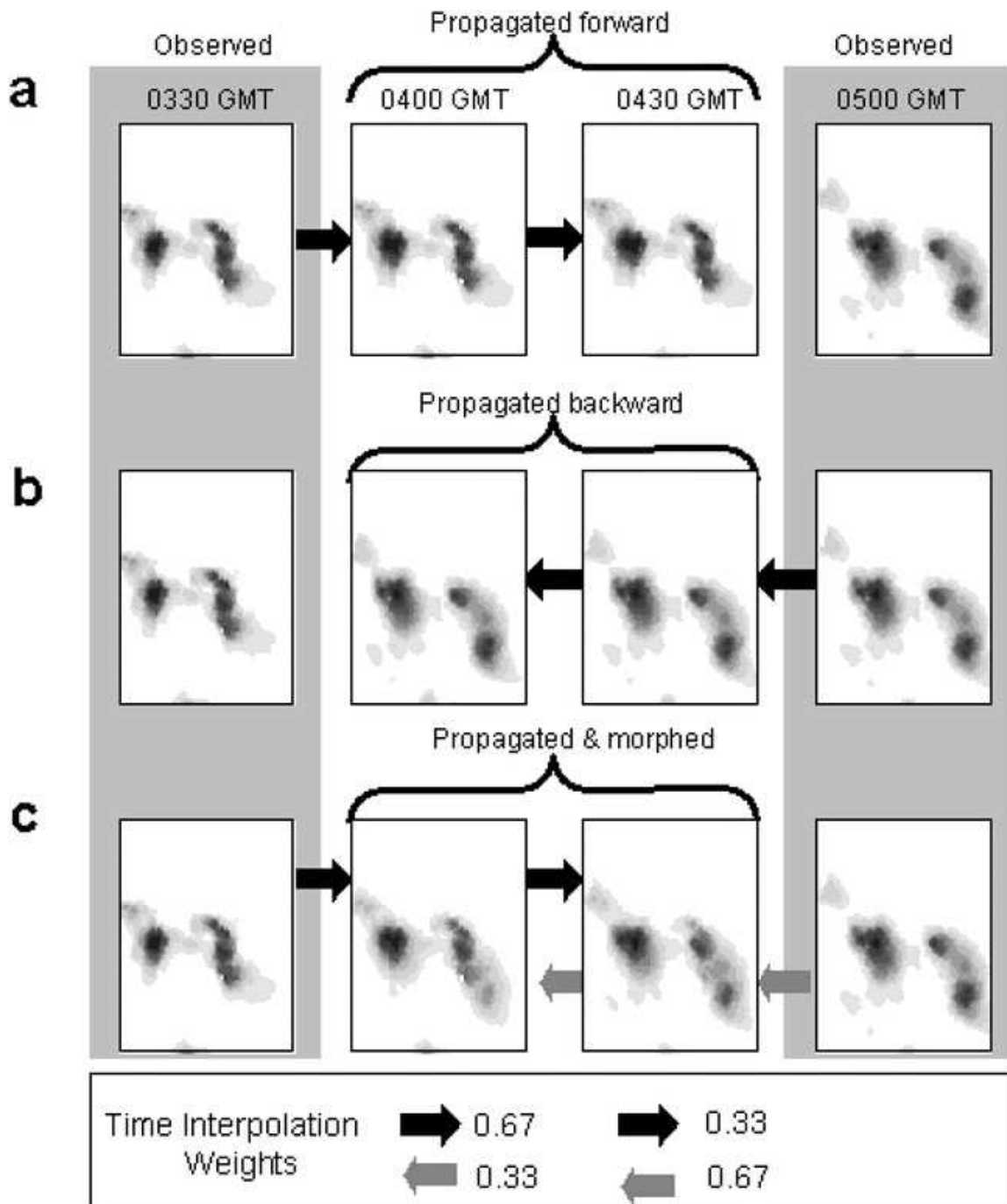


FIGURE 6.5. Illustration of the propagation and morphing process in CMORPH (adopted from Joyce et al. (2004)). The estimates at time frames 03:30 and 05:00UTC are real PMW-based retrievals with no propagation or morphing applied. The estimates at 04:00 and 04:30UTC are (a) forward propagated in time, (b) backward propagated in time, and (c) morphed from propagation in both directions.

$t = 0hr$ that contains observed PMW-based retrievals overwrites the propagated estimates for that time frame. In CMORPH, due to the temporal sampling considerations imposed by the orbital nature of the spacecraft, the backward propagation process must begin at least $5hr$ beyond the current analysis time ($t = 0hr$) in order to have a globally complete field of backward-propagated rainfall field. This is also why there is a 5-hr delay in the operational availability of CMORPH products (Xie et al. 2017). Nevertheless, the results obtained from temporal propagation in both directions in time are improved over a single direction (Joyce et al. 2004). In CMORPH, the propagation of precipitation features will not change the characteristics of those features themselves but will merely translate them to new positions. Changes in the intensity and shape of the PMW-based retrievals are accomplished by inversely weighting both forward- and backward-propagated rainfall fields. The weights are determined by the respective time distances from the current and updated available fields. Again, taking Figure 6.5 as an example, at each grid pixel at time frame $t + 0.5hr$, the estimate is produced by a weighted mean given by:

$$(34) \quad CMORH_{t+0.5hr} = 0.67 \times P_{forward(t+0.5hr)} + 0.33 \times P_{backward(t+0.5hr)}$$

where $P_{forward}$ is the PMW precipitation estimate forward propagated from the initial analysis (03:30UTC), and $P_{backward}$ is the PMW precipitation estimate backward propagated from the updated analysis (05:00 UTC). Similarly, the CMORPH value for the 04:30UTC analysis is computed as follows:

$$(35) \quad CMORH_{t+1hr} = 0.33 \times P_{forward(t+1hr)} + 0.67 \times P_{backward(t+1hr)}$$

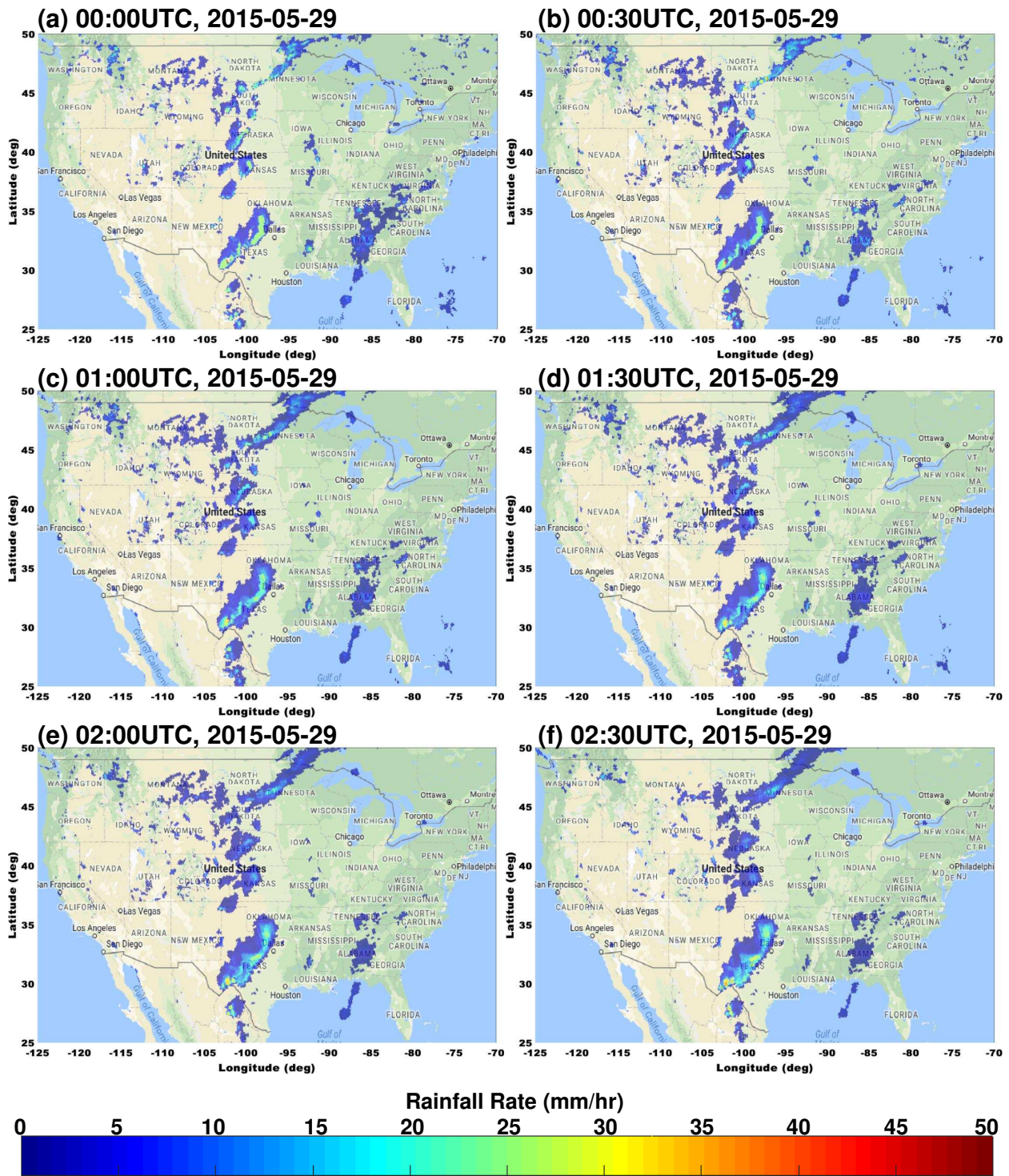


FIGURE 6.6. Sample CMORPH products over the continental U.S. on May 29, 2015. The corresponding PMW and IR data are shown in Figures 6.3 and 6.4, respectively.

Each half-hour estimate and the associated propagation time and satellite information are extracted from this morphing analysis and saved as standard CMORPH products. For illustration purposes, Figure 6.6 shows sample CMORPH products over the continental U.S. on May 29, 2015, for a 3-hr period. The corresponding combined IR data and PMW-based retrievals are shown in Figures 6.4 and 6.3, respectively.

6.2. A MACHINE LEARNING SYSTEM FOR RADAR AND SATELLITE PRECIPITATION

DATA FUSION

6.2.1. BACKGROUND.

As aforementioned, although the ground radar network has usually been used when developing satellite retrieval algorithms or validating the derived precipitation products, the radar data themselves are not used in the operational production of satellite precipitation retrievals. In addition, traditional use of radar in satellite precipitation studies relies on the parametric relations between satellite measurements (e.g., IR data) and radar rainfall estimates. The non-parametric application of radar products in satellite precipitation data fusion is rare to nonexistent. To this end, this study explores the non-parametric approach to satellite precipitation estimation using additional information from ground radar observations. A simplified conceptual diagram is shown in Figure 6.7. This study is also motivated by the rapid development of machine learning techniques in recent years. In particular, the artificial neural network-based deep learning algorithms are extensively investigated and implemented in relation to radar and satellite precipitation data fusion.

Since McCulloch and Pitts (1943) developed the first conceptual model of an artificial neural network in 1943, its application has tremendously expanded over the past few decades. The artificial neural network, which is simply referred to as “neural network” in

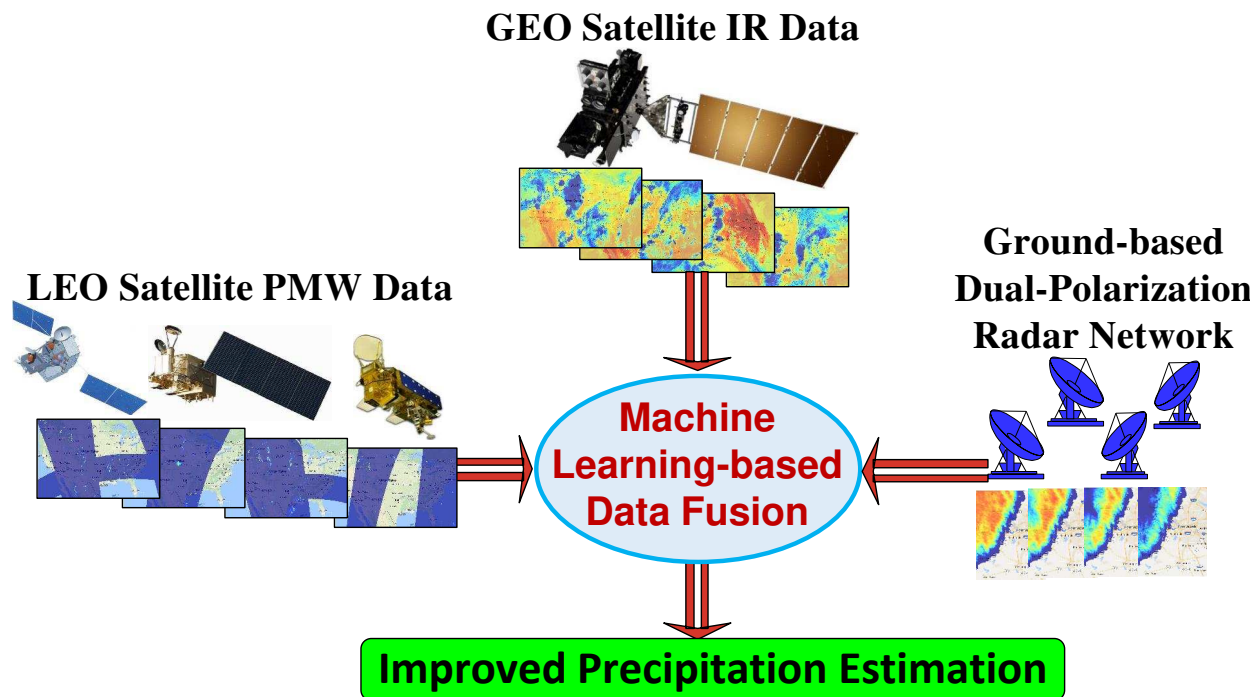
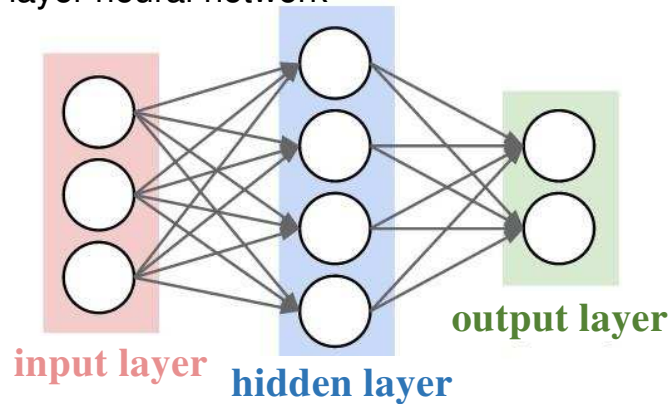


FIGURE 6.7. Simplified diagram of machine learning-based radar and satellite precipitation data fusion.

this study, was designed as a computational model based on the human brain. Nowadays, neural networks are applied in almost every aspect of human life, including research in biology, computer science, geoscience, etc. The neural networks are modelled as collections of neurons that are connected in an acyclic graph. That is, the outputs of some neurons can become inputs to other neurons. Neural network models are often organized into distinct layers of neurons. For regular neural networks, the most common layer type is the fully connected layer in which neurons between two adjacent layers are fully pairwise connected, but neurons within a single layer share no connections. Figure 6.8 illustrates two example neural network topologies that use a stack of fully connected layers. As the fundamental element of a neural network, the artificial neuron is also called a “perceptron”, and takes several inputs and produces a single output. Figure 6.9(a) shows an example perceptron that has n inputs. A simple rule for computing the output is to assign different weights w_1, w_2, \dots, w_n to each input according to the importance of respective inputs to the output. The neuron’s output

(a) A 2-layer neural network



(b) A 3-layer neural network

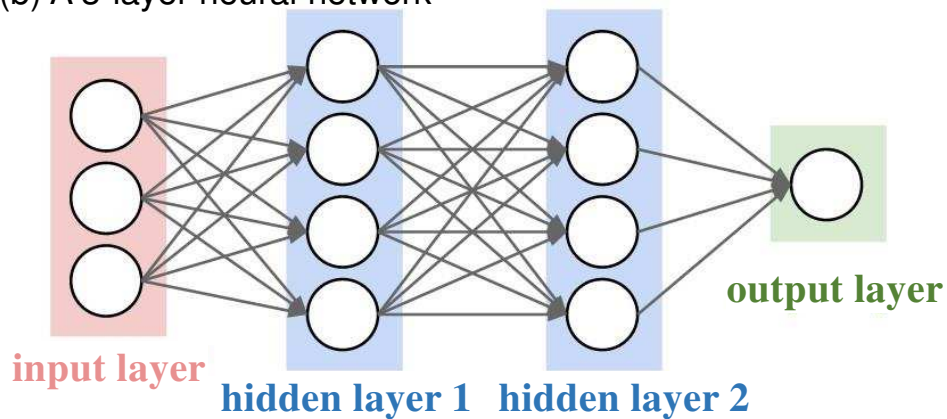


FIGURE 6.8. (a) A 2-layer neural network with three inputs, one hidden layer of 4 neurons, and one output layer with 2 neurons. (b) A 3-layer neural network with three inputs, two hidden layers of 4 neurons each and one output layer. Notice that in both (a) and (b) there are connections between neurons across layers, but not within a layer.

in Equation (36), is determined by whether the weighted sum $\sum_i w_i x_i + b$ is less than or greater than a threshold value. In other words, the perceptron can be considered as a device that makes decisions by weighing the evidence.

$$(36) \quad y = f\left(\sum_{i=1}^n w_i x_i + b_i\right)$$

where x_i is the input element; w_i is the weight assigned to input x_i ; b_i is an error term; f is the activation function; and y is the output.

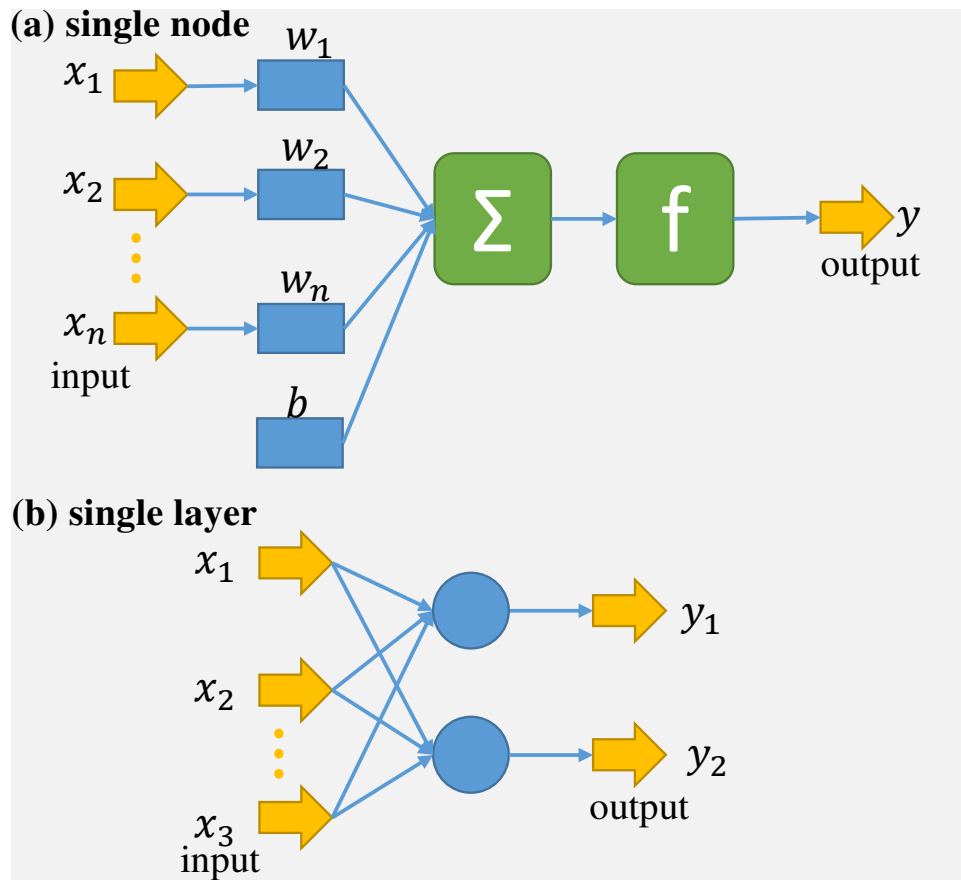


FIGURE 6.9. (a) Example of a perceptron. (b) A single layer with two perceptrons. Each output can be related to the three inputs through the perceptrons.

Traditionally, the activation function is modelled as a sigmoid function $\sigma(x) = \frac{1}{1+e^{-x}}$. The derivative of the sigmoid function is $d\sigma(x)/dx = \sigma(x) * (1 - \sigma(x))$. As shown in Figure 6.10(a), the range of the σ function is between 0 and 1. The maximum of its derivative is equal to 0.25. Obviously, when we have multiple stacked sigmoid layers, by the back propagation derivative rules we get multiple multiplications of $d\sigma(x)/dx$. And as we stack more and more layers the maximum gradient decreases exponentially. This is commonly known as the vanishing gradient problem. The opposite problem is when the gradient is greater than 1, in which case the gradients explode toward infinity (exploding gradient problem).

On the other hand, the rectifier function $f(x) = \max(0, x)$, where x is the input to a neuron, was demonstrated to have more biological and mathematical justifications. It has

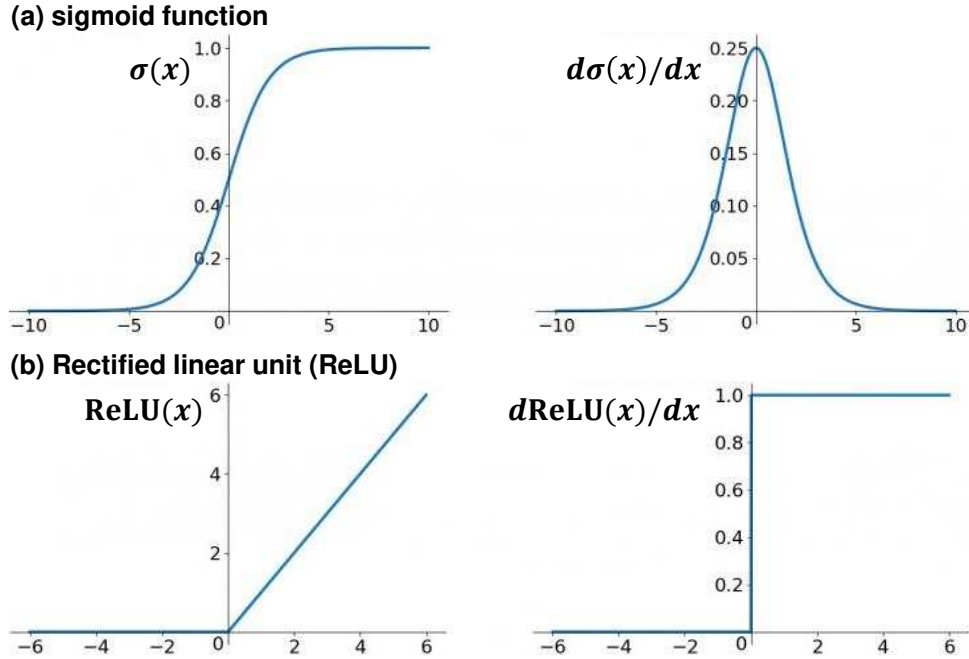


FIGURE 6.10. Activation functions and their derivatives commonly used in neural network. (a) The sigmoid function. (b) The rectified linear unit (ReLU).

been used in neural networks more effectively than the sigmoid function and it is more practical (Nair and Hinton 2010; Glorot et al. 2011). The rectifier linear unit (ReLU) is, as of 2015, the most popular activation function for deep neural networks (LeCun et al. 2015). Figure 6.10(b) illustrates the ReLU function and its derivative. This study applies the ReLU activation function when devising the neural network models for radar and satellite-based precipitation estimation.

It should be noted that when we say N -layer neural network, the input layer is not taken into account. That is, a single-layer neural network describes a network with no hidden layers (input directly mapped to output). Unlike all layers in a neural network, the output layer perceptrons generally do not have an activation function. This is because the last output layer is usually taken to represent the class scores (e.g., in classification), which are arbitrary real-valued numbers, or some kind of real-valued target (e.g., in regression). In addition, the neural networks with two or more layers are also referred to as multi-layer perceptron

(MLP). In the following, a deep MLP (DMLP) model is designed to incorporate radar and satellite observations for precipitation estimation.

6.2.2. ARCHITECTURE OF THE DMLP MODEL FOR RADAR AND SATELLITE PRECIPITATION ESTIMATION.

In this section, the CMORPH technique described in Section 6.1 is referred to extensively. The same input data with CMORPH, including the geostationary satellite IR data and low earth orbit satellite PMW-based precipitation retrievals, are used in the design of the DMLP-based data fusion model. At the same time, ground-based dual-polarization radar observations are used as additional sources in this fusion system. Figure 6.11 illustrates the general idea of developing enhanced precipitation products using the non-parametric MLP methodology. The CMOPRH strategy is also included in Figure 6.11 in order to emphasize the novelty of this study.

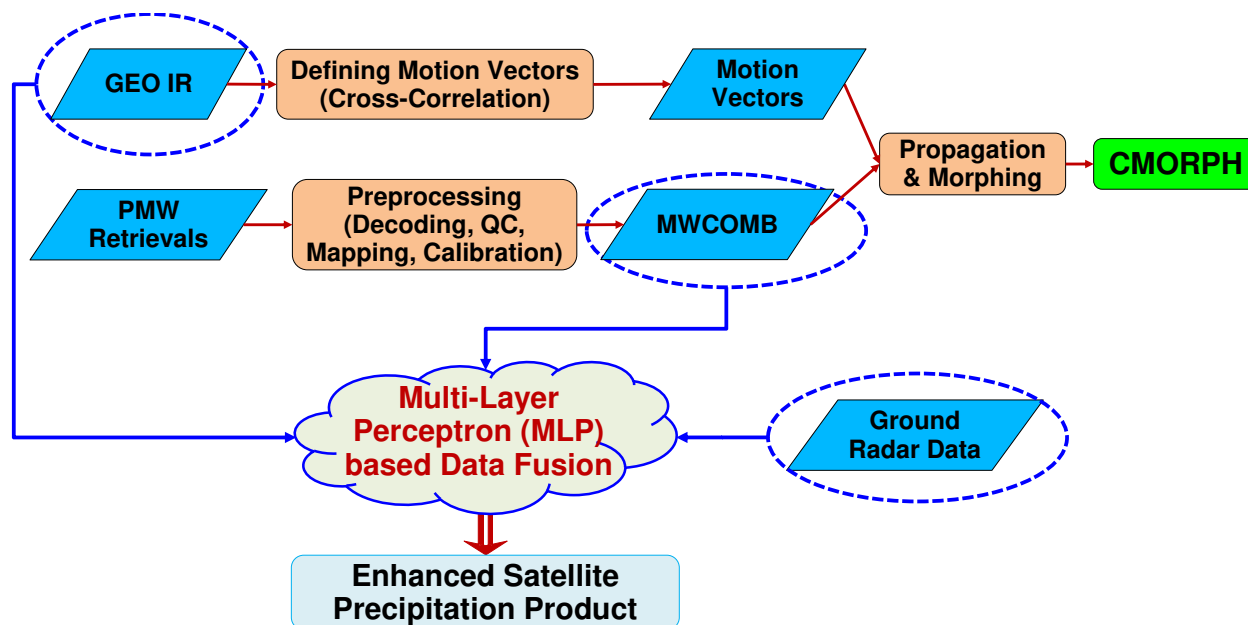


FIGURE 6.11. Generic concept of the application of DMLP model in producing enhanced precipitation products using radar and satellite data.

Compared to a traditional neural network, the deep learning concept (DMLP model) applied here is also a branch of machine learning. The DMLP model attempts to conduct high-level abstractions in the data through using a deep graph with multiple processing layers. It is commonly used in fields such as image processing, automatic speech recognition, natural language processing, and audio recognition.

Figure 6.12 shows a detailed framework of the DMLP model in the context of precipitation estimation. The input data includes PMW sensor measurements and IR data collected from satellites as well as the scan time information of the IR and PMW sensors. The ground radar measurements are used to derive high-resolution rainfall products that are used as training labels for this DMLP model.

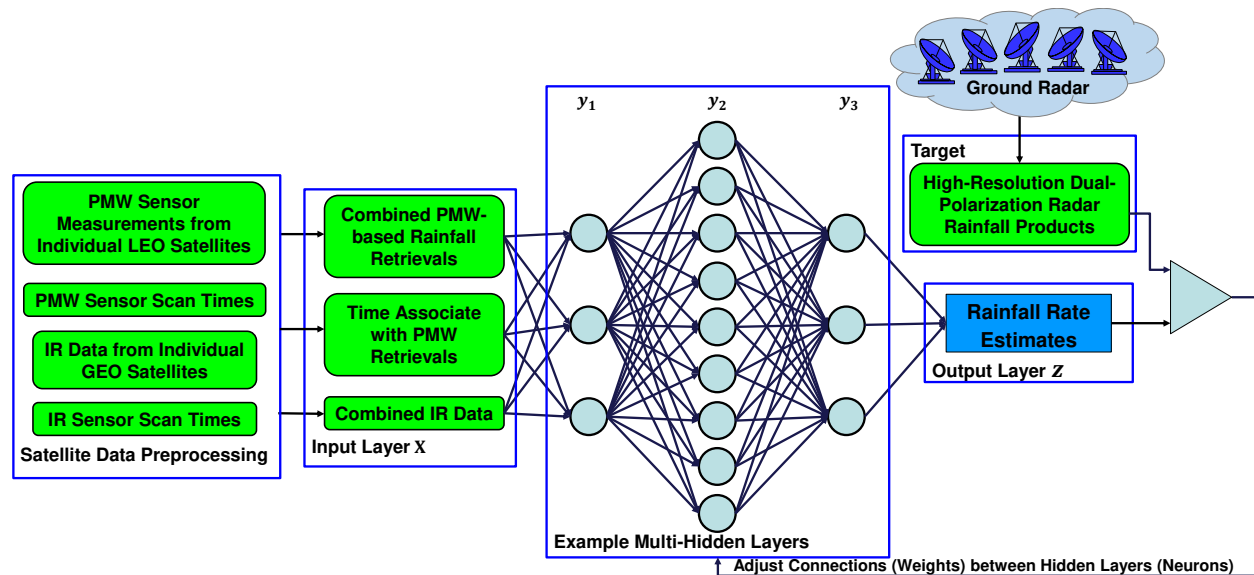


FIGURE 6.12. (a) Overall architecture of the DMLP Model for radar and satellite precipitation estimation.

With the IR data and PMW retrievals from individual satellites, the CMORPH technique is implemented first to obtain combined global IR data (~ 4 km resolution) and PMW-based precipitation estimates (~ 8 km resolution). The combined satellite data and retrievals, along with the associated time of the PMW-based retrievals, serve as the input to the DMLP model.

The input data are denoted by input layer vector \mathbf{x} :

$$(37) \quad \mathbf{x} = [x_1, x_2, x_3]$$

where x_1 represents the PMW-based precipitation retrieval, x_2 represents the time frames when the PMW scans are available, and x_3 represents the combined IR data that are remapped to the PMW retrieval grid resolutions.

Taking the DMLP model in Figure 6.12 as an example, the output \mathbf{z} can be related to the input data \mathbf{x} through the following equations:

$$(38a) \quad \mathbf{y}_1 = f_1(\mathbf{w}_1\mathbf{x} + \mathbf{b}_1)$$

$$(38b) \quad \mathbf{y}_2 = f_2(\mathbf{w}_2\mathbf{y}_1 + \mathbf{b}_2)$$

$$(38c) \quad \mathbf{y}_3 = f_3(\mathbf{w}_3\mathbf{y}_2 + \mathbf{b}_3)$$

$$(38d) \quad \mathbf{z} = f_4(\mathbf{w}_4\mathbf{y}_3 + \mathbf{b}_4)$$

where \mathbf{y}_1 , \mathbf{y}_2 , and \mathbf{y}_3 are the intermediate outputs in the three hidden layers from left to right, respectively; \mathbf{w}_1 , \mathbf{w}_2 , \mathbf{w}_3 , and \mathbf{w}_4 are the weights associated with the input layer and three hidden layers from left to right, respectively (the weights will be updated in the model training and optimization process); \mathbf{b}_1 , \mathbf{b}_2 , \mathbf{b}_3 , and \mathbf{b}_4 are the bias vectors at the input layer and three hidden layers from left to right, respectively; f_1 , f_2 , f_3 , f_4 are the activation functions at different layers. All the activation functions are modelled as ReLU (see Figure

6.10(b)). \mathbf{z} is the derived precipitation field. Equation (38) can also be expressed as:

$$(39) \quad \mathbf{z} = f_4(\mathbf{w}_4 f_3(\mathbf{w}_3 f_2(\mathbf{w}_2 f_1(\mathbf{w}_1 \mathbf{x} + \mathbf{b}_1) + \mathbf{b}_2) + \mathbf{b}_3) + \mathbf{b}_4)$$

which directly relates the derived precipitation field to the input satellite data.

In the model training, the high-resolution rainfall products from a ground radar or radar network will serve as labels (targets). The ground radar products can be derived using any radar or radar network provided that the coverage domain and resolution match the input satellite data coverage domain. In Section 6.3, an urban-scale application of this DMLP model over the DFW metroplex will be detailed, where the high-quality rainfall products from the CASA DFW dense urban radar network QPE system are used as training targets.

However, it should be noted that the three hidden layers in Figure 6.12 are only used for illustration purposes. In reality, the hyper parameters, including the number of hidden layers and the number of perceptrons (nodes) in each layer, are determined using the strategy described below.

6.2.3. MODEL OPTIMIZATION AND HYPERPARAMETER SETTING.

Model Optimization: For the DMLP model with given numbers of layers and nodes, the gradient descent approach is applied to find the optimal solution. Figure 6.13 illustrates the model optimization process. Essentially, the optimization includes forward propagation for estimation and backward propagation for error optimization (or changing weights). The weights are updated with:

$$(40) \quad w_{i,j(new)} = w_{i,j(old)} - \rho \frac{\partial E}{\partial w_{i,j(old)}}$$

where E is the error function, also known as cost function. ρ is the learning rate; $w_{i,j}$ are the weights to be updated in the model optimization. In this study, the mean square error of satellite precipitation estimates with respect to ground radar rainfall estimates is used as cost function E .

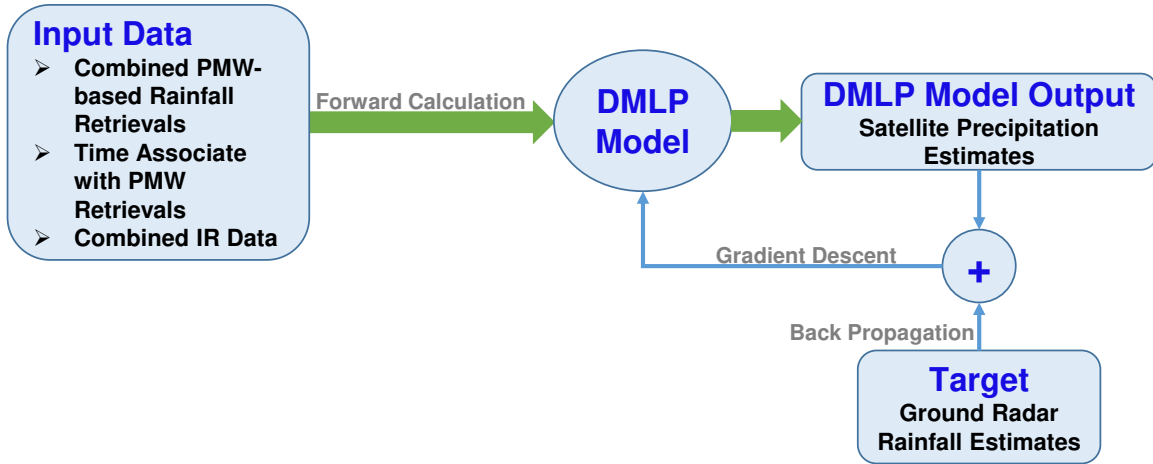


FIGURE 6.13. DMLP model optimization for radar and satellite rainfall estimation.

The model is optimized through the following four steps:

- 1) Forward Calculation: calculate the hidden node outputs \mathbf{y}_i and precipitation estimate \mathbf{z} for given input satellite data \mathbf{x} ;
- 2) Cost Function: calculate the mean square error E of \mathbf{z} using target label \mathbf{z}^* ;
- 3) Backward Propagation: compute the gradient $\frac{\partial E}{\partial w_{i,j}}$ using error E and outputs \mathbf{y}_i and \mathbf{z} ;
- 4) Gradient Descent: calculate the updated weights $w_{i,j}$ using the gradient from step 3).

It should be mentioned that the learning rate ρ must be set to an appropriate value to make sure the gradient descent will work. The learning rate determines how quickly or slowly we will move toward the optimal weights. In addition, the learning rate should satisfy the

condition of being less than $2/\lambda_{min}$ to guarantee convergence to the point of local minimum, where λ_{min} is the minimum eigenvalue of the input covariance matrix.

In real implementations, this study attempts to improve the computational efficiency with the aid of the open source machine learning software library TensorFlow developed by Google. TensorFlow is essentially an interface, or a platform for machine intelligence (Abadi and Coauthors 2015). It is commonly used for developing various machine learning algorithms. At this point, the second-generation TensorFlow is available for the implementation and deployment of large-scale MLP models. TensorFlow takes computations described using a dataflow-like model and maps them onto a wide variety of different hardware platforms. Traditionally, separate systems for large-scale training and small-scale deployment have been used, leading to significant maintenance burdens and leaky abstractions. With the TensorFlow platform, one can span a broad range of systems; it significantly simplifies the real-world use of neural network systems. TensorFlow computations are expressed as stateful dataflow graphs and the system is made both flexible enough for quickly experimenting with new models for research purposes and sufficiently high performance, and robust enough for production training and deployment of machine-learning models. A TensorFlow computation is described by a directed graph, which is composed of a set of nodes. Again, taking the DMLP model in Figure 6.12 as an example, the computation graph will consider $3 \times 9 \times 3$ nodes for the three hidden layers with, respectively, three, nine and three neurons. The graph represents a dataflow computation, with extensions for allowing some kinds of nodes to maintain and update persistent states and for branching and looping control structures within the graph (Abadi and Coauthors 2015). Overall, the TensorFlow is a flexible data

flow-based programming model. The system was born from real-world experience in conducting research. For more details, interested readers are referred to Abadi and Coauthors (2015).

This study constructs the computational graph in the proposed DMLP model using Python. Figure 6.14 shows an example fragment to construct and then execute a TensorFlow graph using the Python front end. The resulting computation graph is also illustrated in Figure 6.14.

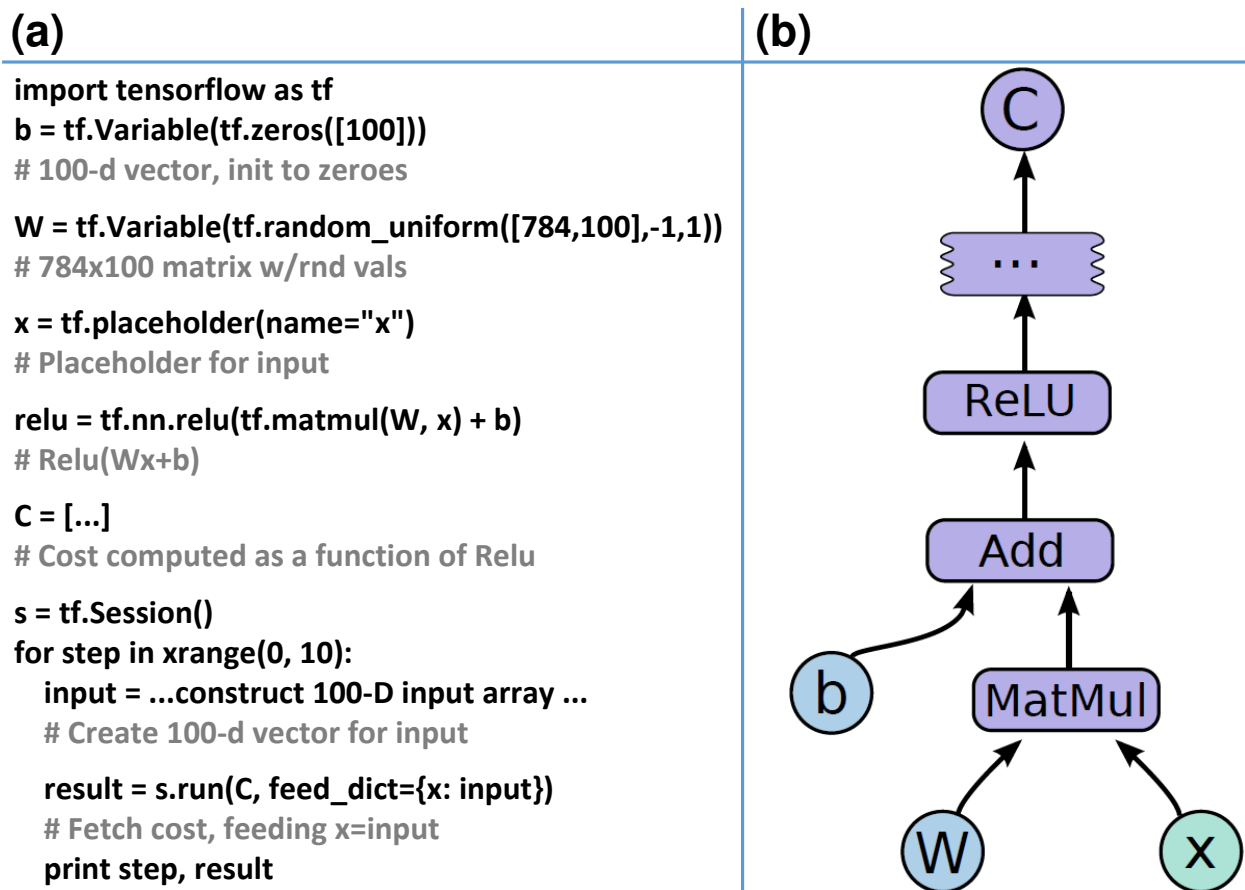


FIGURE 6.14. (a) Example TensorFlow code fragment. (b) Computation graph for (a).

Hyperparameter Setting: Determination of the hyper parameters in the DMLP model is one of the main efforts in this study. The number of hidden layers and the number of perceptrons for each layer should be investigated in order to produce reliable precipitation

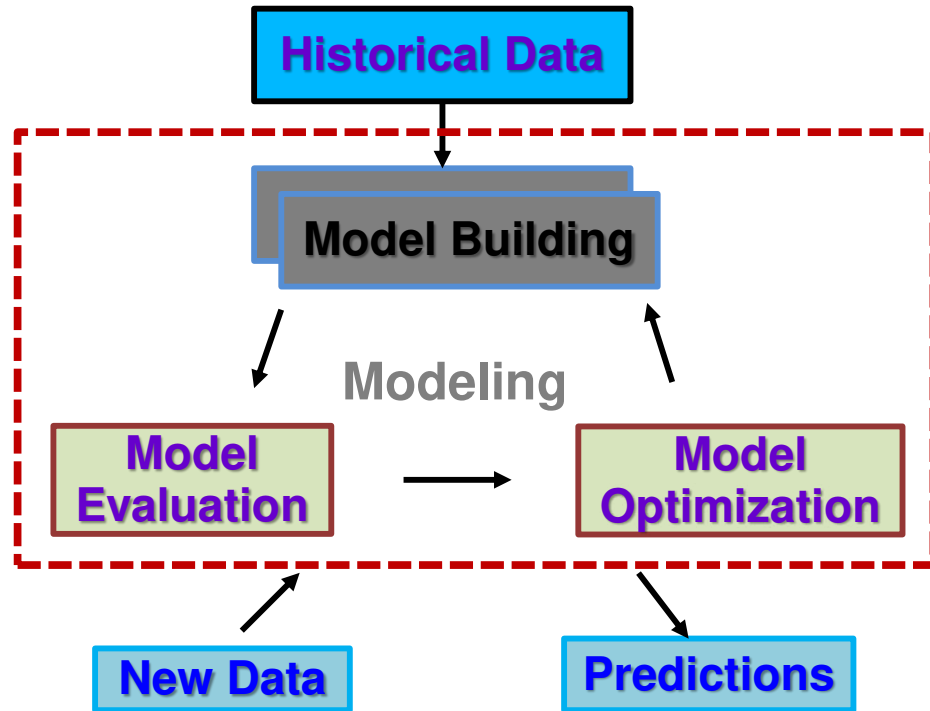
estimates for a given set of radar and satellite data. As aforementioned, for a given set of hyper parameters, the DMLP model can be optimized using gradient descent. Here it is worth noting that even for the same hyper parameters, the DMLP model is updated every now and then provided that new data are available to be included in the training dataset. Figure 6.15(a) shows a conceptual diagram of the update of the DMLP model. In particular, when new satellite and radar data are available, the optimized DMLP model will be re-evaluated and optimized again.

For the hyper parameter setting, this study applies a grid approach. A large number of combinations of different learning rates, number of perceptrons, and number of hidden layers are predefined. Each combination will be trained and tested using ground radar-derived products, and the hyper parameters resulting in the best satellite precipitation performance will be used. Figure 6.15 shows some examples of the pre-defined hyper parameters. In the following, a detailed implementation of the designed DMLP-based data fusion framework over the DFW Metroplex will be given.

6.3. URBAN SCALE APPLICATION OF THE PROPOSED MACHINE LEARNING SYSTEM

As presented in Chapter 5, a high-resolution radar quantitative precipitation system was developed for the CASA DFW dense urban radar network. Comparison between the CASA DFW radar rainfall products and rain gauge observations has demonstrated the excellent performance of this ground radar network. The QPE products from the DFW radar network serve as input to distributed hydrologic models for flash flood warning operations. The DFW QPE products are also used to validate various satellite precipitation estimates, especially the instantaneous rainfall rate products (Chen and Chandrasekar 2016).

(a) Model update for given hyper parameters



(b) Examples of hyper parameters

Learning Rate	Number of Nodes; Number of Layers			
1e-3	1; 40	2; (9, 3)	3; (3, 9, 3)	2; (4, 2)
1e-4	1; 40	2; (9, 3)	3; (3, 9, 3)	2; (4, 2)
1e-5	1; 40	2; (9, 3)	3; (3, 9, 3)	2; (4, 2)
...

FIGURE 6.15. (a) DMLP model update when new training data are available. This is specially for given hyper parameters. (b) Grid approach to the selection of hyper parameters.

In this section, the high-performance rainfall products from the DFW urban radar network are used as target labels to train the proposed DMLP model. In particular, the domain of 96.3°W-98°W longitude, 31.8°N-33.47°N latitude is selected for demonstration purposes. The area of study domain is 200 km×192 km. The PMW and IR measurements used in

CMORPH are used as input to the DMLP model. Note again that the PMW data are obtained from 16 low earth orbit satellites, and the IR data are obtained from five geostationary satellites (see Section 6.1 for details). The CMORPH techniques are implemented first to get combined PMW and IR data. Figure 6.16 illustrates the DMLP model for the DFW domain.

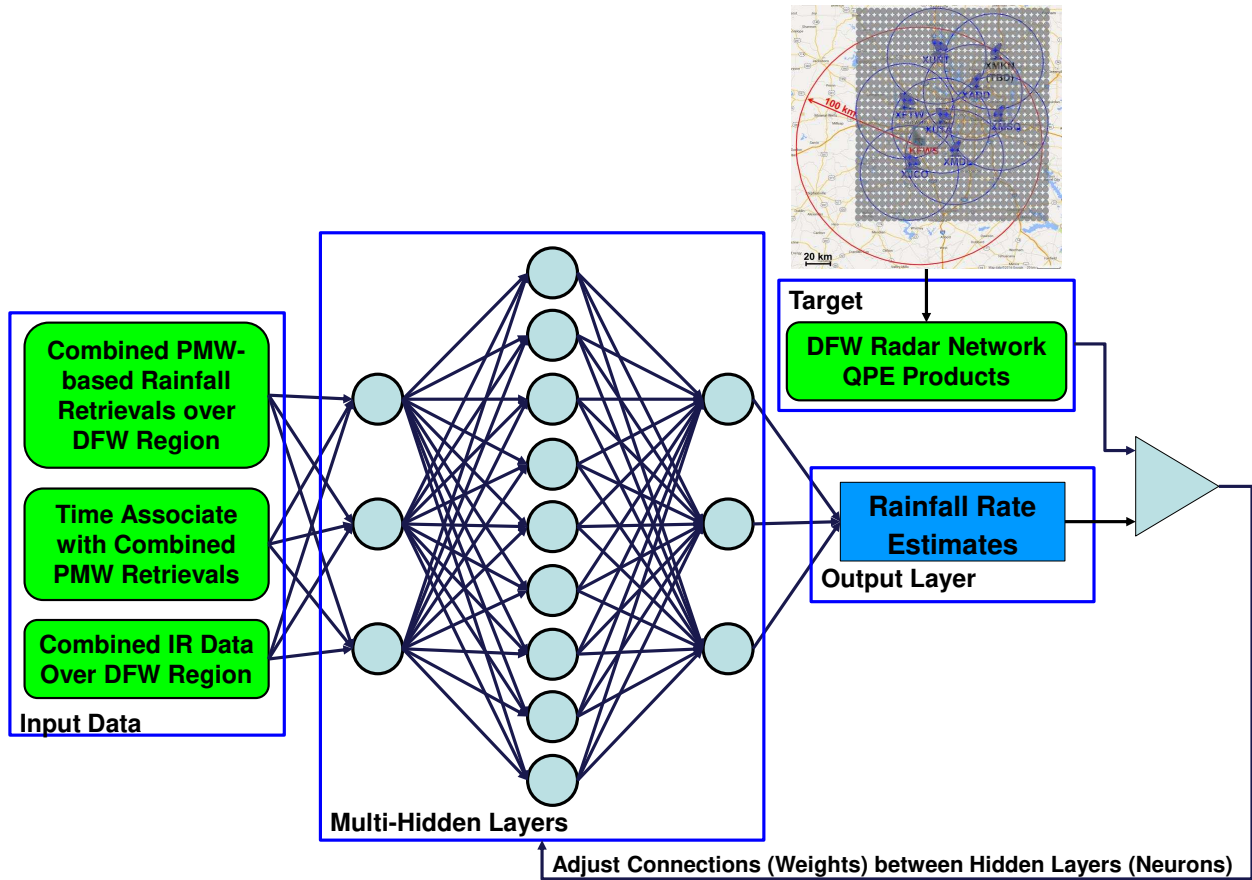


FIGURE 6.16. Urban scale application of the deep multi-layer perceptron (DMLP) model for rainfall estimation over DFW Metroplex.

In this study domain, there are 25×24 grid pixels of PMW-based precipitation retrievals with spatial resolution ~ 8 km, whereas there are 50×48 grid pixels of combined IR data with spatial resolution ~ 4 km. Both IR and PMW data have a temporal resolution of 30 mins. Similar to CMORPH, the spatio-temporal resolution of $8 \text{ km} \times 8 \text{ km} \times 30 \text{ min}$ is used to derived final precipitation products.

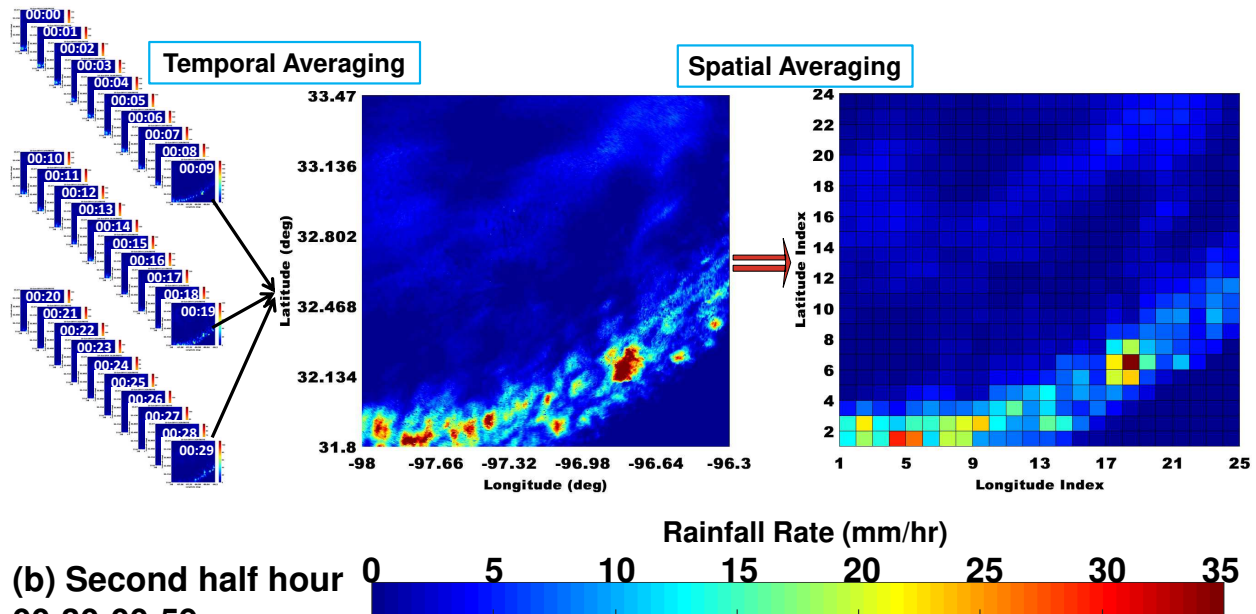
For the high-resolution DFW radar rainfall products, both spatial and temporal averaging are applied. Figure 6.18 illustrates the temporal and spatial averaging of the high-resolution DFW radar rainfall products to match satellite PMW-based precipitation retrievals. The resolution of the ground radar rainfall products is $250 \text{ m} \times 250 \text{ m} \times 1 \text{ min}$. Temporally, 30 frames of DFW radar products from 00-29 mins of each hour are averaged for the first half-hour window, and 30 frames from 30-59 mins are averaged for the second half-hour window. Spatially, 32×32 high-resolution rainfall pixels are averaged to get rainfall estimates matching the $8 \text{ km} \times 8 \text{ km}$ grid.

It should be noted that the linear averaging is applied here only for purposes of simplicity. More complicated and efficient methods need to be investigated in future studies. In addition, although the PMW-based precipitation retrievals are produced every half hour, the retrievals themselves are essentially instantaneous rainfall rates at a certain time within that half-hour window. In other words, the PMW-based retrievals are not the mean of rainfall rates across the half-hour window. However, the processed ground radar products stand for the mean of rainfall rate field for a given half-hour window. The biases introduced by such mismatching are beyond of the scope of this study, but should be researched in future.

Compared to CMORPH, which uses the cloud motion vector derived from IR data to propagate PMW-based retrievals, this study does not apply the motion vector propagation. Instead, a time vector associated with PMW-based retrievals is created and used as a key input to the DMLP model. If the PMW data are available for a given time frame, the time value is assigned with zero, whereas if there are no PMW data available for that time frame the closest (in time) observations are used and the time difference is assigned as the time value.

(a) First half hour

00:00-00:29



(b) Second half hour

00:30-00:59

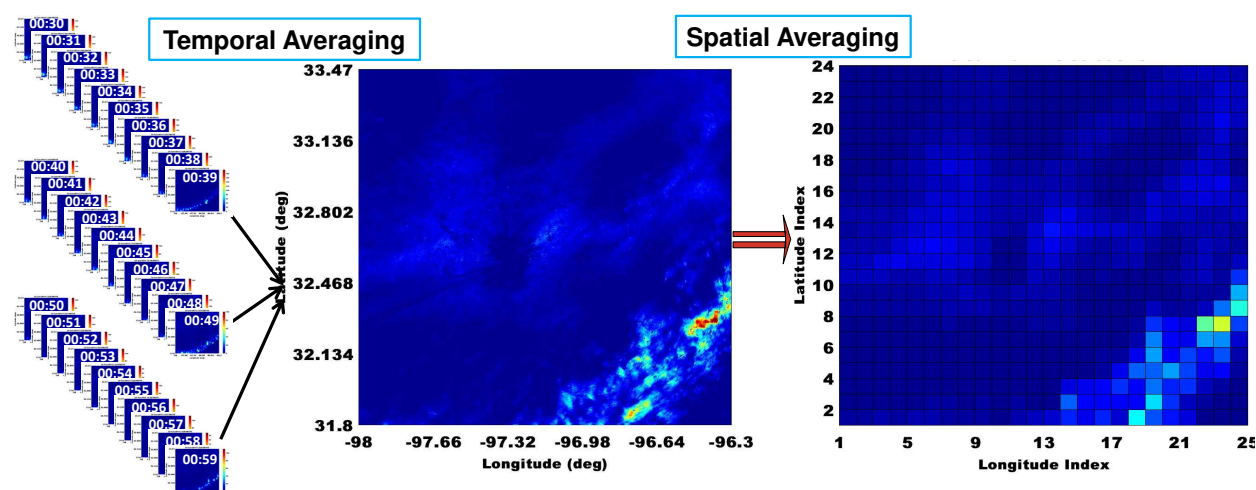


FIGURE 6.18. Temporal and spatial averaging of high-resolution DFW radar rainfall products to match satellite PMW-based precipitation retrievals. Temporally, 30 frames of DFW radar products from 00-29 mins of each hour are averaged for the first half hour window (a), and 30 frames from 30-59 mins are averaged for the second half hour window (b). Spatially, 250m \times 250m high-resolution rainfall products are averaged to 8km \times 8km grid.

6.3.2. MODEL TRAINING.

In order to train the DMLP model for urban-scale applications, 15 precipitation events that occurred in 2013, 2014, and 2015 are taken into account. Among the 15 events, 12 are used

TABLE 6.4. Training and testing events for developing the machine learning-based system merging satellite and ground radar rainfall observations.

Precipitation Cases	Categories
2013-04-17 00 to 2013-04-20 00UTC	Training
2013-05-15 00 to 2013-05-18 00UTC	Training
2013-10-26 00 to 2013-10-29 00UTC	Training
2014-07-16 00 to 2014-07-20 00UTC	Training
2015-03-17 00 to 2015-03-20 00UTC	Training
2015-04-01 00 to 2015-04-04 00UTC	Training
2015-04-08 00 to 2015-04-15 00UTC	Training
2015-05-10 00 to 2015-05-13 00UTC	Training
2015-05-28 00 to 2015-05-31 00UTC	Training
2015-06-16 00 to 2015-06-20 00UTC	Training
2015-11-25 00 to 2015-11-29 00UTC	Training
2015-12-25 00 to 2015-12-29 00UTC	Training
2013-06-08 00 to 2013-06-11 00UTC	Testing
2014-06-23 00 to 2014-06-27 00UTC	Testing
2015-05-28 00 to 2015-05-31 00UTC	Testing

as training cases, while the other 3 are used as testing cases. Table 6.4 lists the events used for training and testing purposes. It should be noted that the selection of training and testing cases is random. In total, the training dataset include 960 hours of data (i.e., 1920 half-hour frames). All the input data, including satellite PMW-based rainfall estimates, IR, and time vectors associated with PMW observations are put on 25×24 grids covering the DFW metroplex. The total number of grid points in the training data is about 1.15 million.

The DFW radar network-based rainfall products are generated for the 15 events listed in Table 6.4. Among them, the products for the training events are used as training labels in the DMLP model. The products for the testing events are used to test the trained model. That is, after training the DMLP model, satellite data (DMLP inputs) for the testing events are processed with the trained DMLP model to produce estimated rainfall fields. The estimated rainfall products based on satellite data will be compared with the testing data products from the DFW radar network.

The methodologies detailed in Section 6.2 are implemented to configure the hyper parameters in the DMLP model and optimize the model for selected hyper parameters. It is concluded that the three hidden layers with three, nine, and three perceptrons, respectively, can render the best results for the 13 testing events. This is also why such hyper parameters are used as examples in Figure 6.16.

6.3.3. PRELIMINARY RESULTS AND PERFORMANCE EVALUATION.

The DMLP model trained with radar and satellite data collected during 12 precipitation events was tested using the 3 independent validation cases. Figure 6.19(b) shows the rainfall estimates with the trained DMLP model using satellite PMW and IR data collected for the validation event of June 24, 2014. For comparison purpose, Figure 6.19(a) illustrates the rainfall products from the DFW radar network and the combined PMW-based rainfall retrievals and CMORPH products are shown in Figure 6.19(c) and (d).

Similarly, Figure 6.20 show the results for another half-hour frame on June 24, 2014, at 23:00UTC. For reference, Figure 6.20 also includes the high-resolution rainfall product from the DFW radar network and the combined IR data information observed at this time frame. The results for other validation events are not given since essentially they show similar performance with the results shown in Figures 6.19 and 6.20. Based on the comparison between the rainfall products shown in Figures 6.19 and 6.20, it is concluded that the products from the designed DMLP model can capture the precipitation pattern fairly well. In order to further demonstrate the performance of the DMLP-based data fusion model for radar and satellite precipitation estimation, rainfall estimates generated for the test events (see Table 6.4) are also used for quantitative evaluation. Here, the ground radar-based rainfall products (after averaging) are used as references in the validation. The normalized standard errors (NSE_{rain}) of combined PMW-based retrievals, CMORPH products, as well as the rainfall

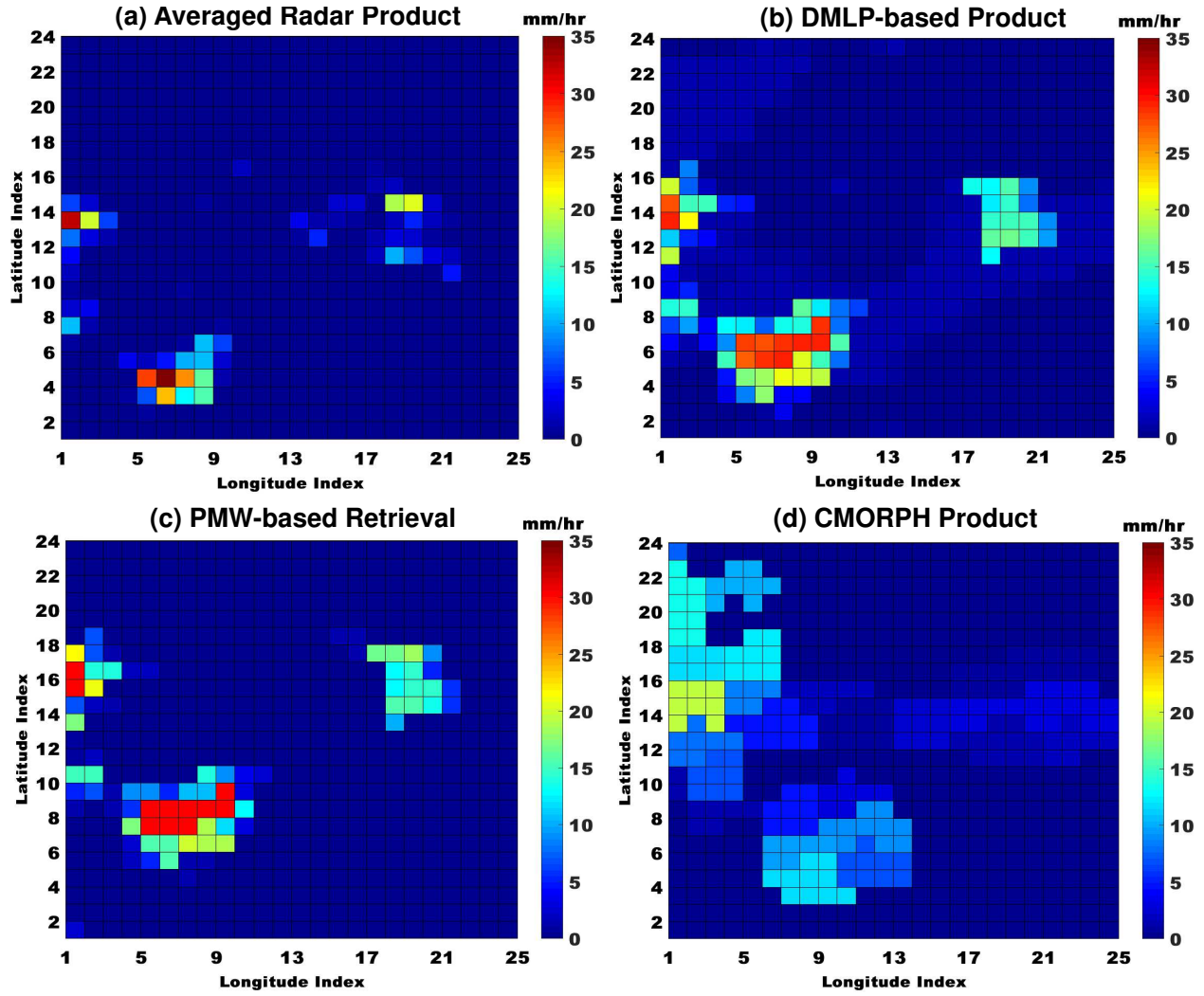


FIGURE 6.19. Cross-comparison of various rainfall products on June 24, 2014, at 20:00UTC. (a) DFW radar network rainfall estimates (after averaging); (b) rainfall estimates from the DMLP model; (c) combined PMW-based rainfall retrieval; (d) CMORPH products.

products derived using the DMLP model, defined below, are computed.

$$(41) \quad NSE_{rain} = \frac{|E_R - R_R|}{R_R}$$

where E_R is the number of rainy pixels in the PMW-based retrievals, CMORPH or DMLP products; R_R is the number of rainy pixels from ground radar rainfall estimates. Here, it is

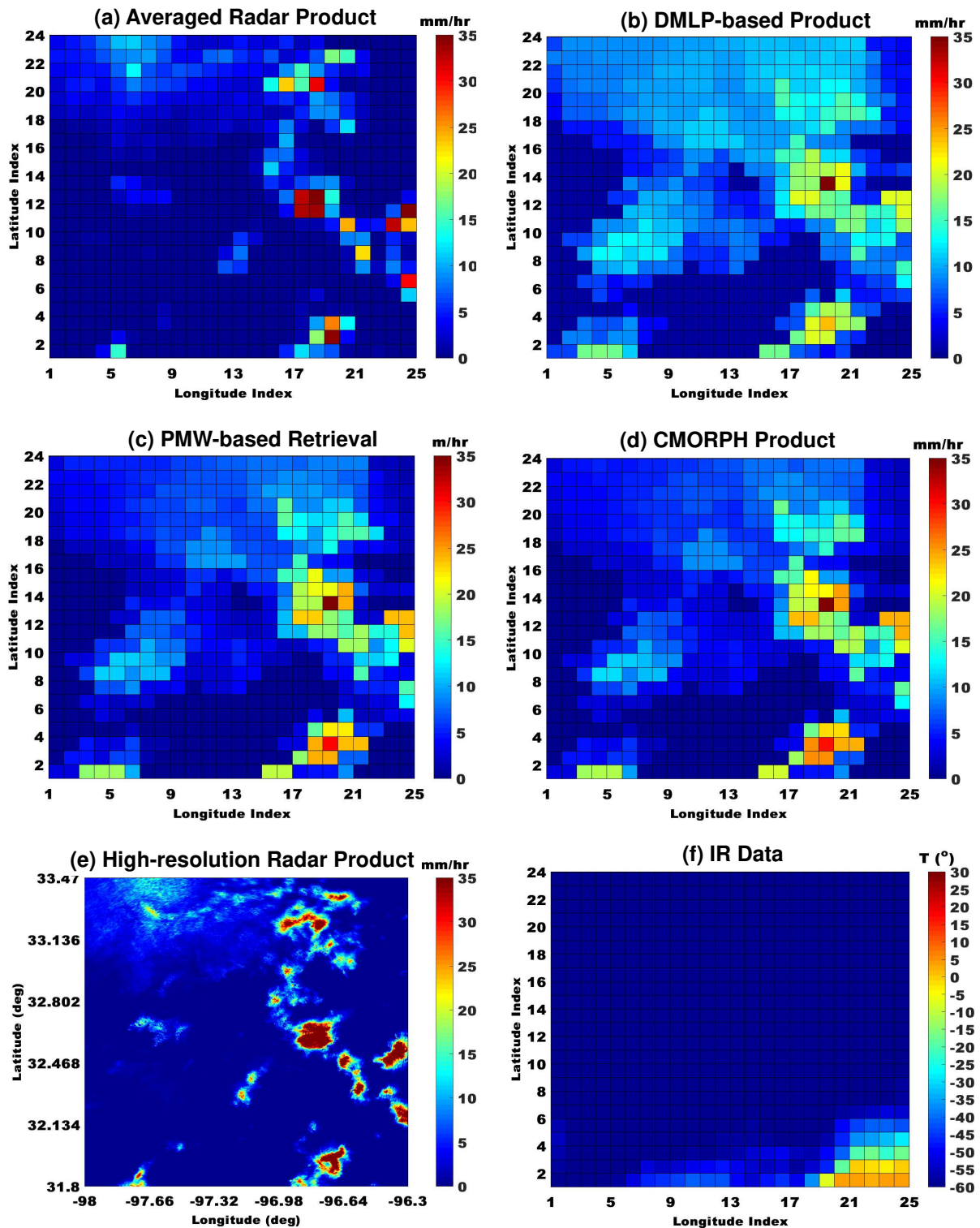


FIGURE 6.20. Cross-comparison of various rainfall products at 23:00UTC, June 24, 2014. (a) DFW radar network rainfall estimates (after averaging); (b) rainfall estimates from the DMLP model; (c) combined PMW-based rainfall retrieval; (d) CMORPH products; (e) high resolution rainfall product from DFW radar network (before averaging); (f) corresponding IR data.

TABLE 6.5. Evaluation results of the CMORPH, DMLP, and combined PMW-based rainfall estimates for the time frame of 20:00UTC, June 24, 2014

	DFW Radar Network	Combined PMW	CMORPH	DMLP
Threshold of 0.5 mm/hr Applied				
E_R	71	82	216	79
NSE_{rain}	-	15.5%	204.2%	11.3%
Threshold of 1 mm/hr Applied				
E_R	57	80	186	78
NSE_{rain}	-	40.3%	226.3%	36.8%

worth mentioning again that R_R for the test events is not used in the DMLP model training process. In other words, R_R is independent from E_R .

Table 6.4 shows the evaluation results of the CMORPH, DMLP, and combined PMW-based rainfall products derived for the time frame of 20:00UTC, June 24, 2014. Obviously, the DMLP model has very good performance in detecting rainfall compared to PMW-only based rainfall retrieval or PMW and IR combined estimates in CMORPH. Nevertheless, it should be noted that this study will not conduct a more quantitative validation since the rainfall rates from ground radar represent an average over half-hour window, whereas the PMW-based retrievals or CMORPH products represent instantaneous rainfall rates sampled within the half-hour window. The temporal mismatching may introduce additional errors in the quantitative analysis.

In addition, the probability distribution function (PDF) of rainfall rates estimated using different techniques is investigated. For illustration purposes, Figure 6.21 shows the PDF for rainfall products derived for the time frame of 23:00UTC, June 24, 2014. Although more case studies are needed, the preliminary results based on the DMLP model are quite promising. In particular, this non-parametric machine learning approach can capture low rainfall rates better than CMORPH or the PMW-based products.

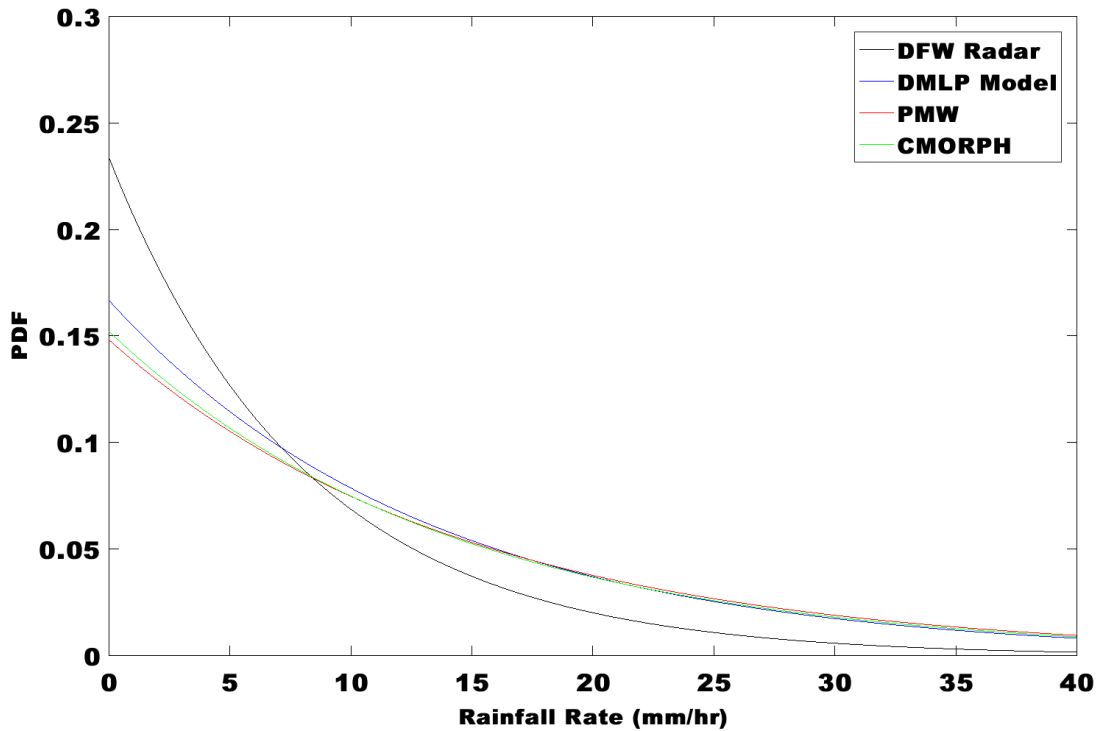


FIGURE 6.21. Probability distribution of rainfall rate estimates from the DFW radar network, PMW measurements, CMORPH, and the DMLP model developed in this study. Results show that the DMLP model-based products capture low rainfall rates better than CMORPH or the PMW-only based products. The products presented here are for the time frame of 23:00UTC, June 24, 2014.

6.4. SUMMARY

Space-based precipitation products are commonly used for regional and/or global hydrologic modelling and climate studies. However, the accuracy of onboard satellite measurements is limited due to spatial-temporal sampling limitations, especially for extreme events such as very heavy or light rain. On the other hand, ground-based radar is a more mature science related to quantitative precipitation estimation (QPE). Presently, ground radars are critical for providing local-scale rainfall estimations for operational forecasters to issue watches and warnings, as well as validation of various space measurements and products. In this chapter, a review of the NOAA CMORPH technique and products has been

given purely based on satellite measurements. In addition, this paper introduces a neural network-based data fusion mechanism to improve satellite-based precipitation retrievals by incorporating dual-polarization measurements from ground-based radar network. The prototype architecture of this fusion system has been detailed. Results from urban-scale application in the DFW metroplex are presented. Comparison with existing PMW-based retrievals and CMORPH product shows the promising performance of the machine learning model designed in this study.

CHAPTER 7

SUMMARY, CONCLUSIONS AND FUTURE WORK

7.1. SUMMARY AND CONCLUSIONS

The measurement of precipitation is an important issue that has been pursued since the earliest time in civilization. Currently, numerous types of infrastructure have been deployed to directly or indirectly measure rainfall rate and amounts, such as rainfall gauges, weather radars, and satellites. Rain gauges can directly measure rainfall at point locations. However, deploying and maintaining a large number of rain gauges to observe the complex spatial and temporal variability of precipitation processes is an extensive and expensive task. In addition, it is challenging to use rain gauges to accurately measure light rain due to the sampling limitations of the gauges. For example, for a gauge with bucket volume resolution of 0.254 mm (or 0.1 inch), it may take too long to get one tip in light rain. Satellites provide good coverage over the globe, and the resulting information plays an important role in understanding global climate and water cycles. However, the space time resolution of precipitation products based on satellite observations is very coarse because of the large footprint of satellite instruments. Compared to rain gauges and satellites, radar has shown great advantages in conducting spatially continuous observations over a large area with small temporal sampling intervals. Currently, long-range microwave (e.g., S- or C-band) radar networks are considered an integral part of the weather sensing and forecasting infrastructure by many nations. In particular, the dual-polarization upgrade of the U.S. operational weather radar network (WSR-88DP) offers a number of advantages for rainfall estimation compared to single-polarization by gleaning more information about precipitation microphysics and raindrop size distribution.

However, it is well known that one limitation of today's operational weather radars is the inability to cover the lower part of atmosphere due to the earth's curvature and terrain blockage. The S-band WSR-88DP radars are spaced about 230 km apart in the eastern U.S. and 345 km apart in the western U.S. At the maximum coverage range of 230 km, the lowest (0.5 degree) beam is about 5.4km above ground level (AGL). As a result, many fine-scale weather features in the lower atmosphere such as tornadoes and flash floods cannot be observed. In order to overcome the coverage and resolution limitations of WSR-88DP, the National Science Foundation Engineering Center for CASA has been dedicated to enhancing the ability to observe, understand, predict, and respond to hazardous weather events using a dense network of small, low-power X-band dual-polarization radars that can sense the lower atmosphere. These smaller and less expensive radars can serve as gap fillers for the WSR-88DP network by providing enhanced sampling of precipitation and winds near the ground. Since 2012, CASA, in collaboration with the NWS and the North Central Texas Council of Governments (NCTCOG), has operated a dense urban X-band radar network in the DFW metroplex for urban weather disaster detection and hazard mitigation. The real-time high-resolution radar observations and products from the DFW network are used and evaluated by a variety of users, including NWS forecasters, emergency managers, and users from transportation, utilities, regional airports, sports, arenas, and the media. In addition, the existing *in-situ* and remote sensors such as WSR-88DP radar and rain gauges are used to generate value-added weather products.

This study explores the potential of ground-based dual-polarization radar network observations for accurate precipitation estimation, and subsequently uses the ground radar-derived products to evaluate and improve satellite-based rainfall retrievals. In particular, an improved S-band dual-polarization radar rainfall methodology has been developed that

can be applied to the operational S-band radar network. Compared to traditional rainfall methodologies, this new algorithm exploits the spatial information content of polarimetric radar observations. It also considers the spatial coherence and quality of hydrometeor classification, as well as the self-aggregation propensity of radar measurements, to produce smooth and clear rainfall products that can be easily interpreted by a variety of users.

In addition, this study presents the principles of high-resolution X-band radar technology and networking for urban hazard mitigation and disaster management, with an emphasis on the warning applications of the DFW dense urban radar network. The high-resolution QPE system developed for the CASA DFW dense urban radar network is detailed. This real-time QPE system is built based on the CASA X-band radar network and a local polarimetric S-band WSR-88DP radar (KFWS radar). The fusion methodology combining both the X-band radar network and KFWS radar observations at different temporal resolutions was developed. The real-time DFW QPE system has been operating for a number of years. Overall, it is very robust and continuously works well without any incidents. The rainfall performance has been demonstrated through comparison between DFW radar network rainfall estimates and rainfall observations from a rain gauge network. The hourly rainfall products operationally produced by the NWS are also included in the evaluation study, which shows that the CASA DFW QPE system product is superior to both the NWS single- and dual-polarization rainfall products. The real-time DFW rainfall products also serve as input to various hydrologic models for downstream applications including urban flash flood forecasting and streamflow prediction.

Furthermore, this study has developed a machine learning model (DMLP) for radar and satellite precipitation estimation. With the combined passive microwave-based rainfall retrievals and IR data from multiple satellites, the DMLP model attempts to improve the

performance of satellite-based rainfall estimates by incorporating high-resolution high-quality ground radar-derived rainfall products as targets to train the core machine learning model. The prototype architecture of the DMLP model and its urban-scale applications in the DFW metroplex are presented. Preliminary results demonstrated the promising performance of this multi-source precipitation estimation system.

7.2. FUTURE WORK

The following items are suggested for future work in this area of study:

Radar Rainfall Methodology

1) The proposed radar rainfall algorithms need to be tested and evaluated in other precipitation regimes especially in complex terrain with orographic enhancement (e.g., the San Francisco Bay Area).

DMLP-based Precipitation Data Fusion System

1) Preprocessing of ground radar-based rainfall products (i.e., before use for training the DMLP model) could be improved to better reflect storm advection during a combined satellite observation time span.

2) For time frames when PMW-based retrievals are not available, ways of using retrievals from previous or subsequent frames to obtain current estimates should be further investigated.

3) Data collected by newer satellites with higher resolutions (i.e., GOES-R) should be combined to improve the DMLP model-based precipitation product.

BIBLIOGRAPHY

- Abadi, M., and Coauthors, 2015: TensorFlow: Large-Scale Machine Learning on Heterogeneous Systems. URL <http://tensorflow.org/>, software available from tensorflow.org.
- Aonashi, K., J. Awaka, M. Hirose, and Coauthors, 2009: GSMaP Passive Microwave Precipitation Retrieval Algorithm: Algorithm Description and Validation. *Journal of the Meteorological Society of Japan*, **87A**, 119–136.
- Atlas, D., R. C. Srivastava, and R. S. Sekhon, 1973: Doppler Radar Characteristics of Precipitation at Vertical Incidence. *Rev. Geophys.*, **11**, 1–35.
- Aydin, K., V. N. Bringi, and L. Liu, 1995: Rain-Rate Estimation in the Presence of Hail Using S-Band Specific Differential Phase and Other Radar Parameters. *Journal of Applied Meteorology*, **34 (2)**, 404–410.
- Aydin, K., T. A. Seliga, and V. Balaji, 1986: Remote Sensing of Hail with a Dual Linear Polarization Radar. *Journal of Climate and Applied Meteorology*, **25**, 1475–1484.
- Bechini, R., and V. Chandrasekar, 2015: A Semisupervised Robust Hydrometeor Classification Method for Dual-Polarization Radar Applications. *Journal of Atmospheric and Oceanic Technology*, **32 (1)**, 22–47.
- Bharadwaj, N., V. Chandrasekar, and F. Junyent, 2010: Signal Processing System for the CASA Integrated Project I Radars. *Journal of Atmospheric and Oceanic Technology*, **27 (9)**, 1440–1460.
- Brandes, E. A., G. Zhang, and J. Vivekanandan, 2002: Experiments in rainfall estimation with a polarimetric radar in a subtropical environment. *J. Appl. Meteor.*, **41**, 674–685.
- Bringi, V. N., and V. Chandrasekar, 2001: *Polarimetric Doppler Weather Radar: Principles and Applications*. 1st ed., Cambridge University Press.

- Carey, L. D., and S. A. Rutledge, 1996: A Multiparameter Radar Case Study of the Microphysical and Kinematic Evolution of a Lightning Producing Storm. *Meteorology and Atmospheric Physics*, **59** (1), 33–64.
- Caylor, I. J., and V. Chandrasekar, 1996: Time-Varying Ice Crystal Orientation in Thunderstorms Observed with Multiparameter Radar. *IEEE Transactions on Geoscience and Remote Sensing*, **34** (4), 847–858.
- Chandrasekar, V., V. N. Bringi, N. Balakrishnan, and D. S. Zrni, 1990: Error Structure of Multiparameter Radar and Surface Measurements of Rainfall. Part III: Specific Differential Phase. *Journal of Atmospheric and Oceanic Technology*, **7** (5), 621–629.
- Chandrasekar, V., H. Chen, and B. Philips, 2017: Principles of High-Resolution Radar Network for Hazard Mitigation and Disaster Management in Urban Environment. *Journal of the Meteorological Society of Japan*, in press.
- Chandrasekar, V., E. Gorgucci, and G. Scarchilli, 1993: Optimization of Multiparameter Radar Estimates of Rainfall. *Journal of Applied Meteorology*, **32** (7), 1288–1293.
- Chandrasekar, V., R. Keranen, S. Lim, and D. Moisseev, 2013: Recent Advances in Classification of Observations from Dual-polarization Weather Radars. *Atmos. Res.*, **119**, 97–111.
- Chandrasekar, V., Y. Wang, and H. Chen, 2012: The CASA Quantitative Precipitation Estimation System: A Five Year Validation Study. *Nat. Hazards Earth Syst. Sci.*, **12**, 2811–2820.
- Chen, H., and V. Chandrasekar, 2015a: Estimation of Light Rainfall Using Ku-band Dual-Polarization Radar. *IEEE Transactions on Geoscience and Remote Sensing*, **53**, 5197–5208.

- Chen, H., and V. Chandrasekar, 2015b: The Quantitative Precipitation Estimation System for Dallas-Fort Worth (DFW) Urban Remote Sensing Network. *Journal of Hydrology*, **531**, 259–271.
- Chen, H., and V. Chandrasekar, 2016: Validation of NASA’s Global Precipitation Measurement mission with a high-resolution ground radar network. *2016 URSI Asia-Pacific Radio Science Conference (URSI AP-RASC)*, 836–839.
- Chen, H., and V. Chandrasekar, 2018: Real-Time Wind Velocity Retrieval in the Precipitation System Using High-Resolution Operational Multi-radar Network. *Remote Sensing of Aerosols, Clouds, and Precipitation*, T. Islam, Y. Hu, A. Kokhanovsky, and J. Wang, Eds., Elsevier, 315–339.
- Chen, H., V. Chandrasekar, and R. Bechini, 2017a: An Improved Dual-Polarization Radar Rainfall Algorithm (DROPS2.0): Application in NASA IFloodS Field Campaign. *Journal of Hydrometeorology*, **18** (4), 917–937.
- Chen, H., S. Lim, V. Chandrasekar, and B.-J. Jang, 2017b: Urban Hydrological Applications of Dual-Polarization X-Band Radar: Case Study in Korea. *Journal of Hydrologic Engineering*, **22** (5), E5016 001.
- Chumchean, S., A. Seed, and A. Sharma, 2004: Application of Scaling in Radar Reflectivity for Correcting Range-Dependent Bias in Climatological Radar Rainfall Estimates. *Journal of Atmospheric and Oceanic Technology*, **21** (10), 1545–1556.
- Cifelli, R., and V. Chandrasekar, 2010: Dual-polarization radar rainfall estimation. *Rainfall: State of the Science. Geophys. Monogr.*, **191**, Amer. Geophys. Union, 105–126.
- Cifelli, R., V. Chandrasekar, H. Chen, and L. E. Johnson, 2017: High Resolution Radar Quantitative Precipitation Estimation in the San Francisco Bay Area: Rainfall Monitoring for the Urban Environment. *Journal of the Meteorological Society of Japan*, (in press).

- Cifelli, R., V. Chandrasekar, S. Lim, P. C. Kennedy, Y. Wang, and S. A. Rutledge, 2011: A New Dual-Polarization Radar Rainfall Algorithm: Application in Colorado Precipitation Events. *Journal of Atmospheric and Oceanic Technology*, **28** (3), 352–364.
- Cressman, G. P., 1959: An Operational Objective Analysis System. *Monthly Weather Review*, **87** (10), 367–374.
- Ferraro, R. R., 1997: Special Sensor Microwave Imager Derived Global Rainfall Estimates for Climatological Applications. *Journal of Geophysical Research: Atmospheres*, **102**, 16 715–16 735.
- Fritsch, F. N., and R. E. Carlson, 1980: Monotone piecewise cubic interpolation. *SIAM J. Numer. Anal.*, **17** (2), 238–246.
- Fulton, R. A., J. P. Breidenbach, D.-J. Seo, D. A. Miller, and T. O’Bannon, 1998: The WSR-88D Rainfall Algorithm. *Weather and Forecasting*, **13** (2), 377–395.
- Giangrande, S. E., and A. V. Ryzhkov, 2008: Estimation of Rainfall Based on the Results of Polarimetric Echo Classification. *Journal of Applied Meteorology and Climatology*, **47** (9), 2445–2462.
- Glorot, X., A. Bordes, and Y. Bengio, 2011: Deep Sparse Rectifier Neural Networks. *Proceedings of the Fourteenth International Conference on Artificial Intelligence and Statistics*, 315–323.
- Gonzalez, R., and R. Woods, 2002: *Digital Image Processing*. 2nd ed., Prentice Hall, 793 pp.
- Gorgucci, E., and L. Baldini, 2015: Influence of Beam Broadening on the Accuracy of Radar Polarimetric Rainfall Estimation. *Journal of Hydrometeorology*, **16** (3), 1356–1371.
- Habib, E., W. F. Krajewski, and A. Kruger, 2001: Sampling Errors of Tipping-Bucket Rain Gauge Measurements. *Journal of Hydrologic Engineering*, **6** (2), 159–166.

- Hong, Y., C. D. Kummerow, and W. S. Olson, 1999: Separation of Convective and Stratiform Precipitation Using Microwave Brightness Temperature. *Journal of Applied Meteorology*, **38** (8), 1195–1213.
- Hou, A. Y., and Coauthors, 2014: The Global Precipitation Measurement Mission. *Bulletin of the American Meteorological Society*, **95** (5), 701–722.
- Hubbert, J., and V. N. Bringi, 1995: An Iterative Filtering Technique for the Analysis of Copolar Differential Phase and Dual-Frequency Radar Measurements. *Journal of Atmospheric and Oceanic Technology*, **12** (3), 643–648.
- Huffman, G. J., and Coauthors, 2007: The TRMM Multisatellite Precipitation Analysis (TMPA): Quasi-Global, Multiyear, Combined-Sensor Precipitation Estimates at Fine Scales. *Journal of Hydrometeorology*, **8** (1), 38–55.
- Humphrey, M. D., J. D. Istok, J. Y. Lee, J. A. Hevesi, and A. L. Flint, 1997: A New Method for Automated Dynamic Calibration of Tipping-Bucket Rain Gauges. *Journal of Atmospheric and Oceanic Technology*, **14** (6), 1513–1519.
- Janowiak, J. E., R. J. Joyce, and Y. Yarosh, 2001: A RealTime Global HalfHourly Pixel-Resolution Infrared Dataset and Its Applications. *Bulletin of the American Meteorological Society*, **82** (2), 205–217.
- Joyce, R. J., J. E. Janowiak, P. A. Arkin, and P. Xie, 2004: CMORPH: A method that produces global precipitation estimates from passive microwave and infrared data at high spatial and temporal resolution. *Journal of Hydrometeorology*, **5**, 487–503.
- Junyent, F., and V. Chandrasekar, 2009: Theory and Characterization of Weather Radar Networks. *Journal of Atmospheric and Oceanic Technology*, **26** (3), 474–491.

- Junyent, F., and V. Chandrasekar, 2016: An Examination of Precipitation Using CSUCHILL Dual-Wavelength, Dual-Polarization Radar Observations. *Journal of Atmospheric and Oceanic Technology*, **33** (2), 313–329.
- Junyent, F., V. Chandrasekar, D. McLaughlin, E. Insanic, and N. Bharadwaj, 2010: The CASA Integrated Project 1 networked radar system. *Journal of Atmospheric and Oceanic Technology*, **27**, 61–78.
- Kidd, C., A. Becker, G. J. Huffman, C. L. Muller, P. Joe, G. Skofronick-Jackson, and D. Kirschbaum, 2017: So, How Much of the Earths Surface Is Covered by Rain Gauges? *Bulletin of the American Meteorological Society*, **98** (1), 69–78.
- Kidd, C., D. R. Kniveton, M. C. Todd, and T. J. Bellerby, 2003: Satellite Rainfall Estimation Using Combined Passive Microwave and Infrared Algorithms. *Journal of Hydrometeorology*, **4** (6), 1088–1104.
- Kidd, C., and V. Levizzani, 2011: Status of Satellite Precipitation Retrievals. *Hydrology and Earth System Sciences*, **15** (4), 1109–1116.
- Kirstetter, P., and Coauthors, 2012: Toward a Framework for Systematic Error Modeling of Spaceborne Precipitation Radar with NOAA/NSSL Ground RadarBased National Mosaic QPE. *Journal of Hydrometeorology*, **13** (4), 1285–1300.
- Kitzmilller, D., S. V. Cooten, and Coauthors, 2011: Evolving Multisensor Precipitation Estimation Methods: Their Impacts on Flow Prediction Using a Distributed Hydrologic Model. *Journal of Hydrometeorology*, **12** (6), 1414–1431.
- Kubota, T., S. Shige, H. Hashizume, K. Aonashi, N. Takahashi, and Coauthors, 2007: Global Precipitation Map Using Satellite-Borne Microwave Radiometers by the GSMaP Project: Production and Validation. *IEEE Transactions on Geoscience and Remote Sensing*, **45** (7), 2259–2275.

- Kummerow, C., Y. Hong, W. S. Olson, and Coauthors, 2001: The Evolution of the Goddard Profiling Algorithm (GPROF) for Rainfall Estimation from Passive Microwave Sensors. *Journal of Applied Meteorology*, **40** (11), 1801–1820.
- Kummerow, C., J. Simpson, D. Thiele, and Coauthors, 2000: The Status of the Tropical Rainfall Measuring Mission (TRMM) after Two Years in Orbit. *Journal of Applied Meteorology*, **39** (12), 1965–1982.
- LeCun, Y., Y. Bengio, and G. Hinton, 2015: Deep learning. *Nature*, **521**, 436–444.
- Lim, S., and V. Chandrasekar, 2016: A Robust Attenuation Correction System for Reflectivity and Differential Reflectivity in Weather Radars. *IEEE Trans. Geoscience and Remote Sensing*, **54** (3), 1727–1737.
- Lim, S., V. Chandrasekar, and V. N. Bringi, 2005: Hydrometeor classification system using dual-polarization radar measurements: model improvements and in situ verification. *IEEE Trans. Geoscience and Remote Sensing*, **43** (4), 792–801.
- Liu, H., and V. Chandrasekar, 2000: Classification of Hydrometeors Based on Polarimetric Radar Measurements: Development of Fuzzy Logic and Neuro-Fuzzy Systems, and In Situ Verification. *Journal of Atmospheric and Oceanic Technology*, **17** (2), 140–164.
- Liu, Z., 2016: Comparison of Integrated Multisatellite Retrievals for GPM (IMERG) and TRMM Multisatellite Precipitation Analysis (TMPA) Monthly Precipitation Products: Initial Results. *Journal of Hydrometeorology*, **17** (3), 777–790.
- Marshall, J. S., and W. M. K. Palmer, 1948: The Distribution of Raindrops with Size. *Journal of Meteorology*, **5** (4), 165–166.
- McCulloch, W. S., and W. Pitts, 1943: A Logical Calculus of the Ideas Immanent in Nervous Activity. *Bulletin of Mathematical Biophysics*, **5** (4), 115–133.

- McLaughlin, D., D. Pepyne, and Coauthors, 2009: Short-wavelength technology and the potential for distributed networks of small radar systems. *Bull. Amer. Meteor. Soc.*, **90**, 1797–1817.
- Miller, L. J., and R. G. Strauch, 1974: A Dual Doppler Radar Method for the Determination of Wind Velocities within Precipitating Weather Systems. *Remote Sensing of Environment*, **3** (4), 219–235.
- Miller, S. W., P. A. Arkin, and R. Joyce, 2001: A combined microwave/infrared rain rate algorithm. *International Journal of Remote Sensing*, **22** (17), 3285–3307.
- Nair, V., and G. E. Hinton, 2010: Rectified Linear Units Improve Restricted Boltzmann Machines. *Proceedings of the 27th International Conference on International Conference on Machine Learning*, 807–814.
- Nepor, V., and B. Sevruk, 1999: Estimation of Wind-Induced Error of Rainfall Gauge Measurements Using a Numerical Simulation. *Journal of Atmospheric and Oceanic Technology*, **16** (4), 450–464.
- Nguyen, C. M., D. N. Moisseev, and V. Chandrasekar, 2008: A Parametric Time Domain Method for Spectral Moment Estimation and Clutter Mitigation for Weather Radars. *Journal of Atmospheric and Oceanic Technology*, **25** (1), 83–92.
- NRC, National Research Council 2005: *Flash Flood Forecasting over Complex Terrain: with an Assessment of the Sulphur Mountain NEXRAD in Southern California*. National Academy Press, 206pp.
- Pei, B., F. Y. Testik, and M. Gebremichael, 2014: Impacts of Raindrop Fall Velocity and Axis Ratio Errors on Dual-Polarization Radar Rainfall Estimation. *Journal of Hydrometeorology*, **15** (5), 1849–1861.

- Petersen, W. A., and Coauthors, 1999: Mesoscale and Radar Observations of the Fort Collins Flash Flood of 28 July 1997. *Bulletin of the American Meteorological Society*, **80** (2), 191–216.
- Ray, P. S., C. L. Ziegler, W. Bumgarner, and R. J. Serafin, 1980: Single- and Multiple-Doppler Radar Observations of Tornadic Storms. *Monthly Weather Review*, **108** (10), 1607–1625.
- Ryzhkov, A. V., 2007: The Impact of Beam Broadening on the Quality of Radar Polarimetric Data. *Journal of Atmospheric and Oceanic Technology*, **24** (5), 729–744.
- Ryzhkov, A. V., M. Diederich, P. Zhang, and C. Simmer, 2014: Potential Utilization of Specific Attenuation for Rainfall Estimation, Mitigation of Partial Beam Blockage, and Radar Networking. *Journal of Atmospheric and Oceanic Technology*, **31** (3), 599–619.
- Ryzhkov, A. V., T. J. Schuur, D. W. Burgess, P. L. Heinselman, S. E. Giangrande, and D. S. Zrnic, 2005: The Joint Polarization Experiment: Polarimetric Rainfall Measurements and Hydrometeor Classification. *Bulletin of the American Meteorological Society*, **86** (6), 809–824.
- Schwaller, M. R., and K. R. Morris, 2011: A Ground Validation Network for the Global Precipitation Measurement Mission. *Journal of Atmospheric and Oceanic Technology*, **28** (3), 301–319.
- Seo, B.-C., B. Dolan, W. F. Krajewski, S. A. Rutledge, and W. Petersen, 2015: Comparison of Single- and Dual-PolarizationBased Rainfall Estimates Using NEXRAD Data for the NASA Iowa Flood Studies Project. *Journal of Hydrometeorology*, **16** (4), 1658–1675.
- Sorooshian, S., K. Hsu, X. Gao, H. V. Gupta, B. Imam, and D. Braithwaite, 2000: Evaluation of PERSIANN System SatelliteBased Estimates of Tropical Rainfall. *Bulletin of the American Meteorological Society*, **81** (9), 2035–2046.

- Tokay, A., D. Wolff, and W. Petersen, 2014: Evaluation of the New Version of the Laser-Optical Disdrometer, OTT Parsivel². *Journal of Atmospheric and Oceanic Technology*, **31 (6)**, 1276–1288.
- Turk, F. J., P. Arkin, M. R. P. Sapiano, and E. E. Ebert, 2008: Evaluating High-Resolution Precipitation Products. *Bulletin of the American Meteorological Society*, **89 (12)**, 1911–1916.
- Turk, F. J., and S. D. Miller, 2005: Toward Improved Characterization of Remotely Sensed Precipitation Regimes with MODIS/AMSR-E Blended Data Techniques. *IEEE Transactions on Geoscience and Remote Sensing*, **43 (5)**, 1059–1069.
- Ulbrich, C. W., 1983: Natural Variations in the Analytical Form of the Raindrop Size Distribution. *Journal of Climate and Applied Meteorology*, **22 (10)**, 1764–1775.
- Ushio, T., K. Sasashige, T. Kubota, S. Shige, and Coauthors, 2009: A Kalman Filter Approach to the Global Satellite Mapping of Precipitation (GSMaP) from Combined Passive Microwave and Infrared Radiometric Data. *Journal of the Meteorological Society of Japan*, **87A**, 137–151.
- Vicente, G. A., S. R. A., and M. P. Menzel, 1998: The Operational GOES Infrared Rainfall Estimation Technique. *Bulletin of the American Meteorological Society*, **79 (9)**, 1883–1898.
- Wang, Y., and V. Chandrasekar, 2009: Algorithm for Estimation of the Specific Differential Phase. *Journal of Atmospheric and Oceanic Technology*, **26 (12)**, 2565–2578.
- Waterman, P. C., 1965: Matrix formulation of electromagnetic scattering. *Proc. IEEE*, **53**, 805–812.
- Willie, D., H. Chen, V. Chandrasekar, R. Cifelli, C. Campbell, D. Reynolds, S. Matrosov, and Y. Zhang, 2017: Evaluation of Multisensor Quantitative Precipitation Estimation in Russian River Basin. *Journal of Hydrologic Engineering*, **22 (5)**, E5016002.

Xie, P., R. Joyce, S. Wu, S.-H. Yoo, Y. Yarosh, F. Sun, and R. Lin, 2017: Reprocessed, Bias-Corrected CMORPH Global High-Resolution Precipitation Estimates from 1998. *Journal of Hydrometeorology*, **18** (6), 1617–1641.

Zhang, J., K. Howard, and Coauthors, 2011: National Mosaic and Multi-Sensor QPE (NMQ) System: Description, Results, and Future Plans. *Bulletin of the American Meteorological Society*, **92** (10), 1321–1338.